Robust design of lightweight wood-based systems in linear vibroacoustics

Corentin Coguenanff

UNIVERSITE PARIS-EST

Ecole doctorale Sciences, Ingénierie et Environnement

Thèse de doctorat

Spécialité : Mécanique

Corentin COGUENANFF

Conception robuste aux incertitudes des systèmes légers bois en vibro-acoustique linéaire

Robust design of lightweight wood-based systems in linear vibroacoustics

---

Soutenue publiquement le 22 octobre 2015 devant le jury composé de:

Mme Delphine BARD	*examinatrice*
M. Christophe DESCELIERS	*directeur de thèse*
M. Jean-François DEÜ	*rapporteur*
Mme Béatrice FAVERJON	*rapportrice*
M. Philippe JEAN	*co-directeur de thèse*
M. Marc MIGNOLET	*examinateur*

Remerciements

Achever la rédaction de son mémoire de thèse se voudrait être un jalon. La clôture d'un volume qui annonce le commencement d'un autre. Je prends alors le temps de retourner aux première pages et de me demander, un peu surpris, par quel douteux concours de circonstances le personnage que je fus il y a huit ans a-t-il pu devenir celui que je suis aujourd'hui. Dans cette démarche, il me tient à coeur de remercier certains et saluer d'autres parmi ceux avec qui le temps s'est écoulé. En tout premier lieu je pense à mes parents et grand-parents qui, de par leur exemple, m'ont donné la plus précieuse des leçon, de celles qui ne sont pas imposées mais s'imposent d'elles mêmes. Avec une autre émotion je pense à la petite troupe d'amis des débuts, amas hétéroclite de naufragés post-bacs avec qui, entre autres aventures, nous avons su rester maigres en nous retrouvant au restaurant universitaire jour après jour. Enfin, plus que tout, je pense à Emilie. D'un cheminement douteux elle fait une évidence.

Au regard de ces trois dernières années, je souhaiterais particulièrement remercier Catherine Guigou pour m'avoir fait confiance, donné la chance de pouvoir continuer à apprendre et surtout pour n'avoir jamais ménagé son temps. D'autre part je remercie Christophe Desceliers pour son implication de tous les jours, sa sympathie et sa patience dans l'épreuve face à un certain doctorant récalcitrant. Dans le même temps je remercie et salue Philippe Jean pour sa passion, sa disponibilité et son inépuisable réserve de cas de validation. Je remercie également Nicolas Picard et Pascal Ducruet, complices des braquages de buffets après de longues et froides journées de mesure, pour leur aide indispensable au bon déroulement des phases expérimentales. Finalement, je salue les différents doctorants avec qui ont été partagées ces années de hauts et de bas, Dang et sa petite famille, Xavier, Alexandre, Olivier, Hussein, Tien et Nicolas.

J'adresse également mes remerciements à Marc Mignolet pour m'avoir fait l'honneur de prendre part au jury, Béatrice Faverjon et Jean-François Deü pour avoir accepté d'être rapporteurs de ce mémoire et Delphine Bard pour avoir accepté d'évaluer ce travail. Enfin, je remercie Christian Soize pour sa présence lors de la soutenance, le temps qu'il a pu dédier à m'orienter ainsi que pour sa passion contagieuse.

Résumé en français

Ce travail de recherche vise à définir des méthodologies pour la prédiction robuste et l'optimisation de la performance acoustique, aux basses fréquences, de systèmes séparatifs dits "légers" du bâtiment. Dans les faits, acceptation et demandes croissantes sont observées au cours des dernières décennies envers la construction bois multi-étages. Cependant, au sein d'une industrie du bâtiment bien structurée autour de la construction dite "lourde", les principes constructifs centrés autour du bois représentent un défi industriel dans de nombreux domaines, parmi lesquels l'évaluation de la qualité acoustique. Ainsi, et malgré un encouragement par des politiques publiques [1] pour atteindre un objectif de 20 % de bois au sein de la construction en France d'ici à 2020, la part globale de la construction légère augmente difficilement [2]. Pourtant, les aspects positifs associés couvrent un large éventail, combinant qualités thermiques intrinsèques, matériaux durables, fabrication industrielle modulaire, rapidité de montage, etc. En particulier, la préfabrication en série de systèmes légers permet un contrôle strict de la qualité et une gestion des ressources améliorée, ouvrant dans le même temps la voie à des processus d'optimisation de structure. En ce qui concerne le confort acoustique, la principale source de complaintes du point de vue des concepteurs résulte du manque de données ou de retours d'expériences, mais aussi de l'absence de méthodes prédictives à un stade précoce de la conception, ce qui a la plupart du temps pour effet un rejet pur et simple des projets ou bien des solutions coûteuses et surdimensionnées. En conséquence, des projets de recherche nationaux ou internationaux ont été initiés (en Europe : Acoubois, AkuLite, AcuWood, COST, Silent Timber Build) pour enrichir la connaissance des structure légères et des principes constructifs à base de bois, et dans le même temps de communiquer les enseignements acquis au cours de ces recherches.

Par suite, une méthodologie a été introduite dans le cadre du COST Action FP0702 (Coopération européenne en science et technologie) [3] pour la prédiction de la performance acoustique à l'échelle du bâtiment. L'approche initiale a été introduite dans [4] comme un moyen d'étendre la méthode SEA (Statistical Energy Analysis) incluse dans le corpus normatif actuel [5] et largement utilisé pour les constructions lourdes. En particulier, une mise à jour des normes NF EN 12354-1 (relative à l'isolement au bruit aérien) et NF EN 12354-2 (relative à l'isolement au bruit d'impact), pour la construction légère, est actuellement soumise à examen. De telles approches nécessitent des indices de performance associés aux chemins de transmission directs des différents systèmes séparatifs mis en oeuvre dans le bâtiment évalué. À l'heure actuelle, ces indices associés à la performance individuelle des systèmes proviennent de mesures expérimentales en laboratoire. Le défi scientifique réside alors dans la grande diversité des systèmes constructifs bois dont les performances doivent être évaluées. En conséquence, le besoin en méthodes prédictives capables de prendre en compte la complexité structurelle de ces systèmes afin d'évaluer leur performance acoustique individuelle est le facteur de motivation pour cette recherche.

Tel que mis en avant par de nombreux chercheurs au cours des années (de manière non exhaustive dans [6–13]), la performance aux basses fréquences de ces structures est critique en ce qui concerne l'acceptation par les habitants. En effet, les mobilités mécaniques de ces dernières (qui sont plus importantes par comparaison avec les systèmes lourds), associées à des niveaux élevés d'énergie injectée dans les basses fréquences (bruits de pas, systèmes audio ou équipements tel que réseau sanitaire, etc.), génèrent insatisfactions ou plaintes si la question de la performance acoustique n'est pas soigneusement traitée. Par suite, les chemins de transmission directs au travers de ces systèmes sont généralement prédominants par rapport aux voies de transmission latérales et motivent une recherche approfondie à l'échelle du système. En outre, les indices uniques de performance sont, dans le cas des systèmes séparatifs légers, dominés majoritairement par les premiers tiers d'octave jusqu'à 200 Hz. En guise

d'argument final, il peut être noté que les éventuelles tentatives de correction acoustique après-coup telles que l'ajout de revêtements de sol, de planchers flottants ou de plafonds découplés sont montrées inefficaces aux très basses fréquences (voir par exemple [7]), ce qui plaide en faveur d'une démarche qui doit être menée lors la phase de conception initiale.

Enfin, compte tenu de la large gamme de performances observées aux basses fréquences pour des systèmes nominalement identiques [14–17], de la complexité des systèmes assemblés et du questionnement récurrent sur l'effet des conditions de mise en oeuvre [18, 19] et, aspect non négligeable, de la nature inhomogène des matériaux de construction légers, les incertitudes constituent une thématique centrale [8, 10, 20, 21]. A la connaissance de l'auteur, seules des approches *a posteriori* sont à ce jour utilisées pour l'évaluation de la robustesse de la performance acoustique des systèmes du bâtiment, de sorte que les incertitudes en sortie de modèle ne dépendent pas de l'état ou des propriétés du système mécanique. En conséquence, les différentes sources d'incertitude ne sont, à l'heure actuelle, pas clairement identifiées et par conséquent ne peuvent pas être propagées aux sorties de modèles numériques ni être intégrées aux processus de conception.

En accord avec le contexte précédemment introduit, et en particulier compte tenu de l'état de l'art des modèles existants et du manque général de connaissances sur le comportement vibro-acoustique associé à de tels systèmes dans la gamme de fréquences d'intérêt, une stratégie de recherche est définie. Tout d'abord, deux efforts de modélisation doivent être menés, le premier portant sur la construction d'un modèle numérique déterministe pertinent vis à vis du problème vibro-acoustique basses fréquences associé aux structures légères, et le second étant dédié à la construction de modèles probabilistes pour les variables aléatoires du problème. En effet, la prédiction de la performance acoustique associée à l'isolement au bruit aérien et au bruit d'impact nécéssite un modèle numérique incluant une description détaillée de domaines structuraux, acoustiques et poroélastiques ainsi que de leurs couplages. A ce titre, la méthode des éléments finis est choisie pour la modélisation de ce problème multi-physique/multi-domaine. Le cadre de la théorie de l'élasto-acoustique linéaire [22, 23] est choisi pour la modélisation des parties structurales et des cavités acoustiques internes, les milieux poroélastiques étant quant à eux modélisés au travers de la théorie de Biot-Allard [24]. En fonction des propriétés mécaniques de la phase solide du matériau poreux, la formulation utilisant les déplacements de la phase solide et de la phase fluide comme variables d'état est avantageusement remplacée par une formulation de fluide équivalent. De plus, en ce qui concerne les connexions des multiples sous-domaines structuraux mis en oeuvre, le modèle présenté dans [25] pour l'analyse des assemblages autour de configurations rigidement liées est utilisé. Par souci de flexibilité et d'adaptabilité, l'ensemble du code de calcul, mailleur, éléments finis et solveurs sont implementés sous Matlab dans un cadre numérique unifié.

Par suite, le modèle numérique qui résulte de la discrétisation par éléments finis du problème vibro-acoustique appartient à une classe donnée de modèles mathématiques avec des entrées et dont les sorties sont utilisées pour la construction des indicateurs de performance acoustique. En raison du processus de modélisation mathématique-mécanique associé à ces systèmes complexes, il existe des erreurs de modélisation qui induisent la propagation d'incertitudes dites de modèle aux observables, et qui ne peuvent être prises en compte par aucune variation des paramètres d'entrée. Parmi les sources sous-jacentes d'incertitudes dans les références [8, 10, 14–21] existent par conséquent deux types d'incertitudes qui doivent être prises en compte pour obtenir une prédiction robuste. Afin de modéliser et de quantifier les fluctuations statistiques parmi les entrées ou les paramètres de conception (ci-après désignés en tant que paramètres du système), ainsi que les incertitudes de modèle induites par les erreurs de modélisation, il est proposé de suivre l'approche probabiliste généralisée des incertitudes introduite par Soize [26]. Une telle approche consiste à remplacer les matrices généralisées d'un modèle éléments finis de dimension réduite par des matrices aléatoires. Les modèles probabilistes de ces matrices aléatoires sont alors construits à partir de variables aléatoires indépendantes modélisant respectivement les fluctuations statistiques associées aux paramètres du système et aux incertitudes de modèle. En particulier, ces dernières sont modélisées au travers de l'approche probabiliste dite non-paramétrique des incertitudes [27, 28].

Il apparait alors nécéssaire de disposer d'un modèle numérique de dimension réduite pour la con-

struction d'un tel modèle probabiliste. La projection du système linéaire en coordonnées physique sur une base tronquée de dimension minimale nécéssite en particulier la définition d'une stratégie pour la construction d'une telle base. Dans le cadre d'un problème vibroacoustique conventionnel, les stratégies de réduction de modèle sont bien définies et utilisent des séries tronquées de vecteurs propres solutions de problèmes aux valeurs propres généralisés respectivement associés à la structure ou au fluide acoustique interne [22, 23, 29, 30]. De même, la définition d'une telle stratégie a été investiguée dans le cadre de milieux poroélastiques. Historiquement, un premier effort a été dirigé vers les formulations mixtes déplacements/pression [31–34] avec des résultats mitigés en raison d'instabilités ou de problèmes de convergence. L'utilisation de bases modales découplées pour un problème fortement couplé pose également la question de la limite de troncature en fréquence. Dans le même temps, des recherches ont été initiées en direction des formulations symétriques en déplacements/déplacements [35–40], pourtant moins populaires en raison de la performance numérique en solveurs directs des quatre degrés de liberté associés aux formulations mixtes. Ce travail s'inscrit en continuité de ces recherches pour la définition d'une stratégie globale de réduction de modèle par sous-structuration dynamique adaptée aux problèmes vibroacoustiques basses fréquences incluant des milieu poroélastiques tridimensionnels.

Faisant suite à un premier effort de modélisation, de l'information expérimentale est recherchée afin d'enrichir la connaissance mécanique des systèmes séparatifs légers du bâtiment. En particulier, des inconnues sont à lever concernant les propriétés élastiques des matériaux mis en oeuvres, les connexions des différents éléments structuraux et les fluctuations statistiques associées. L'objectif est alors triple. Premièrement, les lois de comportement de matériaux peu ou pas documentés sont identifiées. Dans les faits, la caractérisation mécanique des matériaux légers est la plupart du temps limitée à l'évaluation de la résistance à une charge statique définie par la norme et l'information qui en ressort n'est par conséquent pas suffisante pour une modélisation en dynamique. Deuxièmement, le comportement dynamique des assemblages d'éléments structuraux est caractérisé. En effet, une particularité des systèmes de construction légers est la présence d'un nombre élevé de connexions structurelles. Une étape nécessaire dans la compréhension de leur comportement vibroacoustique consiste à être en mesure de modéliser correctement les chemins de transmission vibatoires. Il est alors montré qu'une prise en compte de la flexibilité des connexions est un prérequis pour une bonne prédiction des fonctions de transfert structurelles. Enfin troisièmement, les hyperparamètres des modèles probabilistes précédemment évoqués vont pouvoir être identifiés. Une démarche expérimentale est alors construite. Afin de s'affranchir autant que possible de l'influence de l'inhomogénéité des matériaux ou de conditions aux limites non-maîtrisées sur les données expérimentales, les mesures sont éffectuées sur des éléments structuraux de taille réelle et suspendus. Une excitation des systèmes considérés permet alors l'extraction d'une information dynamique, sous la forme de mobilités. Par suite, des problèmes inverses déterministes et stochastiques sont construits pour l'identification des paramètres ou hyperparamètres des modèles considérés. En particulier, ces derniers sont obtenus par l'intermédiaire d'une stratégie originale. Deux problèmes de maximisation de la vraissemblance sont construits successivement où le premier, peu coûteux, offre un point de départ avantageux au second.

Enfin, la recherche d'une conception optimale parmi un certain nombre de configurations admissibles, constituées de l'assemblage de divers produits manufacturés et dont les caractéristiques doivent être conformes à la réglementation, revient à résoudre un problème combinatoire. En particulier, en raison des valeurs discrètes prises par les paramètres admissibles, il n'existe pas d'application continue entre l'espace de recherche et la performance objective du système. Dérivées et gradients ne peuvent pas être définis et un algorithme évolutionnaire [41], particulièrement adapté aux espaces de recherche discrets et à l'optimisation multi-objectifs, est choisi et mis en œuvre afin de résoudre des problèmes d'optimisation sous-incertitudes. La définition des fonctions de performance objective associées à l'isolement au bruit aérien et au bruit d'impact est éffectuée dans le but de se conformer autant que possible à la performance résultant des essais normalisés en laboratoire. En particulier, une méthode est présentée pour la construction de l'excitation associée à la machine à choc normalisée.

Contents

1 Introduction

Contents

1.1 Context

The present research aims at defining methodologies for the robust prediction and optimisation of the acoustic performance, at low frequencies, of lightweight wood-based separative systems used within building construction. As a matter of fact, an increasing acceptance and demand over multi-storey wooden buildings was observed during the last decades. However, within a well established heavy construction industry, such building techniques represent an industrial challenge in many areas, among which acoustic quality assessment. Thus, despite being stimulated by public policies [1] to reach the objective of 20% of wood within building construction in France by 2020, the share of lightweight construction struggles to increase [2]. Yet, associated positive aspects range from intrinsic thermal qualities to sustainable materials, possible industrial modular manufacturing, quick assembly etc. In particular, serial prefabricated systems allow gains in quality control and resource management as well as open the way to research spendings into structural optimisation processes. In regard to acoustic comfort, most of the blame, from the designers point of view, comes from the lack of data or feedback but also from the lack of predictive methods at the early design stage, ensuing rejection of the projects or costly overdesigned solutions. By way of consequence, national or international research projects were initiated (in regard to Europe : Acoubois, AkuLite, AcuWood, COST Actions, Silent Timber Build) to enrich scientific knowledge about lightweight wood-based structure as well as to release practical information acquired during the course of such researches.

Thus, a methodology was introduced within the COST Action FP0702 (European Cooperation in Science and Technology) [3] for a prediction of the acoustic performance at the building scale. The initial approach was introduced in [4] as a way to extend the predictive capacity of the first order SEA method (Statistical Energy Analysis) included within the current set of standards [5] and extensively used for heavy constructions. In particular, updated editions of the standards NF EN 12354-1 (airborne sound insulation) et NF EN 12354-2 (impact sound insulation) including lightweight buildings are currently submitted for review. Such approaches require the performances associated with the direct transmission paths of the different separative systems involved within the considered building. At the moment, the respective indices associated with the individual performance of the different lightweight systems derive from experimental measurements in laboratory. The challenge consequently lies in the diversity of lightweight wood-based systems whose performances have to be evaluated. Ensuing, the need for predictive methods able to take into account the structural complexity of those systems in order to evaluate their raw acoustic performance is the motivating factor for this research.

Furthermore, as enlightened by many researchers over the years (such as non-exhaustively in [6–13]), the low frequency performance is critical in regard to lightweight structures acceptance by inhabitants. Indeed, such designs display higher mobilities in comparison with heavy systems which, associated with the high levels of energy in the lower frequency bands injected by footsteps, modern audio devices or building service equipments (such as waste water installations, etc..), yields issues and complaints if not carefully considered. Ensuing, direct transmission paths through separative systems are generally predominant in comparison with lateral transmission paths and motivate for extensive research at the system scale. Besides, the global performance indices in regard to lightweight building systems are dominated in most cases by the performance within the first third octave bands up to 200 Hz. More, potential late system rectifications such as floor coverings, floating floors or decoupled ceilings are shown to be inefficient at very low frequencies (see for example [7]) advocating for early considerations at the design phase. However, it can be noted from the previous reference that the medium to high frequency performance is naturally better than the one displayed by heavy structures.

Finally, given the wide range of performances observed at low frequencies with respect to nominally identical systems [14–17], the complexity of the assembled systems associated with the longtime questionning about workmanship effects [18, 19] and, last but not least, lightweight construction materials which are by-nature non-homogeneous, uncertainties constitute a recurrent thematic in regard to lightweight wood-based systems [8, 10, 20, 21]. To the best knowledge of the author, only output error approaches are used to assess the evaluated performance, such that uncertainties are not dependent on the state or properties of the mechanical system. Following, the different intrinsic sources of uncertainties

are, at the present time, not clearly identified and consequently cannot be propagated to the output of a computational model nor be integrated within the design process.

1.2 Objectives

Given the previous context, the following objectives are defined for this research. The **first objective** consists in defining a computational framework, suited to low frequencies and able to handle the structural complexity inherent to lightweight wood-based building systems. In particular, models need to be constructed in regard to the external excitations of the system according to the standard evaluation of airborne and impact sound insulation in laboratory conditions. That way, part of the individual performance required by the above-mentionned prediction method at the building scale can be obtained. Moreover, outputs of the computational models can be compared with laboratory experimental data. Then, the **second objective** consists in validating the computational models associated with the structural components with experimental measurements. At the same time, variations among experimental data as well as discrepancies with respect to the computational model will be investigated to identify potential sources of uncertainties, can they be associated with system parameters or modeling errors. The **third objective** consequently lies within the modeling of the detected sources of uncertainties and the identification of the associated hyperparameters. Uncertainty quantification can then be performed in order to propagate uncertainties to the observables and to construct confidence regions allowing robust prediction. Finally, the **fifth objective** is, given the computational model constructed for the systems, the probabilistic models constructed and identified with respect to uncertainty sources and external excitation models associated with the standard laboratory evaluation procedures, to be able to identify robust optimal designs.

1.3 Strategy

According to the previously formulated objectives associated with this research, the following strategy is defined. First of all two modeling efforts have to be conducted, the first one in regard to deterministic vibroacoustic computational models suited for lightweight building systems within the low frequency range and the second one in regard to probabilistic modeling. Thus, in regard to the prediction of the acoustic performance associated with airborne and impact sound insulation of the complex systems of interest, a computational model requires a detailed description of structural, acoustic and poroelastic components and their coupling. As such, the finite element method is chosen for the construction of computational models suited for such multi-physics coupled problem. The framework of the classical linear elastoacoustic theory [22, 23] is used with respect to the structure and internal acoustic cavities meanwhile poroelastic media are described through the Biot theory [24]. Moreover, in regard to the structural connections of the multiple involved subparts, the model introduced in [25] and suited for the analysis of assemblies around perfectly tied configurations is used. For the sake of flexibility and adaptability, the whole computational code, mesher and finite elements are implemented in Matlab within a unified software framework.

Ensuing, constructed computational models belong to given classes of mathematical models with inputs and whose outputs will be used for the definition of acoustic performance indicators. Due to the mathematical-mechanical modeling process associated with complex systems, modeling errors exist and induce the propagation of model uncertainties to the output of the computational models, that cannot be taken into account by any variation of the inputs. Among the underlying sources of uncertainties within the references [8, 10, 14–21] consequently exist two types of uncertainties that have to be taken into account to obtain a robust prediction. In order to model and quantify statistical fluctuations among the inputs or design parameters (hereinafter denoted as system parameters) as well as model uncertainties induced by modeling errors, it is proposed to follow the generalized probabilistic approach of uncertainties introduced by Soize [26]. Such an approach consists in substituting the generalized matrices of a reduced order computational model with random matrices, whose probabilistic models involve independent random variables respectively associated with system parameters uncertainties and model

uncertainties. Thus, the prior probabilistic models of such random variables are constructed within the framework of the so-called probabilistic approach of system parameters uncertainties and within the framework of the nonparametric approach of model uncertainties induced by modeling errors [27, 28]. Furthermore, the nonparametric approach requires the introduction of a reduced order computational model resulting from the projection of the linear dynamical system in the physical coordinates onto a basis of reduced dimension. Thus, strategies for the construction of *ad hoc* projection basis associated with structural, acoustic and poroelastic media are investigated within the framework of component mode synthesis methods. The generalized probabilistic approach of uncertainties is subsequently implemented within the previously introduced unified software framework.

Following the first modeling effort, experimental information is sought to enrich the mechanical knowledge of the lightweight building systems, be it about the elastic properties of lightweight materials or the connections of the different structural elements. Indeed, the mechanical characterisation of such materials is most of the time limited to the assessment of the static load resistance requirements defined by the standards and consequently not adapted to advanced dynamical modeling. In order to avoid as much as possible an influence of the materials inhomogeneities or uncertain boundary conditions on the experimental data, the measurement setup involves suspended full scale lightweight elements. Then, an output-error approach is used as kinematic quantities are observed and compared with the ones resulting from the solutions of the computational models. Ensuing from such experimental data, deterministic and stochastic inverse problems are constructed with respect to the identification of system parameters and associated prior probabilistic models.

Finally, seeking for optimal designs among admissible configurations, with respect to such systems constituted of the assembly of engineered products and whose characteristics have to be consistent with the regulation, happen to be equivalent to a combinatorial problem. Thus, due to the discrete values taken by the admissible design parameters, there is no continuous mapping from the search space of the configurations to the space of the fitness functions representative of the objective performance of a system. Consequently, derivatives cannot be defined and the class of evolutionnary algorithm [41], particularly well suited for discrete search spaces, is chosen and implemented in order to solve robust optimisation problems.

1.4 Positioning

In an extensive state of the art [10], authors emphasized on the lack of predictive models able to take into account the complexity of lightweight wood-based systems. In regard to airborne sound insulation, the litterature survey undertaken in [42] converges towards the same conclusions after reviewing many models. As previously mentioned, the challenge with respect to such systems lies in the wide spread of admissible configurations resulting from the combination of varying stiffeners, boards, acoustic cavities or insulating materials, and in particular in the fact that such assemblies do not result in classical multi-layered systems, for which case theory is well established. Thus, resulting systems exhibit various transmission paths between outer layers whose prevalence is *a priori* unknown. Without dwelling at length about the history of the predictive models in building acoustics, [10] summarizes the current expectations in regard to the development of reference predictive methodologies, stating that "in lightweight and/or orthotropic structures the capacity of suggesting new solutions, even inventions, lies in the possibility to simulate details beyond the current practise and beyond the capacity of standard or non-standard simplified methods".

The generality and extensive use of the finite element method in regard to low frequency vibroacoustic problems, such as presented in [22, 23, 29, 30], is then attractive for the development of a reference approach. In particular, over the last decade the simulation of the three dimensional behavior of poroelastic media became more and more affordable due to increasing computational resources. Several finite element formulations were proposed with different choices of primary variables. Equivalent fluid models [24, 43–46], with the scalar pressure in the poroelastic medium as primary variable, were presented at an early stage with the distinction between rigid and limp frame models. Depending on the physical

properties and on the problem, the solid phase, or frame, can be considered infinitely rigid and motionless. This is typically the case when the inertial and viscous couplings are weak and the frame is not submitted to a structural excitation (poroelastic material used as a wall covering for example). When using lightweight limp frame poroelastic materials, such as fibrous, as a filling material for panels, the necessity to take into account the inertial effect of the frame was emphasized [44, 46, 47], in particular at low frequencies. For very limp materials, such as fiberglass, it was shown that the structural coupling is not influencial in the sound transmission at low frequencies [48] and the limp frame model is valid. However, in the general case (such as during an optimisation process) one has to take care of the nature of the coupling [49]. Various formulations for the full description of the poroelastic medium were proposed [45, 50–56], with two distinct fields as the primary variables for the two solid and fluid phases. The displacement field is classicaly used for the solid phase while the displacement field, pressure field or combination of pressure and displacement potential can be used to describe the fluid phase leading, depending on the case, to symmetric or nonsymmetric formulations.

In order to model and quantify uncertainties resulting from statistical fluctuations within physical properties or assembly conditions mentioned in [8, 10, 14–21] it is proposed to follow the methodology introduced by Soize [26–28]. In particular, such methodology involves the so-called nonparametric approach of model uncertainties induced by modeling errors, which consists in introducing prior probabilistic models associated with the uncertain symmetric positive definite generalized matrices of the problem. The extension to various applications was undertaken within extensive series of papers from earthquake engineering [57,58], to elasticity theory [59,60], dynamical substructuring [25,61] or vibroacoustic applications [30, 62] including robust optimisation of vibroacoustic systems [63]. Ensuing the construction of probabilistic models suited to computational dynamics, strategies were defined in regard to the identification of the prior probabilistic model associated with system parameters uncertainties as well as with the nonparametric approach of model uncertainties. Thus, in [64, 65], using experimental kinematic quantities resulting from the forced excitation of a set of uncertain systems, deterministic inverse problems are constructed in order to obtain optimal realisations of the random variable of interest. Then, the maximum likelihood method is used to find the optimal probabilistic model associated with such random variable. Later on, a second strategy was introduced in [26, 66, 67]. With respect to the uncertain boundary value problem of interest, an *ad hoc* stochastic computational model is constructed and indexed on a set of hyperparameters. Then, for given values of the hyperameters it is possible to evaluate the statistics of random outputs of the computational model, using a stochastic solver such as the Monte Carlo method for example. Thus, the likelihood of experimental observables can be determined with respect to random outputs of the aforementioned stochastic computational model in order to find optimal hyperparameters.

A framework for uncertain computational classical vibroacoustics at low frequencies is well established and summarised in [22]. In regard to poroelastic materials, probabilistic approaches were initiated with respect to impedance modelings such as for example in [68–70], but are not considered in this work which is focused on a three dimensional continuum modeling. Following the previous introduction of the generalized approach of uncertainties, there is consequently a need for the definition of a reduced order model suited for poroelastic applications. In the context of classical vibroacoustic problems, methodologies are well defined to obtain reduced order models from the projection on truncated series of eigenvectors which are solutions of distinct generalized eigenvalue problem respectively associated with the structure or the internal acoustic fluid [22, 23, 29, 30]. Similarly, the definition of a general methodology through the resolution of a standard eigenvalue problem or set of eigenvalue problems was investigated for poroelastic media. Over the different formulations that were discussed in the previous paragraph, a first effort was directed towards the mixed displacement pressure formulations [31–34] with mixed results due to unstabilities or convergence problems. The use of decoupled modal basis for a strongly coupled problem also asks the question of the definition of the truncation limit, as a number of eigenvectors out of the frequency band of interest will be involved to ensure the convergence. At the same time, investigations were conducted in regard to the symmetric displacement formulations, less popular due to the computational efficiency with respect to direct solvers, of the four degrees of free-

dom per node mixed formulations. A decoupled eigenvectors basis was proposed in [35, 36] which was showing promising results in terms of convergence but dealt with spurious frequencies in the fluid, inherent to the displacement formulation, in a manner that was not adapted to the simple implementation of a standardized procedure. More recently the symmetry of the formulation was used as an advantage to construct a basis of real coupled eigenvectors in a general way, without assumptions on the material properties or the couplings. In [37] the authors compared, for a two dimensionnal poroelastic medium sample submitted to an prescribed displacement, the convergence rate of different truncated basis with respect to the boundary conditions prescribed for the definition of the eigenvalues problems. They also introduced the idea of mixed fixed-free boundary condition respectively for the solid and fluid phase. In [38–40] the real static limit of the complex frequency dependent operators was used for the definition of a generalized eigenvalue problem involving real matrices but the methodology presented convergence problems and a high eigenmode density.

1.5 Structure of the document

This dissertation is structured as follows and thematics articulate according to Fig 1.1.

Chapter 2 presents the boundary value problem associated with a vibroacoustic system constituted of structural, acoustic and poroelastic components. Sesquilinear forms are detailed and the finite element method yields a computational model in physical coordinates. Depending on poroelastic material properties, an alternative computational model using an equivalent fluid formulation is presented.

Chapter 3 reviews typical lightweight building materials as well as noteworthy particularities or manufacturing process. A deterministic inverse problem is constructed in order to identify optimal realisations of elastic parameters in regard to batches of nominally identical elements.

Chapter 4 focuses on the flexible connections of structural elements. Inverse identification is performed and sets of connection parameters are found to improve the prediction of the mean model. Thus, it is shown that with the knowledge of the elastic properties associated with the different structural components as well as with a good enough characterisation of their connections, transfer mobilities can be predicted over a typical shear panel.

Chapter 5 defines a set of standard eigenvalue problems suited to the construction of a reduced order computational model. In particular, in regard to poroelastic materials modeled as coupled solid and fluid phases with displacements as primary variables, it is shown that an adequate choice of boundary conditions improves the computational efficiency in the sense that a smaller number of eigenvectors has to be computed in comparison with most recent methods.

Chapter 6 presents the generalized probabilistic approach of uncertainties. Prior probabilistic models are constructed in regard to system parameters uncertainties as well as model uncertainties induced by modeling errors. Then, a strategy is introduced for the identification of hyperparameters associated with the typical materials treated in Chapter 3.

Chapter 7 introduces a methodology for the prediction of the airborne sound insulation performance in laboratory conditions. Decoupled room models allow the construction of an external excitation for the previously defined computational models as well as the construction of an objective performance criterion.

Chapter 8 introduces a methodology for the prediction of the impact sound insulation performance in laboratory conditions and defines the external excitation resulting from the standard tapping machine. In particular, a novel approach is presented for the quantification of uncertainties propagating from the structure to the force in the impact case.

Chapter 9 presents optimisation cases and analyses trends among generations of the genetic algorithm. Fitness functions associated with the objective performance are constructed according to most recent findings about inhabitant perceptions.

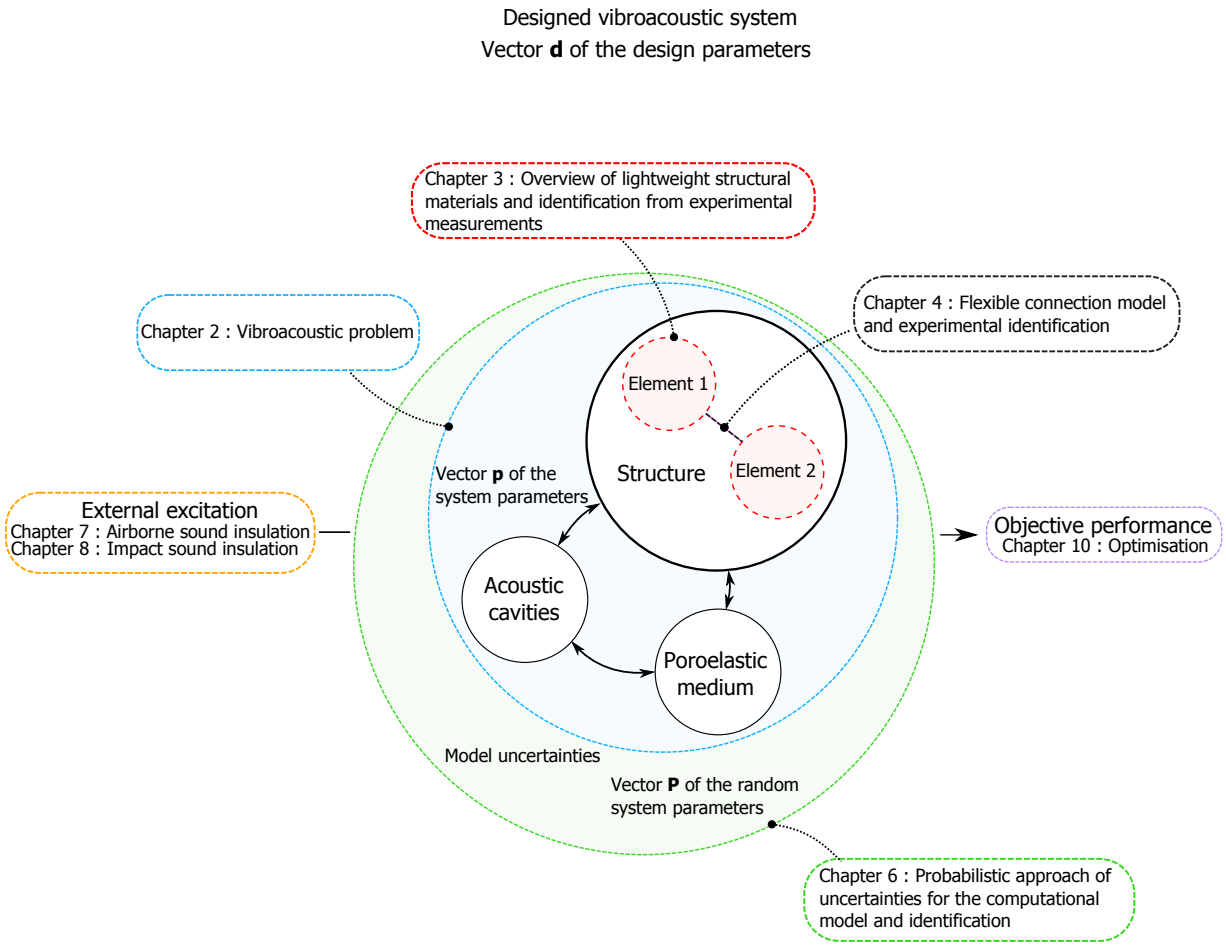

Figure 1.1: Structure of the document.

2
Vibroacoustic problem

Contents

2.1 Introduction

Separative lightweight structures in building constructions, for example walls or floors, are complex assemblies combining the intrinsic properties of each component to meet various constraints: mechanical durability, minimum heat transfer, sound insulation etc. Figure 2.1 gives an example of the geometries and materials that can be encountered within a typical lightweight floor system and highlight the strong structural transmission paths, inherent to most timber based designs and source of most of the insulation problems at low frequencies. A typical lightweight wood-based system is then constituted of a load bearing shear panel consisting in wooden composite boards rigidly connected to a primary wooden frame. Thus, one of the advantages of such design is allowing thermal insulation materials to be comprised within the system, resulting in compact separative solutions. Then, a secondary frame of wooden lath or steel profiles, possibly structurally decoupled from the primary frame, supports the plasterboard facing. Such systems can be set up in parallel in order to obtain double separative solutions with independent primary frames. Three domains of different physical natures are then identified: a solid elastic structure, internal acoustic cavities and poroelastic components. In the following, we focus on giving the hypothesis and details of the mathematical modeling eventually resulting in a computational model.

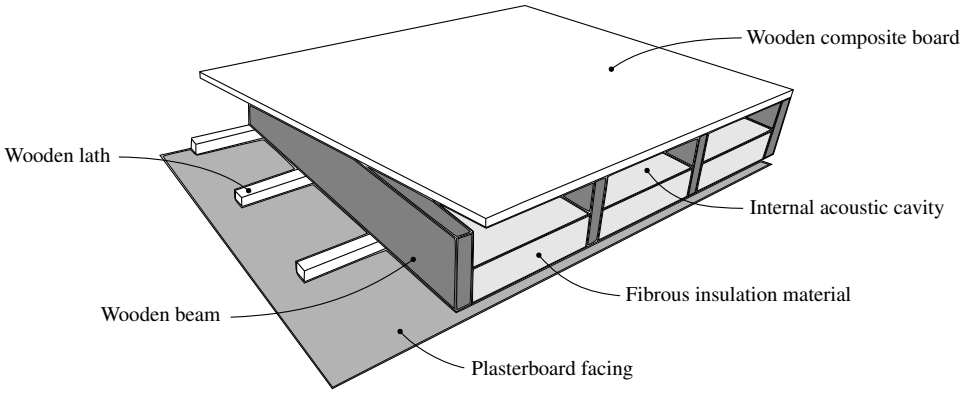

Figure 2.1: Typical lightweight floor system.

2.2 Definition of the vibroacoustic system

Three different physical subdomains occupy respectively the domain Ω^{s} for the viscoelastic structure, Ω^{f} for the internal acoustic fluid medium and Ω^{p} for the poroelastic medium (see Fig. 2.2). Let $\mathbf{u}^{\mathrm{s}}$, $\sigma^{\mathrm{s}}(\mathbf{u}^{\mathrm{s}})$ and $\epsilon^{\mathrm{s}}(\mathbf{u}^{\mathrm{s}})$ respectively be the three dimensional displacement field in Ω^{s}, the Cauchy stress tensor and the strain tensor associated with the structure. Let p be the disturbance of the pressure field in Ω^{f}. Within the general case, the poroelastic medium can be modeled as coupled solid and fluid phases with the classical displacement Biot theory, in which tridimensional displacement fields in the solid and acoustic fluid phases of the poroelastic medium, denoted $\mathbf{u}^{\mathrm{p_s}}$ and $\mathbf{u}^{\mathrm{p_f}}$, are the primary variables. The respective associated stress and strain tensors are denoted $\sigma^{\mathrm{p_s}}(\mathbf{u}^{\mathrm{p_s}}, \mathbf{u}^{\mathrm{p_f}})$, $\sigma^{\mathrm{p_f}}(\mathbf{u}^{\mathrm{p_s}}, \mathbf{u}^{\mathrm{p_f}})$, $\epsilon^{\mathrm{p_s}}(\mathbf{u}^{\mathrm{p_s}})$ and $\epsilon^{\mathrm{p_f}}(\mathbf{u}^{\mathrm{p_f}})$. The total stress tensor in the poroelastic medium is then $\sigma^{\mathrm{P}}(\mathbf{u}^{\mathrm{p_s}}, \mathbf{u}^{\mathrm{p_f}}) = \sigma^{\mathrm{p_s}}(\mathbf{u}^{\mathrm{p_s}}, \mathbf{u}^{\mathrm{p_f}}) + \sigma^{\mathrm{p_f}}(\mathbf{u}^{\mathrm{p_s}}, \mathbf{u}^{\mathrm{p_f}})$. Depending on its physical properties, as seen in [48, 49], the poroelastic medium can also be modeled as an equivalent fluid with the pressure disturbance field p^E as primary variable, which results from a direct simplification of the full displacement model. The coupling equations between the different media are written on the boundaries Π for the structure-acoustic fluid coupling, Γ for the structure-poroelastic coupling and Σ for the acoustic fluid-poroelastic coupling. The interface $\partial\Omega^{\mathrm{s}}_{\mathrm{u}}$ is fixed (homogeneous Dirichlet boundary conditions) and external forces $\mathbf{f}^{\mathrm{s}}$ are applied (Neumann boundary conditions) on $\partial\Omega^{\mathrm{s}}_{\mathrm{n}}$. The problem is treated on the frequency band $\mathbb{B} = [\omega_{min}, \omega_{max}]$ of central frequency ω_{B} such that $0 < \omega_{min} < \omega_{\mathrm{B}} < \omega_{max}$.

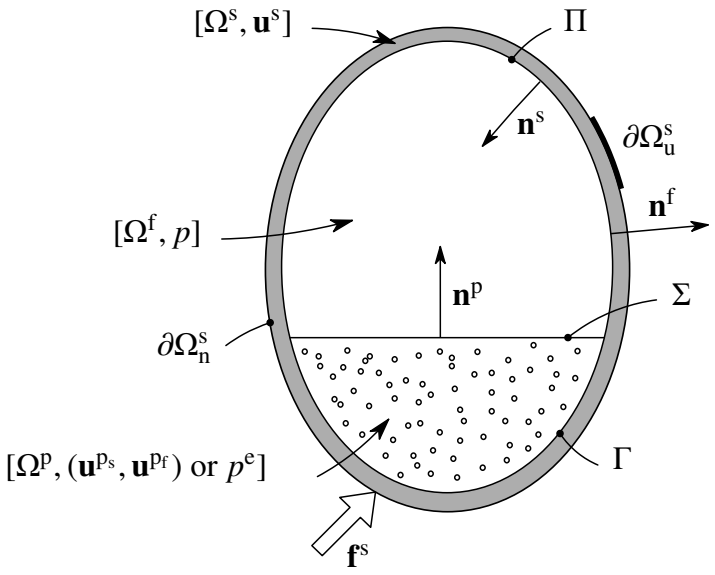

Figure 2.2: Vibroacoustic system with a poroelastic medium.

2.3 Boundary value problem for the vibroacoustic system

2.3.1 Structure

Let ρ^s be the mass density of the elastic structure in Ω^s. The boundary value problem for the solid elastic medium is written, with the implicit summation convention on subscript k and for $j = 1, 2, 3$, as

$$- \omega^2 \rho^s u^s_j - \sigma^s_{jk,k}(\mathbf{u}^s) = 0 \quad \text{in} \quad \Omega^s \,, \tag{2.1}$$

$$u^s_j = 0 \quad \text{on} \quad \partial\Omega^s_u \,, \tag{2.2}$$

$$\sigma^s_{jk}(\mathbf{u}^s)\, n^s_k = f^s_j(\omega) \quad \text{on} \quad \partial\Omega^s_n \,, \tag{2.3}$$

$$\sigma^s_{jk}(\mathbf{u}^s)\, n^s_k = p\, n^f_j \quad \text{on} \quad \Pi \,, \tag{2.4}$$

$$u^s_j = u^{p_s}_j \quad \text{on} \quad \Gamma \,, \tag{2.5}$$

$$u^s_k\, n^s_k = - u^{p_f}_k\, n^p_k \quad \text{on} \quad \Gamma, \tag{2.6}$$

$$\sigma^s_{jk}(\mathbf{u}^s)\, n^s_k = - \sigma^p_{jk}(\mathbf{u}^{p_s}, \mathbf{u}^{p_f})\, n^p_k \quad \text{on} \quad \Gamma \,. \tag{2.7}$$

Moreover, the constitutive equation for the viscoelastic medium with a linear viscous damping term is written, with the implicit summation convention on subscripts l and m, as

$$\sigma^s_{jk}(\mathbf{u}^s) = a^s_{jklm}\, \epsilon^s_{lm}(\mathbf{u}^s) + i\omega\, b^s_{jklm}\, \epsilon^s_{lm}(\mathbf{u}^s) \,, \tag{2.8}$$

in which

$$\epsilon^s_{lm}(\mathbf{u}^s) = \frac{1}{2}(u^s_{l,m} + u^s_{m,l}) \,. \tag{2.9}$$

The linear viscous damping model (Kelvin-Voigt) is constructed such that

$$b^s_{jklm} = \frac{\eta_s}{\omega_B}\, a^s_{jklm} \,, \tag{2.10}$$

where η_s is the structural damping coefficient associated with the frequency band $\mathbb{B}$. Hereinafter, for the derivation of the sesquilinear forms of the problem, the structure is considered free on its boundary Γ with the poroelastic medium. The linear constraints defined by Eqs. (2.5), (2.6) and (2.7) will then be taken into account at the discrete level.

Let C_{Ω^s} be the function space constituted of all the sufficiently differentiable three dimensional complex-valued functions defined on Ω^s, with zero values on $\partial\Omega^s_u$. For any $\mathbf{u}^s$ and $\delta\mathbf{u}^s$ in C_{Ω^s} the usual mass, damping and stiffness sesquilinear forms for the structure are defined by

$$m^s(\mathbf{u}^s, \delta\mathbf{u}^s) = \int_{\Omega^s} \rho^s \, \mathbf{u}^s \cdot \overline{\delta\mathbf{u}^s} \, \mathrm{d}V \,, \tag{2.11}$$

$$d^s(\mathbf{u}^s, \delta\mathbf{u}^s) = \int_{\Omega^s} b^s_{jklm} \, \epsilon^s_{lm}(\mathbf{u}^s) \, \epsilon^s_{jk}(\overline{\delta\mathbf{u}^s}) \, \mathrm{d}V \,, \tag{2.12}$$

$$k^s(\mathbf{u}^s, \delta\mathbf{u}^s) = \int_{\Omega^s} a^s_{jklm} \, \epsilon^s_{lm}(\mathbf{u}^s) \, \epsilon^s_{jk}(\overline{\delta\mathbf{u}^s}) \, \mathrm{d}V \,. \tag{2.13}$$

Moreover, the sequilinear form of the structure-acoustic fluid coupling and the anti linear form of the external loads are respectively defined by

$$c_\Pi(p, \delta\mathbf{u}^s) = \int_\Pi p \, n^f_j \, \overline{\delta u^s_j} \, \mathrm{d}S \,, \tag{2.14}$$

$$f^s(\delta\mathbf{u}^s; \omega) = \int_{\partial\Omega^s_n} f^s_j(\omega) \, \overline{\delta u^s_j} \, \mathrm{d}S \,. \tag{2.15}$$

2.3.2 Internal dissipative acoustic fluid

Let c_0 and ρ^f respectively be the sound velocity and mass density in Ω^f. The boundary value problem is written for $\omega \neq 0$ (see for example [22, 23]) with the implicit summation convention on subscript k as

$$-\omega^2 \, \frac{1}{K^f} \, p - (1 + i\omega\,\tau) \, \frac{1}{\rho^f} \, p_{,kk} = 0 \quad \text{in} \quad \Omega^f \,, \tag{2.16}$$

$$(1 + i\omega\,\tau) \, p_{,k} \, n^f_k = -\omega^2 \, \rho^f \, u^s_k \, n^s_k \quad \text{on} \quad \Pi \,, \tag{2.17}$$

$$(1 + i\omega\,\tau) \, p_{,k} \, n^f_k = -\omega^2 \, \rho^f \, ((1-\phi) \, u^{p_s}_k + \phi \, u^{p_f}_k) \, n^p_k \quad \text{on} \quad \Sigma \,. \tag{2.18}$$

in which $K^f = \rho^f c_0^2$. Parameter τ is used to model the internal acoustic dissipations due to the viscosity of the fluid as well as the dissipations on the boundary layer of the fluid.

Let C_{Ω^f} be the function space constituted of all the sufficiently differentiable complex-valued functions defined on Ω^f. For any p and δp in C_{Ω^f} the usual mass, damping and stiffness sesquilinear forms for the internal acoustic fluid are defined by

$$m^f(p, \delta p) = \frac{1}{K^f} \int_{\Omega^f} p \, \overline{\delta p} \, \mathrm{d}V \,, \tag{2.19}$$

$$d^f(p, \delta p) = \tau \, \frac{1}{\rho^f} \int_{\Omega^f} p_{,k} \, \overline{\delta p_{,k}} \, \mathrm{d}V \,, \tag{2.20}$$

$$k^f(p, \delta p) = \frac{1}{\rho^f} \int_{\Omega^f} p_{,k} \, \overline{\delta p_{,k}} \, \mathrm{d}V \,, \tag{2.21}$$

Moreover, the sesquilinear forms respectively associated with the poroelastic medium solid and fluid phase coupling with the internal acoustic fluid are defined by

$$c^{p_s}_\Sigma(p, \delta\mathbf{u}^{p_s}) = (1-\phi) \int_\Sigma p \, n^f_k \, \overline{\delta u^{p_s}_k} \, \mathrm{d}S \,, \tag{2.22}$$

$$c^{p_f}_\Sigma(p, \delta\mathbf{u}^{p_f}) = \phi \int_\Sigma p \, n^f_k \, \overline{\delta u^{p_f}_k} \, \mathrm{d}S \,. \tag{2.23}$$

2.3.3 Poroelastic medium

The following equations derive from the Biot-Allard theory with the physical quantities, variables and hypothesis detailed in [24]. Let ϕ, σ, α_∞, Λ and Λ' respectively be the intrinsic quantities related

to the porosity, flow resistivity, tortuosity, viscosity and thermal effects and let $\rho^{\mathrm{p_s}}$ be the mass density of the poroelastic medium solid phase material. It should be noted that within the general anisotropic case, σ, α_∞ and related quantities are symmetric second-order tensors [71]. In the following, isotropic poroelastic medium are considered. Among diverse phenomenological models, the Champoux-Allard and Johnson models are respectively chosen for the fluid bulk modulus $\tilde{K}^{\mathrm{f}}(\omega)$ and effective density $\tilde{\rho}^{\mathrm{f}}$. With the standard pressure P_0, heat capacity ratio γ, Prandtl number Pr and dynamic viscosity η_{f} we then have

$$\tilde{K}^{\mathrm{f}}(\omega) = \frac{P_0}{1 - \frac{\gamma-1}{\gamma}\left[1 + \frac{8\eta_{\mathrm{f}}}{i\omega\ \mathrm{Pr}\Lambda'^2\rho^{\mathrm{f}}}\left(1 + \frac{i\omega\ \mathrm{Pr}\Lambda'^2\rho^{\mathrm{f}}}{16\eta_{\mathrm{f}}}\right)^{\frac{1}{2}}\right]^{-1}}\ , \tag{2.24}$$

$$\phi\ \tilde{\rho}^{\mathrm{f}} = \phi\ \rho^{\mathrm{f}} + \rho^a + \frac{\tilde{b}(\omega)}{i\omega}\ , \tag{2.25}$$

Inertial ρ^a and viscous drag $\tilde{b}(\omega)$ coupling factors are defined by

$$\rho^a = \phi\ \rho^{\mathrm{f}}\ (\alpha_\infty - 1)\ , \tag{2.26}$$

$$\tilde{b}(\omega) = \phi^2\sigma\left(1 + \frac{i\omega\ 4\ \alpha_\infty^2\ \eta_{\mathrm{f}}\ \rho^{\mathrm{f}}}{\sigma^2\Lambda^2\phi^2}\right)^{\frac{1}{2}}\ . \tag{2.27}$$

Within the framework of the classical Biot theory with displacements as primary variables for the solid and fluid phases of the poroelastic medium, the boundary value problem in Ω^{p} is written, with an implicit summation on subscript k and for $j = 1, 2, 3$, as

$$-\omega^2\left(((1-\phi)\ \rho^{\mathrm{p_s}} + \rho^a)\ u_j^{\mathrm{p_s}} - \rho^a\ u_j^{\mathrm{p_f}}\right) + i\omega\ \tilde{b}(\omega)\ \left(u_k^{\mathrm{p_s}} - u_k^{\mathrm{p_f}}\right) - \sigma_{jk,k}^{\mathrm{p_s}}(\mathbf{u}^{\mathrm{p_s}}, \mathbf{u}^{\mathrm{p_f}}) = 0 \text{ in } \Omega^{\mathrm{p}}\ , \tag{2.28}$$

$$-\omega^2\left(-\rho^a\ u_j^{\mathrm{p_s}} + (\phi\ \rho^{\mathrm{f}} + \rho^a)\ u_j^{\mathrm{p_f}}\right) + i\omega\ \tilde{b}(\omega)\ \left(-u_j^{\mathrm{p_s}} + u_j^{\mathrm{p_f}}\right) - \sigma_{jk,k}^{\mathrm{p_f}}(\mathbf{u}^{\mathrm{p_s}}, \mathbf{u}^{\mathrm{p_f}}) = 0 \quad \text{in} \quad \Omega^{\mathrm{p}}\ , \tag{2.29}$$

$$u_j^{\mathrm{p_s}} = u_j^{\mathrm{s}} \quad \text{on} \quad \Gamma\ , \tag{2.30}$$

$$u_k^{\mathrm{p_f}}\ n_k^{\mathrm{P}} = -\ u_k^{\mathrm{s}}\ n_k^{\mathrm{s}} \quad \text{on} \quad \Gamma\ , \tag{2.31}$$

$$\sigma_{jk}^{\mathrm{P}}(\mathbf{u}^{\mathrm{p_s}}, \mathbf{u}^{\mathrm{p_f}})\ n_k^{P} = -\ \sigma_{jk}^{\mathrm{s}}(\mathbf{u}^{\mathrm{s}})\ n_k^{\mathrm{s}} \quad \text{on} \quad \Gamma\ , \tag{2.32}$$

$$\sigma_{jk}^{\mathrm{p_s}}(\mathbf{u}^{\mathrm{p_s}}, \mathbf{u}^{\mathrm{p_f}})\ n_k^{\mathrm{p}} = (1-\phi)\ p\ n_j^{\mathrm{f}} \quad \text{on} \quad \Sigma\ , \tag{2.33}$$

$$\sigma_{jk}^{\mathrm{p_f}}(\mathbf{u}^{\mathrm{p_s}}, \mathbf{u}^{\mathrm{p_f}})\ n_k^{\mathrm{p}} = \phi\ p\ n_j^{\mathrm{f}} \quad \text{on} \quad \Sigma\ . \tag{2.34}$$

Moreover, the constitutive equations for both phases of the poroelastic medium, coupled through the potential coupling tensor Q_{jklm}, are written within the framework of the classical displacement formulation [24, 39, 71]. We then have the constitutive equations for the solid phase

$$\sigma_{jk}^{\mathrm{p_s}}(\mathbf{u}^{\mathrm{p_s}}, \mathbf{u}^{\mathrm{p_f}}) = \breve{a}_{jklm}^{\mathrm{p_s}}(\omega)\ \epsilon_{lm}^{\mathrm{p_s}}(\mathbf{u}^{\mathrm{p_s}}) + i\omega\ b_{jklm}^{\mathrm{p_s}}\ \epsilon_{lm}^{\mathrm{p_s}}(\mathbf{u}^{\mathrm{p_s}}) + Q_{jklm}(\omega)\ \epsilon_{lm}^{\mathrm{p_f}}(\mathbf{u}^{\mathrm{p_f}})\ , \tag{2.35}$$

and for the fluid phase

$$\sigma_{jk}^{\mathrm{p_f}}(\mathbf{u}^{\mathrm{p_s}}, \mathbf{u}^{\mathrm{p_f}}) = R_{jklm}(\omega)\ \epsilon_{lm}^{\mathrm{p_f}}(\mathbf{u}^{\mathrm{p_f}}) + Q_{jklm}(\omega)\ \epsilon_{lm}^{\mathrm{p_s}}(\mathbf{u}^{\mathrm{p_s}})\ , \tag{2.36}$$

in which

$$\epsilon_{lm}^{\mathrm{p_s}}(\mathbf{u}^{\mathrm{p_s}}) = \frac{1}{2}(u_{l,m}^{\mathrm{p_s}} + u_{m,l}^{\mathrm{p_s}}) \quad \text{and} \quad \epsilon_{lm}^{\mathrm{p_f}}(\mathbf{u}^{\mathrm{p_f}}) = \frac{1}{2}(u_{l,m}^{\mathrm{p_f}} + u_{m,l}^{\mathrm{p_f}})\ . \tag{2.37}$$

Considering a poroelastic medium with the underlying hypothesis that the frame material at the micro scale is much more stiff than the homogenised elastic material at the macro scale (otherwise see [24, 71] for full expressions), we have

$$\breve{a}_{jklm}^{\mathrm{p_s}}(\omega) = a_{jklm}^{\mathrm{p_s}} + \delta_{jk}\ \delta_{lm}\ \frac{(1-\phi)^2}{\phi}\tilde{K}^{\mathrm{f}}(\omega)\ , \tag{2.38}$$

$$Q_{jklm}(\omega) = \delta_{jk}\ \delta_{lm}\ (1-\phi)\ \tilde{K}^{\mathrm{f}}(\omega)\ , \tag{2.39}$$

$$R_{jklm}(\omega) = \delta_{jk}\ \delta_{lm}\ \phi\ \tilde{K}^{\mathrm{f}}(\omega)\ , \tag{2.40}$$

where δ_{jk} denotes the Kronecker's delta. Tensor $a^{\mathrm{p_s}}_{jklm}$ is the in-vacuo or zero pore pressure elasticity tensor of the homogenised elastic frame. Thus, if one considers viscous damping within the elastic frame, damping tensor $b^{\mathrm{p_s}}_{jklm}$ can be written as

$$b^{\mathrm{p_s}}_{jklm} = \frac{\eta_{\mathrm{p_s}}}{\omega_{\mathrm{B}}}\, a^{\mathrm{p_s}}_{jklm} \,. \tag{2.41}$$

In regard to the derivation of sesquilinear forms and in a similar fashion than for the structure, the poroelastic medium is considered free on its boundary Γ with the structure and linear constraints defined by Eqs. (2.30) and (2.31) will be taken into account at the discrete level. Thus, let $C_{\Omega^{\mathrm{p}}}$ be the function space constituted of all the sufficiently differentiable three dimensional complex-valued functions defined on Ω^{p}. For any $\mathbf{u}^{\mathrm{p_s}}$, $\mathbf{u}^{\mathrm{p_f}}$, $\delta\mathbf{u}^{\mathrm{p_s}}$ and $\delta\mathbf{u}^{\mathrm{p_f}}$ in $C_{\Omega^{\mathrm{p}}}$ the sesquilinear forms associated with the solid and fluid phases of the poroelastic medium and their coupling are respectively defined by, for the mass

$$m^{\mathrm{p_s}}(\mathbf{u}^{\mathrm{p_s}}, \delta\mathbf{u}^{\mathrm{p_s}}) = \left((1-\phi)\,\rho^{\mathrm{p_s}} + \rho^{a}\right) \int_{\Omega^{\mathrm{p}}} u^{\mathrm{p_s}}_j\, \overline{\delta u^{\mathrm{p_s}}_j}\, \mathrm{d}V \,, \tag{2.42}$$

$$m^{\mathrm{p_f}}(\mathbf{u}^{\mathrm{p_f}}, \delta\mathbf{u}^{\mathrm{p_f}}) = \left(\phi\,\rho^{\mathrm{f}} + \rho^{a}\right) \int_{\Omega_{\mathrm{p}}} u^{\mathrm{p_f}}_j\, \overline{\delta u^{\mathrm{p_f}}_j}\, \mathrm{d}V \,, \tag{2.43}$$

$$m^{\mathrm{p_{sf}}}(\mathbf{u}^{\mathrm{p_f}}, \delta\mathbf{u}^{\mathrm{p_s}}) = -\,\rho^{a} \int_{\Omega_{\mathrm{p}}} u^{\mathrm{p_f}}_j\, \overline{\delta u^{\mathrm{p_s}}_j}\, \mathrm{d}V \,, \tag{2.44}$$

for the damping

$$d^{\mathrm{p_s}}(\mathbf{u}^{\mathrm{p_s}}, \delta\mathbf{u}^{\mathrm{p_s}}; \omega) = \int_{\Omega^{\mathrm{p}}} b^{\mathrm{p_s}}_{jklm}\, \epsilon^{\mathrm{p_s}}_{lm}(\mathbf{u}^{\mathrm{p_s}})\, \epsilon^{\mathrm{p_s}}_{jk}(\overline{\delta\mathbf{u}^{\mathrm{p_s}}})\, \mathrm{d}V + \tilde{b}(\omega) \int_{\Omega^{\mathrm{p}}} u^{\mathrm{p_s}}_j\, \overline{\delta u^{\mathrm{p_s}}_j}\, \mathrm{d}V \,, \tag{2.45}$$

$$d^{\mathrm{p_f}}(\mathbf{u}^{\mathrm{p_f}}, \delta\mathbf{u}^{\mathrm{p_f}}; \omega) = \tilde{b}(\omega) \int_{\Omega^{\mathrm{p}}} u^{\mathrm{p_f}}_j\, \overline{\delta u^{\mathrm{p_f}}_j}\, \mathrm{d}V \,, \tag{2.46}$$

$$d^{\mathrm{p_{sf}}}(\mathbf{u}^{\mathrm{p_f}}, \delta\mathbf{u}^{\mathrm{p_s}}; \omega) = -\,\tilde{b}(\omega) \int_{\Omega^{\mathrm{p}}} u^{\mathrm{p_f}}_j \overline{\delta u^{\mathrm{p_s}}_j}\, \mathrm{d}V \,, \tag{2.47}$$

and finally for the stiffness

$$k^{\mathrm{p_s}}(\mathbf{u}^{\mathrm{p_s}}, \delta\mathbf{u}^{\mathrm{p_s}}; \omega) = \int_{\Omega^{\mathrm{p}}} \breve{a}^{\mathrm{p_s}}_{jklm}(\omega)\, \epsilon^{\mathrm{p_s}}_{lm}(\mathbf{u}^{\mathrm{p_s}})\, \epsilon^{\mathrm{p_s}}_{jk}(\overline{\delta\mathbf{u}^{\mathrm{p_s}}})\, \mathrm{d}V \,, \tag{2.48}$$

$$k^{\mathrm{p_f}}(\mathbf{u}^{\mathrm{p_f}}, \delta\mathbf{u}^{\mathrm{p_f}}; \omega) = \int_{\Omega^{\mathrm{p}}} R_{jklm}(\omega)\, \epsilon^{\mathrm{p_f}}_{lm}(\mathbf{u}^{\mathrm{p_f}})\, \epsilon^{\mathrm{p_f}}_{jk}(\overline{\delta\mathbf{u}^{\mathrm{p_f}}})\, \mathrm{d}V \,, \tag{2.49}$$

$$k^{\mathrm{p_{sf}}}(\mathbf{u}^{\mathrm{p_f}}, \delta\mathbf{u}^{\mathrm{p_s}}; \omega) = \int_{\Omega^{\mathrm{p}}} Q_{jklm}(\omega)\, \epsilon^{\mathrm{p_f}}_{lm}(\mathbf{u}^{\mathrm{p_f}})\, \epsilon^{\mathrm{p_s}}_{jk}(\overline{\delta\mathbf{u}^{\mathrm{p_s}}})\, \mathrm{d}V \,. \tag{2.50}$$

2.4 Computational model for the vibroacoustic problem

A computational model is constructed to solve Eqs. (2.1) to (2.50) using the finite element method. Primary variables for the description of the structure and of the internal acoustic fluid repectively are the displacement field $\mathbf{u}^{\mathrm{s}}$ and the acoustic fluid pressure disturbance field p. Primary variables for the description of the poroelastic medium are the solid and fluid phases displacements fields $\mathbf{u}^{\mathrm{p_s}}$ and $\mathbf{u}^{\mathrm{p_f}}$. Ensuing, we have compatible finite element meshes of Ω^{s}, Ω^{f} and Ω^{p} and those fields are interpolated on their nodal values by a finite element basis.

2.4.1 Finite element implementation

The whole finite element procedure as well as the mesher are implemented from scratch in Matlab such that a limited array of input parameters controls the construction of the computational model. Three dimensional eight nodes volumic elements as well as two dimensional four nodes shell elements with normal rotational degree of freedom are used for the discretization of the sesquilinear form associated

with the structure. Those elements are constructed following the references [72–74] in which specific reduced integration of the shear stress with respect to the hexahedron element and a modified flexibility with respect to the shell elements allow to avoid the different locking phenomena inherent to elements with low degree interpolating polynomials. The finite elements involved in the discretization of the acoustic fluid and poroelastic fluid phase are the classical eight nodes isoparametric fully integrated elements. In particular, the finite element implementation with respect to the Biot displacement formulation is validated in Appendix A according to the cases presented in [35] and previously introduced in [75].

2.4.2 Computational model

Let $\mathbb{U}^{\mathrm{s}}$ and $\mathbb{P}$ respectively be the vectors of the nodal values of $\mathbf{u}^{\mathrm{s}}$ on Ω^{s} and p on Ω^{f}. Let $\mathbb{U}^{\mathrm{p}}$ be the vector of the nodal values of $\mathbf{u}^{\mathrm{p_s}}$ and $\mathbf{u}^{\mathrm{p_f}}$ on Ω^{p}. The dynamical system is also dependent on a set of system parameters, some of which are identified as uncertain, assembled into the vector $\mathbf{p} = (p_1, \ldots, p_{n_p})$ belonging to an admissible set $C_{par} \subset \mathbb{R}^{n_p}$ [26]. For any $\omega > 0$, the nominal finite element model of a vibroacoustic system with a poroelastic medium modeled with Biot theory as coupled solid and fluid phases with displacements as primary variables, subjected to an external excitation, is written in the physical coordinates and in the frequency domain as

$$[\mathbb{A}^{\mathrm{s}}(\omega;\mathbf{p})]\,\mathbb{U}^{\mathrm{s}} + [\mathbb{C}_{\Pi}(\mathbf{p})]\,\mathbb{P} = \mathbb{F}^{\mathrm{s}}(\omega;\mathbf{p})\,, \tag{2.51}$$

$$[\mathbb{A}^{\mathrm{f}}(\omega;\mathbf{p})]\,\mathbb{P} + \omega^2[\mathbb{C}_{\Pi}(\mathbf{p})]^{\mathrm{T}}\mathbb{U}^{\mathrm{s}} + \omega^2[\mathbb{C}_{\Sigma}(\mathbf{p})]^{\mathrm{T}}\mathbb{U}^{\mathrm{p}} = 0\,, \tag{2.52}$$

$$[\mathbb{A}^{\mathrm{p}}(\omega;\mathbf{p})]\,\mathbb{U}^{\mathrm{p}} + [\mathbb{C}_{\Sigma}(\mathbf{p})]\,\mathbb{P} = 0\,, \tag{2.53}$$

$$[\mathcal{B}^{\mathrm{s}}]\,\mathbb{U}^{\mathrm{s}} + [\mathcal{B}^{\mathrm{p}}]\,\mathbb{U}^{\mathrm{p}} = 0\,. \tag{2.54}$$

The displacement continuities between the structure and the poroelastic medium defined by Eqs. (2.5), (2.6) or (2.30) and (2.31) are discretized to give Eq. (2.54), a set of linear constraints that can be treated in the general case with Lagrange multiplayers or, depending on the properties of $[\mathcal{B}^{\mathrm{s}}]$ and $[\mathcal{B}^{\mathrm{p}}]$, with equation transformation as presented in [76]. Hereinafter we detail the different properties of the matrices from the computational model as a preamble for the construction of a set of standard eigenvalue problems eventually resulting in a tailored reduction strategy.

Structure

In Eq. (2.51) the $(N_{\mathrm{s}}\times N_{\mathrm{s}})$ complex dynamical stiffness matrix $[\mathbb{A}^{\mathrm{s}}(\omega;\mathbf{p})]$ associated with the structure is defined by

$$[\mathbb{A}^{\mathrm{s}}(\omega;\mathbf{p})] = -\omega^2[\mathbb{M}^{\mathrm{s}}(\mathbf{p})] + i\omega\,[\mathbb{D}^{\mathrm{s}}(\mathbf{p})] + [\mathbb{K}^{\mathrm{s}}(\mathbf{p})]\,, \tag{2.55}$$

where $[\mathbb{M}^{\mathrm{s}}(\mathbf{p})]$, $[\mathbb{D}^{\mathrm{s}}(\mathbf{p})]$ and $[\mathbb{K}^{\mathrm{s}}(\mathbf{p})]$ repectively are the $(N_{\mathrm{s}} \times N_{\mathrm{s}})$ real symmetric positive definite mass, damping and stiffness matrices resulting from the discretization of the sequilinear forms $m^{\mathrm{s}}(\mathbf{u}^{\mathrm{s}}, \delta\mathbf{u}^{\mathrm{s}})$, $d^{\mathrm{s}}(\mathbf{u}^{\mathrm{s}}, \delta\mathbf{u}^{\mathrm{s}})$ and $k^{\mathrm{s}}(\mathbf{u}^{\mathrm{s}}, \delta\mathbf{u}^{\mathrm{s}})$, associated with the structure with fixed interface $\partial\Omega^{\mathrm{s}}_{\mathrm{u}}$ and free interfaces $\partial\Omega^{\mathrm{s}}_{\mathrm{n}}$, Γ and Π. The coupling matrices between the structure and the internal acoustic fluid $[\mathbb{C}_{\Pi}(\mathbf{p})]$ and the vector of the discretized frequency dependent external load onto the structure $\mathbb{F}^{\mathrm{s}}(\omega;\mathbf{p})$ respectively ensue from the discretization of the sesquilinear form $c_{\Pi}(p, \delta\mathbf{u}^{\mathrm{s}})$ and antilinear form $f^{\mathrm{s}}(\delta\mathbf{u}^{\mathrm{s}};\omega)$.

Internal dissipative acoustic fluid

In Eq. (2.52) the $(N_{\mathrm{f}} \times N_{\mathrm{f}})$ complex acoustical dynamic stiffness matrix $[\mathbb{A}^{\mathrm{f}}(\omega;\mathbf{p})]$ is defined by

$$[\mathbb{A}^{\mathrm{f}}(\omega;\mathbf{p})] = -\omega^2[\mathbb{M}^{\mathrm{f}}(\mathbf{p})] + i\omega\,[\mathbb{D}^{\mathrm{f}}(\mathbf{p})] + [\mathbb{K}^{\mathrm{f}}(\mathbf{p})]\,, \tag{2.56}$$

where $[\mathbb{M}^{\mathrm{f}}(\mathbf{p})]$, $[\mathbb{D}^{\mathrm{f}}(\mathbf{p})]$ and $[\mathbb{K}^{\mathrm{f}}(\mathbf{p})]$ repectively are the $(N_{\mathrm{f}}\times N_{\mathrm{f}})$ real symmetric positive definite mass and positive semidefinite damping and stiffness matrices resulting from the discretization of the sequilinear forms $m^{\mathrm{f}}(p, \delta p)$, $d^{\mathrm{f}}(p, \delta p)$ and $k^{\mathrm{f}}(p, \delta p)$, associated with the internal acoustic fluid with rigid boundary.

Poroelastic medium

In Eq. (2.53) the $(N_\mathrm{p} \times N_\mathrm{p})$ complex dynamic stiffness matrix $[\mathbb{A}^\mathrm{p}(\omega;\mathbf{p})]$, associated with both poroelastic medium coupled phases, is defined by

$$[\mathbb{A}^\mathrm{p}(\omega;\mathbf{p})] = -\omega^2[\mathbb{M}^\mathrm{p}(\mathbf{p})] + i\omega\,[\mathbb{D}^\mathrm{p}(\omega;\mathbf{p})] + [\mathbb{K}^\mathrm{p}(\omega;\mathbf{p})]\,, \tag{2.57}$$

in which

$$\begin{gathered}[\mathbb{M}^\mathrm{p}(\mathbf{p})] = \begin{bmatrix} [\mathbb{M}^{\mathrm{p_S}}] & [\mathbb{M}^{\mathrm{p_{SF}}}] \\ [\mathbb{M}^{\mathrm{p_{SF}}}]^\mathrm{T} & [\mathbb{M}^{\mathrm{p_F}}] \end{bmatrix} \quad , \quad [\mathbb{D}^\mathrm{p}(\omega;\mathbf{p})] = \begin{bmatrix} [\mathbb{D}^{\mathrm{p_S}}] & [\mathbb{D}^{\mathrm{p_{SF}}}] \\ [\mathbb{D}^{\mathrm{p_{SF}}}]^\mathrm{T} & [\mathbb{D}^{\mathrm{p_F}}] \end{bmatrix} \\ \text{and} \quad [\mathbb{K}^\mathrm{p}(\omega;\mathbf{p})] = \begin{bmatrix} [\mathbb{K}^{\mathrm{p_S}}] & [\mathbb{K}^{\mathrm{p_{SF}}}] \\ [\mathbb{K}^{\mathrm{p_{SF}}}]^\mathrm{T} & [\mathbb{K}^{\mathrm{p_F}}] \end{bmatrix}\,,\end{gathered} \tag{2.58}$$

where the different block matrices result from the discretization of the sequilinear forms defined by Eqs. (2.42) to (2.50), associated with the poroelastic medium with free interfaces Γ and Σ.

Following, the mass, damping and stiffness matrices $[\mathbb{M}^\mathrm{p}(\mathbf{p})]$, $[\mathbb{D}^\mathrm{p}(\omega;\mathbf{p})]$ and $[\mathbb{K}^\mathrm{p}(\omega;\mathbf{p})]$ respectively are $(N_\mathrm{p} \times N_\mathrm{p})$ real symmetric positive definite and complex frequency dependent matrices. Moreover, according to Eq. (2.45), the matrix $[\mathbb{D}^\mathrm{p}(\omega;\mathbf{p})]$ verifies by construction

$$[\mathbb{D}^\mathrm{p}(\omega;\mathbf{p})] = [\mathbb{D}^\mathrm{p}_1(\mathbf{p})] + \tilde{b}(\omega)\,[\mathbb{D}^\mathrm{p}_2(\mathbf{p})]\,, \tag{2.59}$$

where $[\mathbb{D}^\mathrm{p}_1(\mathbf{p})]$ and $[\mathbb{D}^\mathrm{p}_2(\mathbf{p})]$ are real positive semidefinite matrices. Furthermore, as emphasized in [39], the real standard pressure P_0 is the static limit of the complex effective fluid bulk modulus $\tilde{K}_\mathrm{f}(\omega)$ such that

$$\lim_{\omega\to 0} \tilde{K}_\mathrm{f}(\omega) = P_0\,, \tag{2.60}$$

and the matrix $[\mathbb{K}^\mathrm{p}(\omega;\mathbf{p})]$ can be written as

$$[\mathbb{K}^\mathrm{p}(\omega;\mathbf{p})] = [\mathbb{K}^\mathrm{p}_1(\mathbf{p})] + (\tilde{K}_\mathrm{f}(\omega) - P_0)\,[\mathbb{K}^\mathrm{p}_2(\mathbf{p})]\,, \tag{2.61}$$

where $[\mathbb{K}^\mathrm{p}_1(\mathbf{p})]$ and $[\mathbb{K}^\mathrm{p}_2(\mathbf{p})]$ are real positive semidefinite matrices.

Finally, according to the numbering used in Eq. (2.58), the coupling matrix between the internal acoustic fluid and the poroelastic medium $[\mathbb{C}_\Sigma(\mathbf{p})]$ is written as

$$[\mathbb{C}_\Sigma(\mathbf{p})] = \begin{bmatrix} [\mathbb{C}^{\mathrm{p_S}}_\Sigma] \\ [\mathbb{C}^{\mathrm{p_F}}_\Sigma] \end{bmatrix} \tag{2.62}$$

where the different block matrices ensue from the discretization of the sesquilinear forms $c^{\mathrm{p_S}}_\Sigma(p, \delta\mathbf{u}^{\mathrm{p_S}})$ and $c^{\mathrm{p_F}}_\Sigma(p, \delta\mathbf{u}^{\mathrm{p_F}})$ defined by Eqs. (2.22) and (2.23).

2.5 Alternative computational model with limp frame poroelastic medium modeled as an equivalent fluid

Let $\mathbb{P}^\mathrm{e}$ be the vectors of the nodal values of the equivalent fluid pressure disturbance field p^e in Ω^p. Ensuing the classical derivations (see [24, 52]), briefly summarized in Appendix B, for any $\omega > 0$, the nominal finite element model of a vibroacoustic system with a limp frame poroelastic medium modeled as an equivalent fluid, subjected to an external excitation, is written in the physical coordinates and in the frequency domain as

$$[\mathbb{A}^\mathrm{s}(\omega;\mathbf{p})]\,\mathbb{U}^\mathrm{s} + [\mathbb{C}_\Pi(\mathbf{p})]\,\mathbb{P} + [\mathbb{C}_\Gamma(\mathbf{p})]\,\mathbb{P}^\mathrm{e} = \mathbb{F}^\mathrm{s}(\omega;\mathbf{p})\,, \tag{2.63}$$

$$[\mathbb{A}^\mathrm{f}(\omega;\mathbf{p})]\,\mathbb{P} + \omega^2[\mathbb{C}_\Pi(\mathbf{p})]^\mathrm{T}\mathbb{U}^\mathrm{s} = 0\,, \tag{2.64}$$

$$[\mathbb{A}^\mathrm{e}(\omega;\mathbf{p})]\,\mathbb{P}^\mathrm{e} + \omega^2[\mathbb{C}_\Gamma(\mathbf{p})]^\mathrm{T}\mathbb{U}^\mathrm{s} = 0\,, \tag{2.65}$$

$$[\mathcal{B}^\mathrm{f}]\,\mathbb{P} + [\mathcal{B}^\mathrm{e}]\,\mathbb{P}^\mathrm{e} = 0\,. \tag{2.66}$$

In Eq. (2.63) the coupling matrix between the structure and the poroelastic medium modeled as an equivalent acoustic fluid $[\mathbb{C}_\Gamma(\mathbf{p})]$ derives from the discretization of the sesquilinear form $c_\Gamma(p^{\mathrm{e}}, \delta\mathbf{u}^{\mathrm{s}})$ defined by Eq. (B.13). The pressure continuity between the internal acoustic fluid and the poroelastic medium defined by Eq. (B.6) is discretized to give Eq. (2.66), a set of linear constraints that can be treated in a similar way than Eq. (2.54). In Eq. (2.65) the $(N_{\mathrm{e}} \times N_{\mathrm{e}})$ complex matrix $[\mathbb{A}^{\mathrm{e}}(\omega; \mathbf{p})]$ is defined as

$$[\mathbb{A}^{\mathrm{e}}(\omega; \mathbf{p})] = -\omega^2[\mathbb{M}^{\mathrm{e}}(\mathbf{p})] + [\mathbb{K}^{\mathrm{e}}(\mathbf{p})] \,, \tag{2.67}$$

where $[\mathbb{M}^{\mathrm{e}}(\mathbf{p})]$ and $[\mathbb{K}^{\mathrm{e}}(\mathbf{p})]$ repectively are the $(N_{\mathrm{e}} \times N_{\mathrm{e}})$ complex symmetric mass and stiffness matrices resulting from the discretization of the sequilinear forms $m^{\mathrm{e}}(p, \delta p)$ and $k^{\mathrm{e}}(p, \delta p)$ defined by Eqs. (B.11) and (B.12), associated with the equivalent acoustic fluid with rigid boundary. As emphasized in [46], the real total mass density of the poroelastic medium ρ_t^{p}, defined by Eq. (B.10), is the static limit of the complex corrected effective mass density $\tilde{\rho}^{\mathrm{f}\prime}(\omega)$ such that

$$\lim_{\omega \to 0} \tilde{\rho}^{\mathrm{f}\prime}(\omega) = \rho_t^{\mathrm{p}} \,. \tag{2.68}$$

Consequently, the complex frequency dependent stiffness matrix $[\mathbb{K}^{\mathrm{e}}(\omega; \mathbf{p})]$ can be written as

$$[\mathbb{K}^{\mathrm{e}}(\omega; \mathbf{p})] = [\mathbb{K}_1^{\mathrm{e}}(\mathbf{p})] + \left(\frac{\phi}{\tilde{\rho}^{\mathrm{f}\prime}(\omega)} - \frac{\phi}{\rho_t^{\mathrm{p}}}\right) [\mathbb{K}_2^{\mathrm{e}}(\mathbf{p})] \,, \tag{2.69}$$

where $[\mathbb{K}_1^{\mathrm{e}}(\mathbf{p})]$ and $[\mathbb{K}_2^{\mathrm{e}}(\mathbf{p})]$ are real symmetric positive semidefinite matrices. Moreover, according to Eq. (2.60) the complex frequency dependent mass matrix $[\mathbb{M}^{\mathrm{f}}(\omega; \mathbf{p})]$ can be written as

$$[\mathbb{M}^{\mathrm{e}}(\omega; \mathbf{p})] = [\mathbb{M}_1^{\mathrm{e}}(\mathbf{p})] + \left(\frac{\phi}{\tilde{K}^{\mathrm{f}}(\omega)} - \frac{\phi}{P_0}\right) [\mathbb{M}_2^{\mathrm{e}}(\mathbf{p})] \,, \tag{2.70}$$

where $[\mathbb{M}_1^{\mathrm{e}}(\mathbf{p})]$ and $[\mathbb{M}_2^{\mathrm{e}}(\mathbf{p})]$ are real symmetric positive definite matrices.

2.6 Conclusion

In this chapter were given the equations and the boundary conditions for a vibroacoustic system with poroelastic medium. The primary variables respectively describing the different media are the displacement field for the structure, the acoustic pressure disturbance field for the internal acoustic fluid and the displacement fields of the solid and fluid phases of the poroelastic medium. In the case where the latter is sufficiently limp such that an equivalent fluid model is valid, an alternative model was presented. Then, a computational model was derived from the discretization through the finite element method of sesquilinear operators which construction was explicitly defined. Finally, notations and matrix decompositions were introduced as a preamble for the construction of a reduction basis and a stochastic computational model. The whole computational code, mesher and finite elements were implemented in Matlab such that a limited array of input parameters controls the construction of the computational model. Fast realisations of system whose geometries and material properties belong to a broad range of admissible designs was then possible. This approach is moreover adapted to distributed computing with minimum data exchange as every step takes place within a unique software framework.

3

Overview of lightweight structural materials and identification from experimental measurements

Contents

3.1 Introduction

In this chapter, the methodology used for the experimental identification of system parameters, such as for example the elastic properties of the different structural elements that make up a standard lightweight building separative system, is introduced. Among those elements are found typical wood industry products, from particle boards or oriented strand boards (OSB) to mere wooden beams, which, due to the fabrication process or the material itself, are highly inhomogeneous [77]. The scale of the inhomogeneities being around the centimeter, the representative elementary volume, in the sense of [78] "sufficiently large to be statistically representative of the composite", is consequently the element itself. In order to avoid cumbersome sampling procedures, the measurements were then carried out at the building element scale to obtain effective values of the parameters. Moreover, as some of those elements might be oversized, difficult to manipulate and non-adapted to classical experimental devices, a specific measurement protocol was implemented to extract the informations from dynamic data. Similar approaches were used in [79,80] for experimental identification of wooden elements damping properties. The experimental setup is such that the structural elements are suspended, close to free boundary conditions, and excited through steady punctual hammer impacts performed manually. This protocol allows to remove eventual boundary condition influence as well as to have the necessary versatility to treat bulky systems. The impact force is then measured and a set of mobilities, according to the usual definition [81], is derived from the velocities of different points of the element.

3.2 System parameters identification problem

3.2.1 Definition of the admissible set for the structural system parameters

The structure, constituted of the assembly of different elements supposed homogeneous, is described through the knowledge of parameters associated with its geometry, elasticity tensors and mass densities. Elements of vector $\mathbf{p}$ associated with materials elastic properties are then typically Young's moduli E_j, shear moduli G_{jk}, Poisson's ratios ν_{jk}. Let C_E, C_G and C_ν respectively be the admissible set for the three kind of elastic parameters. Positiveness of the strain energy implies the strict positiveness of Young's moduli as well as of shear moduli such that $C_E =]0, +\infty[$ and $C_G =]0, +\infty[$. For isotropic materials, Poisson's ratio are bounded and we have $C_\nu = [-1, 0.5]$. Within the general anisotropic case, Poisson's ratio is not bounded [82] and belong to $\mathbb{R}$, with the constraint that the strain energy remains positive. Hereinafter, given the considered class of materials, the support of Poisson's ratios is chosen such that $C_\nu = \mathbb{R}$. Moreover, the mass density ρ^s belong to $C_\rho =]0, +\infty[$. Consequently, within the case of elastic parameters identification, the admissible set C_{par} for the vector of the system parameters $\mathbf{p}$ is defined by

$$C_{par} = \left\{ \mathbf{p} \in \mathbb{R}^{n_p} \mid \forall j,k,\ E_j \in C_E, G_{jk} \in C_G, \nu_{jk} \in C_\nu, \rho^s \in C_\rho \right\} . \tag{3.1}$$

3.2.2 Definition of the optimisation problem

A computational model is constructed for the frequency band $\mathbb{B} = [\omega_{min}, \omega_{max}]$, according to Section 2.4, and parametrized by the vector $\mathbf{p}$ belonging to C_{par} subset of $\mathbb{R}^{n_p}$. For n_{ex} excitation points, n_{obs} mobility functions are experimentally measured and subsequently computed. According to the usual notations, $y_{jk}(\omega)$ denotes the mobility associated with the point k when the point j is submitted to an excitation. The parameter dependent error estimator $\mathbf{p} \mapsto E^{\mathbf{p}}(\mathbf{p})$ is then defined by

$$E^{\mathbf{p}}(\mathbf{p}) = \sum_{j=1}^{n_{ex}} \sum_{k=1}^{n_{obs}} \int_{\omega_{min}}^{\omega_{max}} | \log_{10}\left(|y_{jk}(\omega;\mathbf{p})|\right) - \log_{10}\left(|y_{jk}^{mes}(\omega)|\right) |^2 \, \mathrm{d}\omega \, , \tag{3.2}$$

where $y_{jk}(\omega;\mathbf{p})$ and $y_{jk}^{mes}(\omega)$ respectively are the mobilities ensuing from the computational model and from the measurements. The use of the logarithm of the mobilities within the objective function allows to give a comparable weight to the resonances and antiresonances such that the model fits over the whole

frequency band of interest. A subspace exploration algorithm is then used to find the optimal vector $\mathbf{p}^{opt}$ solution of the optimisation problem

$$\mathbf{p}^{opt} = \arg \min_{\mathbf{p} \in \mathcal{C}_{par}} E^{\mathbf{p}}(\mathbf{p}) \, . \tag{3.3}$$

It should be noted that the updating strategy then belongs to the class of output-errors methods, opposite to the input-errors methods as presented in [83], as the objective function is constructed from the inverses of updated operators. Moreover, it can be noted that the full modal analysis of each measured system is not considered. Given the high number of real systems to be analysed, such a strategy would be inefficient implementation wise as well as time consuming.

3.3 Validation of the computational model and identification of the elastic parameters for typical lightweight building elements

3.3.1 Wooden beams

Solid wood is described in the references as an orthotropic material due to its growth patterns [77] allowing to distinguish longitudinal (l), radial (r) and tangential directions (t). Associated elasticity tensor can consequently be described through nine independent parameters: three elasticity moduli (respectively denoted E_l, E_r and E_t), three shear moduli (G_{lr}, G_{lt} and G_{rt}) and three Poisson's ratios (ν_{lr}, ν_{lt} and ν_{rt}). Within most structural applications, solid wood elements are to be stressed in bending or with axial efforts such that the longitudinal Young's modulus is the first order parameter. By way of consequence, the longitudinal Young's modulus E_l is most of the time the only measured and given design parameter while the remainder are defined by a ratio with respect to E_l. Among the diversity of wood species used for structural construction, following prior nominal properties (see Table. 3.1) are chosen according to the available data [77, 84] for those belonging to the general "pine" denomination.

E_l [GPa]	E_t [GPa]	E_r [GPa]	G_{tl} [GPa]	G_{lr} [GPa]	G_{rt} [GPa]	ν_{rt}	ν_{lr}	ν_{lt}	ρ^s [kg/m^3]
9	0.3	0.3	0.7	0.7	0.05	0.1	0.1	0.1	400

Table 3.1: Pine nominal physical properties

A suspended wooden beam, of dimensions 2.873 m $\times$ 0.045 m $\times$ 0.145 m, is excited on point 1 (see Fig.3.1), in the z direction, with steady hammer impacts and experimental mobilities are measured over the frequency band $\mathbb{B} = [10, 1000]$ Hz with respect to the velocities in the z direction of points 1 and 2, whose coordinates are given in Table 3.2. A computational model for one beam is then constructed for the frequency band $\mathbb{B}$, in which the structural loss factor is fixed to $\eta_s = 0.02$.

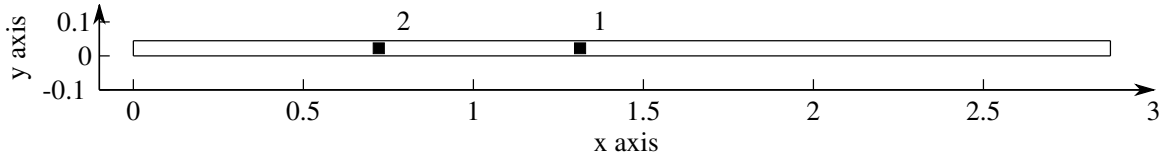

Figure 3.1: Wooden beam. Observation points (squares).

Given the measured mass density for one beam, the optimal longitudinal Young's modulus was determined as the solution of the optimisation problem defined by Eq. (3.3), in which the error estimator $E^{\mathbf{p}}(\mathbf{p})$ is evaluated with the computational model. Figure 3.2 compares the squared modulus of the mobilities measured and computed with the optimal longitudinal Young's modulus and mass density for different points on one beam. The homogeneous orthotropic model is then able to correctly represent the bending of a wooden beam element in the frequency band $\mathbb{B}$ of interest.

	Point 1	Point 2
x [m]	1.325	0.022
y [m]	0.735	0.022

Table 3.2: Observation point coordinates.

Accordingly, the optimal longitudinal Young's modulus as well as the mass densities were determined for two independent batches constituted of eight beams each. The respective identified values are summarized in Tables 3.3 and 3.4. Large statistical dispersion is observed, in particular with respect to the elastic properties, and is emphazised by the measurement envelope for the entire set of beams.

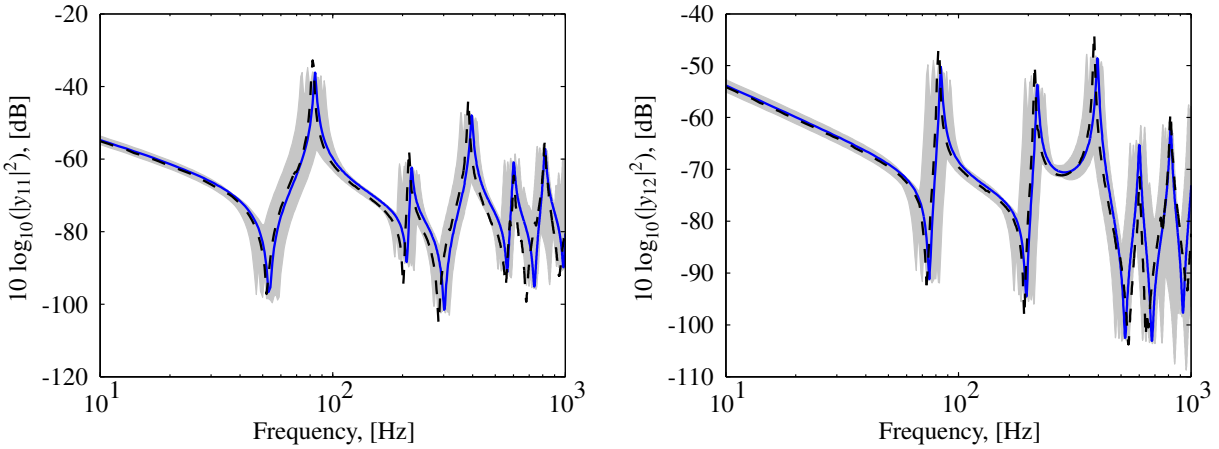

Figure 3.2: Set of mobilities obtained for an excitation on point 1. Experimental measurements (thin black dashed lines); computational model updated with optimal physical parameters (thin blue solid line); envelope obtained for the entire set of beams (grey areas).

	B1	B2	B3	B4	B5	B6	B7	B8
E_l [GPa]	12.5	11.2	10.8	9.2	10	12.5	15	10.5
ρ^s [kg/m^3]	467	464	448	459	448	491	517	456

Table 3.3: Batch 1: wooden beams identified physical properties.

	B1	B2	B3	B4	B5	B6	B7	B8
E_l [GPa]	8	8	12.5	12.5	10.5	11	11	9.5
ρ^s [kg/m^3]	394	445	469	496	517	480	448	426

Table 3.4: Batch 2: wooden beams identified physical properties.

3.3.2 Lightweight boards

Among the different boards used within lightweight building construction, noteworthy are plasterboards and wood-based composite boards. As illustrated by the rich content of manufacturers product indexes, very diverse material properties can be encountered but quite few are sufficiently documented to allow accurate dynamical modeling. Indeed, if the mass densities of those products are known, their elastic properties were subjected to little investigation while critical for low frequencies analysis. Thus, in

regard to wood-based composite boards for example, whose elastic properties and mass densities depend on the length of the wood flakes or wood particles, the property of the adhesive matrix or the manufacturing process, high contrasts can be observed among the different products [77,85,86]. Given the objective of establishing robust predictions of the vibroacoustic behavior at low frequencies, property fluctuations of typical lightweight board elements were investigated before any workmanship took place. Ensuing, series of ten nominally identical boards from the same batches were analysed.

In order to easily carry out series of measurement for various boards from different materials, a standard protocol was established. For any board of dimensions $a \times b$, the input mobilities y_{jj} as well as the cross mobilities y_{jk} were measured with respect to the points 1 and 2 whose normalised coordinates with respect to the boards dimensions can be found in Table 3.5. Given the measured mass densities for each board, the optimal elastic parameters for the computational model to fit the measurements were then determined according to the optimisation problem defined in Section 3.2. A parameter sensitivity analysis shows that among the elastic parameters involved in the description of the two dimensional elastic behavior, E_x, E_y, G_{xy} and ν_{xy} can be identified from the given dynamic information within the frequency band $\mathbb{B} = [6, 200]$ Hz.

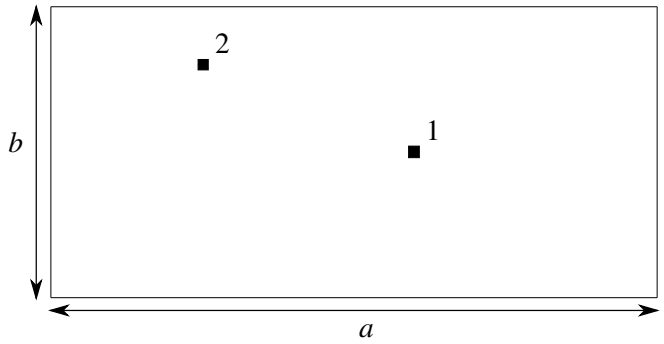

Figure 3.3: Lightweigth boards. Observation points (black squares).

	Point 1	Point 2
x [m]	0.6a	0.25a
y [m]	0.5b	0.8b

Table 3.5: Observation point coordinates.

Oriented strand boards

Constituted of bonded and compressed wood flakes, oriented strand boards offer high mechanical properties and are consequently used for structural load bearing roles, as bracing panels within walls or floors. The associated manufacturing process induces preferential directions for the flakes resulting in a slight orthotropy [85, 87] strengthening the longitudinal direction of the board. Usually modeled as isotropic in the structural acoustic litterature [21] the effect of this orthotropy is limited as long as the panel is mounted with the long direction across the supports. According to the available data [8, 21, 77, 85, 86] prior nominal properties are chosen and given in Table. 3.6 for oriented strand boards class 2 (indoor structural use in dry conditions).

E_x [GPa]	E_y [GPa]	G_{xy} [GPa]	G_{yz} [GPa]	G_{xz} [GPa]	ν_{xy}	ρ^s [kg/m^3]
5	2	1.5	1	2	0.3	550

Table 3.6: OSB nominal physical properties

A computational model for one oriented strand board of dimensions $a = 2.5$ m, $b = 1.25$ m and 12 mm thick is constructed for the frequency band $\mathbb{B} = [6, 200]$ Hz, in which the structural loss factor is fixed to $\eta_s = 0.02$. Table 3.7 gives the optimal parameters determined for the set of ten boards. Figure 3.4 compares the squared modulus of the mobilities measured and computed with the optimal physical parameters for different points on one board. The envelope obtained for the set of ten boards

is also drawn. As showed by the large span of the envelope for the frequency responses below 10 Hz, the bad spectral coherence at very low frequencies leads to discard the information given by the first mode around 5 Hz that could also be influenced by the suspension system. Some discrepancies can be observed but the Mindlin-Ressner homogeneous orthotropic plate model is overall able to give a good prediction of the bending behavior of the oriented strand boards below 200 Hz. The discrepancies observable around antiresonances shall be put in perspective with the apparent inconsistencies of the measured cross mobilities y_{12} and y_{21} around those frequencies, where the signal to noise ratio tends to be low.

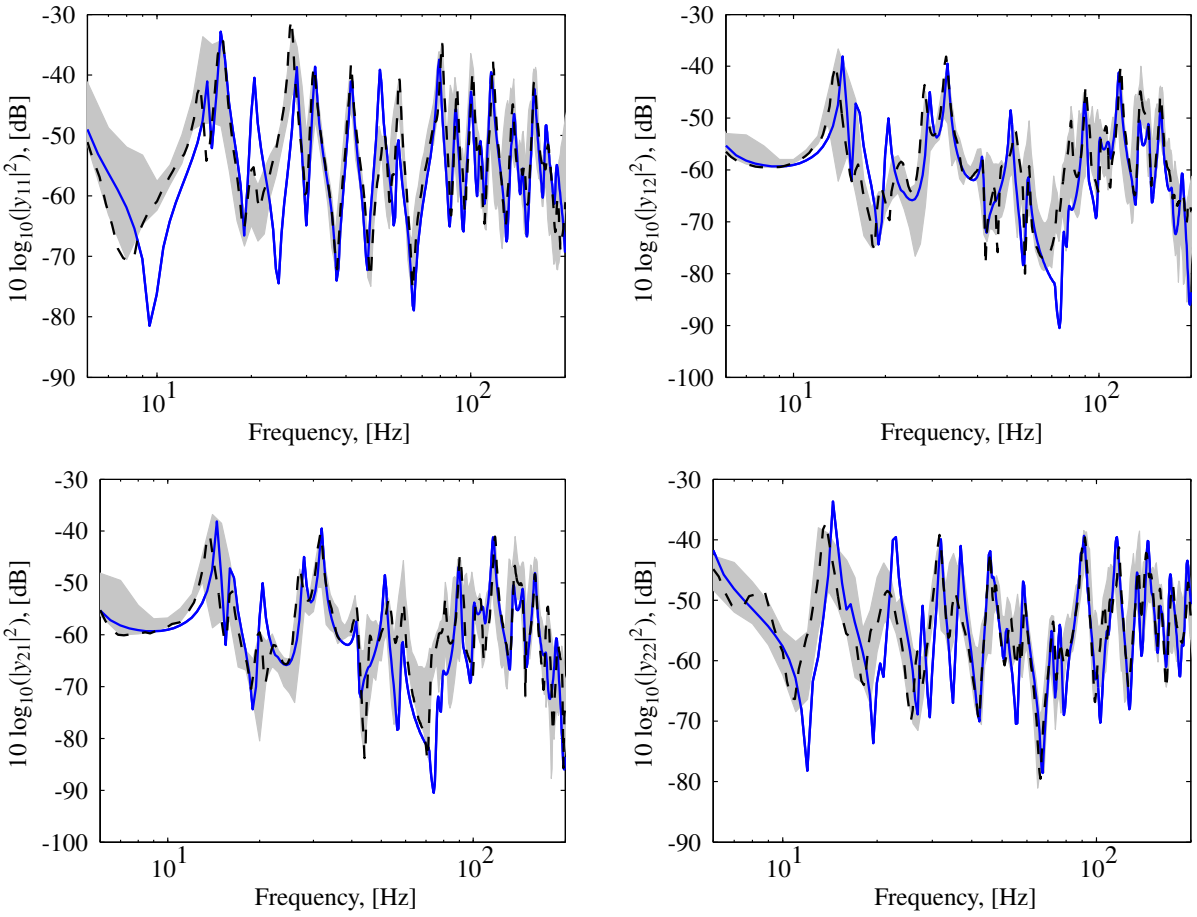

Figure 3.4: Oriented strand board. Set of mobilities obtained for excitations on point 1 and 2. Experimental measurements for one board (thin black dashed lines); computational model updated with optimal physical parameters for one board (thin blue solid line); envelope obtained for the set of ten measured boards (grey areas).

	B1	B2	B3	B4	B5	B6	B7	B8	B9	B10
E_x [GPa]	4.54	3.95	3.59	3.52	3	3.76	3.73	3.39	3.49	3.4
E_y [GPa]	2.47	2	2.07	1.81	1.52	1.93	1.84	1.73	2.07	1.93
G_{xy} [GPa]	1.04	0.97	0.94	0.8	0.83	0.96	0.93	0.94	0.94	1.0
ν_{xy}	0.15	0.15	0.32	0.45	0.43	0.4	0.41	0.42	0.34	0.39
ρ^s [kg/m^3]	592	589	573	581	552	581	586	570	568	586

Table 3.7: Oriented strand boards, identified physical properties.

Particle boards

Particle boards are typically constituted of wooden particles which are small in comparison with the flakes used for oriented strand boards [77, 85]. Their manufacturing process does not aim to create significative material orientation but a weak orthotropy can be observed. Ensuing from the smaller particles, high mechanical properties of wood fibers are not exploited as well for the particle boards than for the oriented strand boards. The resulting stiffness properties at the board scale are then usually slightly inferior. As a consequence, a superior thickness is commonly used within building constructions resulting in a higher mass per square meter than for oriented strand boards. According to the available data [21,77,85,86], prior nominal properties are chosen and given in Table. 3.8 for oriented strand boards whose thickness is comprised between 20 and 25 mm, adapted for indoor structural use in dry conditions.

E_x [GPa]	E_y [GPa]	G_{xy} [GPa]	G_{yz} [GPa]	G_{xz} [GPa]	ν_{xy}	ρ^s [kg/m^3]
2.7	2.7	0.8	1	1	0.3	600

Table 3.8: Particle boards nominal physical properties

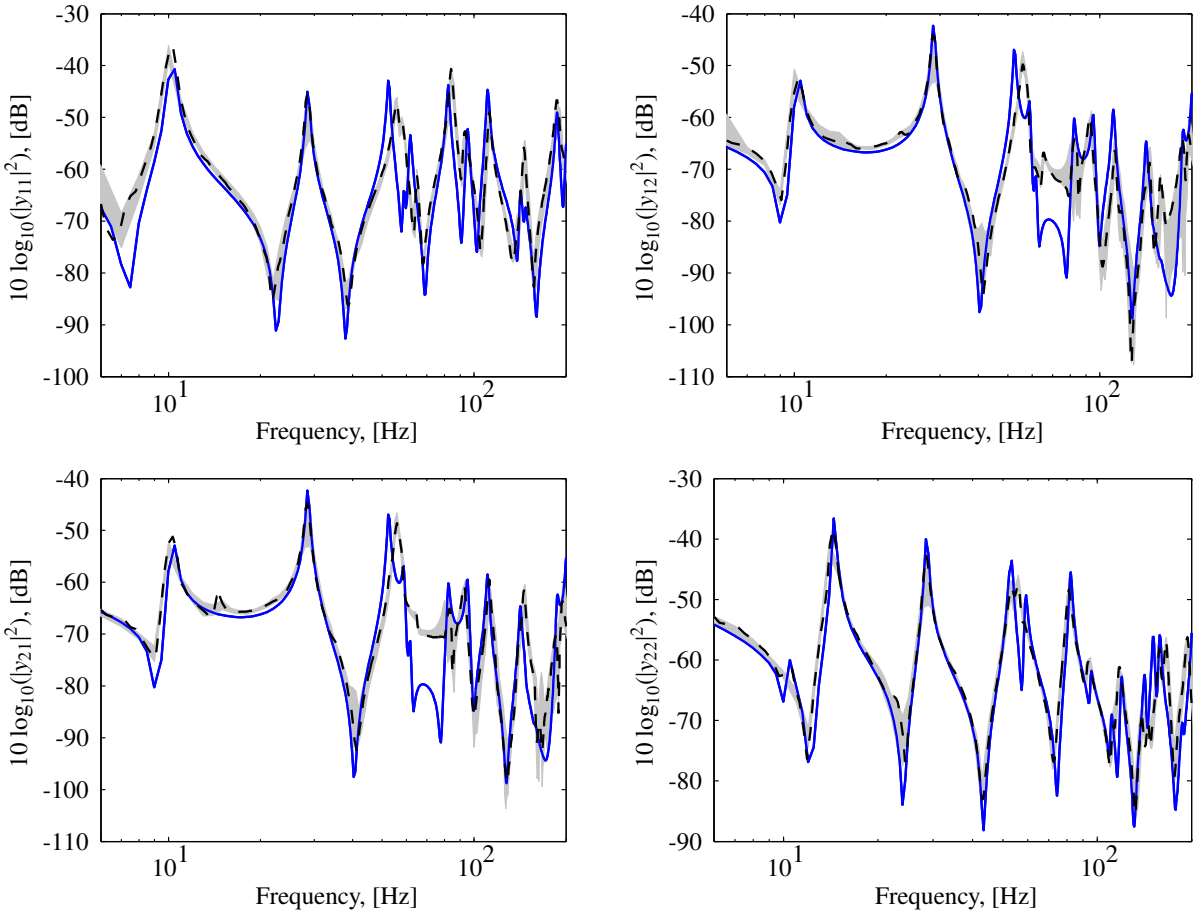

Figure 3.5: Particle boards. Set of mobilities obtained for excitations on point 1 and 2. Experimental measurements for one board (thin black dashed lines); computational model updated with optimal physical parameters for one board (thin blue solid line); envelope obtained for the set of ten measured boards (grey areas).

A computational model for one particle board of dimensions $a = 2.060$ m, $b = 0.920$ m and 22 mm thickness is constructed for the frequency band $\mathbb{B} = [6, 200]$ Hz, in which the structural loss factor is fixed to $\eta_s = 0.02$. Very limited fluctuations are observed and identified over the identified elastic

properties or measured mass densities given in Table 3.9. Figure 3.5 compares the squared modulus of the mobilities measured and computed with the optimal physical parameters for different points on one particle board. As it could be expected with regard to the homegeneous design of the material, the envelope obtained from the ten measured boards shows very little fluctuations and the Mindlin-Ressner plate homogeneous orthotropic model is able to give a good prediction of the bending behavior of the particle board below 200 Hz.

	B1	B2	B3	B4	B5	B6	B7	B8	B9	B10
E_x [GPa]	2.24	2.19	1.95	2.37	2.27	2.33	2.14	2.34	2.34	2.13
E_y [GPa]	2.86	2.88	2.79	2.98	2.9	2.9	2.93	2.89	2.89	2.85
G_{xy} [GPa]	1.03	1.03	1.02	0.99	0.88	1.02	1.03	1.08	1.02	1.02
ν_{xy}	0.13	0.16	0.23	0.1	0.18	0.1	0.2	0.08	0.08	0.18
ρ^s [kg/m^3]	633	645	645	636	633	638	640	638	633	633

Table 3.9: Particleboards, identified physical properties.

Plasterboards

Typical plasterboards are constituted of one layer of isotropic plaster between two layers of orthotropic cardboards [88]. The elasticity tensor associated with the resulting effective homogeneous material consequently displays a slight orthotropy. Moreover, in order to fulfill fire or impact resistance criteria, a range of products is fiber reinforced or manufactured to keep a high level of chemically combined water, then drastically modifying the mechanical properties. In order to assess mechanical durability according to CE marking standards, the standard [89] solely takes care of evaluating a bending strength criterion. The only sources of engineering data for advanced mechanical design consequently ensue from previous researches that obviously cannot cover the whole range of manufacturers and their respective products. In the following are investigated the differences in mechanical properties between three representative products used within textbook acoustical solutions, as well as the potential fluctuations associated with each of them. Table 3.10 gives the nominal values of the physical properties for a typical plasterboard according to the available data [8, 21, 86].

E_x [GPa]	E_y [GPa]	G_{xy} [GPa]	G_{yz} [GPa]	G_{xz} [GPa]	ν_{xy}	ρ^s [kg/m^3]
2.5	2	1	1	1	0.3	700

Table 3.10: Plasterboards nominal physical properties

Standard 12.5 mm The standard 12.5 mm thick plasterboard is the most basic product from the gypsum industry and does not involve any fiber reinforcement or specific fire resistance treatment. In the same fashion than for wooden composite boards, Table 3.11 gives the optimal parameters determined for the set of ten boards in the sense of the optimisation problem defined in Section 3.2 as well as the measured mass densities. Identified values are then consistent with the nominal ones.

Figure 3.6 compares the squared modulus of the mobilities measured and computed with the optimal identified physical parameters for different points on one plasterboard of dimensions $a = 2.500$ m, $b = 1.200$ m and of thickness 12.5 mm. Quite good match is observed but it can be seen once again with the discrepencies around the first modes that the system might by influenced by the suspension conditions.

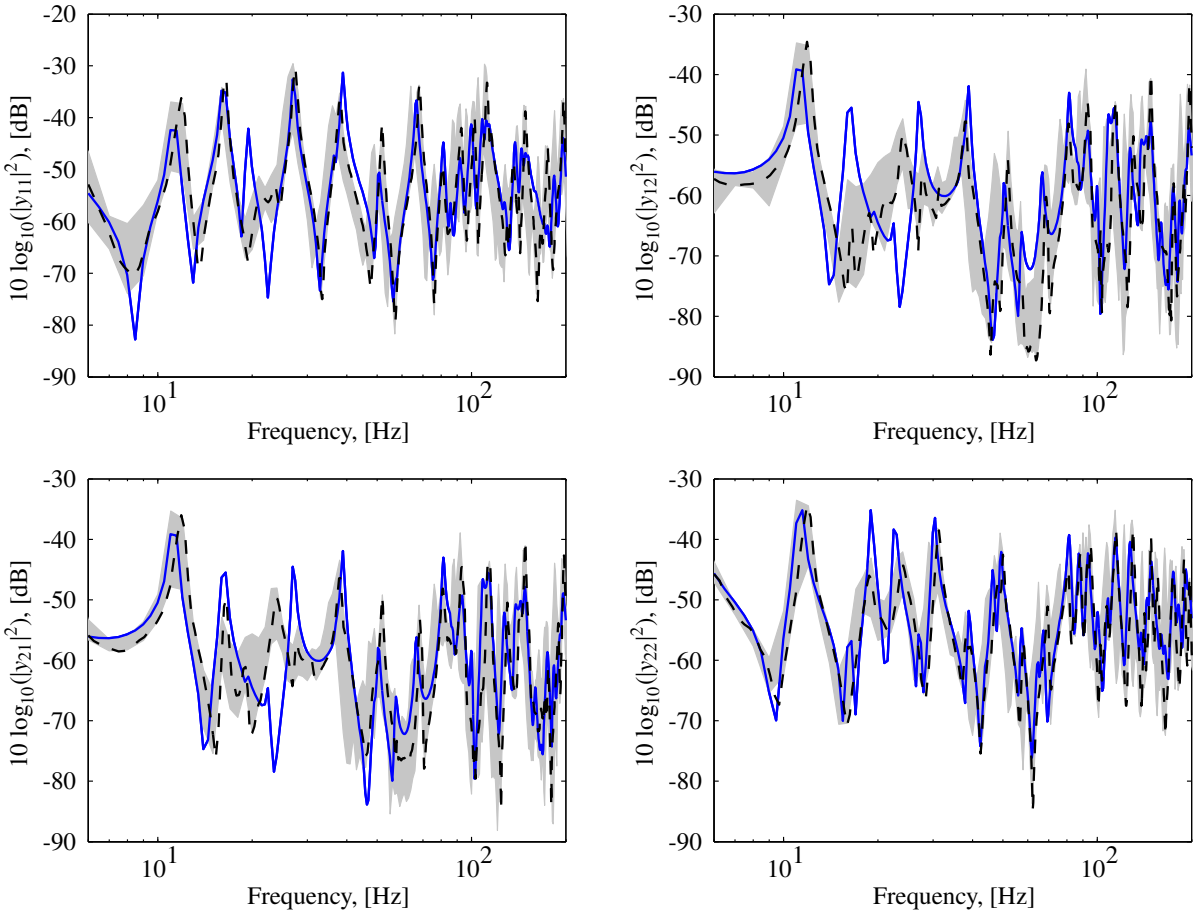

Figure 3.6: Plasterboard 12.5mm. Set of mobilities obtained for excitations on point 1 and 2. Experimental measurements for one board (thin black dashed lines); computational model updated with optimal physical parameters for one board (thin blue solid line); envelope obtained for the set of ten measured boards (grey areas).

	B1	B2	B3	B4	B5	B6	B7	B8	B9	B10
E_x [GPa]	2.95	2.88	2.88	2.9	2.85	2.87	2.84	2.88	2.55	1.97
E_y [GPa]	2.32	2.34	2.28	2.32	2.27	2.35	2.28	2.32	2.08	2.39
G_{xy} [GPa]	1.07	1.1	1.12	1.12	1.12	1.09	1.13	1.05	0.96	0.88
ν_{xy}	0.19	0.22	0.2	0.22	0.2	0.15	0.2	0.3	0.22	0.28
ρ^s [kg/m^3]	712	706	706	712	704	704	706	712	704	688

Table 3.11: Plasterboard 12.5 mm, identified physical properties.

Fire resistant 15 mm The 15 mm thick fire resistant plasterboard includes glass fibers as well as additives within the plaster core such that remains a high level of chemically combined water. Table 3.12 gives the optimal elastic parameters as well as the mass densities determined for the set of ten boards. The higher mechanical properties as well as mass densities illustrate the consequences of the previous remarks. Moreover, as the effective material orthotropy level seems to increase, the orientation of the boards for the mounting with respect to the secondary frame might become a first order concern at low frequencies (see experimental observations in [90]).

Figure 3.7 compares the squared modulus of the mobilities measured and computed with the optimal physical parameters for different points on one particle board of dimensions $a = 2.600$ m, $b = 1.200$ m and of thickness 15 mm. Good match is observed over the whole frequency band however the level of

structural damping appears at too high as the frequency increases.

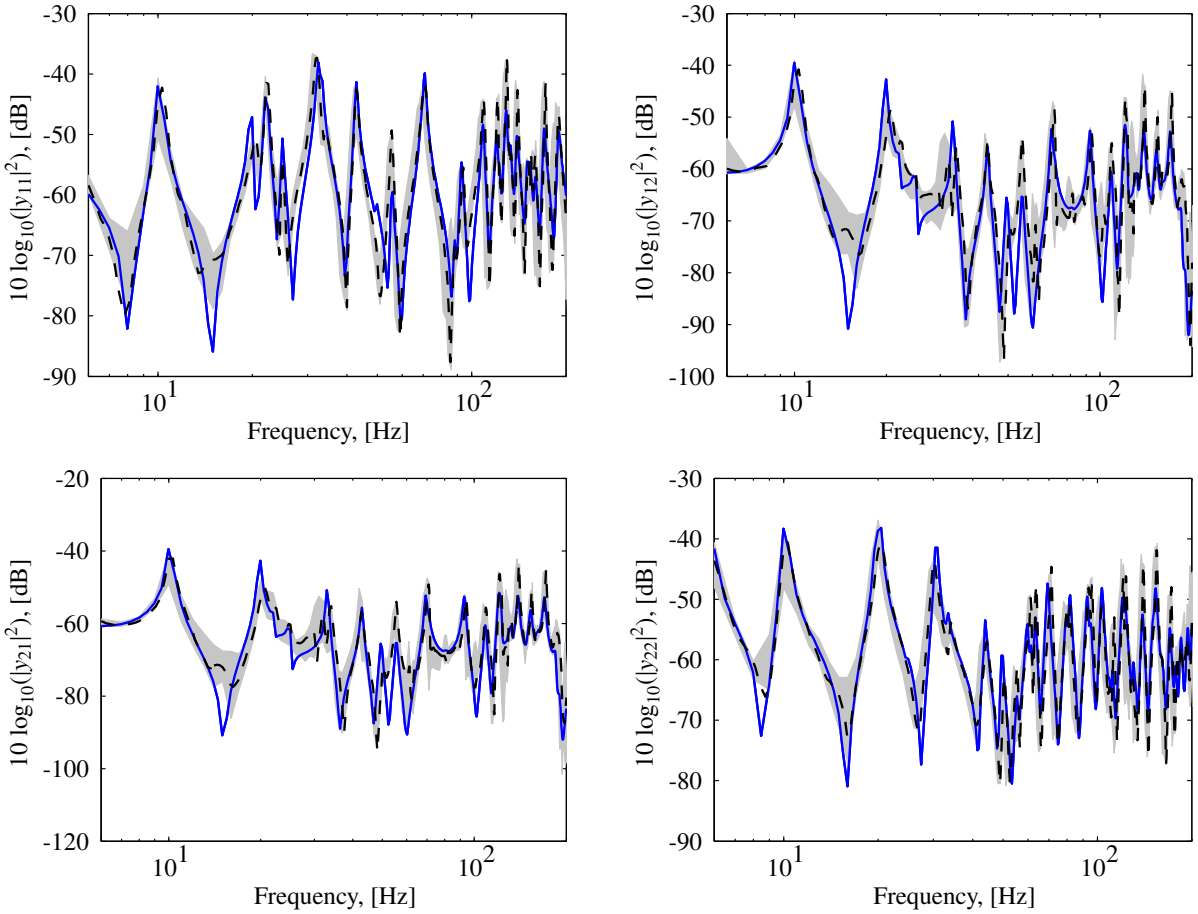

Figure 3.7: Plasterboard 15mm. Set of mobilities obtained for excitations on point 1 and 2. Experimental measurements for one board (thin black dashed lines); computational model updated with optimal physical parameters for one board (thin blue solid line); envelope obtained for the set of ten measured boards (grey areas).

	B1	B2	B3	B4	B5	B6	B7	B8	B9	B10
E_x [GPa]	2.27	2.34	2.21	2.32	2.34	2.36	2.22	2.29	2.24	2.34
E_y [GPa]	4.38	4.43	4.18	4.36	4.34	4.45	4.2	4.38	4.24	4.41
G_{xy} [GPa]	1.42	1.36	1.32	1.4	1.37	1.39	1.3	1.35	1.34	1.37
ν_{xy}	0.08	0.26	0.22	0.08	0.22	0.24	0.2	0.12	0.16	0.2
ρ^s [kg/m^3]	1100	1075	1053	1060	1080	1080	1053	1057	1053	1068

Table 3.12: Plasterboard 15 mm, identified physical properties.

Standard 18 mm The standard 18 mm thick plasterboard is marketed as a high density and hardness product, which reflects in the identified properties given in Table 3.13. Thus, three very different materials were considered during this overview of gypsum products, for which mechanical properties are hardly found or transmitted to the designer.

Figure 3.8 compares the squared modulus of the mobilities measured and computed with the optimal physical parameters for different points on one particle board of dimensions $a = 2.600$ m, $b = 1.200$ m and 18 mm thickness.

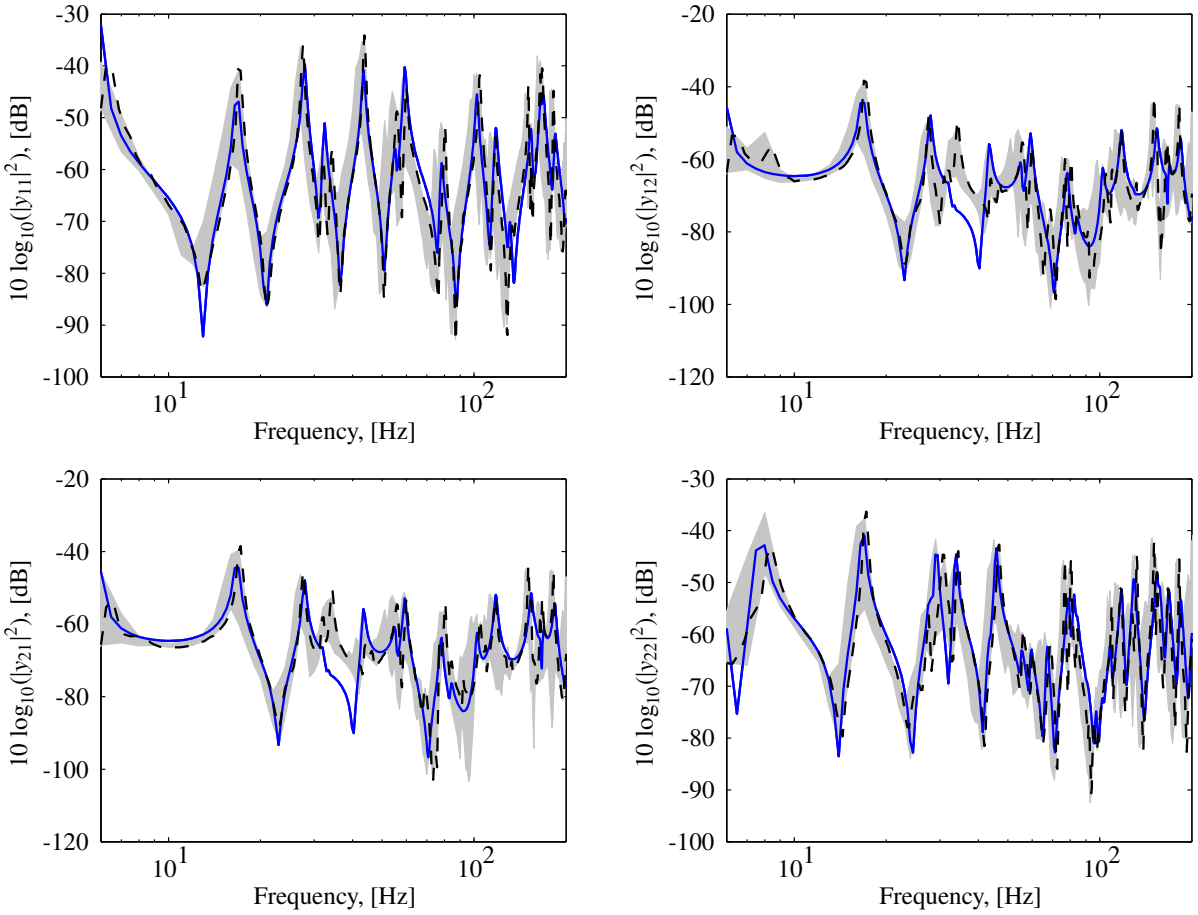

Figure 3.8: Plasterboard 18mm. Set of mobilities obtained for excitations on point 1 and 2. Experimental measurements for one board (thin black dashed lines); computational model updated with optimal physical parameters for one board (thin blue solid line); envelope obtained for the set of ten measured boards (grey areas).

	B1	B2	B3	B4	B5	B6	B7	B8	B9	B10
E_x [GPa]	4.04	4.45	4.41	3.85	4	4.24	4.06	3.92	3.9	4.22
E_y [GPa]	3.93	4	3.96	3.99	3.81	4.09	4.05	3.7	3.69	4.12
G_{xy} [GPa]	1.78	1.74	1.5	1.49	1.58	1.73	1.67	1.55	1.54	1.7
ν_{xy}	0.14	0.24	0.15	0.15	0.22	0.12	0.25	0.27	0.27	0.12
ρ^s [kg/m^3]	913	918	897	917	900	915	931	899	904	918

Table 3.13: Plasterboard 18 mm, identified physical properties.

3.4 Conclusion

In this chapter, a methodology was presented to identify effective elastic properties associated with typical lightweight building elements. Considering the large span of nominal values that could be observed in the litterature [21, 77, 85, 86] and the frequently emerging uncertainty concerns in building construction [8, 10, 14, 16–21], batches of nominally identical lightweight elements were measured, thus initiating a systematic approach to discriminate the different sources of uncertainties going from the single subpart to the whole assembled system. Fluctuations among the materials involved within typical lightweight building construction were then highlighted, before any workmanship took place. The level of known inhomogeneity for each material was consistent with the level of fluctuations observed within

the elastic properties or mass densities, reaching an expected maximum for mere wooden beams. What could not be quantified however are the statistical fluctuations for a given product among different manufacturers or different batches. Various mechanical behavior and material symmetries observed within the overview of classical products definitely illustrates the diversity of properties available to the design of lightweight separative systems.

4

Flexible connection model and experimental identification

Contents

4.1 Introduction

The complex systems of interest, constituted of the rigid assembly of multiple elastic subparts, might exhibit uncontrolled residual flexibilities within the connections of their elements. While many work in the past focused on modeling assemblies (non-exhaustively [20,21,35,81,91–101]) for structural acoustic applications, few models involved a sufficiently high level of detail to be interested in the characterisation of the connections by themselves. The residual flexibilities in the latter derive from the technological nature of the assembly and is emphasized for screwed or nailed elements in [21,97], in which perfectly tied models are overly stiffened in comparison with the experimental measurements. In particular, in [97], a statistical energy analysis strategy is presented to filter moment transmissions through the connections but this approach is not adapted at low frequencies as significant discrepancies between predicted and measured levels are noticeable. In [20], following the work initiated in [100], several measurements on nominally identical particle board onto beam assemblies were presented and fluctuations were highlighted, but whether those fluctuations come from the materials or the workmanship could not be concluded.

In order to model and propagate the effects of the different flexible couplings involved within typical lightweight elements onto the performance indicators at low frequencies, it is proposed to follow the methodology introduced in [25] for the construction of a coupling operator at the discrete level, from the finite element model of the different assembled elements. This approach allows to investigate the dynamic behavior of an assembly around the perfectly tied configuration, with a minimum parameterizing, and benefits from an inherent good matrix conditioning. The methodology is then attractive as for experimental identification as well as for systematic implementation, keeping an eye on automatic generations of computational models, associated with given designs, within the framework of an optimisation process.

4.2 Computational model for flexible mounting

Hereinafter, we briefly introduce the approach presented in [25] through treating the case of two coupled substructures, but the extension to any number of substructures is straightforward. Let the structure be constitued of two uncoupled elastic subparts occupying the domains $\Omega^{\mathrm{s}_d}_{d=1,2}$, partition of Ω^{s}. Let denote B the interface through which the two subparts are connected with compatible meshes. Let $\mathbb{U}^{\mathrm{s}_d}_{\mathrm{B}}$ be the vector of the nodal values of the structure displacement field $\mathbf{u}^{\mathrm{s}_d}$ on B and let $\mathbb{U}^{\mathrm{s}_d}_{\mathrm{I}}$ be the vector of the internal degrees of freedom in Ω^{s_d}. Accordingly, we have the following block decomposion of the stiffness matrices

$$[\mathbb{K}^{\mathrm{s}_d}(\mathbf{p})] = \begin{bmatrix} [\mathbb{K}^{\mathrm{s}_d}_{\mathrm{I}}] & [\mathbb{K}^{\mathrm{s}_d}_{\mathrm{IB}}] \\ [\mathbb{K}^{\mathrm{s}_d}_{\mathrm{IB}}]^{\mathrm{T}} & [\mathbb{K}^{\mathrm{s}_d}_{\mathrm{B}}] \end{bmatrix} . \tag{4.1}$$

Ensuing [25], the matrix used to model the flexible assembly of the two subparts is defined by

$$[\hat{\mathbb{K}}^{\mathrm{s}}] = k_{\mathrm{B}} \left([\mathbb{K}^{\mathrm{s}_1}_{\mathrm{B}}] + [\mathbb{K}^{\mathrm{s}_2}_{\mathrm{B}}] \right) , \tag{4.2}$$

such that the stiffness matrix of the assembled system is written as

$$[\mathbb{K}^{\mathrm{s}}(\mathbf{p})] = \begin{bmatrix} [\mathbb{K}^{\mathrm{s}_1}_{\mathrm{I}}] & [\mathbb{K}^{\mathrm{s}_1}_{\mathrm{IB}}] & 0 & 0 \\ [\mathbb{K}^{\mathrm{s}_1}_{\mathrm{IB}}]^{\mathrm{T}} & [\mathbb{K}^{\mathrm{s}_1}_{\mathrm{B}}] + [\hat{\mathbb{K}}^{\mathrm{s}}] & 0 & -[\hat{\mathbb{K}}^{\mathrm{s}}] \\ 0 & 0 & [\mathbb{K}^{\mathrm{s}_2}_{\mathrm{I}}] & [\mathbb{K}^{\mathrm{s}_2}_{\mathrm{IB}}] \\ 0 & -[\hat{\mathbb{K}}^{\mathrm{s}}]^{\mathrm{T}} & [\mathbb{K}^{\mathrm{s}_2}_{\mathrm{IB}}]^{\mathrm{T}} & [\mathbb{K}^{\mathrm{s}_2}_{\mathrm{B}}] + [\hat{\mathbb{K}}^{\mathrm{s}}] \end{bmatrix} . \tag{4.3}$$

The assembly is consequently dependent on the respective system parameters asociated with each subpart as well as on the new parameter k_{B} which characterises the mounting. Infinite values of this parameter yields perfectly tied assembly in a penalty method fashion while zero value means total decoupling. In fact, the perfectly tied configuration is reached as soon as parameter k_{B} is of the order of unity [25] which

ensures a good numerical conditioning. Within the framework of this model, the system is considered assembled through pure stiffness components and is therefore designed for low frequencies around rigid configurations. Hereinafter, parameter k_B is included into the vector $\mathbf{p}$ of the system parameters.

4.3 Experimental identification of mounting parameters

It should be noted that the run through the present approach was carried out in reverse: given an assembled shear panel fresh out the manufacture, measurements were carried out and the system gradually dismantled in order to perform different sets of measurements focusing on different identification problems. This also explains why, in Section 4.4, the properties of only one board could have been identified due to the delicate and destructive take off of the boards from the beam structure. Consequently, in the following, we first endeavour to model an assembly of beams and then the assembly of one board on beams in order to translate the obtained information to the whole assembled shear panel.

4.3.1 Assembly of beam elements

A suspended assembly of wooden beam elements, of dimensions 2.975 m × 2.990 m × 0.140 m, is excited on different points and experimental mobilities are measured over the frequency band $\mathbb{B} = [10, 280]$ Hz. The system is consituted of eight beams and five spacer elements (see Fig. 4.1). The cross sectional dimensions of beam 1 are 140 mm × 80 mm while we have 140 mm × 45 mm for beams 2 to 8 and spacers 1 to 5. Beams 2 to 6 are regularly spaced by 600 mm intervals.

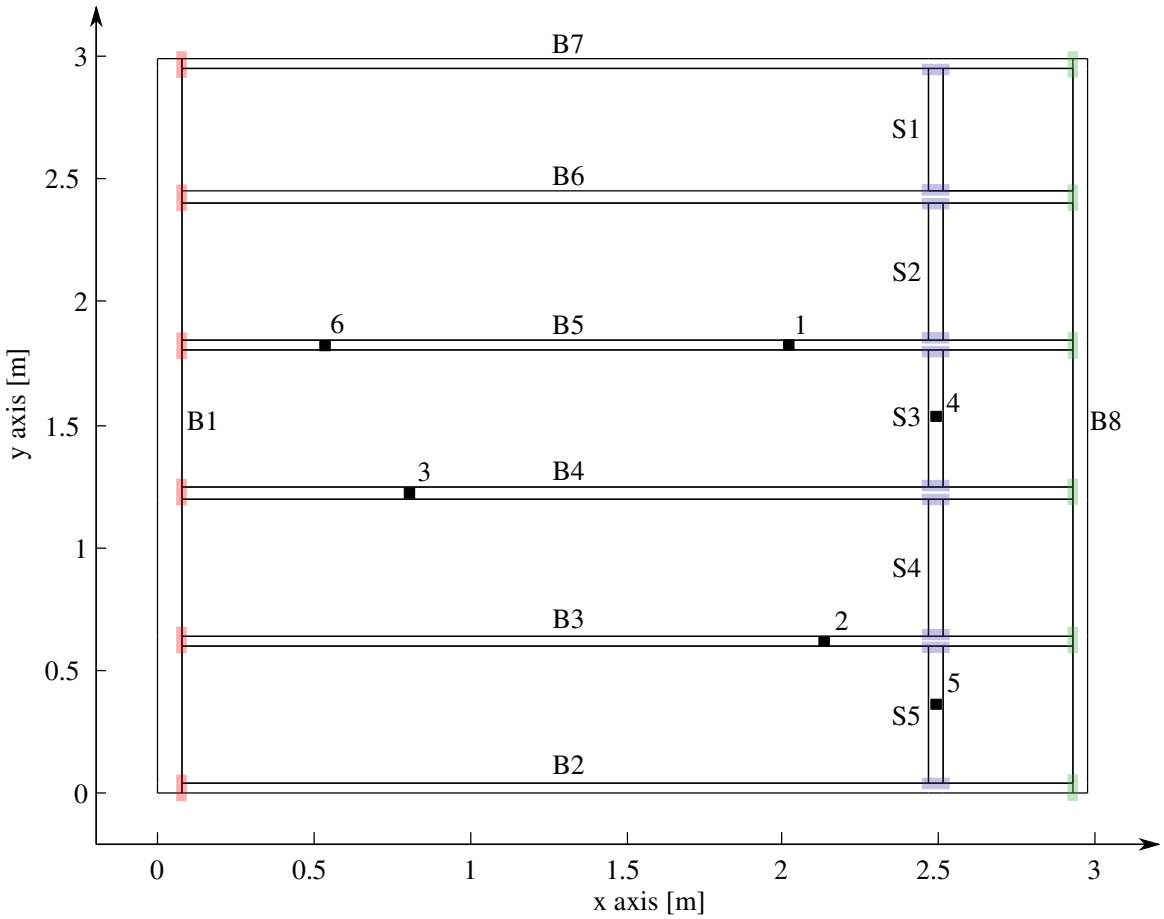

Figure 4.1: Assembly of wooden beam elements. Observation points (black squares). Distinct technological mountings (colored areas).

A computational model is constructed for the frequency band $\mathbb{B}$, in which the structural loss factor is

fixed to $\eta_s = 0.02$. The mass densities and longitudinal Young's modulus are identified from experimental measurements for each beam according to the methodology presented in Section 3.3.1, while nominal values are chosen for the spacers (see Table 4.1).

	B1	B2	B3	B4	B5	B6	B7	B8	S1-5
E_l [GPa]	12.5	11.2	10.8	9.2	10	12.5	15	10.5	9
ρ^s [kg/m^3]	467	464	448	459	448	491	517	456	400

Table 4.1: Wooden beams physical properties.

Within the assembly, are distinguished three different technological mounting (tenon, nailing, etc.), denoted by the colored areas on Fig. 4.1, and a parameter k_B, element of the vector of the system parameters $\mathbf{p}$, is associated to each of them. The parameter dependent error estimator $\mathbf{p} \mapsto E^p(\mathbf{p})$ defined by Eq. (3.2) is then minimised to obtain an optimal set of mounting parameters given in Table 4.2. In order to deal with well-posed inverse problems, the identification is carried out in two steps. In a first one, the system without spacers is considered such that the mounting parameters associated with the connections types denoted by the red and green areas are identified. Then, the mounting parameter associated with the connection type denoted by the blue areas is identified on the full beam assembly with spacers.

Following, every connection displays some level of flexibility. While it is reasonable to assume that, given this configuration, the connections types denoted by the red and green areas mostly influence the torsional modes of the frame that, in fact, would disappear with appropriate boundary conditions, the one type denoted by the blue areas clearly controls the flexural stiffening of the beams by the spacers.

Assembly type	1 (red)	2 (blue)	3 (green)
Numerical value of parameter "k_B"	0.028	0.017	0.053

Table 4.2: Identified mounting parameters.

Figure 4.2 displays the squared modulus of the mobilities associated with the velocities in the z direction on observations points 1 to 6, whose coordinates are given in Table. 4.3, for an excitation in the z direction on point 1. In the case of a perfect rigid mounting, we observe that most of the resonances are shifted upward and that the perfectly tied model of the beam assembly is effectively over stiffened as mentioned in [97]. Moreover, the flexible mounting model is able to provide a satisfactory prediction of the frequency response functions of this assembly of beam elements over the frequency band of interest. In particular, the good prediction of transfer mobilities between points quite distant all over the structure, and consequently of the associated transmission paths, is noticeable. However, as the frequency increases, a discrepancy between the measurements and the computational model appears that cannot be taken into account within the framework of this flexible mounting model.

	Point 1	Point 2	Point 3	Point 4	Point 5	Point 6
x [m]	2.060	2.120	0.760	2.490	2.490	0.570
y [m]	1.830	0.640	1.230	1.540	0.400	1.830

Table 4.3: Observation point coordinates.

Moreover, it should be noted that only one parameter was associated with respectively six, six and ten connections for the red, green and blue types. This leads towards the conclusion that, for this system which was built in a manufacture, involving repeatable processes, no fluctuation associated with one given technological type of mounting is propagating to the observable in the frequency band of interest. Those potential fluctuations might however be part of the reason for the discrepancies that appear past 200 Hz but are out of the scope of this work.

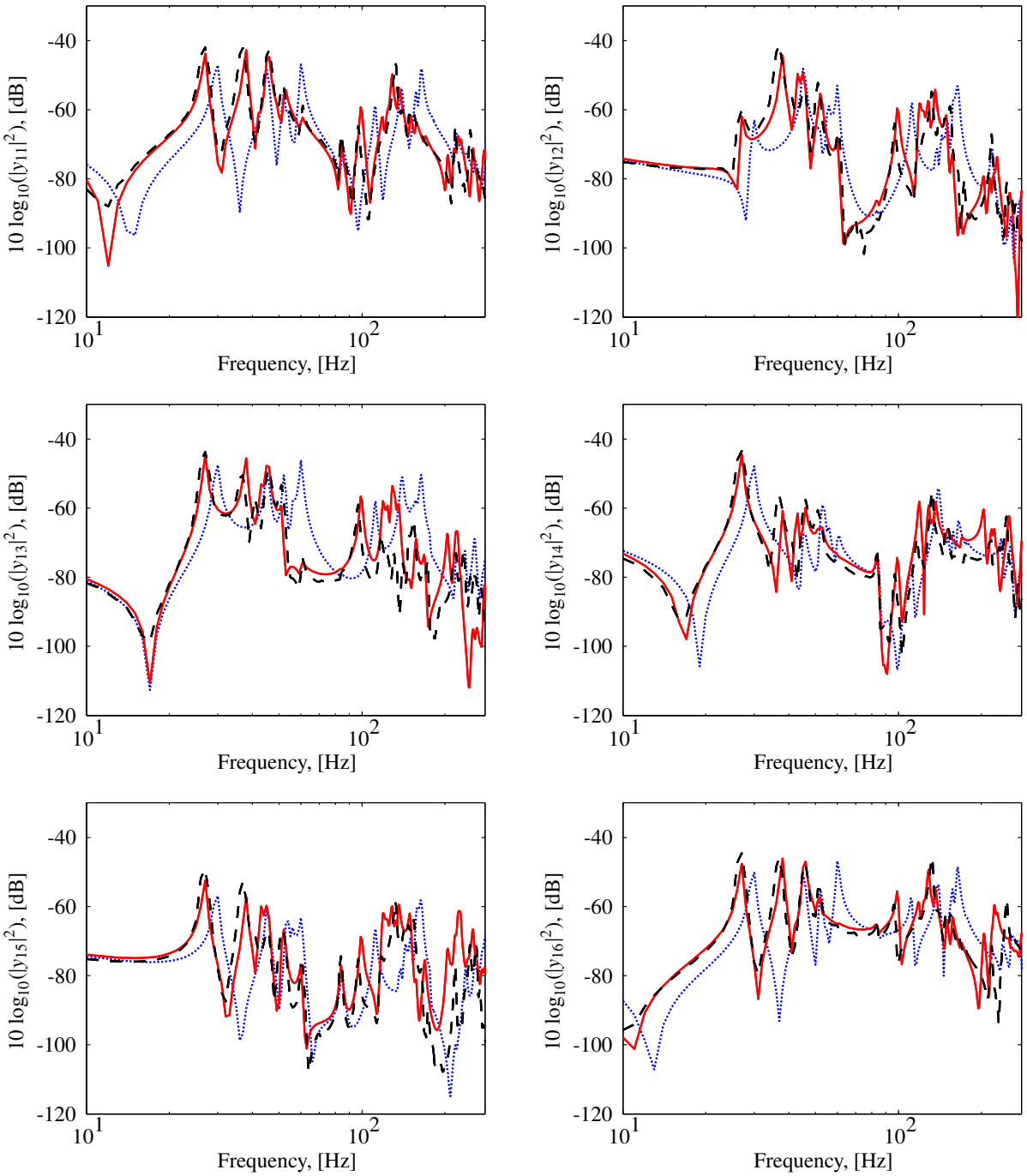

Figure 4.2: Set of mobilities obtained for an excitation on point 1. Experimental measurements (thin black dashed lines); computational model with perfect rigid mounting (thin blue dashed line); computational model with optimal set of mounting parameters (thin red solid line).

4.3.2 Assembly of one oriented strand board and beam elements

In order to investigate such potential flexible effects in regard to board onto beam assemblies, as well as to assess for the latter possibility to be taken into account with the previous model, a simple system is designed, built, and experimental measurements are carried out. A suspended assembly of one oriented strand board on top of four wooden beams (see Fig. 4.3), of dimensions 2.405 m $\times$ 0.635 m $\times$ 0.152 m, is excited on different points and experimental mobilities are measured over the frequency band $\mathbb{B} = [10, 280]$ Hz. Beams 1 and 2 are of dimension 2405 mm $\times$ 45 mm $\times$ 140 mm while beams 3 and 4 are

of dimension 45 mm × 545 mm × 140 mm and the board has a thickness of 12 mm. A computational model is constructed for the frequency band $\mathbb{B}$, in which the structural loss factor is once gain fixed to $\eta_s = 0.02$. The different physical properties, identified from experimental measurements according to the methodology introduced in Chapter 3, are given in Tables 4.4 and 4.5. Noteworthy is the fact that the oriented strand board has not the same origin than those treated in Section 3.3.2, thus explaining the large discrepancies between identified elastic properties and mass densities for the former, given in Table 3.7 with respect to those of the latter. Unfortunately, only one board specimen could have been measured but, given the range of properties observed in Section 3.3.2, the considered oriented strand board is most likely not a realisation from the same product.

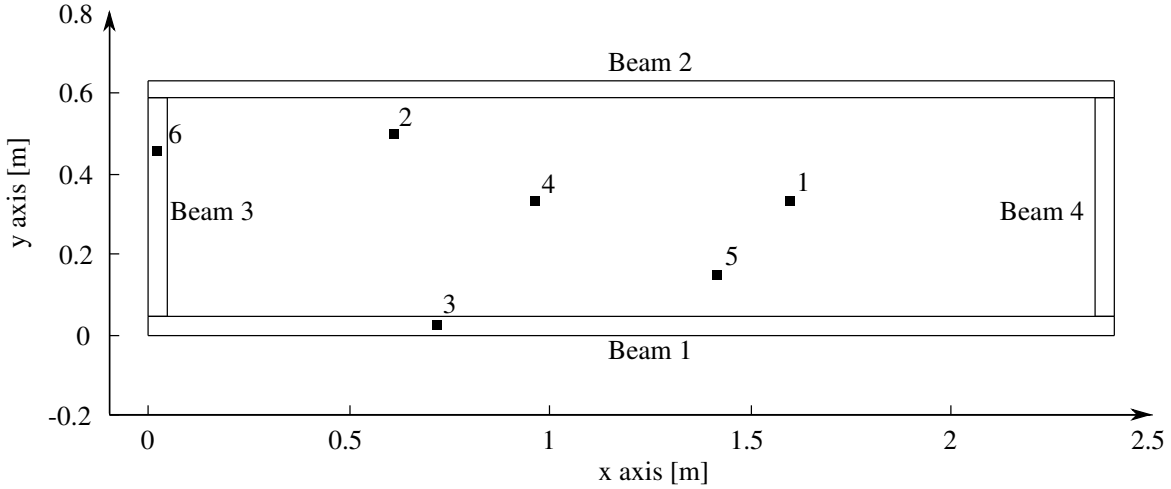

Figure 4.3: Assembly of one oriented strand board on top of wooden beam elements. Observation points (black squares).

	B1	B2	B3	B4
E_l [GPa]	12.5	12.5	9	9
ρ^s [kg/m^3]	469	496	460	460

Table 4.4: Wooden beams physical properties.

E_x GPa	E_y GPa	G_{xy} GPa	G_{yz} GPa	G_{xz} GPa	ν_{xy}	ρ^s kg/m^3
5.5	3	1.5	1	1	0.25	650

Table 4.5: OSB physical properties.

The system involves two types of assemblies: beam onto beam and board onto beam. In order to discriminate the effects of each, the methodology was deployed in two steps. The assembly of beam elements was first considered and experimental measurements of mobilities were carried out. Identical mounting parameters were then associated with each of the four beam onto beam assemblies and identified with the same methodology than within the previous Section 4.3.1. Subsequently, experimental measurements were performed considering the whole structure consisting in the strand board mounted onto the beams. Identical mounting parameters were associated with each of the board onto four beam assemblies and identified using the computational model updated with the mounting parameters associated with the beams only. The identified numerical values for the different kind of mounting parameters are given in Table 4.6. It should be noted that, while the technological realisation of the mounting for the beam onto beam assembly differs (screws) from the ones involved within the structure treated in

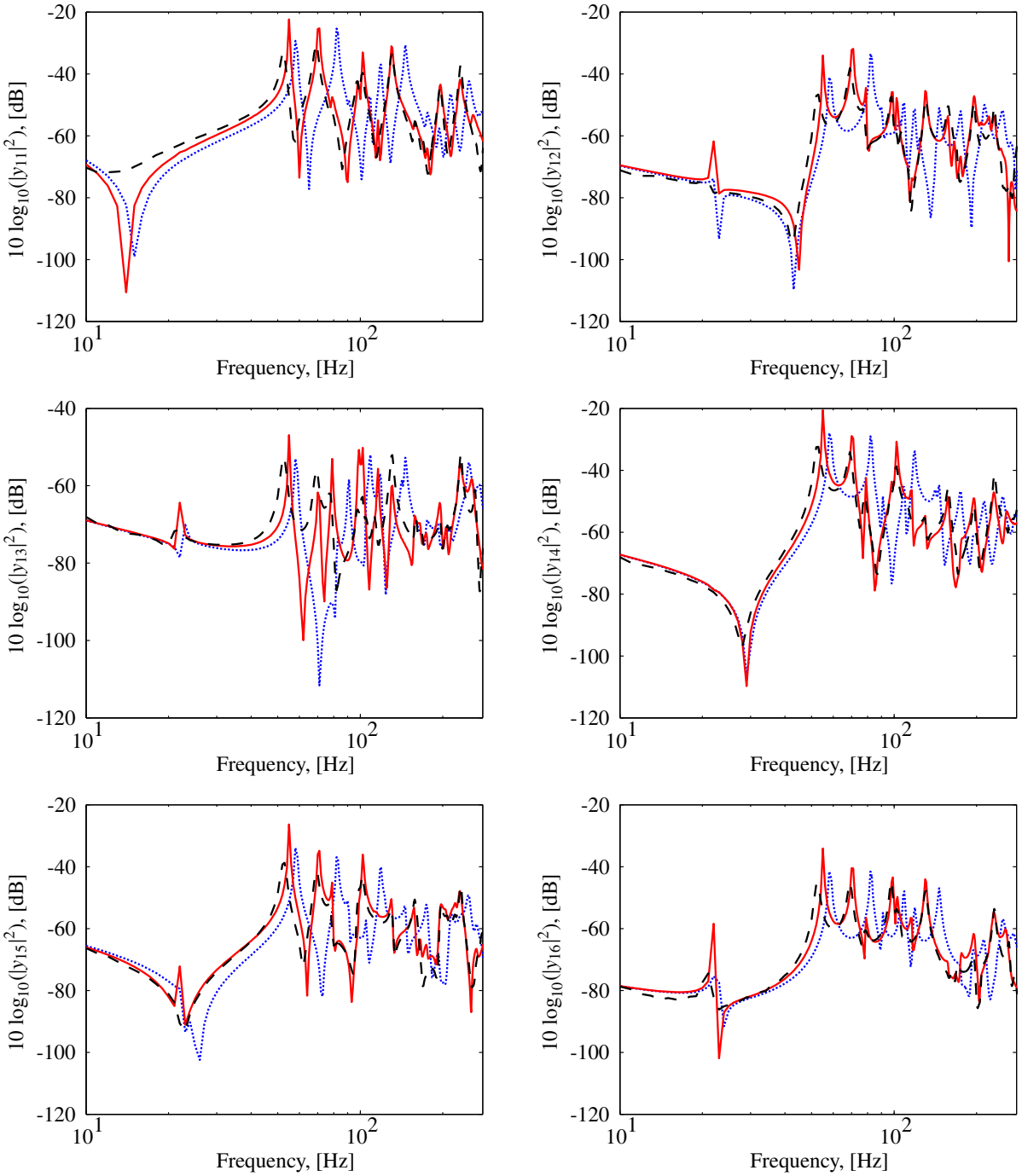

Figure 4.4: Set of mobilities obtained for an excitation on point 1. Experimental measurements (thin black dashed lines); computational model with perfect rigid mounting of the strand board (thin blue dashed line); computational model with optimal set of mounting parameters (thin red solid line).

Section 4.3.1, the identified parameter in this case is quite close to a perfectly rigid assembly. Due to its smaller dimensions, the system is in fact less sensitive to residual flexibilities as torsional modes are hardly excited for example, but also as its frequency regime is different with a lower modal density in an identical frequency range. Figure 4.4 displays the squared modulus of the mobilities associated with the observations points 1 to 6, whose coordinates are given in Table. 4.7. In the case of a perfect rigid mounting of the board onto the beams, we observe here again that the model is over stiffened. Thus, the flexible mounting model is able to improve the predictive model even for the observation points 3 and 6 directly located on top of beams, which validates the continuous connection model for this type of

mounting in this frequency range.

Assembly type	Beam/Beam	Beam/Board
Numerical value of parameter "k_B"	1	0.042

Table 4.6: Identified mounting parameters.

	Point 1	Point 2	Point 3	Point 4	Point 5	Point 6
x [m]	1.610	0.595	0.770	0.995	1.410	0.020
y [m]	0.330	0.500	0.035	0.315	0.140	0.480

Table 4.7: Observation point coordinates.

4.4 Whole assembled shear panel

In Sections 4.3.1 and 4.3.2, parameters associated with the flexible model were identified for different configurations. In this paragraph, the acquired information is applied in the case of a whole assembled shear panel, constituted of oriented strand boards mounted on an assembly of beams. The beam assembly treated in Section 4.3.1 is now covered with five oriented strand boards, delimited by the grey areas on Fig. 4.5. Two new observation points, whose coordinates are given in Table 4.8, are placed on the boards such that accelerometers on each side of the system provide transfer mobilities from boards to boards and boards to beams.

A computational model is constructed for the frequency band $\mathbb{B} = [10, 280]$ Hz, in which the structural loss factor is fixed to $\eta_s = 0.02$. The different physical properties are given in Tables 4.1 and 4.5. Each oriented strand board is modeled with an identical mass density and elasticity tensor. Boards are however not connected with eachother on the edges, as an air gap of the order of 5 mm is observed between them. Mounting parameters for the beam assembly are those identified in Section 3.3.2 and given in Table 4.2, which are effectively identical as the system is the same, while the mounting parameter associated with the board onto beam connections is the one identified in Section 4.3.2 and given in Table 4.6 which is chosen as a prior nominal value because none of the board onto beam connections of the systems exactly corresponds to the ones treated within the previous section.

Figure 4.2 displays the squared modulus of the mobilities associated with the velocities in the z direction on observations points 1, 7, 8 and 9 for an excitation in the z direction on points 7 and 8. First of all, for any of the observation point, the model taking into account the flexible mounting improves the prediction in comparison with the model using perfectly tied connections. However, the input mobility y_{88}, located on a board straight on top of a central beam, shows that the updated model fails to give a good prediction for the points located directly on the connections, starting from 100 Hz approximately. According to the french standards ([102] in regard to walls and [103] in regard to floors) the boards were nailed every 15 cm to the sidelong beams and 30 cm to the central beams. Moreover, an approximation of the bending wavelength, function of the frequency, can be computed using the analytical dispersion relation associated with an a isotropic thin plate given in [81] such that

$$k^4 = \omega^2 \frac{\rho^s h}{B} , \tag{4.4}$$

in which $B = Eh^3/(12(1-\nu^2))$ and h denotes the thickness of the plate. Consequently, as the bending wavelenght for such plate is around 70 cm at 100 Hz, half a wavelength can be comprised between two connection points thus explaining the discrepancies in term of modification in the frequency regime of the system, from low to medium frequencies. In constraining the board on the whole surface of

contact with the beams for which the nails are placed every 30 cm, the model is consequently locally over stiffened in regard to the experimental observation were the board is free to distort between the nails. This transition in the dynamic behavior is consistent with the one mentioned in [96, 99] and was not observed in Section 4.3.2 where the connection points were placed every 15 cm on the side of the board, consequently increasing the frequency limit of validity for the model. The flexible model with continuous connections is however able to give a good prediction of the transfer mobilities regardless of the position of the observation point, which can be explained by the fact that long distance transmissions are dominated by the low frequency modes with large wavelengths, still correctly taken into account in the model.

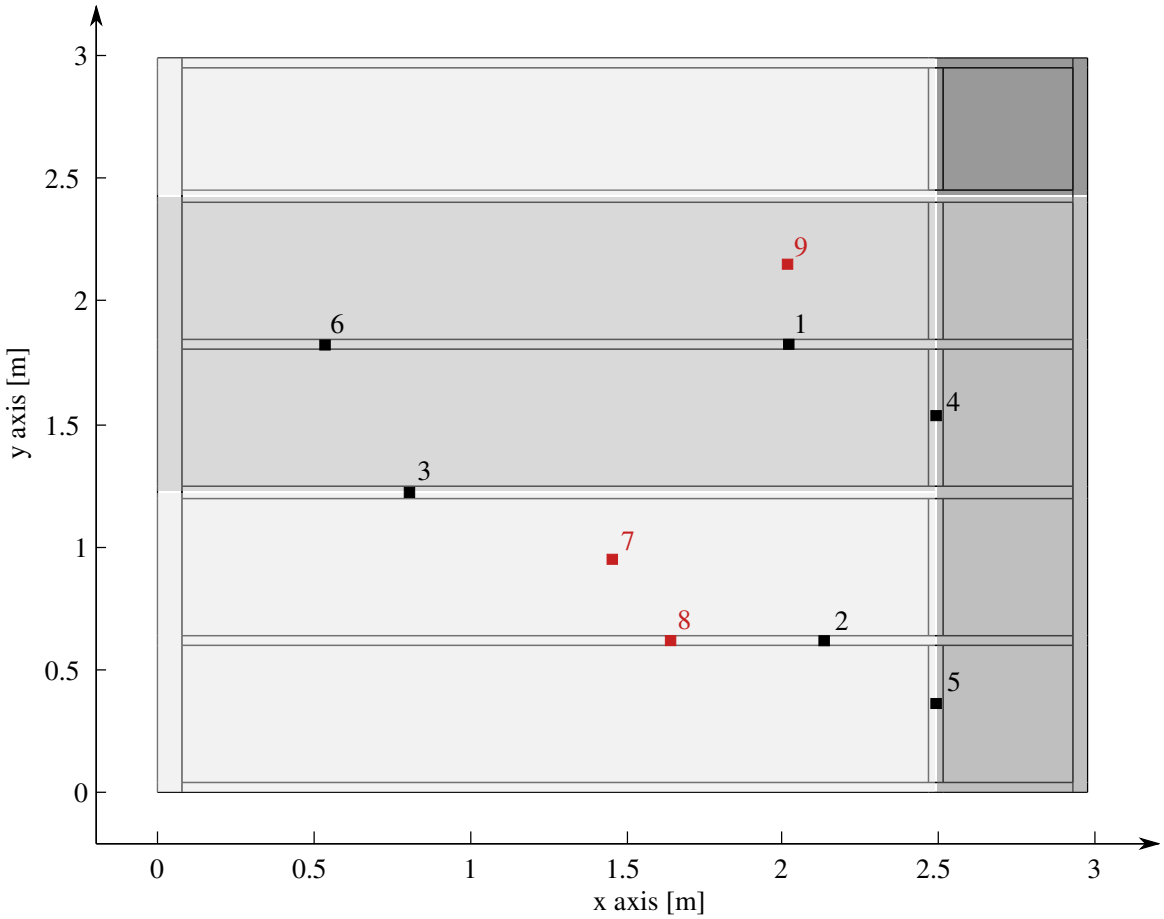

Figure 4.5: Assembled shear panel. Observation points on the beam side (black squares). Observation points on the board side (red squares). Distinct boards (five shades of grey).

	Point 7	Point 8	Point 9
x [m]	1.410	1.680	2.060
y [m]	0.980	0.640	2.150

Table 4.8: Observation point coordinates on the OSB side.

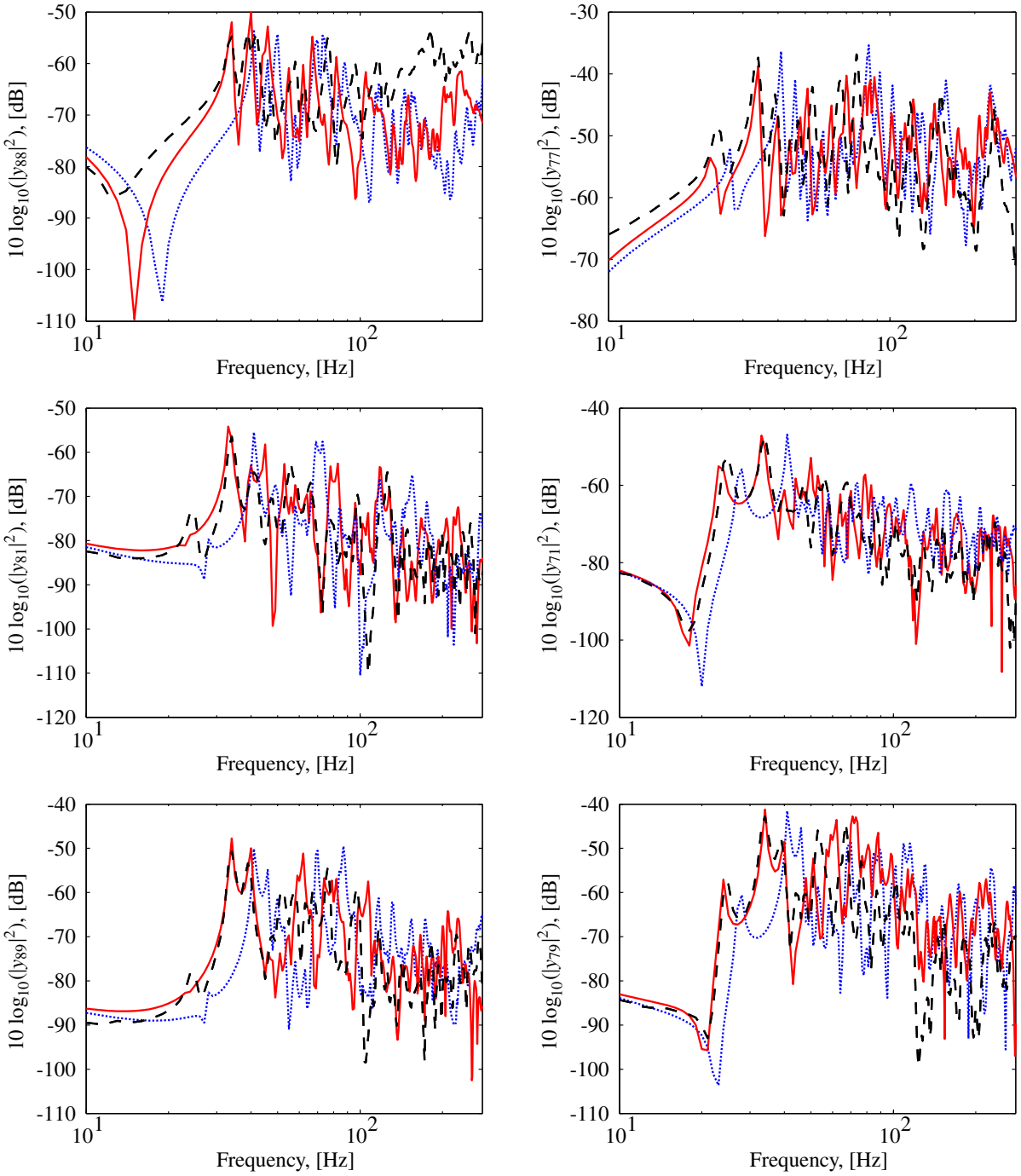

Figure 4.6: Set of mobilities obtained for an excitation on points 7 and 8. Experimental measurements (thin black dashed lines); computational model with perfect rigid mounting of the strand board (thin blue dashed line); computational model with optimal set of mounting parameters (thin red solid line).

4.5 Conclusion

In this chapter, a flexible mounting model was used and its parameters were identified for typical lightweight wood-based assemblies. It was shown that perfect rigid mounting effectively over stiffens the model and that a flexible mounting model improves the overall prediction of the mobilities between various points of the boards and beams of a typical shear panel. This simple flexible mounting model was however shown to be limited by the flexural wavelength in the boards and the distance between the connection points. Those considerations might become critical within walls where thin boards and large

spacings between screws or nail can be found. For floors however, boards are much stiffer such that the validity of the continuous connection model is extended in frequency as an identical spacing of nails or screws is set within the standards.

Regardless of the possible identification of flexible models for given technological mountings, this approach allowed a step forward in the comprehension of the systems of interest. Heretofore, the knowledge of the material properties associated with each elastic subpart as well as a correct modeling and characterisation of the connections allows to obtain an accurate deterministic predictive model for the core constituent of most lightweight separative elements at low frequencies. In the following, the problematic will consequently be to provide a robust prediction while facing a downgrade with regard to the available information.

5

Reduced order computational model for the vibroacoustic problem

Contents

5.1 Introduction

In this chapter, the dynamical problem in physical coordinates is projected onto a reduced functionnal basis. Such basis results from the resolution of a set of generalized eigenvalue problems associated with each medium. Model reduction strategies in regard to the structure and internal acoustic cavities are classical and documented [22, 23, 29, 30] meanwhile reduced order models adapted to poroelastic problems are subject of ongoing research [31–34, 36–40]. In Chapter 2, for the construction of the computational model, the displacement field was chosen as the primary variable for the description of the solid and fluid phases of the poroelastic medium. This choice was motivated by the generality of the model with respect to an implementation within the framework of an optimisation algorithm exploring various admissible configurations, as well as by the promising results associated with the reduction strategies recently presented in [37, 39]. However, within a significant part of lightweight building constructions, insulation materials belong to the class of limp frame poroelastic materials and can be modeled accordingly, leading to an alternative computational model which was defined in Section 2.5. Hereinafter, reduction strategies are investigated and presented for both computational models.

5.2 Reduced order model for the structure

5.2.1 Construction of the truncated projection basis

A truncated modal expansion of $\mathbb{U}^{\mathrm{s}}$, the vector of the nodal values of the displacement field $\mathbf{u}^{\mathrm{s}}$ in Ω^{s}, is constructed on an *ad hoc* set of eigenvectors. We then introduce the following generalized eigenvalue problem: find the eigenvectors $\mathbb{U}^{\mathrm{s}}_{\alpha}(\mathbf{p})$ respectively associated with the eigenvalues $\lambda^{\mathrm{s}}_{\alpha}(\mathbf{p})$ such that

$$[\mathbb{K}^{\mathrm{s}}(\mathbf{p})]\,\mathbb{U}^{\mathrm{s}}_{\alpha}(\mathbf{p}) = \lambda^{\mathrm{s}}_{\alpha}(\mathbf{p})\,[\mathbb{M}^{\mathrm{s}}(\mathbf{p})]\,\mathbb{U}^{\mathrm{s}}_{\alpha}(\mathbf{p})\,. \tag{5.1}$$

Vectors $\mathbb{U}^{\mathrm{s}}_{\alpha}(\mathbf{p})$ constitute an orthonormal family of $\mathbb{R}^{N_{\mathrm{s}}}$ with respect to the inner product defined with the mass matrix $[\mathbb{M}^{\mathrm{s}}(\mathbf{p})]$ such that $\langle[\mathbb{M}^{\mathrm{s}}(\mathbf{p})]\mathbb{U}^{\mathrm{s}}_{\alpha}(\mathbf{p}), \mathbb{U}^{\mathrm{s}}_{\beta}(\mathbf{p})\rangle = \delta_{\alpha\beta}$. The modal matrix $[\mathcal{U}^{\mathrm{s}}(\mathbf{p})]$ is introduced as the matrix whose columns are the eigenvectors $\mathbb{U}^{\mathrm{s}}_{\alpha}(\mathbf{p})$ respectively associated with the first n_{s} smallest eigenvalues $\lambda^{\mathrm{s}}_{\alpha}(\mathbf{p})$. We then have the following approximation

$$\mathbb{U}^{\mathrm{s}} \simeq [\mathcal{U}^{\mathrm{s}}(\mathbf{p})]\,\mathbf{q}^{\mathrm{s}}\,, \tag{5.2}$$

where $\mathbf{q}^{\mathrm{s}}$ is the complex vector of the generalized coordinates associated with the structure.

5.2.2 Generalized matrices for the reduced order model

The projection of the dynamic stiffness matrix $[\mathbb{A}^{\mathrm{s}}(\omega;\mathbf{p})]$ associated with the structure, defined by Eq. (2.55), according to Eq. (5.2), gives the $(n_{\mathrm{s}}\times n_{\mathrm{s}})$ complex symmetric matrix $[A^{\mathrm{s}}(\omega;\mathbf{p})]$ such that

$$[A^{\mathrm{s}}(\omega;\mathbf{p})] = -\omega^2[M^{\mathrm{s}}(\mathbf{p})] + i\omega\,[D^{\mathrm{s}}(\mathbf{p})] + [K^{\mathrm{s}}(\mathbf{p})]\,. \tag{5.3}$$

The generalized mass matrix $[M^{\mathrm{s}}(\mathbf{p})]$, damping matrix $[D^{\mathrm{s}}(\mathbf{p})]$ and stiffness matrix $[K^{\mathrm{s}}(\mathbf{p})]$ respectively are, due to the boundary conditions, $(n_{\mathrm{s}}\times n_{\mathrm{s}})$ real symmetric positive definite matrices defined by

$$\begin{gathered}[M^{\mathrm{s}}(\mathbf{p})] = [\mathcal{U}^{\mathrm{s}}(\mathbf{p})]^{\mathrm{T}}[\mathbb{M}^{\mathrm{s}}(\mathbf{p})][\mathcal{U}^{\mathrm{s}}(\mathbf{p})] \quad , \quad [D^{\mathrm{s}}(\mathbf{p})] = [\mathcal{U}^{\mathrm{s}}(\mathbf{p})]^{\mathrm{T}}[\mathbb{D}^{\mathrm{s}}(\mathbf{p})][\mathcal{U}^{\mathrm{s}}(\mathbf{p})] \\ \text{and} \quad [K^{\mathrm{s}}(\mathbf{p})] = [\mathcal{U}^{\mathrm{s}}(\mathbf{p})]^{\mathrm{T}}[\mathbb{K}^{\mathrm{s}}(\mathbf{p})][\mathcal{U}^{\mathrm{s}}(\mathbf{p})]\,.\end{gathered} \tag{5.4}$$

Moreover, the generalized external load onto the structure is written as

$$\mathbf{f}^{\mathrm{s}}(\omega;\mathbf{p}) = [\mathcal{U}^{\mathrm{s}}(\mathbf{p})]^{\mathrm{T}}\mathbb{F}^{\mathrm{s}}(\omega;\mathbf{p})\,. \tag{5.5}$$

5.3 Reduced order model for the internal acoustic fluid

5.3.1 Construction of the truncated projection basis

In a similar way than for the structure, a modal expansion of $\mathbb{P}$ the vector of the nodal values of the pressure disturbance field p in Ω^{f} is constructed on a set of eigenvectors and we introduce the following generalized eigenvalue problem: find the eigenvectors $\mathbb{P}_\alpha(\mathbf{p})$ respectively associated with the eigenvalues $\lambda^{\mathrm{f}}_\alpha(\mathbf{p})$ such that

$$[\mathbb{K}^{\mathrm{f}}(\mathbf{p})]\,\mathbb{P}_\alpha(\mathbf{p}) = \lambda^{\mathrm{f}}_\alpha(\mathbf{p})\,[\mathbb{M}^{\mathrm{f}}(\mathbf{p})]\,\mathbb{P}_\alpha(\mathbf{p})\,. \tag{5.6}$$

Vectors $\mathbb{P}_\alpha(\mathbf{p})$ constitute an orthonormal family of $\mathbb{R}^{N_{\mathrm{f}}}$ with respect to the inner product defined with the mass matrix $[\mathbb{M}^{\mathrm{f}}(\mathbf{p})]$ such that $\langle[\mathbb{M}^{\mathrm{f}}(\mathbf{p})]\mathbb{P}_\alpha(\mathbf{p}), \mathbb{P}_\beta(\mathbf{p})\rangle = \delta_{\alpha\beta}$. The modal matrix $[\mathcal{P}(\mathbf{p})]$ is introduced as the matrix whose columns are the eigenvectors $\mathbb{P}_\alpha(\mathbf{p})$ respectively associated with the first n_{f} smallest eigenvalues $\lambda^{\mathrm{f}}_\alpha(\mathbf{p})$ and we have the following approximation

$$\mathbb{P} \simeq [\mathcal{P}(\mathbf{p})]\,\mathbf{q}^{\mathrm{f}}\,, \tag{5.7}$$

where $\mathbf{q}^{\mathrm{f}}$ is the complex vector of the generalized coordinates associated with the acoustic fluid medium.

5.3.2 Generalized matrices for the reduced order model

The projection of the acoustical dynamic stiffness matrix $[\mathbb{A}^{\mathrm{f}}(\omega;\mathbf{p})]$ defined by Eq. (2.56) according to Eq. (5.7) gives the $(n_{\mathrm{f}} \times n_{\mathrm{f}})$ complex symmetric matrix $[A^{\mathrm{f}}(\omega;\mathbf{p})]$ such that

$$[A^{\mathrm{f}}(\omega;\mathbf{p})] = -\omega^2[M^{\mathrm{f}}(\mathbf{p})] + i\omega\,[D^{\mathrm{f}}(\mathbf{p})] + [K^{\mathrm{f}}(\mathbf{p})]\,. \tag{5.8}$$

The generalized acoustical mass matrix $[M^{\mathrm{f}}(\mathbf{p})]$, damping matrix $[D^{\mathrm{f}}(\mathbf{p})]$ and stiffness matrix $[K^{\mathrm{f}}(\mathbf{p})]$ repectively are $(n_{\mathrm{f}}\times n_{\mathrm{f}})$ real symmetric positive definite and real symmetric positive semidefinite matrices defined by

$$\begin{gathered}[M^{\mathrm{f}}(\mathbf{p})] = [\mathcal{P}(\mathbf{p})]^{\mathrm{T}}[\mathbb{M}^{\mathrm{f}}(\mathbf{p})][\mathcal{P}(\mathbf{p})] \quad , \quad [D^{\mathrm{f}}(\mathbf{p})] = [\mathcal{P}(\mathbf{p})]^{\mathrm{T}}[\mathbb{D}^{\mathrm{f}}(\mathbf{p})][\mathcal{P}(\mathbf{p})] \\ \text{and} \quad [K^{\mathrm{f}}(\mathbf{p})] = [\mathcal{P}(\mathbf{p})]^{\mathrm{T}}[\mathbb{K}^{\mathrm{f}}(\mathbf{p})][\mathcal{P}(\mathbf{p})]\,.\end{gathered} \tag{5.9}$$

Moreover, the $(n_{\mathrm{s}} \times n_{\mathrm{f}})$ reduced coupling matrix between the structure and the internal acoustic fluid is written as

$$[C_\Pi(\mathbf{p})] = [\mathcal{U}^{\mathrm{s}}(\mathbf{p})]^{\mathrm{T}}[\mathbb{C}_\Pi(\mathbf{p})][\mathcal{P}(\mathbf{p})]\,. \tag{5.10}$$

5.4 Reduced order model for the poroelastic medium modeled as coupled solid and fluid phases with displacements as primary variables

Although promising results were mentioned in regard to model reduction strategies based on the symmetric displacement formulation for the poroelastic medium, intrinsic issues remain associated with the use of the displacement field for the description of fluid domains. In particular, quite high modal densities are observed [40]. Indeed, the rotational part of the fluid displacement field is only coupled to the rotational part of the displacement field through inertial and viscous effects. Shear strain components associated with the fluid phase of the poroelastic medium are not coupled through Biot stress-strain relations defined by Eqs. (2.35) to (2.36) and remain free. Thus, it induces the presence of numerous low frequency coupled eigenmodes in the poroelastic medium (see Fig. 5.1) similar to the circulation modes observed in pure acoustical applications. In the context of acoustics, such eigenmodes are spurious and have been extensively treated in the literature. For example in [104] with the creation of an artificial stiffness *via* a penalty method (the idea was later transposed to the poroelastic medium in [105]), or [106] with a reduced integration of the elementary stiffness matrix and mode filtering by projection of the elementary mass matrix, and more recently in [107] and [108], with the choice of irrotational interpolation functions or additional constraint equations to satisfy irrotationality. However it was shown in [35]

and [56] that an hypothesis of irrotationnal fluid within the poroelastic medium formulation, which results in an overestimation of relative solid and fluid displacements, ultimately yields an overestimation of viscous dissipation.

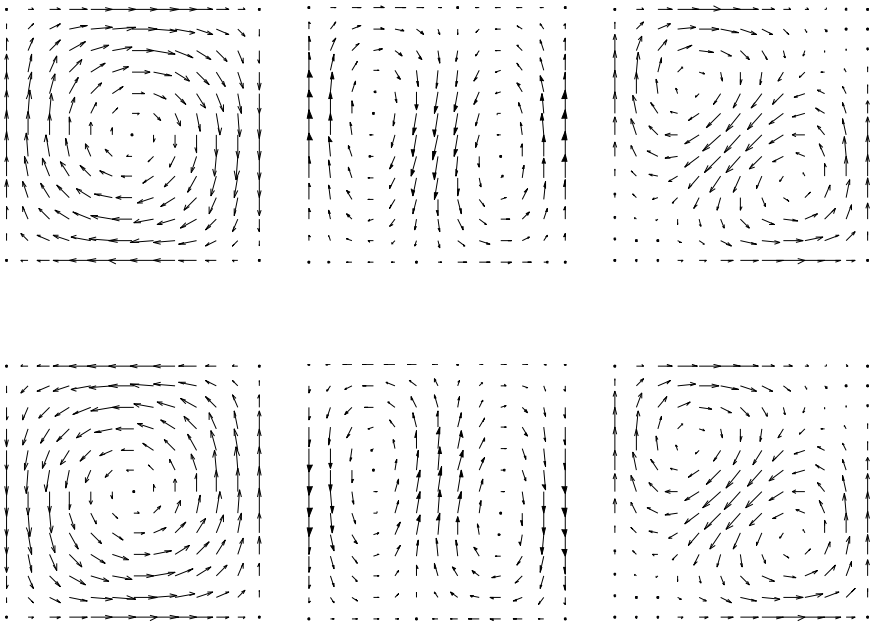

(a) Coupled mode 1 (b) Coupled mode 2 (c) Coupled mode 3

Figure 5.1: Example of low frequency coupled modes in the poroelastic medium. Solid displacement (top) and fluid displacement (bottom).

Following, due to the high modal density associated with the poroelastic medium at low frequencies, the convergence rate with respect to the dimension of the projection basis is of prime importance. Thus, appropriate strategy has to be investigated in order to minimise the number of required eigenmodes or attachment functions to reach a given level of precision with respect to a direct reference resolution of the linear system in physical coordinates. Unlike classical structural-acoustics problems, in which cases *in vacuo* modes of the structure can be used as a good projection basis due to the weak influence of the fluid, the poroelastic medium and in particular its fluid phase is strongly influenced by the fluid particle displacement continuity condition (see Eqs. (2.22) and (2.23)) at the boundary with acoustic cavities. Then, the projection on a truncated functional basis such that no constraint is prescribed on the boundary with the acoustic fluid is not optimal in terms of a convergence using a minimal number of eigenfunctions. In order to improve the latter point, it was proposed in [39] to add the contribution of the non-kept eigenmodes of higher natural frequencies through the static response of the poroelastic medium domain to the excitation from the acoustic cavities. The pressure formulation then allows to use the acoustic pressure generalized coordinates for the static solution and to avoid keeping the restriction of the poroelastic phases displacement fields on the boundary with the acoustic fluid. However, a great number of modes was still to be taken into account to converge whereas some showed a negligible participation [40]. In a general context, a mixed boundary conditions approach was proposed in [37] Such approach belongs to the class of hybrid component mode synthesis methodologies according to the review of presented in [109]. The boundary of the poroelastic medium subjected to an external load is set free for the solid phase and fixed for the fluid phase for the computation of the coupled eigenmodes and the convergence is observed for a two dimensionnal application. This ultimately induces a trade off between keeping interface degrees of freedom and improving the convergence depending of the physical nature of the boundary conditions. In the particular case of this work with a poroelastic medium coupled with an acoustic cavity, it is shown that the convergence rate is particularly improved due to better match of computed eigenmodes with effective physical displacements. Hereinafter we detail the different generalized

matrices resulting from an original hybrid reduction strategy for the vibroacoustic computational model with poroelastic medium.

First, we introduce the notations for the derivation of the hybrid component mode synthesis methodology associated with the poroelastic medium. Let $\mathbb{U}_\Gamma^{p_S}$ be the vector of the N_Γ nodal values of $\mathbf{u}^{p_s}$ on the interface of the poroelastic medium with the structure Γ. Let $\mathbb{U}_{\Gamma,\mathbf{n}}^{p_F}$ and $\mathbb{U}_{\Sigma,\mathbf{n}}^{p_F}$ respectively be the vectors of the $N_{\Gamma,\mathbf{n}}$ and $N_{\Sigma,\mathbf{n}}$ nodal values of $\mathbf{u}^{p_f} \cdot \mathbf{n}^p$ on Γ and the interface of the poroelastic medium with the internal acoustic cavities Σ. Let us assume that within the appropriate reference frame, the vector $\mathbb{U}^p$ has the following numbering

$$\mathbb{U}^p = \begin{bmatrix} \mathbb{U}_I^p \\ \mathbb{U}_\Gamma^{p_S} \\ \mathbb{U}_{\Gamma,\mathbf{n}}^{p_F} \\ \mathbb{U}_{\Sigma,\mathbf{n}}^{p_F} \end{bmatrix} , \tag{5.11}$$

where $\mathbb{U}_I^p$ is the vector of dimension $N_I = N_p - (N_\Gamma + N_{\Gamma,\mathbf{n}} + N_{\Sigma,\mathbf{n}})$, gathering every so called "internal" remaining nodal value of $\mathbf{u}^{p_S}$ and $\mathbf{u}^{p_F}$ in Ω^p.

5.4.1 Construction of the truncated projection basis

In this paragraph we first introduce a standard generalized eigenvalue problem in order to construct the truncated basis used for the modal expansion of vector $\mathbb{U}_I^p$, combined with classical static boundary functions improving the convergence. Then, the vectors of the interface degrees of freedom with the structure $\mathbb{U}_\Gamma^{p_S}$ and $\mathbb{U}_{\Gamma,\mathbf{n}}^{p_F}$ are condensed out using the set of linear constraints derived from the discretization of the displacement continuity equations.

Reduced set of vectors for the projection of the internal degrees of freedom

According to the numbering defined by Eq. (5.11), let $[\mathbb{K}_{I,I}^p(\mathbf{p})]$ and $[\mathbb{M}_I^p(\mathbf{p})]$ respectively be the block matrices in $[\mathbb{K}_I^p(\mathbf{p})]$ and $[\mathbb{M}^p(\mathbf{p})]$ that correspond to the degrees of freedom $\mathbb{U}_I^p$. We then introduce the following generalized eigenvalue problem: find the eigenvectors $\mathbb{U}_\alpha^p(\mathbf{p})$ respectively associated with the eigenvalues $\lambda_\alpha^p(\mathbf{p})$ such that

$$[\mathbb{K}_{I,I}^p(\mathbf{p})]\, \mathbb{U}_\alpha^p(\mathbf{p}) = \lambda_\alpha^p(\mathbf{p})\, [\mathbb{M}_I^p(\mathbf{p})]\, \mathbb{U}_\alpha^p(\mathbf{p}) \, . \tag{5.12}$$

Vectors $\mathbb{U}_\alpha^p(\mathbf{p})$ constitute an orthonormal family of $\mathbb{R}^{N_I}$ with respect to the inner product defined with the mass matrix $[\mathbb{M}_I^p(\mathbf{p})]$ such that $\langle [\mathbb{M}_I^p(\mathbf{p})] \mathbb{U}_\alpha^p(\mathbf{p}), \mathbb{U}_\beta^p(\mathbf{p}) \rangle = \delta_{\alpha\beta}$. The modal matrix $[\mathcal{U}^p]$ is introduced as the matrix whose columns are the coupled solid-fluid phases eigenmodes $\mathbb{U}_\alpha^p$ respectively associated with the first n_I smallest eigenvalues $\lambda_\alpha^p(\mathbf{p})$. We then have the following approximation

$$\mathbb{U}_I^p \simeq [\mathcal{U}^p]\, \mathbf{q}_I^p + [\mathbb{S}_\Gamma^s]\, \mathbb{U}_\Gamma^{p_S} + [\mathbb{S}_\Gamma^f]\, \mathbb{U}_{\Gamma,\mathbf{n}}^{p_F} + [\mathbb{S}_\Sigma]\, \mathbb{U}_{\Sigma,\mathbf{n}}^{p_F} \, , \tag{5.13}$$

where $\mathbf{q}_I^p$ is the complex vector of the generalized coordinates associated with the internal values of the poroelastic medium solid and fluid phases. Moreover, $[\mathbb{S}_\Gamma^s]$, $[\mathbb{S}_\Gamma^f]$ and $[\mathbb{S}_\Sigma]$ are classical elastostatic lifting operators [110, 111] constructed from matrix $[\mathbb{K}_I^p(\mathbf{p})]$ through a set of static problems.

Elimination of the interface degrees of freedom with the structure

Let $\mathbb{U}_\Gamma^s$ be the vector of the nodal values of the structure displacement field $\mathbf{u}^s$ on Γ and $\mathbb{U}_I^s$ be the vector of the remaining internal degrees of freedom in Ω^s. Then, let us assume that we have the following numbering

$$\mathbb{U}^s = \begin{bmatrix} \mathbb{U}_I^s \\ \mathbb{U}_\Gamma^s \end{bmatrix} . \tag{5.14}$$

Let $\mathbb{U}^{\mathrm{s}}_{\Gamma,\mathbf{n}}$ be the vector of the nodal values of the normal displacement field $\mathbf{u}^{\mathrm{s}} \cdot \mathbf{n}^{\mathrm{p}}$ on Γ. We introduce the $(N_\Gamma \times N_{\mathrm{s}})$ localization matrix $[\mathcal{Q}^{\mathrm{s}}]$, extracting the interface degrees of freedom vector $\mathbb{U}^{\mathrm{s}}_\Gamma$ from the vector $\mathbb{U}^{\mathrm{s}}$ of the nodal values of the displacement field $\mathbf{u}^{\mathrm{s}}$ in Ω^{s}, as well as the $(N_{\Gamma,\mathbf{n}} \times N_\Gamma)$ projection matrix $[\mathcal{N}]$ such that

$$\mathbb{U}^{\mathrm{s}}_\Gamma = [\mathcal{Q}^{\mathrm{s}}]\, \mathbb{U}^{\mathrm{s}} \quad \text{and} \quad \mathbb{U}^{\mathrm{s}}_{\Gamma,\mathbf{n}} = [\mathcal{N}]\, \mathbb{U}^{\mathrm{s}}_\Gamma \,. \tag{5.15}$$

The discretization of the displacement continuity conditions between the structure and the poroelastic medium, defined by Eqs. (2.5) and (2.6) or (2.30) and (2.31) yields the set of linear constraints defined by Eq. (2.54). Then, according to the numbering defined by Eq. (5.11) and Eq. (5.14), matrices $[\mathcal{B}^{\mathrm{p}}]$ and $[\mathcal{B}^{\mathrm{s}}]$ are written as

$$[\mathcal{B}^{\mathrm{p}}] = \begin{bmatrix} 0 & [\mathrm{I}_{N_\Gamma}] & 0 & 0 \\ 0 & 0 & [\mathrm{I}_{N_{\Gamma,\mathbf{n}}}] & 0 \end{bmatrix} \quad , \quad [\mathcal{B}^{\mathrm{s}}] = \begin{bmatrix} 0 & -[\mathrm{I}_{N_\Gamma}] \\ 0 & -[\mathcal{N}] \end{bmatrix} . \tag{5.16}$$

Given the modal expansion of the vector $\mathbb{U}^{\mathrm{s}}$ defined by Eq. (5.2), vectors $\mathbb{U}^{\mathrm{p_S}}_\Gamma$ and $\mathbb{U}^{\mathrm{p_F}}_{\Gamma,\mathbf{n}}$ can then be expanded on a truncated vector basis such that

$$\mathbb{U}^{\mathrm{p_S}}_\Gamma = [\mathcal{Q}^{\mathrm{s}}][\mathcal{U}^{\mathrm{s}}(\mathbf{p})]\, \mathbf{q}^{\mathrm{s}} \,, \tag{5.17}$$

$$\mathbb{U}^{\mathrm{p_F}}_{\Gamma,\mathbf{n}} = [\mathcal{N}][\mathcal{Q}^{\mathrm{s}}][\mathcal{U}^{\mathrm{s}}(\mathbf{p})]\, \mathbf{q}^{\mathrm{s}} \,. \tag{5.18}$$

Finally, using Eqs. (5.17) and (5.18) into Eq. (5.13) yields

$$\mathbb{U}^{\mathrm{p}}_{\mathrm{I}} \simeq [\mathcal{U}^{\mathrm{p}}]\, \mathbf{q}^{\mathrm{p}}_{\mathrm{I}} + [\mathbb{S}^{\mathrm{s}}_\Gamma][\mathcal{Q}^{\mathrm{s}}][\mathcal{U}^{\mathrm{s}}(\mathbf{p})]\, \mathbf{q}^{\mathrm{s}} + [\mathbb{S}^{\mathrm{f}}_\Gamma]\, [\mathcal{N}][\mathcal{Q}^{\mathrm{s}}][\mathcal{U}^{\mathrm{s}}(\mathbf{p})]\, \mathbf{q}^{\mathrm{s}} + [\mathbb{S}_\Sigma]\, \mathbb{U}^{\mathrm{p_F}}_{\Sigma,\mathbf{n}} \,. \tag{5.19}$$

We then introduce the following approximation for the vector $\mathbb{U}^{\mathrm{p}}$ gathering the nodal values of the poroelastic medium solid and fluid phases

$$\mathbb{U}^{\mathrm{p}} \simeq [\mathcal{H}(\mathbf{p})]\, \mathbf{q}^{\mathrm{p}} \,, \tag{5.20}$$

where the vector of the generalized coordinates $\mathbf{q}^{\mathrm{p}}$ is defined by

$$\mathbf{q}^{\mathrm{p}} = \begin{bmatrix} \mathbf{q}^{\mathrm{p}}_{\mathrm{I}} \\ \mathbf{q}^{\mathrm{s}} \\ \mathbb{U}^{\mathrm{p_F}}_{\Sigma,n} \end{bmatrix} , \tag{5.21}$$

and with the transformation matrix $[\mathcal{H}(\mathbf{p})]$ written as

$$[\mathcal{H}(\mathbf{p})] = \begin{bmatrix} [\mathcal{U}^{\mathrm{p}}] & ([\mathbb{S}^{\mathrm{s}}_\Gamma] + [\mathbb{S}^{\mathrm{f}}_\Gamma][\mathcal{N}])[\mathcal{Q}^{\mathrm{s}}][\mathcal{U}^{\mathrm{s}}(\mathbf{p})] & [\mathbb{S}_\Sigma] \\ 0 & [\mathcal{Q}^{\mathrm{s}}][\mathcal{U}^{\mathrm{s}}(\mathbf{p})] & 0 \\ 0 & [\mathcal{N}][\mathcal{Q}^{\mathrm{s}}][\mathcal{U}^{\mathrm{s}}(\mathbf{p})] & 0 \\ 0 & 0 & [I_{n_{\Sigma,\mathbf{n}}}] \end{bmatrix} . \tag{5.22}$$

In the most general case and as potential future prospects, constraint modes [109] are methodologies to be investigated to additionally reduce the dimension of the interface degrees of freedom on Σ which is already of one degree of freedom per poroelastic medium interface node.

5.4.2 Generalized matrices for the reduced order model

Let n_{p} be the dimension of the reduced order model for the poroelastic medium such as $n_{\mathrm{p}} = n_{\mathrm{I}} + n_{\mathrm{s}} + N_{\Sigma,\mathbf{n}}$. The projection of the dynamic stiffness matrix $[\mathbb{A}^{\mathrm{p}}(\omega;\mathbf{p})]$ defined by Eq. (2.57) according to Eq. (5.20) gives the $(n_{\mathrm{p}} \times n_{\mathrm{p}})$ complex symmetric matrix $[A^{\mathrm{p}}(\omega;\mathbf{p})]$ such that

$$[A^{\mathrm{p}}(\omega;\mathbf{p})] = -\omega^2 [M^{\mathrm{p}}(\mathbf{p})] + i\omega\, [D^{\mathrm{p}}(\omega;\mathbf{p})] + [K^{\mathrm{p}}(\omega;\mathbf{p})] \,, \tag{5.23}$$

in which, according to Eqs. (2.59) and (2.61) we have

$$[D^{\mathrm{p}}(\omega;\mathbf{p})] = [D^{\mathrm{p}}_1(\mathbf{p})] + \tilde{b}(\omega)\, [D^{\mathrm{p}}_2(\mathbf{p})] \,, \tag{5.24}$$

$$[K^{\mathrm{p}}(\omega;\mathbf{p})] = [K^{\mathrm{p}}_1(\mathbf{p})] + (\tilde{K}_{\mathrm{f}}(\omega) - P_0)\, [K^{\mathrm{p}}_2(\mathbf{p})] \,. \tag{5.25}$$

The generalized matrices $[M^{\mathrm{p}}(\mathbf{p})]$, $[D_1^{\mathrm{p}}(\mathbf{p})]$, $[D_2^{\mathrm{p}}(\mathbf{p})]$, $[K_1^{\mathrm{p}}(\mathbf{p})]$ and $[K_2^{\mathrm{p}}(\mathbf{p})]$ repectively are $(n_{\mathrm{p}} \times n_{\mathrm{p}})$ real symmetric positive definite and real symmetric positive semidefinite matrices defined by

$$[M^{\mathrm{p}}(\mathbf{p})] = [\mathcal{H}(\mathbf{p})]^{\mathrm{T}}[\mathbb{M}^{\mathrm{p}}(\mathbf{p})][\mathcal{H}(\mathbf{p})] \,, \tag{5.26}$$

$$[D_1^{\mathrm{p}}(\mathbf{p})] = [\mathcal{H}(\mathbf{p})]^{\mathrm{T}}[\mathbb{D}_1^{\mathrm{p}}(\mathbf{p})][\mathcal{H}(\mathbf{p})] \quad \text{and} \quad [D_2^{\mathrm{p}}(\mathbf{p})] = [\mathcal{H}(\mathbf{p})]^{\mathrm{T}}[\mathbb{D}_2^{\mathrm{p}}(\mathbf{p})][\mathcal{H}(\mathbf{p})] \,, \tag{5.27}$$

$$[K_1^{\mathrm{p}}(\mathbf{p})] = [\mathcal{H}(\mathbf{p})]^{\mathrm{T}}[\mathbb{K}_1^{\mathrm{p}}(\mathbf{p})][\mathcal{H}(\mathbf{p})] \quad \text{and} \quad [K_2^{\mathrm{p}}(\mathbf{p})] = [\mathcal{H}(\mathbf{p})]^{\mathrm{T}}[\mathbb{K}_2^{\mathrm{p}}(\mathbf{p})][\mathcal{H}(\mathbf{p})] \,. \tag{5.28}$$

Moreover the $(n_{\mathrm{p}} \times n_{\mathrm{f}})$ reduced coupling matrix between the poroelastic medium and the acoustic fluid is written as

$$[C_\Sigma] = [\mathcal{H}]^{\mathrm{T}}[\mathbb{C}_\Sigma][\mathcal{P}] \,. \tag{5.29}$$

5.4.3 Comparison of different reduction strategies for a poroelastic medium coupled with an acoustic cavity

The three dimensional case presented in [39] also treated in [35, 36] is used to compare three reduction strategies related to the problem of a poroelastic medium, with displacements as primary variable for the solid and fluid phases, coupled with an acoustic cavity. All three strategies use coupled eigenmodes, solutions of the generalized eigenvalue problem constructed with the poroelastic medium mass matrix and the static limit of the poroelastic medium stiffness matrix. The first one involves a projection of the poroelastic medium equations onto the eigenmodes with free interface with the fluid. The second one involves a projection onto the eigenmodes with free interface with the fluid and with an additionnal attachment operator as proposed in [38,39]. The last one involves the mixed boundary condition strategy as presented in Section 5.4. The cavity is of dimension 0.6 m × 0.4 m × 0.75 m. A 5 cm thick poroelastic layer, whose properties are given in Table 5.1, covers one of the wall in the longest cavity direction (meaning that the effective depth of the internal acoustic cavity is 0.7 m). The poroelastic medium is bonded to the covered wall (all solid displacement and normal fluid displacement are constrained) and sliding on the sides (normal solid displacement and normal fluid displacement constrained).

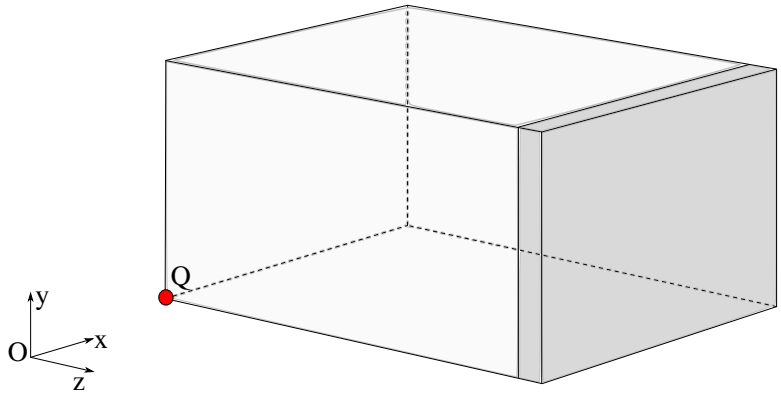

Figure 5.2: Three dimensional case treated in [35, 36, 39].

A punctual acoustical source is placed into the cavity such that $Q(\mathbf{x};\omega) = |Q_S|\,\omega^2\,\delta(\mathbf{x}-\mathbf{x}_Q)$, where $\mathbf{x}_Q$ denotes the coordinates of one of the corners opposite to the layer and $|Q_S| = 10^{-9}$. The internal acoustic fluid is discretized by a $12 \times 8 \times 15$ mesh of hexahedric pressure elements while the poroelastic medium is discretized by a $12 \times 8 \times 5$ mesh of hexahedric elements. The finite element discretization consequently yields $N_{\mathrm{p}} = 3260$ degrees of freedom for the poroelastic medium and $N_{\mathrm{f}} = 1872$ degrees of freedom for the internal acoustic cavity.

After resolution of the computational model over the frequency band $\mathbb{B} = [1, 1000]$ Hz the spatial average of the quadratic pressure within the internal cavity is computed as

$$P^2(\omega) = \frac{1}{V}\int_V |p(\mathbf{x};\omega)|^2 \,\mathrm{d}V \,, \tag{5.30}$$

Young's modulus [kPa]	845
Poisson's ratio	0.3
Mass density $(1-\phi)\rho^{p_s}$ [kg/m^3]	30
Porosity ϕ	0.96
Flow resistivity σ [N.s/m^4]	32000
Tortuosity α_∞	1.7
Viscous length Λ [μm]	90
Thermal length Λ' [μm]	165
Structural loss factor η_{ps}	0

(a) Poroelastic medium parameters.

Standard pressure P_0	1.015×10^5 Pa
Mass density ρ^f	1.21 kg/m^3
Heat capacity ratio γ	1.4
Sound velocity c_f	340 m/s
Prandtl number Pr	0.72
Dynamic viscosity η_f	1.81×10^{-5} N.s/m^2

(b) Air parameters.

Table 5.1: Poroelastic medium and air parameters.

and the mean quadratic pressure level is defined by

$$L(\omega) = 10 \log_{10}\left(\frac{P^2(\omega)}{p_{ref}^2}\right), \tag{5.31}$$

in which $p_{ref} = 2 \times 10^{-5}$ Pa. In order to evaluate the convergence rate of the different strategies, an error estimator is constructed such that

$$Er(n_p) = \frac{1}{\omega_{max} - \omega_{min}} \int_{\omega_{min}}^{\omega_{max}} |L^{n_p}(\omega) - L^{ref}(\omega)|^2 \, d\omega \,, \tag{5.32}$$

where L^{n_p} is the mean quadratic pressure level obtained with the reduced order computational model projected on a truncated basis of n_p eigenmodes for the poroelastic medium. L^{ref} is the mean quadratic pressure level computed with the computational model in the physical coordinates.

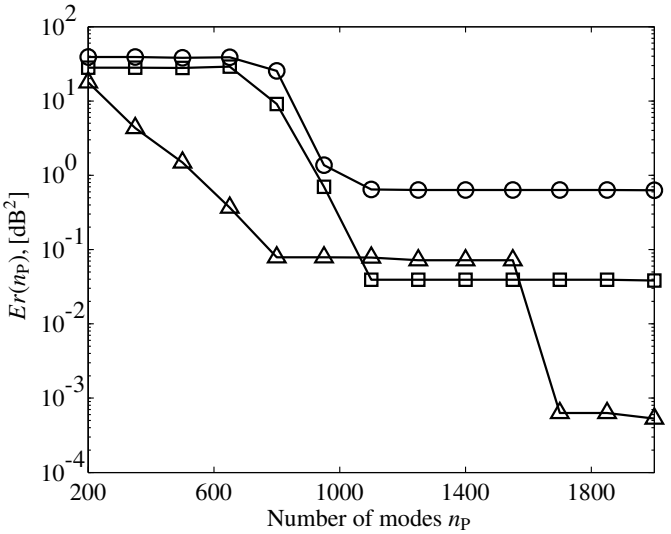

Figure 5.3: Error estimator function of n_p for three strategies, computed with respect to the frequency band [1,1000] Hz. Free interface (circles); free interface and attachment operator according to [38, 39] (squares); hybrid boundary conditions (upward-pointing triangles).

Figure 5.3 displays the error estimator function of n_p. The consideration of the gradient of the error estimator with respect to the number of modes included within the projection basis illustrates the problem raised in [40], as numerous modes have to be computed without participating in the response, resulting in a stagnation of the convergence rate over the frequency range [700,1600] Hz. The hybrid boundary

conditions approach displays comparable stagnation but shifted towards higher number of poroelastic modes such that a satisfactory precision could possibly be reached before. Within the case of the hybrid boundary conditions method we have $N_{\Sigma,\mathbf{n}} = 117$ the number of remaining physical degrees of freedom at the interface. The trade off between keeping those degrees of freedom and improving the convergence is consequently advantageous as an acceptable error level is reached earlier than with respect to the aforementioned other strategies.

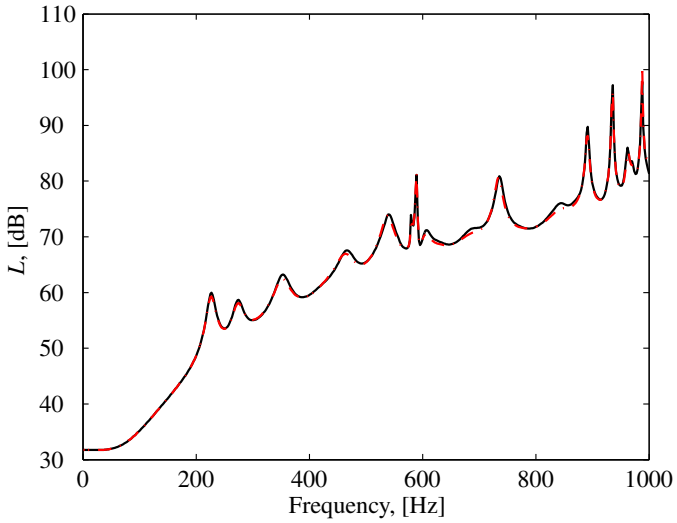

Figure 5.4: Sound pressure level. Reference solution (thin black solid line); hybrid boundary condition strategy with $n_{\mathrm{p}} = 800$ (thin red dash-dot line).

Figure 5.4 compares the mean quadratic pressure level obtained with the reference solution and with the reduced model using the hybrid boundary condition strategy with $n_{\mathrm{p}} = 800$ coupled eigenmodes and displays the ability of the chosen strategy to converge towards the reference solution.

5.5 Reduced order model for the poroelastic medium modeled as an equivalent fluid with pressure as the primary variable

In this paragraph, a reduction strategy for the poroelastic medium equations within the framework of a limp frame equivalent fluid model introduced in Section 2.5, is presented. The disturbance of the pressure field of an equivalent fluid is then the primary variable for the description of the poroelastic medium. In the continuity of previous reduction strategies, a component mode synthesis approach is carried out. Thus, eigenmodes of the equivalent fluid with fixed interface with the internal acoustic fluid, combined with static boundary functions, are used as a projection basis. Then, the vector of the interface degrees of freedom with the internal acoustic fluid is condensed out using the pressure continuity condition at the boundary with the internal acoustic fluid, defined by Eq. (B.6), and the modal expansion of the pressure disturbance field in Ω^{f} defined by Eq. (5.7). It should be noted that, due to the pressure continuity condition at the boundary with the internal acoustic fluid, domains Ω^{f} and Ω^{p} can be seen as a unique internal acoustic cavity whith contrasts in physical properties, which are complex and frequency dependent in Ω^{p}. Following, a unique reduction basis could have been constructed for the expansion of the pressure disturbance field in both domains, using a frequency dependent family of eigenfunctions for example. Within the context of this work, component mode synthesis methodologies are particularly attractive and favored due to their modular flexibility, allowing to distinguish and handle different physics with dedicated solvers.

5.5.1 Construction of the truncated projection basis

First, let $\mathbb{P}^{\mathrm{e}}_{\Sigma}$ be the vector of the $N_{\Sigma,\mathbf{n}}$ nodal values of p^{E} on the interface of the poroelastic medium with the internal acoustic fluid Γ and let $\mathbb{P}^{\mathrm{e}}_{\mathrm{I}}$ be the vector of dimension $N_{\mathrm{e,I}} = N_{\mathrm{e}} - N_{\Sigma,\mathbf{n}}$ gathering every other "internal" nodal value of p^{e} in Ω^P. Hereinafter, let us assume that we have the following numbering

$$\mathbb{P}^{\mathrm{e}} = \begin{bmatrix} \mathbb{P}^{\mathrm{e}}_{\mathrm{I}} \\ \mathbb{P}^{\mathrm{e}}_{\Sigma} \end{bmatrix} . \tag{5.33}$$

Reduced set of vectors for the projection of the internal degrees of freedom

According to the numbering defined by Eq. (5.33), let $[\mathbb{K}^{\mathrm{e}}_{1,\mathrm{I}}(\mathbf{p})]$ and $[\mathbb{M}^{\mathrm{e}}_{1,\mathrm{I}}(\mathbf{p})]$ respectively be the block matrices in $[\mathbb{K}^{\mathrm{e}}_{1}(\mathbf{p})]$ and $[\mathbb{M}^{\mathrm{e}}_{1}(\mathbf{p})]$, defined by Eqs. (2.69) and (2.70), that correspond to the degrees of freedom $\mathbb{P}^{\mathrm{e}}_{\mathrm{I}}$. We then introduce the following generalized eigenvalue problem: find the eigenvectors $\mathbb{P}^{\mathrm{e}}_{\alpha}(\mathbf{p})$ respectively associated with the eigenvalues $\lambda^{\mathrm{e}}_{\alpha}(\mathbf{p})$ such that

$$[\mathbb{K}^{\mathrm{e}}_{1,\mathrm{I}}(\mathbf{p})]\, \mathbb{P}^{\mathrm{e}}_{\alpha}(\mathbf{p}) = \lambda^{\mathrm{e}}_{\alpha}(\mathbf{p})\, [\mathbb{M}^{\mathrm{e}}_{1,\mathrm{I}}(\mathbf{p})]\, \mathbb{P}^{\mathrm{e}}_{\alpha}(\mathbf{p}) . \tag{5.34}$$

Vectors $\mathbb{P}^{\mathrm{e}}_{\alpha}(\mathbf{p})$ constitute an orthonormal family of $\mathbb{R}^{N_{\mathrm{e,I}}}$ with respect to the inner product defined with the mass matrix $[\mathbb{M}^{\mathrm{e}}_{1,\mathrm{I}}(\mathbf{p})]$ such that $\langle [\mathbb{M}^{\mathrm{e}}_{1,\mathrm{I}}(\mathbf{p})] \mathbb{P}^{\mathrm{e}}_{\alpha}(\mathbf{p}), \mathbb{P}^{\mathrm{e}}_{\beta}(\mathbf{p}) \rangle = \delta_{\alpha\beta}$. The modal matrix $[\mathcal{P}^{\mathrm{e}}(\mathbf{p})]$ is introduced as the matrix whose columns are the eigenvectors $\mathbb{P}^{\mathrm{e}}_{\alpha}(\mathbf{p})$ respectively associated with the first $n_{\mathrm{e,I}}$ smallest eigenvalues $\lambda^{\mathrm{e}}_{\alpha}(\mathbf{p})$ and we have the following approximation

$$\mathbb{P}^{\mathrm{e}}_{\mathrm{I}} \simeq [\mathcal{P}^{\mathrm{e}}(\mathbf{p})]\, \mathbf{q}^{\mathrm{e}}_{\mathrm{I}} + [\mathbb{S}^{\mathrm{e}}_{\Sigma}]\, \mathbb{P}^{\mathrm{e}}_{\Sigma} , \tag{5.35}$$

where $\mathbf{q}^{\mathrm{e}}$ is the complex vector of the generalized coordinates associated with the internal nodal values of the equivalent fluid pressure disturbance field. Moreover, the elastostatic lifting operator $[\mathbb{S}^{\mathrm{e}}_{\Sigma}]$ is computed from matrix $[\mathbb{K}^{\mathrm{e}}_{1}(\mathbf{p})]$ as

$$[\mathbb{S}^{\mathrm{e}}_{\Sigma}] = -[\mathbb{K}^{\mathrm{e}}_{1,\mathrm{I}}(\mathbf{p})]^{-1} [\mathbb{K}^{\mathrm{e}}_{1,\mathrm{I}\Sigma}(\mathbf{p})] , \tag{5.36}$$

where $[\mathbb{K}^{\mathrm{e}}_{1,\mathrm{I}}(\mathbf{p})]$ is inversible due to the fixed interface.

Elimination of the interface degrees of freedom with the internal acoustic fluid

Let $\mathbb{P}_{\Sigma}$ be the vector of the $N_{\Sigma,\mathbf{n}}$ nodal values of the acoustic pressure disturbance field p on Σ and $\mathbb{P}_{\mathrm{I}}$ be the vector of the remaining internal degrees of freedom in Ω^{f}. Then, let us assume that we have the following numbering

$$\mathbb{P} = \begin{bmatrix} \mathbb{P}_{\mathrm{I}} \\ \mathbb{P}_{\Sigma} \end{bmatrix} . \tag{5.37}$$

The discretization of the pressure continuity condition defined by Eq. (B.6), between the internal acoustic fluid and the equivalent fluid modeling the poroelastic medium, yields the set of linear constraints Eq. (2.54). According to the numbering defined by Eqs. (5.33) and Eq. (5.37), matrices $[\mathcal{B}^{\mathrm{f}}]$ and $[\mathcal{B}^{\mathrm{e}}]$ are written as

$$[\mathcal{B}^{\mathrm{f}}] = \begin{bmatrix} 0 & [I_{N_{\Sigma,\mathbf{n}}}] \end{bmatrix} \quad , \quad [\mathcal{B}^{\mathrm{e}}] = \begin{bmatrix} 0 & -[I_{N_{\Sigma,\mathbf{n}}}] \end{bmatrix} . \tag{5.38}$$

Moreover, we introduce the $(N_{\Sigma,\mathbf{n}} \times N_{\mathrm{f}})$ localization matrix $[\mathcal{Q}^{\mathrm{f}}]$, extracting the interface degrees of freedom vector $\mathbb{P}_{\Sigma}$ from the vector $\mathbb{P}$ of the nodal values of the internal acoustic fluid pressure disturbance field p in Ω^{f}, such that

$$\mathbb{P}_{\Sigma} = [\mathcal{Q}^{\mathrm{f}}]\, \mathbb{P} . \tag{5.39}$$

Given the modal expansion of vector $\mathbb{P}$ defined by Eq. (5.7), the vector $\mathbb{P}^{\mathrm{e}}_{\Sigma}$ can then be expanded on a truncated basis such that

$$\mathbb{P}^{\mathrm{e}}_{\Sigma} = [\mathcal{Q}^{\mathrm{f}}][\mathcal{P}]\, \mathbf{q}^{\mathrm{f}} , \tag{5.40}$$

and finally, using Eq. (5.40) into Eq. (5.35), yields

$$\mathbb{P}^{\mathrm{e}}_{\mathrm{I}} \simeq [\mathcal{P}^{\mathrm{e}}(\mathbf{p})]\, \mathbf{q}^{\mathrm{e}}_{\mathrm{I}} + [\mathbb{S}^{\mathrm{e}}_{\Sigma}][\mathcal{Q}^{\mathrm{f}}][\mathcal{P}]\, \mathbf{q}^{\mathrm{f}} \,. \tag{5.41}$$

We then introduce the following approximation for the vector $\mathbb{P}^{\mathrm{e}}$

$$\mathbb{P}^{\mathrm{e}} \simeq [\mathcal{L}(\mathbf{p})]\, \mathbf{q}^{\mathrm{e}} \,, \tag{5.42}$$

which does not involve any physical coordinates anymore and where the vector of the generalized coordinates $\mathbf{q}^{\mathrm{e}}$ is defined by

$$\mathbf{q}^{\mathrm{e}} = \begin{bmatrix} \mathbf{q}^{\mathrm{e}}_{\mathrm{I}} \\ \mathbf{q}^{\mathrm{f}} \end{bmatrix} \,. \tag{5.43}$$

Moreover, according to Eqs. (5.40) and (5.41) the transformation matrix $[\mathcal{L}]$ is written as

$$[\mathcal{L}(\mathbf{p})] = \begin{bmatrix} [\mathcal{P}^{\mathrm{e}}] & [\mathbb{S}^{\mathrm{e}}_{\Sigma}][\mathcal{Q}^{\mathrm{f}}][\mathcal{P}] \\ 0 & [\mathcal{Q}^{\mathrm{f}}][\mathcal{P}] \end{bmatrix} \,. \tag{5.44}$$

5.5.2 Generalized matrices for the reduced order model

Let n_{e} be the dimension of the reduced model for the poroelastic medium such as $n_{\mathrm{e}} = n_{\mathrm{e,I}} + n_{\mathrm{f}}$. The projection of the dynamic stiffness matrix $[\mathbb{A}^{\mathrm{e}}(\omega;\mathbf{p})]$ defined by Eq. (2.67) according to Eq. (5.42) gives the $(n_{\mathrm{e}} \times n_{\mathrm{e}})$ complex symmetric matrix $[A^{\mathrm{e}}(\omega;\mathbf{p})]$ such that

$$[A^{\mathrm{f}}(\omega;\mathbf{p})] = -\omega^2 [M^{\mathrm{e}}(\omega;\mathbf{p})] + [K^{\mathrm{e}}(\omega;\mathbf{p})] \,, \tag{5.45}$$

in which, according to Eqs. (2.69) and (2.70), we have

$$[M^{\mathrm{e}}(\omega;\mathbf{p})] = [M^{\mathrm{e}}_1(\mathbf{p})] + (\frac{\phi}{\tilde{K}_{\mathrm{e}}(\omega)} - \frac{\phi}{P_0})\, [M^{\mathrm{e}}_2(\mathbf{p})] \,, \tag{5.46}$$

$$[K^{\mathrm{e}}(\omega;\mathbf{p})] = [K^{\mathrm{e}}_1(\mathbf{p})] + (\frac{\phi}{\tilde{\rho}^{\mathrm{f}\prime}(\omega)} - \frac{\phi}{\rho^{\mathrm{p}}_t})\, [K^{\mathrm{e}}_2(\mathbf{p})] \,. \tag{5.47}$$

The generalized matrices $[M^{\mathrm{e}}_1(\mathbf{p})]$, $[M^{\mathrm{e}}_2(\mathbf{p})]$, $[K^{\mathrm{e}}_1(\mathbf{p})]$ and $[K^{\mathrm{e}}_2(\mathbf{p})]$ respectively are $(n_{\mathrm{e}} \times n_{\mathrm{e}})$ real symmetric positive definite matrices real symmetric positive semidefinite matrices. Moreover, the $(n_{\mathrm{s}} \times n_{\mathrm{e}})$ reduced coupling matrix between the structure and the equivalent acoustic fluid is written

$$[C_{\Gamma}(\mathbf{p})] = [\mathcal{U}^{\mathrm{s}}(\mathbf{p})]^{\mathrm{T}} [\mathbb{C}_{\Gamma}(\mathbf{p})][\mathcal{L}(\mathbf{p})] \,. \tag{5.48}$$

5.6 Assembled reduced order computational models

Depending on the properties of the poroelastic medium or on its physical coupling with the structure, two reduced order computational models are presented. The first one derives from a modeling of the poroelastic medium as coupled solid and fluid phases with displacements as primary variables and is consequently adapted to a broad class of vibroacoustic systems, being able to take into account shear waves into the poroelastic media. Such a model should be suitable for most recent prefabricated systems in which can be found, for example, high compacity wood fiber insulation glued together with the structure. Its dimension is however higher in comparison with the second one.

$$[A^{\mathrm{s}}(\omega;\mathbf{p})]\, \mathbf{q}^{\mathrm{s}} + [C_{\Pi}(\mathbf{p})]\, \mathbf{q}^{\mathrm{f}} = \mathbf{f}^{\mathrm{s}}(\omega;\mathbf{p}) \,, \tag{5.49}$$

$$[A^{\mathrm{f}}(\omega;\mathbf{p})]\, \mathbf{q}^{\mathrm{f}} + \omega^2 [C_{\Pi}(\mathbf{p})]^{\mathrm{T}} \mathbf{q}^{\mathrm{s}} + \omega^2 [C_{\Sigma}(\mathbf{p})]^{\mathrm{T}} \mathbf{q}^{\mathrm{p}} = 0 \,, \tag{5.50}$$

$$[A^{\mathrm{p}}(\omega;\mathbf{p})]\, \mathbf{q}^{\mathrm{p}} + [C_{\Sigma}(\mathbf{p})]\, \mathbf{q}^{\mathrm{f}} = 0 \,. \tag{5.51}$$

The second derives from a modeling of a limp poroelastic medium as an equivalent acoustic fluid with pressure as primary variable and is consequently adapted to limp or decoupled with the structure

poroelastic media. In most classical building construction systems, involving filling of cavities with lightweight fibrous materials, this model is consequently suitable.

$$[A^{\mathrm{s}}(\omega;\mathbf{p})]\,\mathbf{q}^{\mathrm{s}} + [C_{\Pi}(\mathbf{p})]\,\mathbf{q}^{\mathrm{f}} + [C_{\Gamma}(\mathbf{p})]\,\mathbf{q}^{\mathrm{e}} = \mathbf{f}^{\mathrm{s}}(\omega;\mathbf{p})\,, \tag{5.52}$$

$$[A^{\mathrm{f}}(\omega;\mathbf{p})]\,\mathbf{q}^{\mathrm{f}} + \omega^2[C_{\Pi}(\mathbf{p})]^{\mathrm{T}}\mathbf{q}^{\mathrm{s}} = 0\,, \tag{5.53}$$

$$[A^{\mathrm{e}}(\omega;\mathbf{p})]\,\mathbf{q}^{\mathrm{e}} + \omega^2[C_{\Gamma}(\mathbf{p})]^{\mathrm{T}}\mathbf{q}^{\mathrm{s}} = 0\,, \tag{5.54}$$

5.7 Conclusion

In this chapter were presented strategies for the construction of two reduced order computational models. In particular, with a follow-up work in regard to recent publications [37, 39], a standard generalized eigenvalue problem was defined for the reduction of poroelastic medium equations using the symmetric formulation with displacements as primary variables for the solid and fluid phases. An appropriate choice of boundary conditions for the construction of the truncated eigenmode basis was shown, on a three dimensional example, to improve the convergence rate with respect to the dimension of the projection basis, which was demonstrated as critical in [40]. Then, a similar component mode synthesis approach was presented with respect to the computational model taking into account the poroelastic medium as an equivalent acoustic fluid, which was previously derived as a simplification of the full displacement model. Finally, the respective signatures of the different generalized matrices involved within the reduced computational models were precised as a preamble for the construction of stochastic computational models.

6

Probabilistic approach of uncertainties for the computational model and identification

Contents

6.1 Introduction

The computational models introduced within the previous chapters belong to a given class of mathematical models with inputs and whose outputs will be used for the construction of acoustic performance indicators. Statistical fluctuations among the system parameters, or design parameters, which are the inputs of the computational model, were previously highlighted. Moreover, modeling errors happen to exist, consequences of the mechanical modeling process of complex systems. By way of consequence, model uncertainties are propagating to the output of the computational model, inherent to its class, for any set of system parameters. In this research, it is chosen to follow the generalized proabilistic approach of uncertainties introduced in [26–28]. Independent prior probabilistic models are then constructed in order to take into account statistical fluctuations associated with system parameters as well as with model uncertainties. In particular, the vector of system parameters $\mathbf{p}$ is substituted with a random vector whose prior probabilistic model is constructed, within the framework of the information theory [112,113], using the maximum entropy principle under the constraint of the available information. Then, the nonparametric probabilistic approach of model uncertainties induced by modeling errors is used for the direct construction of the prior probabilistic model of the generalized matrices of the reduced order computational model. Such approach was associated with substructuring techniques [61] and presented for vibroacoustic applications [22, 30, 62] including robust optimisation of vibroacoustic systems [63].

In a second phase, using the available experimental data, an original identification strategy is presented with respect to the hyperparameters associated with the probabilistic approach of system parameters uncertainties. Such strategy involves a first set of values for the system parameters, identified from experimental data through deterministic inverse problems. Then, a first set of hyperparameters is identified using the maximum likelihood method [114] and the analytical probability density functions associated with the prior probabilistic models. Thus, this first set of hyperparameters can be used as an advantageous starting point for the standard identification method presented in [26, 67] which consists in finding the optimal hyperparameters by maximising the likelihood of the experimental frequency responses with respect to the random solutions of the stochastic computational model.

Finally, uncertainty quantification is performed with respect to the shear panel treated in Section 4.4. In regard to the mobilities resulting from the updated stochastic computational model, confidence regions associated with a given level of probability are compared with experimental measurements in order to assess the ability of the probabilistic approach to take into account structural uncertainties.

6.2 Stochastic computational model and uncertainty quantification

6.2.1 Stochastic reduced order computational model

The probabilistic approach of uncertainties introduced in [26–28] consists in substituting the deterministic generalized matrices of the computational model for random matrices whose prior probabilistic model is constructed using the generalized probabilistic approach of uncertainties. With respect to the first reduced computational model introduced in Section 5.6, the generalized dynamic stiffness matrices $[A^{\mathrm{s}}(\omega;\mathbf{p})]$, $[A^{\mathrm{f}}(\omega;\mathbf{p})]$ and $[A^{\mathrm{p}}(\omega;\mathbf{p})]$ are respectively substituted with the random matrices $[\mathbf{A}^{\mathrm{s}}(\omega)]$, $[\mathbf{A}^{\mathrm{f}}(\omega)]$ and $[\mathbf{A}^{\mathrm{p}}(\omega)]$. The deterministic generalized vectors $\mathbf{q}^{\mathrm{s}}$, $\mathbf{q}^{\mathrm{f}}$ and $\mathbf{q}^{\mathrm{p}}$ of respective dimension n_{s}, n_{f} and n_{p} are consequently modeled by the random complex vectors $\mathbf{Q}^{\mathrm{s}}$, $\mathbf{Q}^{\mathrm{f}}$ and $\mathbf{Q}^{\mathrm{p}}$ and the resulting stochastic reduced order computational model is written as

$$[\mathbf{A}^{\mathrm{s}}(\omega)]\,\mathbf{Q}^{\mathrm{s}} + [\mathbb{C}_{\Pi}]\,\mathbf{Q}^{\mathrm{f}} = \mathbf{f}^{\mathrm{s}}(\omega;\mathbf{p})\,, \tag{6.1}$$

$$[\mathbf{A}^{\mathrm{f}}(\omega)]\,\mathbf{Q}^{\mathrm{f}} + \omega^2[\mathbb{C}_{\Pi}]^{\mathrm{T}}\mathbf{Q}^{\mathrm{s}} + \omega^2[\mathbb{C}_{\Sigma}]^{\mathrm{T}}\mathbf{Q}^{\mathrm{p}} = 0\,, \tag{6.2}$$

$$[\mathbf{A}^{\mathrm{p}}(\omega)]\,\mathbf{Q}^{\mathrm{p}} + [\mathbb{C}_{\Sigma}]\,\mathbf{Q}^{\mathrm{f}} = 0\,. \tag{6.3}$$

Within the framework of the second computational model in which a limp poroelastic medium can be modeled as an equivalent fluid, the generalized dynamic stiffness matrix $[A^{\mathrm{e}}(\omega;\mathbf{p})]$ is then substituted with the random matrix $[\mathbf{A}^{\mathrm{e}}(\omega)]$. Moreover, the vector of the generalized coordinates $\mathbf{q}^{\mathrm{e}}$ is modeled

by the random complex vectors $\mathbf{Q}^{\mathrm{e}}$ and the resulting stochastic reduced order computational model is written as

$$[\mathbf{A}^{\mathrm{s}}(\omega)]\,\mathbf{Q}^{\mathrm{s}} + [\mathbb{C}_{\Pi}]\,\mathbf{Q}^{\mathrm{f}} + [\mathbb{C}_{\Gamma}]\,\mathbf{Q}^{\mathrm{e}} = \mathbf{f}^{\mathrm{s}}(\omega;\mathbf{p})\,, \tag{6.4}$$

$$[\mathbf{A}^{\mathrm{f}}(\omega)]\,\mathbf{Q}^{\mathrm{f}} + \omega^2[\mathbb{C}_{\Pi}]^{\mathrm{T}}\mathbf{Q}^{\mathrm{s}} = 0\,, \tag{6.5}$$

$$[\mathbf{A}^{\mathrm{e}}(\omega)]\,\mathbf{Q}^{\mathrm{e}} + \omega^2[\mathbb{C}_{\Gamma}]^{\mathrm{T}}\,\mathbf{Q}^{\mathrm{s}} = 0\,. \tag{6.6}$$

Following, the uncertainty quantification consists in propagating the uncertainties associated with the generalized random matrices to the random vectors $\mathbf{Q}^{\mathrm{s}}$, $\mathbf{Q}^{\mathrm{f}}$, $\mathbf{Q}^{\mathrm{p}}$ or $\mathbf{Q}^{\mathrm{e}}$ solutions of the stochastic reduced order computational model.

6.2.2 Convergence of the random solution

The Monte Carlo method [115] is used to solve the previously defined stochastic reduced order computational model. Independent realisations of the different random matrices are used to construct a set of linear equations which is subsequently inverted. The convergence of the associated random solution must be carefully checked with respect to the truncation of the functional basis as well as with the number N_{mc} of independent realisations from the Monte Carlo method. Let $\mathbf{Q}^{\mathrm{r}}$ denote any of the random vectors of the generalized coordinates associated with the structure, internal acoustic fluid or poroelastic medium. The mean square convergence is assessed in constructing an estimator of the norm defined by

$$|||\mathbf{Q}^{\mathrm{r}}|||_{\mathbb{B}}^2 = E\left\{\int_{\mathbb{B}} \|\mathbf{Q}^{\mathrm{r}}\|^2 \mathrm{d}\omega\right\}\,. \tag{6.7}$$

6.2.3 Confidence regions for the observables

Confidence regions can be constructed with respect to observables which derive from the random vectors $\mathbf{Q}^{\mathrm{s}}$, $\mathbf{Q}^{\mathrm{f}}$, $\mathbf{Q}^{\mathrm{p}}$ or $\mathbf{Q}^{\mathrm{e}}$, solutions of the reduced order computational model, using the quantile method. Let $W \in \mathbb{R}$ be such random observable and let $x \mapsto p_W(x)$ from $\mathbb{R}$ to $\mathbb{R}^+$ be its associated probability density function. Given a probability P_c such that $0 < P_c < 1$, the function $P_c \mapsto \zeta(P_c)$ from $]0,1[$ to $\mathbb{R}$ is defined by

$$\zeta(P_c) = \arg\min_{w\in\mathbb{R}} \left| \int_{-\infty}^{w} p_W(x)\,\mathrm{d}x - P_c \right|\,. \tag{6.8}$$

The envelope of the confidence region associated with the probability P_c for the random observable W is then defined by

$$w_{min} = \zeta\left(\frac{1-P_c}{2}\right) \quad \text{and} \quad w_{max} = \zeta\left(\frac{1+P_c}{2}\right)\,, \tag{6.9}$$

and estimated with the Monte Carlo method.

6.3 Generalized probabilistic approach of uncertainties

Hereinafter, the generalized probabilistic approach of uncertainties is shortly presented in order to construct the prior probabilistic model of the generalized random matrices associated with the structure, internal acoustic fluid and poroelastic media. Let $\mathbb{M}_n(\mathbb{R})$ be the set of all the $(n \times n)$ real symmetric matrices. For the sake of simplicity, let $[A(\mathbf{p})]$ in $\mathbb{M}_n(\mathbb{R})$ denote any of the real symmetric generalized matrices for a given $\mathbf{p}$ in C_{par} and defined according to Sections 5.2.2, 5.3.2, 5.4.2 and 5.5.2. Matrix $[A(\mathbf{p})]$ is symmetric positive definite or positive semidefinite of rank $m \leq n$ and consequently it exists a factorization of $[A(\mathbf{p})]$ such that

$$[A(\mathbf{p})] = [B(\mathbf{p})]^{\mathrm{T}}[B(\mathbf{p})]\,, \tag{6.10}$$

where $[B(\mathbf{p})]$ is a $(m \times n)$ matrix that can be constructed, depending on the rank m, with Cholesky factorization or singular value decomposition.

According to [26], the vector of the uncertain model parameters $\mathbf{p}$ is modeled by the random variable $\mathbf{P} = (P_1, \ldots, P_{n_p})$ with values in $C_{par} \subset \mathbb{R}^{n_p}$, whose prior probabilistic model is defined by the probability density function $\mathbf{p} \mapsto p_{\mathbf{P}}(\mathbf{p}; \boldsymbol{\delta}_{\mathbf{p}})$ from C_{par} to $\mathbb{R}^+$. Thus, the probabilistic model associated with system parameter uncertainties depends on the vector of the probabilistic model hyperparameters $\boldsymbol{\delta}_{\mathbf{p}}$ belonging to an admissible set $C_{\mathbf{p}}$. Moreover, let $[\mathbf{G}_A]$ be a random matrix with values in the set $\mathbb{M}_m^+(\mathbb{R})$ of all the $(m \times m)$ real symmetric positive definite matrix. Then, the generalized probabilistic model of the random matrix $[\mathbf{A}]$, modeling the statistical fluctuations in $[A(\mathbf{p})]$, is written as

$$[\mathbf{A}] = [B(\mathbf{P})]^{\mathrm{T}} [\mathbf{G}_A] [B(\mathbf{P})] \,, \tag{6.11}$$

where the random variables $\mathbf{P}$ and $[\mathbf{G}_A]$ are statistically independent. The prior probabilistic model of random matrix $[\mathbf{G}_A]$ is constructed, within the framework of the so-called nonparametric approach of uncertainties, using the maximum entropy principle with the constraints given by the available information, whose derivation can be found with more details in [27,28]. Let $[G] \mapsto p_{[\mathbf{G}_A]}([G])$ from $\mathbb{M}_m^+(\mathbb{R})$ to $\mathbb{R}^+$ be the probability density function of $[\mathbf{G}_A]$ with respect to the measure $\mathrm{d}G = 2^{m(m-1)/4} \prod_{1 \leq j \leq k \leq l} dG_{jk}$. The available objective information is then written as

$$[\mathbf{G}_A] \in \mathbb{M}_m^+(\mathbb{R}) \,, \tag{6.12}$$

$$E\{[\mathbf{G}_A]\} = [I_m] \,, \tag{6.13}$$

$$E\{\|[\mathbf{G}_A]\|_{\mathrm{f}}^2\} < +\infty \,, \tag{6.14}$$

where $E\{\cdot\}$ is the mathematical expectation operator and $\|A\|_{\mathrm{f}} = (\mathrm{tr}\{AA^{\mathrm{T}}\})^{\frac{1}{2}}$ denotes the Froebenius norm. Equation (6.14) yields that the solutions of the resulting stochastic computational model are second order random variables. The probability density function $p_{[\mathbf{G}_A]}$ consequently has to verify a set of constraints which is derived from the available information. First, the normalization condition of $p_{[\mathbf{G}_A]}$ with respect to the support $\mathbb{M}_m^+(\mathbb{R})$ is written as

$$\int_{\mathbb{M}_m^+(\mathbb{R})} p_{[\mathbf{G}_A]}([G]) \mathrm{d}G = 1 \,. \tag{6.15}$$

Moreover, following Eqs. (6.13) and (6.14), the probability density function $p_{[\mathbf{G}_A]}$ respectively verifies

$$\int_{\mathbb{M}_m^+(\mathbb{R})} [G] p_{[\mathbf{G}_A]}([G]) \mathrm{d}G = [I_m] \,, \tag{6.16}$$

$$\int_{\mathbb{M}_m^+(\mathbb{R})} \ln(\det\{[G]\}) p_{[\mathbf{G}_A]}([G]) \mathrm{d}G < +\infty \,. \tag{6.17}$$

Furthermore, the entropy $p_{[\mathbf{G}_A]} \mapsto S(p_{[\mathbf{G}_A]})$ is defined by Shannon [112], within the framework of the information theory, by

$$S(p_{[\mathbf{G}_A]}) = -\int_{\mathbb{M}_m^+(\mathbb{R})} p_{[\mathbf{G}_A]}([G]) \ln(p_{[\mathbf{G}_A]}([G])) \mathrm{d}G \,. \tag{6.18}$$

The construction of the probabilistic model of $[\mathbf{G}_A]$ is then carried out constructing the probability density function $p_{[\mathbf{G}_A]}$ that maximises S under the constraints defined by Eqs. (6.15) to (6.17). According to [27,28] we then have

$$p_{[\mathbf{G}_A]}([G]) = \mathbb{1}_{\mathbb{M}_m^+(\mathbb{R})}([G])\, C_G \det\{[G]\}^a \, \mathrm{e}^{-b\, \mathrm{tr}\{[G]\}} \,, \tag{6.19}$$

in which

$$a = (m+1)\frac{(1-\delta_A^2)}{2\delta_A^2} \quad \text{and} \quad b = \frac{m+1}{2\delta_A^2} \,. \tag{6.20}$$

Moreover, $\mathbb{1}_{\mathbb{M}_m^+(\mathbb{R})}([G]) = 1$ if $[G]$ belongs to $\mathbb{M}_m^+(\mathbb{R})$ and $\mathbb{1}_{\mathbb{M}_m^+(\mathbb{R})}([G]) = 0$ otherwise. C_G is a positive normalization constant which is written as

$$C_G = \frac{(2\pi)^{-m(m-1)/4}\, b^{mb}}{\prod_{i=1}^m \Gamma\left(b + \frac{1-i}{2}\right)} \,, \tag{6.21}$$

where $\Gamma(z) = \int_0^{+\infty} t^{z-1} \mathrm{e}^{-t} \mathrm{d}t$ is the gamma function. Following, the prior probabilistic model of random matrix $[\mathbf{G}_A]$ is only dependent on the hyperparameter δ_A which has to verify the condition

$$0 < \delta_A < \sqrt{\frac{m+1}{m+5}} \,, \tag{6.22}$$

and which by construction verifies

$$\delta_A = \sqrt{\frac{E\left\{ \| [\mathbf{G}_A] - [I_m] \|_{\mathrm{f}}^2 \right\}}{\| [I_m] \|_{\mathrm{f}}^2}} \,. \tag{6.23}$$

An algebraic construction of $[\mathbf{G}_A] \in \mathbb{M}_m^+(\mathbb{R})$ is moreover proposed within the previous references as

$$[\mathbf{G}_A] = [\mathbf{B}_G]^{\mathrm{T}} [\mathbf{B}_G] \,, \tag{6.24}$$

in which $[\mathbf{B}_G]$ is a random upper triangular matrix. The elements $[\mathbf{B}_G]_{ij}$, $i \leq j$, of matrix $[\mathbf{B}_G]$ are statistically independent random variables defined by

$$[\mathbf{B}_G]_{ii} = \sigma_m \sqrt{2V_i} \,, \tag{6.25}$$

$$[\mathbf{B}_G]_{ij} = \sigma_m U_{ij}, \; i < j \,. \tag{6.26}$$

The family $\{V_i \,,\, i = 1, \ldots, m\}$ is constituted of statistically independent gamma random variables. The associated scale and shape parameters are respectively equal to one and $\alpha_{m,i}$ which is written as

$$\alpha_{m,i} = b + \frac{1-i}{2} \,. \tag{6.27}$$

Moreover, the family $\{U_{ij} \;,\; i \leq j \;,\; j = 1, \ldots, m\}$ is constituted of statistically independent gaussian random variable whose means and variances are respectively equal to zero and one. Finally, the constant σ_m is written as

$$\sigma_m = \frac{\delta_A}{\sqrt{m+1}} \,. \tag{6.28}$$

Following, the prior generalized probabilistic model of uncertainties, taking into account system parameters uncertainties as well as model uncertainties associated with matrix $[A(\mathbf{p})]$, is dependent on the vector of hyperparameters $\boldsymbol{\delta}_{\mathbf{p}} \in C_{\mathbf{p}}$ as well as on the hyperparameter δ_A. Such vectors are respectively associated with the probabilistic approach of system parameters uncertainties and with the nonparametric approach of model uncertainties induced by modeling errors.

6.4 Probabilistic approach of system parameters uncertainties

Within the context of this work, few experimental information is available and, consequently, statistical dependency of the different random variables cannot be determined. Following, the maximum entropy principle yields that the respective probabilistic models associated with the different random variables are constructed as statistically independent. Hereinafter, the probabilistic approach of system parameters uncertainties is carried out with respect to the structural parameters only. Indeed, fluctuations around the nominal values of the system parameters associated with the internal acoustic fluid such that mass density and sound velocity are considered sufficiently limited to be eventually taken into account using only the nonparametric approach. The same considerations are made for the system parameters associated with the poroelastic medium.

Following, the prior probabilistic models associated with the elastic properties as well as mass densities for the structural elements have to be constructed. First, such probabilistic models are constructed using the maximum entropy principle with the constraint of the available information. Then, as few experimental information is available, moments of order two cannot be determined and the respective hyperparameters are identified through a stochastic inverse problem using experimental data and the maximum likelihood method [114].

6.4.1 Prior probabilistic model of uncertainties for the structure parameters

In this paragraph we precise the construction, using the maximum entropy principle, of the different probabilistic models associatied with typical lightweight structural elements. With respect to wooden beam, prior probabilistic models are solely constructed with respect to the longitudinal Young's modulus and the mass density, which are the first order parameters controlling the bending behavior at low frequencies. Whereas in regard to the different lightweight boards, a prior probabilistic model is directly constructed for the elasticity tensor in order to take into account the fluctuations of the various contributing elastic parameters at low frequencies.

Prior probabilistic model of uncertainties for random variables with values in $\mathbb{R}^+$

Let P_i be a random variable, element of the random vector $\mathbf{P}$, modeling the statistical fluctuations of a strictly positive system parameter such as a Young's modulus or mass density. The prior probabilistic model associated with such random variable, with values in $]0, +\infty[$, is then constructed using the maximum entropy principle with the constraints given by the available information. Let $\underline{p}_i = E\{P_i\}$ be the mean value of P_i. Moreover, P_i^{-1} is a second order random variable. Let σ_{P_i} be the standard deviation associated with P_i and let $\delta_{P_i} = \sigma_{P_i}/\underline{p}_i$ be a dispersion parameter. According to [26, 28], the maximum entropy principle yields that the prior probabilistic model associated with P_i is a gamma random variable whose probability density function is written for $0 \leq \delta_{P_i} < 1/\sqrt{2}$ as

$$p_{P_i}(x) = \mathbb{1}_{]0,+\infty[}(x) \frac{x^{(\delta_{P_i}^{-2}-1)} \mathrm{e}^{-x\underline{p}_i^{-1}\delta_{P_i}^{-2}}}{(\underline{p}_i\delta_{P_i}^2)^{\delta_{P_i}^{-2}}\Gamma(\delta_{P_i}^{-2})} \,. \tag{6.29}$$

Prior probabilistic model of uncertainties for random anisotropic elasticity tensor

In Section 3.3.2, homogeneous orthotropic mean material hypothesis was formulated for the modeling of lightweight boards and the deterministic identification of system parameters. Moreover, the sensitivity of the observables, within the frequency band of interest, to several elastic parameters among which Young's moduli, shear moduli and Poisson's ratio, was highlighted. Hereinafter, it is proposed to construct the straight probabilistic model of the elastic tensor associated with each material, taking into account anisotropic fluctuations around the mean orthotropic model. Using Voigt notation for the matrix representation of the generalized Hooke's law, the $(m \times m)$ elasticity matrix $[\mathrm{C}^{\mathrm{ela}}(\mathbf{p})]$ is introduced as the symmetric positive definite matrix whose components are related, through index mapping, to those of the elasticity tensor. Then, a prior probabilistic model of such matrix can be constructed using the nonparametric probabilistic approach. Thus, the statistical dependency of the different elastic parameters is taken into account and the positiveness of the elasticity matrix is as well guaranteed. Such an approach was for example used in [59], or [60] in which additional matrix decomposition allowed to construct the probabilistic model of elasticity matrix belonging to a given symmetry class.

First, we introduce the mean symmetric positive definite elasticity matrix $[\underline{\mathrm{C}}^{ela}]$, for which consequently exists a factorization such that

$$[\underline{\mathrm{C}}^{ela}] = [B^{ela}]^{\mathrm{T}}[B^{ela}] \,. \tag{6.30}$$

Following, the prior probabilistic model of the random elasticity matrix $[\mathbf{C}^{ela}]$ modeling the statistical fluctuations in $[\mathrm{C}^{\mathrm{ela}}(\mathbf{p})]$ is constructed as

$$[\mathbf{C}^{ela}] = [B^{ela}]^{\mathrm{T}}[\mathbf{G}_{ela}][B^{ela}] \,, \tag{6.31}$$

where $[\mathbf{G}_{ela}]$ is a $(m \times m)$ random symmetric positive definite matrix whose probabilistic model is constructed according to the nonparametric approach (see Section 6.3). The prior probabilistic model associated with the elastic properties is then indexed by the hyperparameter δ_{ela} controlling the level of statistical fluctuations in $[\mathbf{C}^{ela}]$.

6.4.2 Strategies for the identification of the prior probabilistic model hyperparameters from experimental measurement

With respect to stochastic inverse problems presented in [26, 64–67] for the identification of hyperparameters associated with prior probabilistic models, two main strategies stand out.

(i) The first strategy consists in identifying deterministic values of the system parameters from experimental data through a set of deterministic inverse problems, which were carried out in Chapter 3 for example. Then, for a given probabilistic model, it is possible to evaluate the likelihood of those identified values. This strategy implies the resolution of as much deterministic inverse problems as there are available measurements on real systems but then, the evaluation of the objective function is costless. However the result is strongly dependent on a well-posed deterministic problem for the identification of the values of the system parameters.

(ii) The second strategy consists, for a given probabilistic model, in propagating the uncertainties to the observable through the computational model. Then, it is possible to determine the probability density functions associated with the observables from the realisations of the computational model and to evaluate the likelihood of the experimental data in regard to those probability density functions. This strategy implies the resolution of a stochastic dynamical problem for each evaluation of the objective function, with a high number of Monte Carlo independent realisations required to reach the convergence due to the log weighting of the probability densities evaluated at extreme values. Moreover, as the information consists in multiple random observables at various frequency values, the evaluation of the likelihood and, in particular, of the joint probability density function associated with the observables requires further enlightenment. By way of consequence, the numerical cost associated with this strategy increases quickly with the dimension of the stochastic inverse problem. However, this approach might give a better estimate (in the sense of a less conservative modeling) of the hyperparameters as the prior probabilistic models can be identified using the information propagated, from the different probabilistic models, to the computed observables.

Hereinafter, an original mixed strategy is introduced and investigated, which combines the advantages of both previously discussed methodologies. In a first step, a set of deterministic inverse problems is solved to identify deterministic values of the system parameters from experimental data (see Chapter 3). Then, a first set of parameters in regard to the prior probabilistic models can be identified with the maximum likelihood method, which corresponds to the first strategy. In a second step, the previously identified probabilistic models are used as a first guess, or starting point, for the stochastic inverse problem associated with the second strategy. Thus, the dependency on the well-posedness of deterministic inverse problems is minimised as they only provide a first guess to run through the second strategy, for which the search space dimension and consequently the computational effort associated with the stochastic inverse problem are drastically lowered. The aim would then to obtain less conservative probabilistic models, refined using the additional information.

First step

Let us assume that we have N_{mes} independent realisations of a random system. We then have a number of statistically independent realisations of a random observable defined on a probability space $(\Theta_{mes}, \mathcal{T}_{mes}, \mathcal{P}_{mes})$. The latter is constructed from N_{mes} experimental realisations of the random vector of the N_{freq} mobility modulus for and excitation on point j and an observation on point k, such that

$$\mathbf{Y}^{mes}(\theta_i) = \left(10\log_{10}\left(|Y^{mes}_{jk}(\omega_1;\theta_i)|^2\right), \ldots, 10\log_{10}\left(|Y^{mes}_{jk}(\omega_{N_{freq}};\theta_i)|^2\right)\right) \ , \ \theta_i \in \Theta_{mes} \ , \tag{6.32}$$

where the $|Y^{mes}_{jk}(\omega_h)|$ are dependent random variables indexed on the frequency. The first step consists in identifying an optimal vector of the probabilistic model hyperparameters $\boldsymbol{\delta}^{opt}_{\mathbf{p}}$ using the family of independent realisations of the vector of system parameters $\{\mathbf{p}^{exp}(\theta_1), \ldots, \mathbf{p}^{exp}(\theta_{N_{mes}})\}$ identified from experimental data through N_{mes} deterministic inverse problems. We then introduce the log-likelihood

estimator $\boldsymbol{\delta}_\mathbf{p} \mapsto \mathcal{L}^{\mathrm{I}}_\mathbf{p}(\boldsymbol{\delta}_\mathbf{p})$ from $C_\mathbf{p}$ into $\mathbb{R}$, such that

$$\mathcal{L}^{\mathrm{I}}_\mathbf{p}(\boldsymbol{\delta}_\mathbf{p}) = \sum_{i=1}^{N_{mes}} \ln\left(p_\mathbf{P}(\mathbf{p}^{exp}(\theta_i); \boldsymbol{\delta}_\mathbf{p})\right) . \tag{6.33}$$

The optimal vector of the probabilistic model hyperparameters $\boldsymbol{\delta}^{\mathrm{I}}_\mathbf{p}$ is then solution of the optimisation problem

$$\boldsymbol{\delta}^{\mathrm{I}}_\mathbf{p} = \arg\max_{\boldsymbol{\delta}_\mathbf{p} \in C_\mathbf{p}} \mathcal{L}^{\mathrm{I}}_\mathbf{p}(\boldsymbol{\delta}_\mathbf{p}) . \tag{6.34}$$

Second step

For a given prior probabilistic model indexed by the vector $\boldsymbol{\delta}_\mathbf{p}$, let $\mathbf{Y}(\boldsymbol{\delta}_\mathbf{p})$ be the random vector written as

$$\mathbf{Y}(\boldsymbol{\delta}_\mathbf{p}) = \left(10\log_{10}\left(|Y_{jk}(\omega_1; \boldsymbol{\delta}_\mathbf{p})|^2\right), \ldots, 10\log_{10}\left(|Y_{jk}(\omega_{N_{freq}}; \boldsymbol{\delta}_\mathbf{p})|^2\right)\right) , \tag{6.35}$$

whose statistics can be evaluated from the stochastic computational model. Following, the associated joint probability density function $p_\mathbf{Y}\left(10\log_{10}\left(|y_{jk}(\omega_1)|^2\right), \ldots, 10\log_{10}\left(|y_{jk}(\omega_{N_{freq}})|^2\right); \boldsymbol{\delta}_\mathbf{p}\right)$ from $\mathbb{R}^{N_{freq}}$ into $\mathbb{R}^+$ is estimated. Then, the log-likelihood estimator $\boldsymbol{\delta} \mapsto \mathcal{L}^{\mathrm{II}}_\mathbf{p}(\boldsymbol{\delta})$ from $C_\mathbf{p}$ into $\mathbb{R}$, associated with the second step, is constructed such that

$$\mathcal{L}^{\mathrm{II}}_\mathbf{p}(\boldsymbol{\delta}_\mathbf{p}) = \sum_{i=1}^{N_{mes}} \ln\left(p_\mathbf{Y}\left(10\log_{10}\left(|Y^{mes}_{jk}(\omega_1; \theta_i)|^2\right), \ldots, 10\log_{10}\left(|Y^{mes}_{jk}(\omega_{N_{freq}}; \theta_i)|^2\right); \boldsymbol{\delta}_\mathbf{p}\right)\right) . \tag{6.36}$$

Due to the numerical cost of evaluating the joint probability density function for a large number N_{freq} of frequency points, two suitable approximations were presented in [67]. The first one consists in substituting the joint probability density function $p_\mathbf{Y}$ with the product of the marginal probability density functions associated with each random variable $|Y_{jk}(\omega_h)|$. Thus, Eq. (6.36) becomes

$$\hat{\mathcal{L}}^{\mathrm{II}}_\mathbf{p}(\boldsymbol{\delta}_\mathbf{p}) = \sum_{i=1}^{N_{mes}} \sum_{h=1}^{N_{freq}} \ln\left(p_{Y_{jk}(\omega_h); \boldsymbol{\delta}_\mathbf{p})}\left(10\log_{10}\left(|Y^{mes}_{jk}(\omega_h; \theta_i)|^2\right); \boldsymbol{\delta}_\mathbf{p}\right)\right) . \tag{6.37}$$

The optimal vector of the probabilistic model hyperparameters $\hat{\boldsymbol{\delta}}^{\mathrm{II}}_\mathbf{p}$ is then solution of the optimisation problem

$$\hat{\boldsymbol{\delta}}^{\mathrm{II}}_\mathbf{p} = \arg\max_{\boldsymbol{\delta}_\mathbf{p} \in C_\mathbf{p}} \hat{\mathcal{L}}^{\mathrm{II}}(\boldsymbol{\delta}_\mathbf{p}) , \tag{6.38}$$

in which a first guess $\boldsymbol{\delta}^{\mathrm{I}}_\mathbf{p}$, resulting from the first step, is used to run through the optimisation algorithm. It should be noted that a second approximation was presented in [67] and later in [26] using a Karhunen–Loève expansion of the random vector $\mathbf{Y}(\boldsymbol{\delta}_\mathbf{p})$ in order to construct an approximated log-likelihood function in the space of the resulting uncorrelated generalized coordinates random variables. This approach was introduced in order to mitigate the possibly too conservative consequences of the hypothesis of statistical independence of the random variables $|Y_{jk}(\omega_h)|$, using uncorrelated variables instead. Hereinafter, this methodology is not considered, as it presented numerical problems at the first glance that were not any further investigated due to the already satisfying results obtained from the standard method.

6.4.3 Identification of the prior probabilistic model hyperparameters for typical structural lightweight components

In this paragraph, the previously introduced identification strategy is undertaken in order to identifiy the optimal hyperparameters associated with the prior probabilistic models constructed for the elastic properties and mass densities of the typical lightweight materials that were reviewed within Chapter 3. In a first step, the hyperparameters are identified for the random variables related to elasticity and mass

density according to the optimisation problem defined by Eq. (6.34). From the consideration of the confidence regions resulting from the stochastic computational model updated with the first set of optimal hyperameters, it might appear that this updated probabilistic model is too conservative. Indeed, hypothesis such as statistical independence of the random variables, used for the construction of the prior probabilistic models, might yield such consequences. Following, the second step of the strategy is investigated in its ability to refine the identification, using the statistical information provided by the different random variables indexed on frequency that constitute the experimental observable.

Wooden beams

The prior probabilistic models associated with the longitudinal Young's modulus E_l and mass density ρ^{s}, with values in $C_E =]0, +\infty[$ and $C_\rho =]0, +\infty[$, whose respective probability density function are constructed according to Eq. (6.29), are identified according to the optimisation problem defined by Eq. (6.34) using the previously identified values given in Tables 3.3 and 3.4. Those values result from a set of deterministic inverse problems that were constructed in Chapter 3 using experimental measurements. First, it is assumed that with the available data, a correct estimation of the mean values for the longitudinal Young's modulus and mass density can be written as

$$\underline{E}_l = \frac{1}{N_{mes}} \sum_{i=1}^{N_{mes}} E_l^{exp}(\theta_i) \quad \text{and} \quad \underline{\rho}^{\mathrm{s}} = \frac{1}{N_{mes}} \sum_{i=1}^{N_{mes}} \rho_{exp}^{\mathrm{s}}(\theta_i) \, . \tag{6.39}$$

Then, the optimal hyperparameters associated with the respective prior probabilistic models are investigated.

First step Figure 6.1 displays the values of $\mathcal{L}_{\mathbf{p}}^{\mathrm{I}}$ function of δ_{E_l} and δ_{rho} respectively associated with the probabilistic models of the longitudinal Young's modulus and mass density. We then obtain the optimal hyperparameters $\underline{E}_l = 10.9$ GPa and $\delta_{E_l}^{\mathrm{I}} = 0.16$ for the prior probabilistic model associated with the longitudinal Young's modulus and $\underline{\rho}^{\mathrm{s}} = 464$ kg/m^3 and $\delta_\rho^{\mathrm{I}} = 0.065$ for the prior probabilistic model associated with the mass density of pine wooden beams.

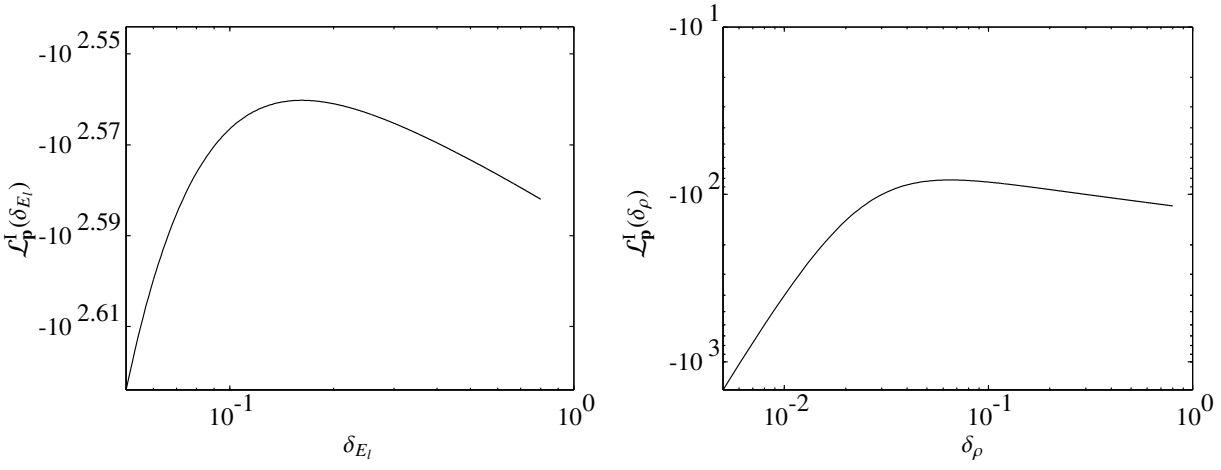

(a) Longitudinal Young's modulus (b) Mass density

Figure 6.1: Wooden beams. First step log-likelihood estimator function of the hyperparameters δ_{E_l} and δ_ρ respectively associated with the probabilistic models of the longitudinal Young's modulus and mass density.

The confidence regions associated with a probability $P_c = 0.98$ for the mobilities resulting from the optimal stochastic computational model are displayed on Fig. 6.2 and compared with the experimental mobilities. The updated probabilistic model is effectively conservative in the sense that the confidence

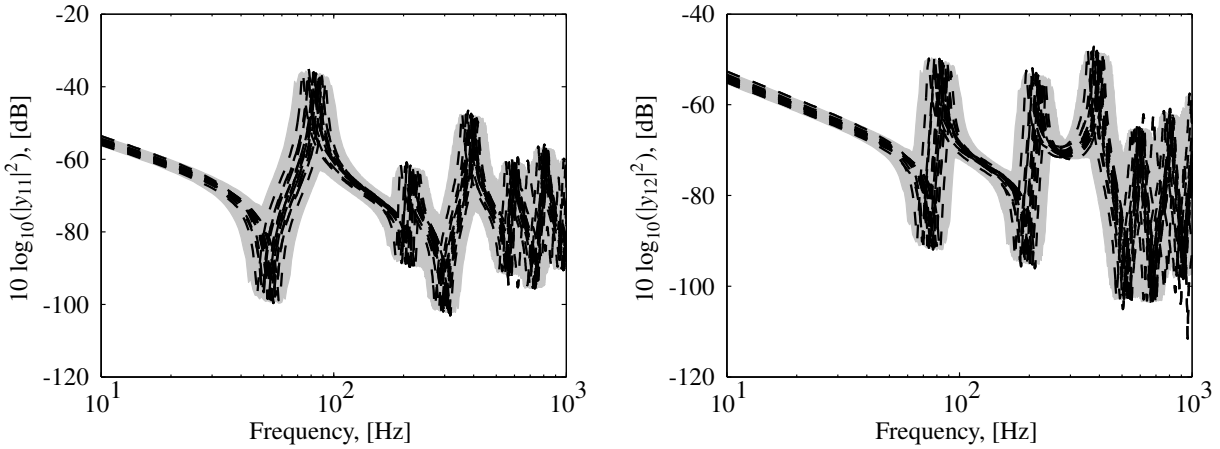

Figure 6.2: Wooden beams. Confidence region associated with a probability $P_c = 0.98$ for the mobilities resulting from the optimal stochastic computational model in the sense of the first step (grey areas). Experimental measurements (thin black dashed lines).

regions around given modes are quite large in comparison with the statistical fluctuations observed on the experimental mobilities.

Second step Following, the second step of the identification strategy is undertaken. As the mass density was measured and not identified from kinematic of dynamic quantities, higher trust exists with respect to its probabilistic model, and the associated hyperparameters $\underline{\rho}^{\mathrm{s}} = 464$ kg/m^3 and $\delta_\rho = 0.065$ are kept untouched. Further refinement is consequently investigated on the hyperparameter δ_{E_l} associated with the longitudinal Young's modulus, whose optimal value with respect to the optimisation problem defined by Eq. (6.38) is sought around the optimal value $\delta^{\mathrm{I}}_{E_l} = 0.16$ resulting from the first step. For a given probabilistic model indexed by δ_{E_l} we then consider the random vector $\mathbf{Y}(\delta_{E_l})$ defined according to Eq. (6.35) and gathering the $N_{freq} = 77$ random variables associated with the values of the mobilities sampled with respect to a frequency resolution of 10 Hz, sufficient due to the low modal density, in the frequency band $\mathbb{B} = [40, 800]$ Hz. A number of 10000 Monte Carlo simulations allow to construct, from the computational model, an estimation of the probability density functions associated with each of the N_{freq} and assumed statistically indepent random variables $|Y_{jk}(\omega_h)|$ indexed on frequency. Then, a maximum for the objective function $\delta_{E_l} \mapsto \hat{\mathcal{L}}^{\mathrm{II}}_{\mathbf{p}}(\delta_{E_l})$ is investigated.

Figure 6.3 displays the values of $\hat{\mathcal{L}}^{\mathrm{II}}_{\mathbf{p}}$ function of δ_{E_l} and we obtain the new optimal hyperparameter $\hat{\delta}^{\mathrm{II}}_{E_l} = 0.08$, thus divided by two, for the prior probabilistic model associated with the longitudinal Young's modulus. Fig. 6.4 displays the confidence regions associated with a probability $P_c = 0.98$ for the mobilities resulting from the stochastic computational model updated with $\hat{\delta}^{\mathrm{II}}_{E_l}$. Given the additional statistical information propagated from the probabilistic model of the mass density to the observables, the probabilistic model is then refined in a less conservative manner. Thus, the confidence regions display a better match with respect to experimental mobilities. Table 6.1 summarizes, for each step, the resulting values of the hyperparameters associated with each prior probabilistic model.

	Young's modulus		Mass density	
	$\underline{E}_l$ [GPa]	δ_{E_l}	$\underline{\rho}^{\mathrm{s}}$ [kg/m^3]	δ_ρ
Step I	10.9	0.16	464	0.065
Step II	10.9	0.08	464	0.065

Table 6.1: Summary, for each step, of the numerical values for the hyperparameters associated with each prior probabilistic model.

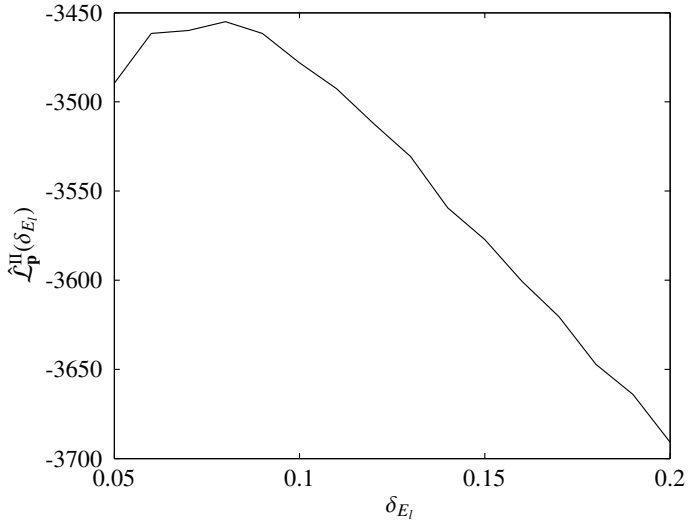

Figure 6.3: Wooden beams. Second step log-likelihood estimator function of the hyperparameters δ_{E_l}.

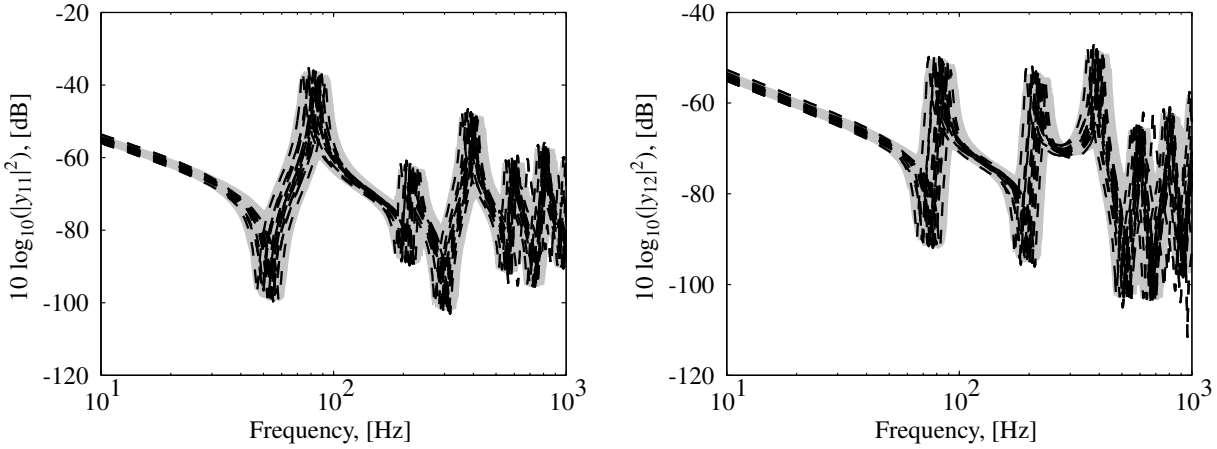

Figure 6.4: Wooden beams. Confidence region associated with a probability $P_c = 0.98$ for the mobilities resulting from the optimal stochastic computational model in the sense of the second step (grey areas). Experimental measurements (thin black dashed lines).

Lightweight boards

The statistical fluctuations of the elastic properties are taken into account substituting the deterministic elasticity matrix $[\mathrm{C}^{\mathrm{ela}}(\mathbf{p})]$ with the random elasticity matrix $[\mathbf{C}^{ela}]$ whose probabilistic model is constructed using the nonparametric approach. In the following, the case of the oriented strand boards is treated and the extension to other material models is straightforward. Within the framework of the Mindlin-Ressner plate theory [116], elasticity matrix $[\mathrm{C}^{\mathrm{ela}}(\mathbf{p})]$ is a (5×5) symmetric positive definite matrix. Then, according to Eq. (6.22), the hyperparameter δ_{ela} which controls the level of statistical fluctuations within the random elasticity matrix $[\mathbf{C}^{ela}]$ belongs to the interval $]0, 0.7746[$. A preliminary parametric study allows to analyse the sensitivity of the confidence regions, constructed according to Section 6.2.3 using the quantile method, for the mobilities resulting from the stochastic computational models indexed on δ_{ela}, to the nonparametric modeling of uncertainties constructed on the elasticity matrix. Thus, for a deterministic mass density $\underline{\rho}^{\mathrm{s}} = 578$ kg/m^3, Fig. 6.5 displays the above-mentioned confidence regions associated with values of $\delta_{ela} = 0.1, 0.3, 0.5, 0.7$. First, it can be noted that extremum values within the frequency passbands associated with resonances, which are damping controlled, remain comparable among the four probabilistic models. This means that although uncertainties propagate

to the damping operators, constructed from the Kelvin-Voigt model, the sensitivity of the observable to damping uncertainties is low. However, the statistical fluctuations of the resonance frequencies, which define the frequency width of the confidence regions around resonances, is effectively dependent on the values of δ_{ela}. Moreover, given the different confidence regions, the optimal value of δ_{ela} is most likely comprised between 0.1 and 0.3.

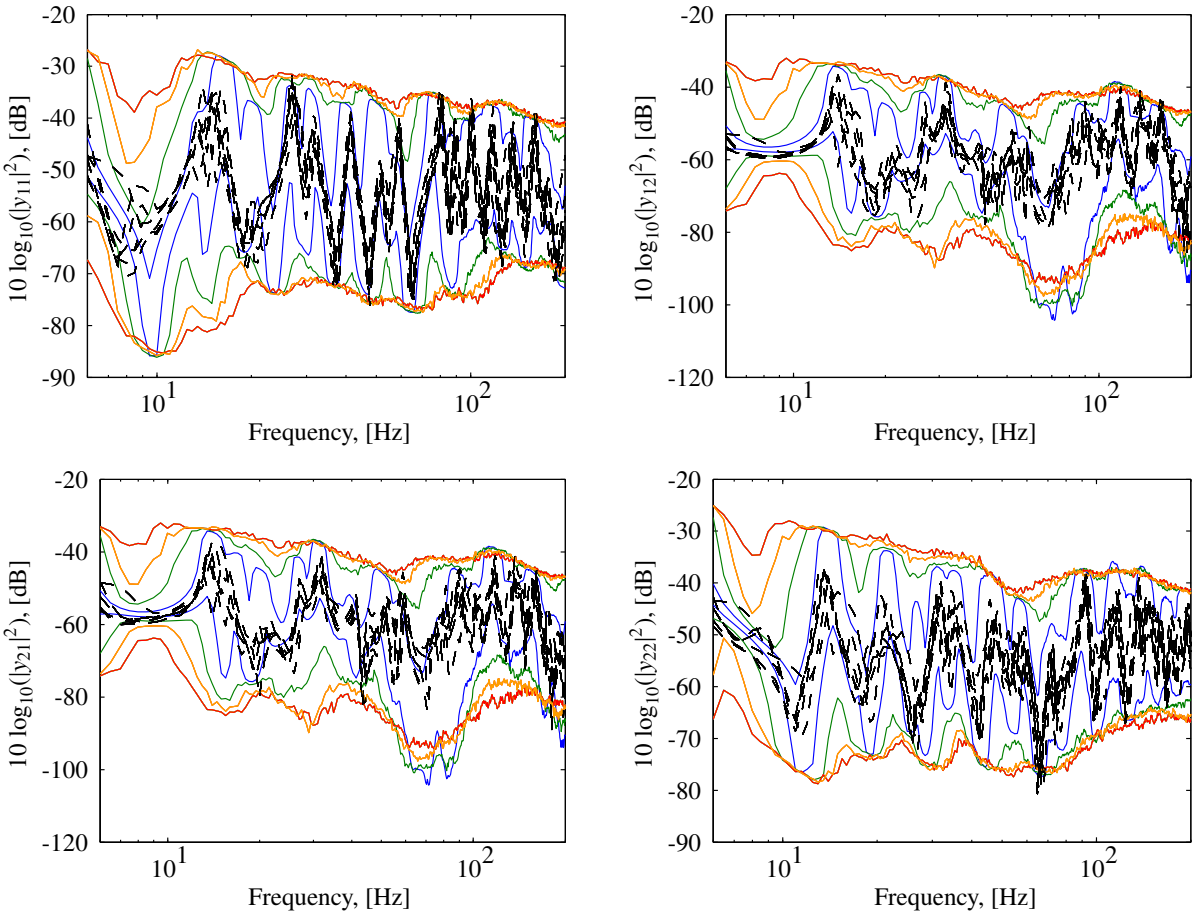

Figure 6.5: Oriented strand boards. Confidence regions associated with a probability $P_c = 0.98$ for the mobilities resulting from the optimal stochastic computational model with $\delta_{ela} = 0.1$ (thin blue solid lines), $\delta_{ela} = 0.30$ (thin green solid lines), $\delta_{ela} = 0.50$ (thin orange solid lines) and $\delta_{ela} = 0.70$ (thin red solid lines). Experimental measurements (thin black dashed lines).

First step Given $\{\mathbf{p}^{exp}(\theta_1), \ldots, \mathbf{p}^{exp}(\theta_{N_{mes}})\}$ the family of independent realisations of the vector of system parameters identified from experimental measurements, the first step of the strategy introduced in Section 6.4.2 then consists in finding the optimal probabilistic model hyperparameter $\delta^{\mathrm{I}}_{ela}$ solution of the optimisation problem defined by Eq. (6.34). Consequently, the probability density function $\mathbf{p} \mapsto p_{\mathbf{P}}(\mathbf{p}; \boldsymbol{\delta}_{ela})$ has to be constructed. First, it is assumed once again that with the available data a correct estimation of the mean elasticity matrix from the identified values of the system parameters can be written as

$$[\underline{\mathrm{C}}^{ela}] = \frac{1}{N_{mes}} \sum_{i=1}^{N_{mes}} [\mathrm{C}^{\mathrm{ela}}(\mathbf{p}^{exp}(\theta_i))] \, . \tag{6.40}$$

Then, according to [27], the probability density function of the $(m \times m)$ matrix $[\mathbf{C}^{ela}]$ such that the entropy is maximised is such that

$$p_{[\mathbf{C}^{ela}]}([\mathrm{C}]) = \mathbb{1}_{\mathbb{M}^+_{\mathrm{m}}(\mathbb{R})}([\mathrm{C}]) \, \mathrm{C_C} \, \det\{[\mathrm{C}]\}^{\mathrm{a}} \, \mathrm{e}^{-\mathrm{b} \, \mathrm{tr}\{[\underline{\mathrm{C}}^{\mathrm{ela}}]^{-1}[\mathrm{C}]\}} \, , \tag{6.41}$$

in which

$$a = (m+1)\frac{(1-\delta^2)}{2\delta^2} \quad \text{and} \quad b = \frac{m+1}{2\delta^2} \,. \tag{6.42}$$

Moreover, $\mathbb{1}_{\mathbb{M}_m^+(\mathbb{R})}([\mathrm{C}]) = 1$ if [C] belongs to $\mathbb{M}_m^+(\mathbb{R})$ and $\mathbb{1}_{\mathbb{M}_m^+(\mathbb{R})}([\mathrm{C}]) = 0$ otherwise. C_C is a positive normalization constant which is written as

$$C_\mathrm{C} = \frac{(2\pi)^{-m(m-1)/4}\, b^{mb}}{\prod_{i=1}^m \Gamma\left(b + \frac{1-i}{2}\right) \det\{[\underline{\mathrm{C}}^{ela}]\}^b} \,. \tag{6.43}$$

The hyperparameter $\delta \neq \delta_{ela}$ which depends on δ_{ela} is defined by

$$\delta(\delta_{ela}) = \sqrt{\frac{E\left\{\|[\mathbf{C}^{ela}] - [\underline{\mathrm{C}}^{ela}]\|_\mathrm{f}^2\right\}}{\|[\underline{\mathrm{C}}^{ela}]\|_\mathrm{f}^2}} \,, \tag{6.44}$$

and the mapping $\delta_{ela} \mapsto \delta(\delta_{ela})$ can be estimated with the Monte Carlo method. Thus, the log-likelihood estimator associated with the first step can be evaluated as

$$\mathcal{L}_\mathbf{p}^\mathrm{I}(\delta_{ela}) = \sum_{i=1}^{N_{mes}} \ln\left(p_{[\mathbf{C}^{ela}]}([\mathrm{C}^{ela}(\mathbf{p}^{exp}(\theta_i))]; \delta_{ela})\right) \,, \tag{6.45}$$

and maximised in order to obtain the optimal hyperparameter δ_{ela}^I, for the prior probabilistic model associated with the elastic properties of a given board material. Figure 6.6 displays the values of $\mathcal{L}_\mathbf{p}^\mathrm{I}$ function of δ_{ela} associated with the probabilistic model of the elasticity tensor for oriented strand boards. The optimal hyperparameters resulting from the first identification strategy are consequently $\delta_{ela}^\mathrm{I} = 0.14$ and $\delta_\rho^\mathrm{I} = 0.02$.

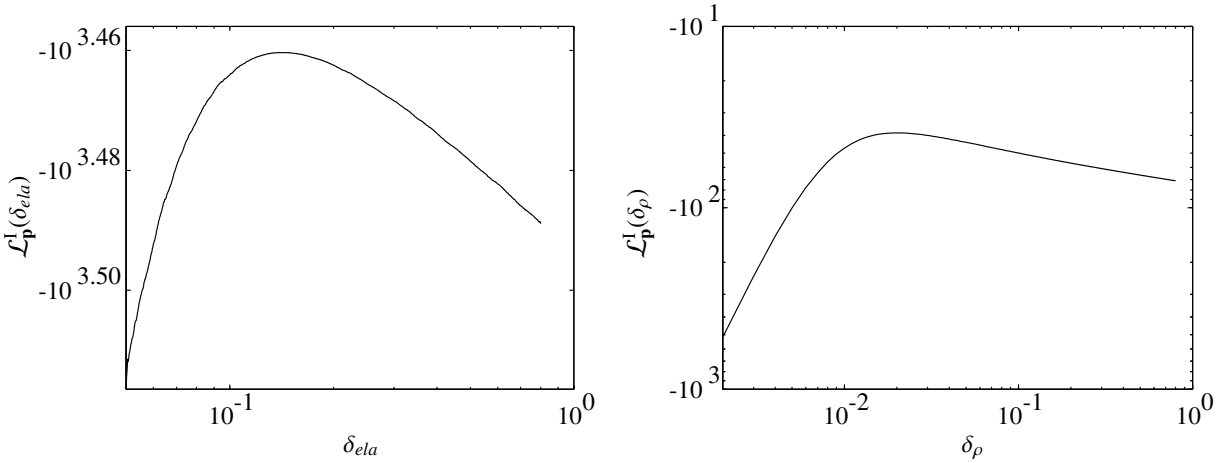

(a) Elasticity tensor (b) Mass density

Figure 6.6: Oriented strand boards. First step log-likelihood estimator function of the hyperparameters δ_{ela} and δ_ρ respectively associated with the probabilistic models of the elasticity tensor and mass density.

The confidence regions associated with a probability $P_c = 0.98$ for the mobilities resulting from the optimal stochastic computational model are displayed on Fig. 6.7 and compared with the experimental mobilities. As expected from the different hypothesis from which ensue the different prior probilistic models, such as statistical independence of the random variables, the model is conservative in the sense that the confidence regions around given modes are too large in comparison with the observed statistical fluctuations. With the exception of the very low frequencies, below 20 Hz, where model uncertainties induced by the not perfectly flexible suspension of the system cannot be taken into account with the probabilistic approach of system parameters uncertainties, the confidence regions capture most of the random dynamic response of the real board system.

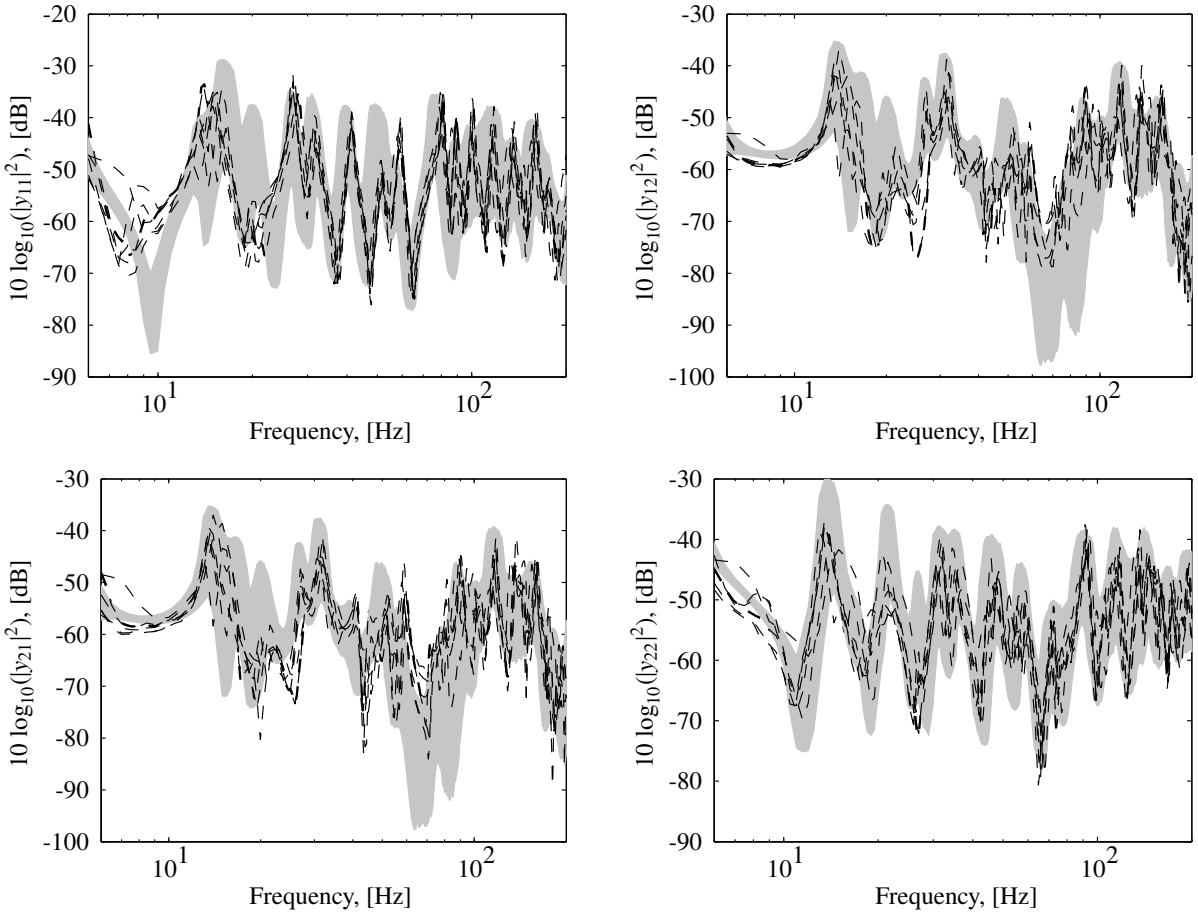

Figure 6.7: Oriented strand boards. Confidence regions associated with a probability $P_c = 0.98$ for the mobilities resulting from the optimal stochastic computational model (grey areas). Experimental measurements (thin black dashed lines).

Second step In accordance with the previously defined strategy, the second step is undertaken in a similar way than for the wooden beams. Further refinement is consequently investigated on the hyperparameter δ_{ela} of the prior probabilistic model associated with the elastic properties, whose optimal value with respect to the optimisation problem defined by Eq. (6.38) is sought around the optimal value $\delta^{\mathrm{I}}_{E_l} = 0.16$ resulting from the first step.

For a given probabilistic model indexed by δ_{ela} we then consider the random vector $\mathbf{Y}(\delta_{ela})$ defined according to Eq. (6.35) and gathering the $N_{freq} = 39$ random variables associated with the values of the mobilities sampled every 5 Hz in the frequency band $\mathbb{B} = [10, 200]$ Hz. Thus, a maximum for the objective function $\delta_{ela} \mapsto \hat{\mathcal{L}}^{\mathrm{II}}_{\mathbf{p}}(\delta_{ela})$ is investigated. Figure 6.8 displays the values of $\hat{\mathcal{L}}^{\mathrm{II}}_{\mathbf{p}}$ function of δ_{E_l} for different frequency samplings. Thus, when only considering the frequency band $[10, 40]$ Hz, in which modeling errors are influential due to the suspension conditions, the maximum likelihood gives a conservative value of $\hat{\delta}^{\mathrm{II}}_{E_l} = 0.14$ in an attempt to take into account modeling uncertainties. However, considering the frequency band $[80, 200]$ Hz, the sensitivity of the model to uncertainties is naturally increasing with frequency such that a lower value of $\hat{\delta}^{\mathrm{II}}_{E_l} = 0.07$ would be convenient. In order to discriminate the model uncertainties associated with the suspension from the material uncertainties and to obtain a probabilistic model suited for the whole frequency band, the value of $\hat{\delta}^{\mathrm{II}}_{E_l} = 0.11$ associated with the frequency sampling over the band $[40, 200]$ Hz is chosen.

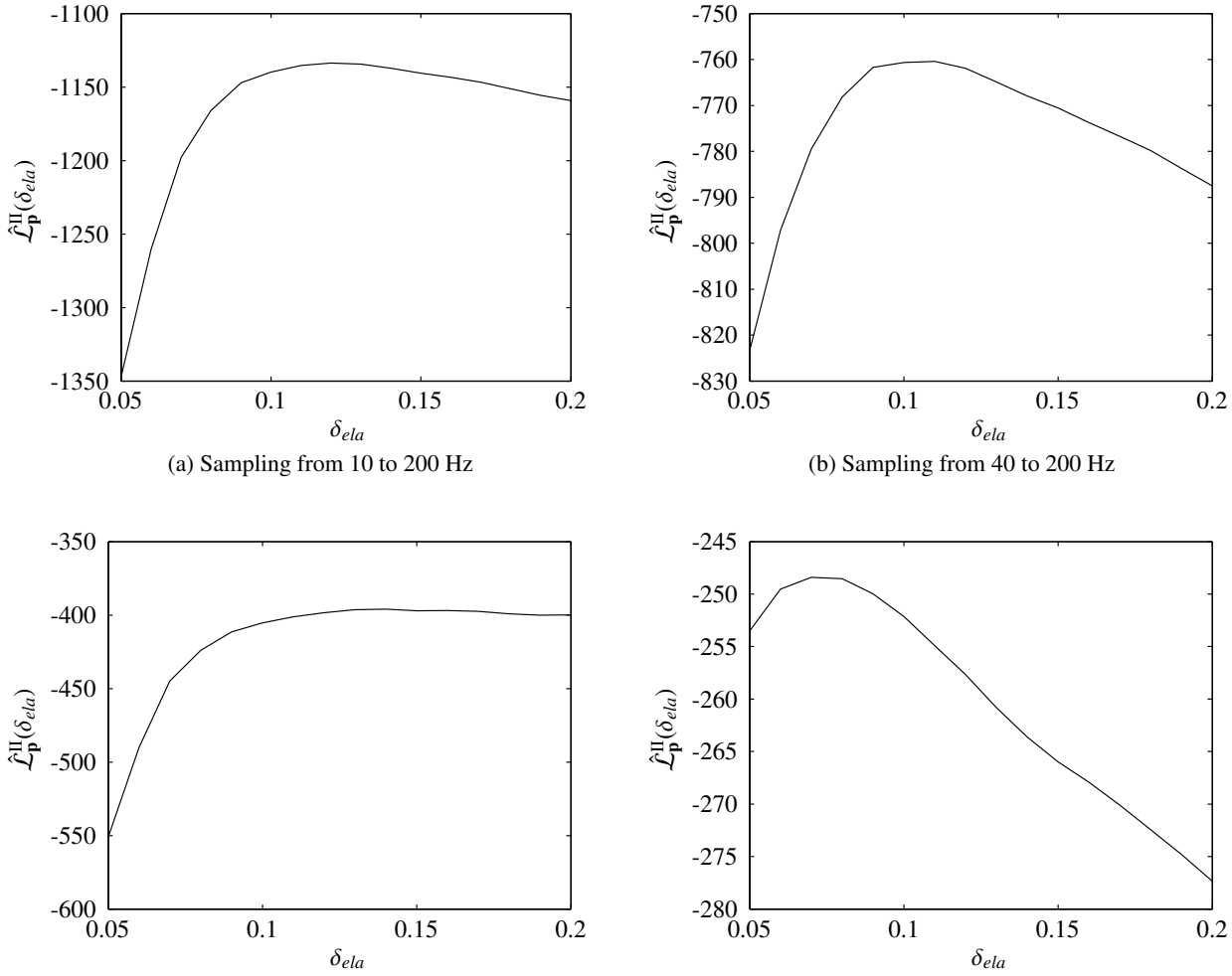

(a) Sampling from 10 to 200 Hz

(b) Sampling from 40 to 200 Hz

(c) Sampling from 10 to 40 Hz

(d) Sampling from 80 to 200 Hz

Figure 6.8: Oriented strand boards. Second step log-likelihood estimator function of the hyperparameters δ_{ela} for different frequency samplings.

Extension and remarks Table 6.2 gives the optimal hyperparameters identified according to both steps for the set of typical lightweight boards (oriented strand boards or OSB, particle boards and plasterboards) that were considered within Chapter 3. It should be noted that with the exception of oriented strand boards, the resulting level of statistical fluctuations after the second step is actually increasing from the first step. Indeed, with respect to those materials, the deterministic identification was mostly dominated by resonances. Even if resonant and non resonant portions of the frequency response have the same weight, the sensitivity of the the objective function defined in Section 3.2 to variations around resonances is much more important because of the associated steep gradient. Two distinct behaviours are then enlightened. In regard to oriented strand boards, the first modes were disturbed by the suspension conditions such that the deterministic inverse problems were erroneously evaluating the elastic parameters in order to capture the dynamic behavior, leading to an overestimation of the statistical fluctuations from the first step which was corrected within the second step. However, in regard to other materials, modeling errors were sufficiently low to not be too influential on the resonances, leading to an estimation of the elastic parameters for which a given level of fluctuation was associated in the first step. The increasing level of statistical fluctuation in the second step then arise from the experimental fluctuations in the portions of the frequency response in which no resonance take place and where otherwise second order phenomena are contributing.

The previous remarks are illustrated by Fig. 6.9, which displays the confidence regions associated

	OSB		Particle boards		Plasterboards 12.5		Plasterboards 15		Plasterboards 18	
	$\delta^{\mathrm{I}}_{ela}$	δ_ρ	$\delta^{\mathrm{I}}_{ela}$	δ_ρ	$\delta^{\mathrm{I}}_{ela}$	δ_ρ	$\delta^{\mathrm{I}}_{ela}$	δ_ρ	$\delta^{\mathrm{I}}_{ela}$	δ_ρ
Step I	0.14	0.020	0.05	0.007	0.07	0.009	0.05	0.014	0.07	0.011
Step II	0.10	0.020	0.08	0.007	0.15	0.009	0.10	0.014	0.11	0.011

Table 6.2: Dispersion hyperparameters identified for typical lightweight boards.

with a probability $P_c = 0.98$ for the mobilities resulting from the optimal stochastic computational model constructed with respect to particle boards and updated with $\delta_{ela} = 0.05, 0.08$. Thus, in regard to the stochastic computational model in which $\delta_{ela} = 0.05$, experimental values belong to the confidence regions around resonances but often take values outside of the envelope otherwise, which is corrected by the second step using $\delta_{ela} = 0.08$.

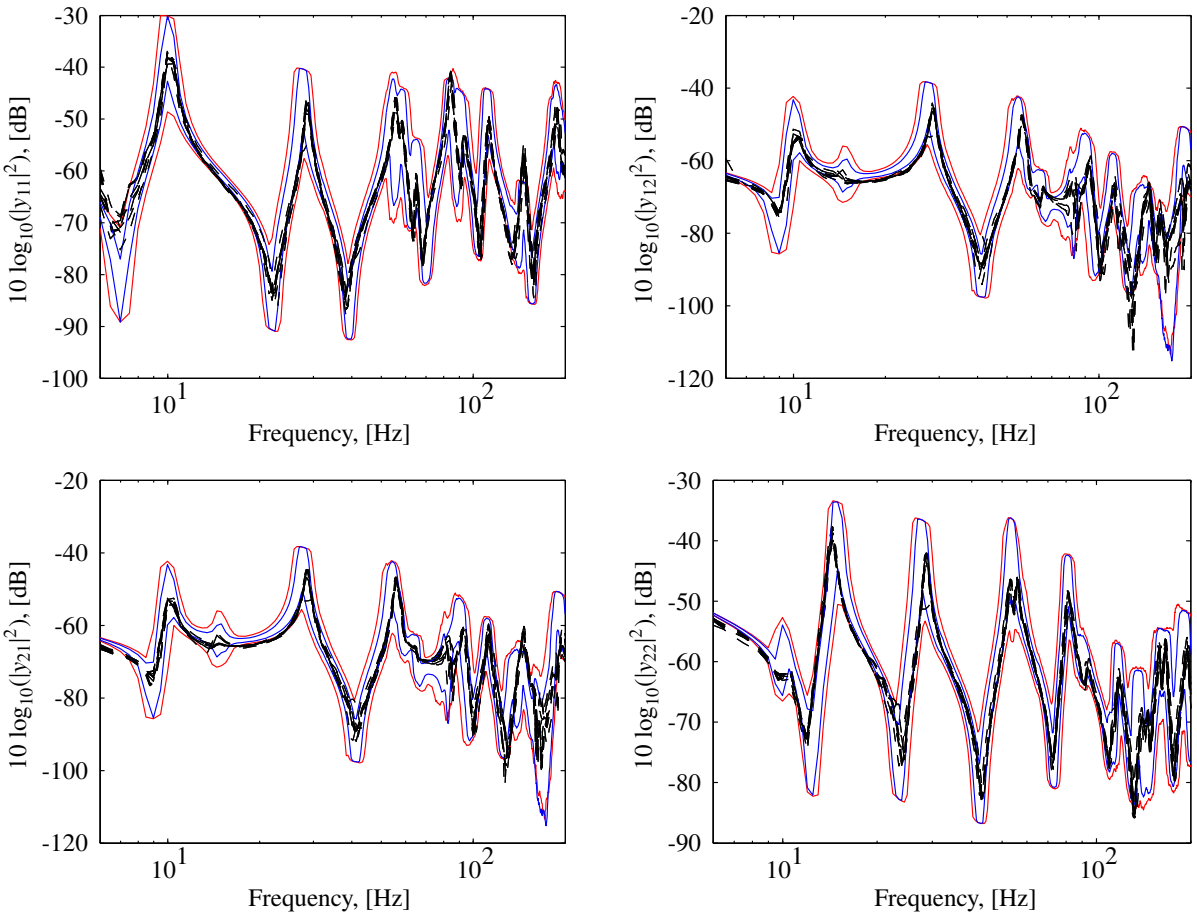

Figure 6.9: Particle boards. Confidence regions associated with a probability $P_c = 0.98$ for the mobilities resulting from the optimal stochastic computational model with $\delta_{ela} = 0.05$ (thin blue solid lines) and $\delta_{ela} = 0.08$ (thin red solid lines). Experimental measurements (thin black dashed lines).

Consequently, results from both steps have to be carefully interpreted. The methodology associated with the first step is sensitive to model uncertainties meanwhile the methodology associated with the second step is sensitive to potential measurement uncertainties or anomalies occuring within low signal to noise ratio frequency response portions. With respect to the considered stochastic inverse problems, both methods end up giving comparable values for the probabilistic models hyperparameters due to the simplicity of the treated systems and respective qualities of the experimental measurements and mean computational models.

6.5 Uncertainty quantification for a shear panel and comparison with experimental measurements

The shear panel consisting in OSB mounted on wooden beams, treated in Section 4.4, is now considered. Prior probabilistic models are constructed with respect to the elastic properties and mass densities of its lightweight components. Thus, the different dispersion parameters associated with wooden beams and oriented strand boards that were identified in the previous section are used to update the stochastic computational model. In regard to oriented strand boards, the mean elasticity tensor is constructed from the nominal values that were given in Table 4.5 as they constitute the only available information on a product that might be different from the batch of oriented strand boards that was treated within Chapter 3. For the sake of clarity, the mean physical parameters as well as probabilistic model hyperparameters are briefly recalled within Tables 6.3 to 6.5

E_l [GPa]	E_t [GPa]	E_r [GPa]	G_{tl} [GPa]	G_{lr} [GPa]	G_{rt} [GPa]	ν_{rt}	ν_{lr}	ν_{lt}	ρ^{s} [kg/m^3]
10.9	0.3	0.3	0.7	0.7	0.05	0.1	0.1	0.1	464

Table 6.3: Pine mean physical properties

E_x [GPa]	E_y [GPa]	G_{xy} [GPa]	G_{yz} [GPa]	G_{xz} [GPa]	ν_{xy}	ρ [kg/m^3]
5.5	3	1.5	1	1	0.25	650

Table 6.4: OSB mean physical properties.

Pine beams		OSB	
δ_{E_l}	δ_ρ	δ_{ela}	δ_ρ
0.08	0.065	0.10	0.020

Table 6.5: Dispersion hyperparameters with respect to each structural component.

With respect to the connections of the different components, two mean models are successively considered. The first one uses the flexible mounting model that was presented and whose parameters were identified from experimental measurements within Chapter 4. The second involves perfectly rigid connections, consequently introducing a higher level of modeling errors. The ability of the generalized probabilistic approach of uncertainties to take into account system parameters uncertainties as well as model uncertainties is investigated with respect to both cases.

6.5.1 Mean model taking into account flexible connections

At first, identical mounting parameters are chosen such that the model considered in Section 4.4 is the mean model of the present stochastic computational model. Moreover, in a first step, only the probabilistic approach of system parameters uncertainties is considered and the propagation of the latter to the different mobilities of system is invesigated. Following, the confidence regions associated with a proability $P_c = 0.98$, resulting from the stochastic computational model, are displayed on Fig. 6.10 and compared with experimental values. It can be seen that the stochastic computational model constructed solely from the probabilistic approach of system parameters uncertainties is able to improve the quality of the prediction. Thus, experimental measurements are comprised within a confidence region that can be constructed from a computational model enriched with the knowledge of few probabilistic information.

It should be noted that, as expected, the probabilistic approach of system parameters uncertainties only is not able to take into account the model uncertainties resulting from the continuous connection

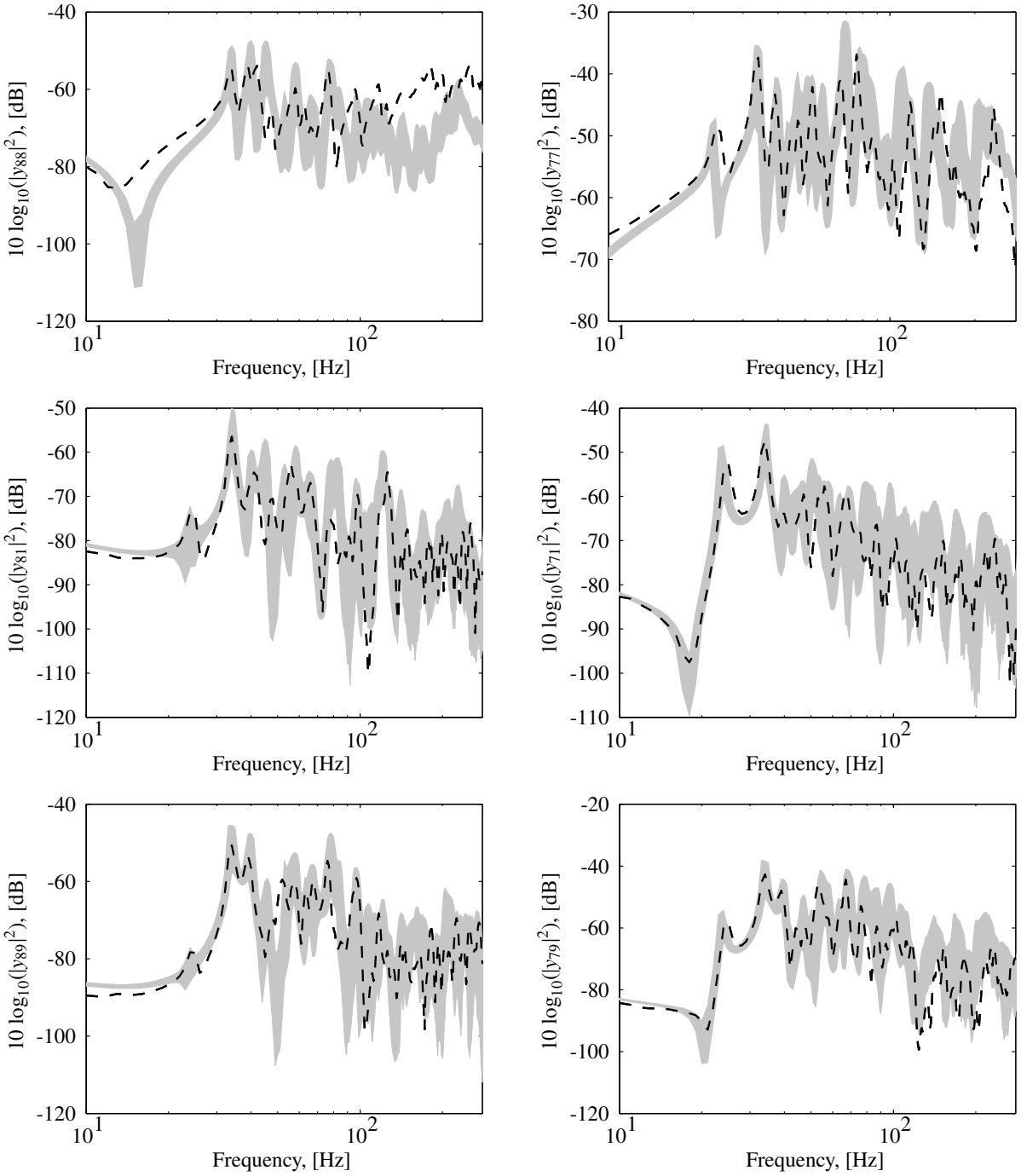

Figure 6.10: Set of mobilities obtained for an excitation on points 7 and 8. Confidence regions associated with a probability $P_c = 0.98$ for the mobilities resulting from the optimal stochastic computational model (grey areas); experimental measurements (thin black dashed lines).

modeling on top of the beams (as can be seen with the mobility y_{88}) for which the nails that realise the mechanical assembly of the oriented stand boards on the beams is such that a bending wavelength of the boards can be comprised between two real punctual connections. However, as it was highlighted in Chapter 4, the resulting modeling errors and consequently associated uncertainties remain localized such that most of the displacement and velocity fields over the structure can be accurately predicted over the frequency band $[10, 280]$ Hz. Heretofore, an accurate probabilistic predictive model can be constructed for a lightweight shear panel at low frequencies, core constituent of most lightweight separative elements, using statistical information on the involved materials and a correct modeling and characteri-

sation of the connections. Assuming that this characterisation is inaccessible and that the elastic subparts are connected through perfectly rigid connections, it is investigated within the next paragraph how the generalized probabilistic approach of uncertainties would be able to provide a prediction taking into account this downgrade with regard to the available information.

6.5.2 Mean model including modeling errors induced by perfectly rigid connections

In this paragraph, an inherent level of modeling errors is associated with the mean model as a consequence of its construction using perfectly rigid connections. As a result, the computational model belong to a class of model that cannot represent the dynamic behavior of the real system given any variation of its input parameters and, consequently, the associated uncertainties cannot be taken into account with the probabilistic approach of system parameters uncertainties. Figure 6.11 illustrates this point in comparing the confidence regions associated with a probability $P_c = 0.98$ (grey areas) for the mobilities resulting from the stochastic computational model constructed from the mean model using perfectly rigid connections and the probabilistic approach of system parameters only. Thus, it can then be seen that the experimental observables do not belong to the confidence regions resulting from the probabilistic approach of system parameters uncertainties at low frequencies. Indeed, a general result with respect to such parametric approach is that the confidence regions are spanned by the variations of the resonance frequencies around their mean values [26]. Consequently, in the very low frequency range where the modal density is low, such approach can not reasonably take into account the much more influential effects of the connections, or in the general case of the boundary conditions.

Following, the generalized probabilistic approach of uncertainties is fully undertaken in order to assess its ability to take into account model uncertainties. Let δ_{M^s}, δ_{D^s} and δ_{K^s} respectively be the hyperparameters associated with the random matrices $[\mathbf{G}_{M^s}]$, $[\mathbf{G}_{D^s}]$ and $[\mathbf{G}_{K^s}]$ and controlling the nonparametric statistical fluctuations within random mass matrix $[\mathbf{M}^s]$, damping matrix $[\mathbf{D}^s]$ and stiffness matrix $[\mathbf{K}^s]$ associated with the structure, according to the prior probabilistic model recalled in Section 6.3. A stochastic computational model is constructed using identical hyperparameters for the probabilistic models associated with the elastic properties and mass densities than obtained and used within the previous paragraphs. Moreover, in regard to the nonparametric approach, values of $\delta_{M^s} = \delta_{D^s} = \delta_{K^s} = 0.3$ are arbitrarily chosen, in order do demonstrate that it exists a set of hyperparameter such that experimental mobilities belong to the confidence regions resulting from the stochastic computational model. Such optimal set can be identified according to the methodologies presented in [26, 67] from experimental measurements but this problem is not further investigated due to limited available experimental information. The resulting confidences regions are displayed on Fig 6.11, denoted by the thin black solid lines, and manifest the ability of the generalized probabilistic approach to take into account system parameter as well as model uncertainties, using independent and suited probabilistic models. However, the prime importance of a good predictive mean model is enlightened by the width of the confidence regions required to take into account model uncertainties. The fewer available knowledge of the system the bigger the confidence regions will consequently be, which can be problematical when trying to rate the relative performance of given systems during an optimisation process.

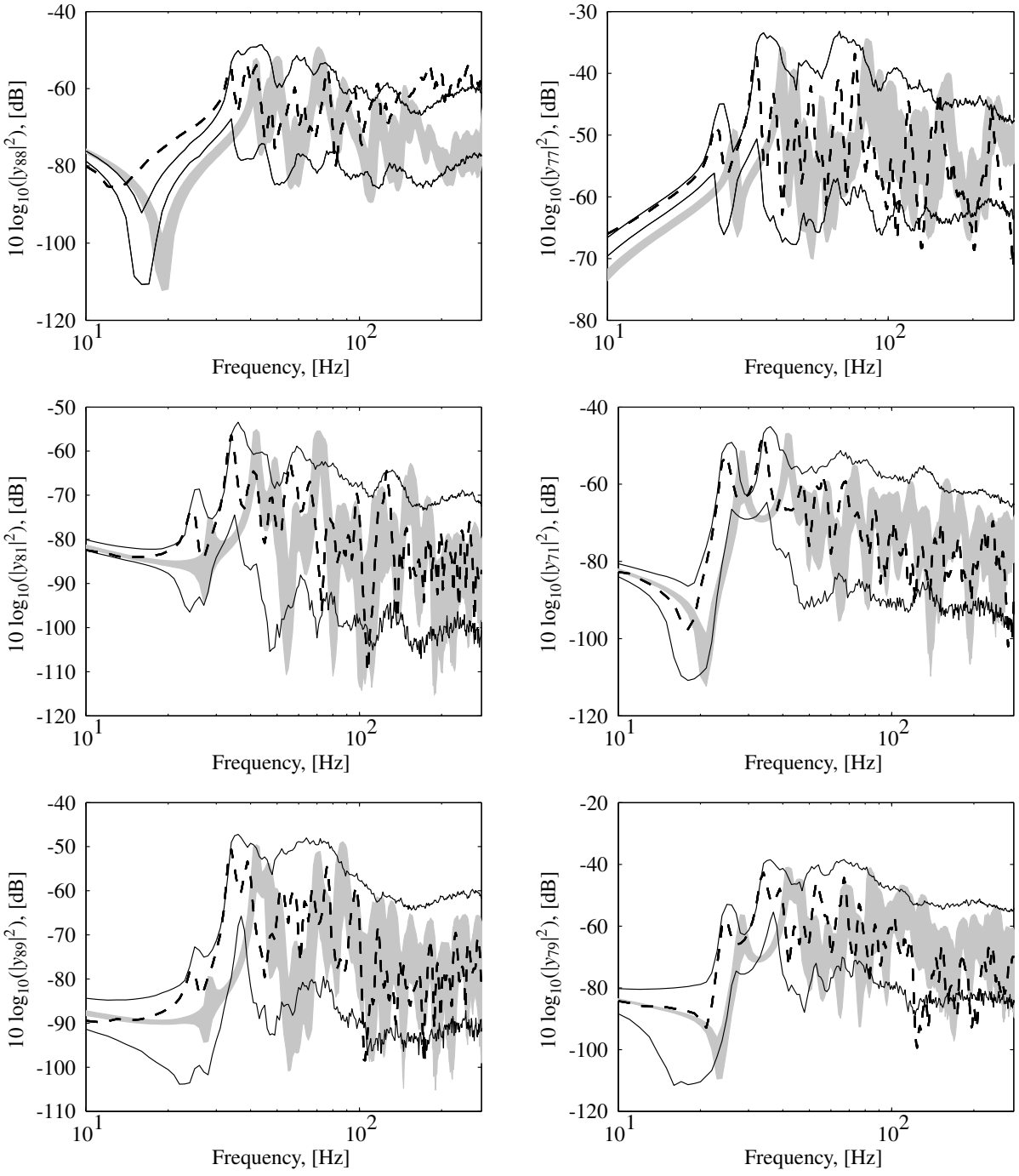

Figure 6.11: Set of mobilities obtained for an excitation on points 7 and 8. Confidence regions associated with a probability $P_c = 0.98$ for the mobilities resulting from the probabilistic approach of system parameters uncertainties (grey areas) and generalized probabilistic approach of uncertainties (thin black solid lines); experimental measurements (thin black dashed lines).

6.6 Conclusion

In this chapter, a stochastic computational model suited for vibroacoustic systems including poroelastic media was presented, within the framework of the generalized probabilistic approach of uncertainties that was introduced in [26–28]. With respect to the structure, the probabilistic approach of system parameters uncertainties allowed the construction of prior probabilistic models associated with the elastic properties and mass densities of typical lightweight building components. Then, a novel two step strategy was introduced in order to identify the respective hyperparameters associated with each prior probabilistic model from experimental measurements. Finally, uncertainty quantification was performed on the previously treated lightweight shear panel (OSB mounted on beams) using a stochastic computational model updated with the identified hyperparameters for each material. Depending on the choice of the mean model, involving or not flexible connections of the elastic subparts, the probabilistic approach of system parameters uncertainties as well as the nonparametric approach of model uncertainties induced by modeling errors demonstrated their ability to improve the prediction through the construction of confidence regions consistent with the experimental observables.

7

Airborne sound insulation

Contents

7.1 Introduction

As it was previously introduced, this research is aligned with a predictive methology at the building scale, adapted to lightweight building construction. The latter was initially introduced in [4] then further matured within the COST Action FP0702 (European Cooperation in Science and Technology) with the aim to be presented as an extension of the current set of standards [5], extensively used for heavy constructions. Thus, among other inputs that do not belong to the scope of this work, this methodology requires the performances (sound reduction indices and normalised impact sound levels) associated with the direct transmission paths of the different separative elements involved within the considered building. In this chapter, we introduce a computational model suited to the evaluation of the airborne sound insulation performance of diverse lightweight building elements. Following on from the previous chapters in which deterministic and stochastic computational model dedicated to the description of the systems were introduced, this work consequently focuses on the definition of *ad hoc* external excitations and observables in order to derive performance indicators.

Within laboratory conditions, evaluated systems are inserted between one source room, which is acoustically excited, and one receiving room. According to the standard [117], successive loudspeaker positions or two or more fixed loudspeakers can be used to generate a steady excitation of the source room. The aim is to evaluate the sound reduction index R, defined by the ratio of the incident and radiated sound power such that

$$R = 10 \log_{10}\left(\frac{W_S}{W_R}\right) . \tag{7.1}$$

In the early years of building acoustics, only the sound pressure was accessible to measurement and, by way of consequence, adapted methodologies were introduced with respect to the evaluation of the sound reduction index. As soon as the modal density becomes sufficiently large, the steady state power flows W_S and W_R can be approximated according to Sabine, using the spatial averages of the quadratic presure fields P_S^2 and P_R^2 within the source and receiving room, as

$$W_S = S\frac{P_S^2}{4\rho^{\mathrm{f}}c_{\mathrm{f}}} \quad \text{and} \quad W_R = A\frac{P_R^2}{4\rho^{\mathrm{f}}c_{\mathrm{f}}} , \tag{7.2}$$

where S and A respectively are the surface of the evaluated element and the acoustic equivalent absorption area associated with the receiving room. Moreover, given the reverberation time T_{60}, wich is the time required to observe a decay of 60 dB after interruption of a sound source, the Sabine formula yields

$$A = 0.161\frac{V_R}{T_{60}} , \tag{7.3}$$

where V_R is the volume of the receiving room. Following on Eqs (7.1) and (7.2), the standard [117] defines the sound reduction index by

$$R = L_S - L_R + 10 \log_{10}\left(\frac{S}{A}\right) , \tag{7.4}$$

where the quantities L_S and L_R are the sound pressure levels respectively associated with the source and receiving rooms. Aforementioned levels are defined with respect to the reference value $p_{ref} = 2{\times}10^{-5}$ Pa such that

$$L_S = 10 \log_{10}\left(\frac{P_S^2}{p_{ref}^2}\right) \quad \text{and} \quad L_R = 10 \log_{10}\left(\frac{P_R^2}{p_{ref}^2}\right) , \tag{7.5}$$

Then, the airborne sound insulation performance of the evaluated system can then be rated according to [118].

At this point, it should be noted that at low frequencies the estimation of the sound reduction index R defined by Eq. (7.4) is not representative anymore of the power flows within the vibroacoustic system. However, pressure averaging based methods for the evaluation of the sound reduction index are extensively used and standardized [117]. By way of consequence, most experimental laboratory data ensue

from aforesaid methods. For such reasons, an intensimetry approach, even though generally accepted as more accurate at low frequencies, is not considered in this work due to intricate interpretation of the predicted quantities, resulting from a simulated intensity approach, with respect to laboratory experimental data resulting from room pressure averaging approaches.

Quick reminder for the definition of the levels in regard to different signals in dynamics. With respect to a signal q whose reference value is conventionally set to q_{ref}, the respective level is defined by

$$L_q = 10 \log_{10} \left(\frac{|q|^2}{q_{ref}^2} \right) . \tag{7.6}$$

Thus, in regard to a pressure p, to a displacement d, to a velocity v or to an acceleration a, the reference values respectively are $p_{ref} = 2 \times 10^{-5}$ Pa, $d_{ref} = 10^{-12}$ m, $v_{ref} = 10^{-9}$ m.s^{-1} and $a_{ref} = 10^{-6}$ m.s^{-2}.

7.2 Model for the evaluation of airborne sound insulation

7.2.1 Parallelepiped room model

Although field measurements as well as laboratory measurements reproductibilities are questioned at low frequencies [10, 119–123] and historically the reason for measurements to begin at 100 Hz, good repeatability was experimentally observed down to 50 Hz [8]. Such good repeatability and poor reproductibility are even stated within the standard [124]. Thus, if the evaluated performance at low frequencies depends on the laboratory, the measured quantities are at least reapeatable within identical laboratory conditions, which allows to compare designs to each others. Due to the dependence of the evaluated performance on the room geometries, reverberation times or modal smoothing from diffusers, authors advocated for a room model minimizing this influence [125], in order to evaluate designs in a more neutral environment. Hereinafter, the adopted standpoint is that the *in fine* evaluation of the performance will be performed in a laboratory with given attributes. Consequently, we set and implement a methodology trying to be as close to laboratory conditions as possible such that numerical and experimental quantities are comparable as far as this could be relevant. Without model updating at the laboratory setup scale, such an approach remains exploratory and first and foremost aims to define a suitable work basis. Following, the considered dynamical system is constituted of a source room, the evaluated parting wall and a receiving room as depicted in Fig. 7.1. The characteristic dimensions are $L_x^S \times L_y^S \times L_z^S$ for the source room, $L_x^R \times L_y^R \times L_z^R$ for the receiving room and $L_y^W \times L_z^W$ for the parting wall.

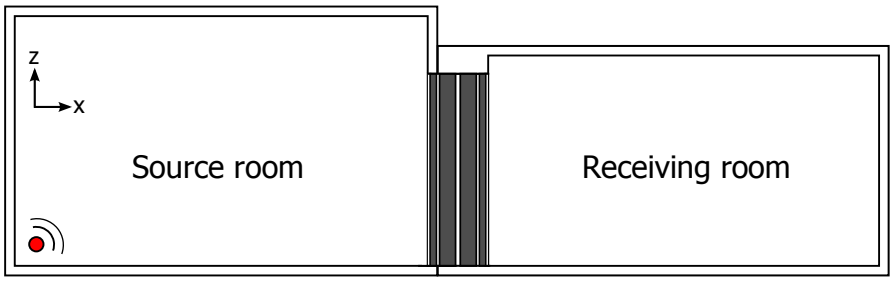

Figure 7.1: Laboratory setup for the evaluation of a parting wall.

The pressure field and the sound pressure level in the source room as well as the sound pressure level in the receiving room are determined through the analytical solution of the Helmoltz Eq. (2.16) in a parallelepiped room. Similar approaches for the study of the sound transmission through parting walls were presented using analytical functionnal basis, full discretization of the rooms with the finite element method or Rayleigh's integrals [9, 35, 126–132]. In particular in [130, 131], with respect to laboratory volumes, decoupled approach in which air loadings are neglected are shown to display consistent results with fully coupled approaches. Hereinafter such decoupled approach is then adopted and no feedback

from the evaluated system onto the source room nor from the receiving room onto the system is taken into account. The source room and receiving room are not considered as internal acoustic cavities and treated in a distinct manner. However it should be noted that any remaining internal air cavity or layer is fully coupled with the structure and poroelastic media according to the remarks in [133]. Furthermore, comparisons with experimental measurements in [9, 127, 128] display good agreement of such rigid parallelepiped models with respect to rooms with rigid heavy boundaries (plastered brick walls and concrete floor), corresponding to usual laboratory facilities, as long as the damping is properly known.

7.2.2 Analytical modal expansion of the pressure field in the rooms

In this paragraph, the pressure field in the aforementioned source room or receiving room is expanded on the truncated basis constituted of the first analytical eigenfunctions associated with such parallelepiped acoustic cavities with rigid boundaries. Thus, given an acoustical excitation, the pressure field as well as the spatial average of the quadratic pressure field can be evaluated. First, the truncated modal expansion of the pressure field is written as

$$p_{room}(\omega;\mathbf{x}) = \sum_{p,q,r} A_{p,q,r}(\omega)\ \phi_{p,q,r}(\mathbf{x})\ , \tag{7.7}$$

where the analytical eigenfunctions are such that

$$\phi_{p,q,r}(\mathbf{x}) = \frac{1}{N_{p,q,r}}\cos\left(\frac{p\pi}{L_x}x\right)\cos\left(\frac{q\pi}{L_y}y\right)\cos\left(\frac{r\pi}{L_z}z\right)\ . \tag{7.8}$$

It can be verified that the eigenfunctions are orthogonal with respect to the usual inner product and the mass normalization factor $N_{p,q,r}$ is defined by

$$N^2_{p,q,r} = \int_{V_R}\frac{1}{\rho^F c_F^2}\left(\cos\left(\frac{p\pi}{L_x}x\right)\cos\left(\frac{q\pi}{L_y}y\right)\cos\left(\frac{r\pi}{L_z}z\right)\right)^2 \mathrm{d}V\ . \tag{7.9}$$

According to the modal expansion defined by Eq. (7.7), the projection of the Helmoltz Eq. (2.16) with a source $Q_{room}(\omega;\mathbf{x})$ with respect to an eigenfunction $\phi_{p,q,r}(\mathbf{x})$ yields the expression of the generalized coordinate $A_{p,q,r}(\omega)$ such that

$$A_{p,q,r}(\omega) = \frac{\int_{\Gamma_R} Q_{room}(\omega;\mathbf{x})\ \phi_{p,q,r}(\mathbf{x})\ \mathrm{d}S}{\omega^2_{p,q,r} + 2i\ \xi_{p,q,r}\omega\omega_{p,q,r} - \omega^2}\ . \tag{7.10}$$

Moreover, with the knowledge of the reverberation time $T_{60}(f)$ indexed on frequency, indicative of the dissipated acoustic energy within a room, the modal damping ratio $\xi_{p,q,r}$ can be constructed, according to [134], as

$$\xi_{p,q,r} = \frac{1}{2}\frac{2.2}{f_{p,q,r}\ T_{60}(f_{p,q,r})}\ . \tag{7.11}$$

Furthermore, in order to enrich the characterisation of the systems and to identify phenomena associated with specific frequency bands, analogic time signals where historically filtered through octave or third octave passband filters. Thus, sound pressure levels are computed per band, resulting in sound reduction indices associated with each band. Let H_b be the frequency response function of an idealized passband filter, associated with an octave or third octave band. The spatial and time average of the quadratic pressure in a given room per filter band is then given with the Parseval identity as

$$P^2_{room,b} = \frac{1}{V_s}\int_{V_s}\int_{-\infty}^{+\infty}|H_b\ p_{room}(\omega;\mathbf{x})|^2\ \mathrm{d}\omega\mathrm{d}V\ , \tag{7.12}$$

where V_s is the sampling volume for the spatial averaging of the quadratic pressure field.

7.2.3 Decoupled approach for the evaluation of the sound reduction index

For the sake of clarity, the adopted decoupled approach for the sound reduction index is briefly summarized. As a **first step**, the source room is considered as an independent dynamical system. With respect to a given acoustical excitation, the sound pressure field can be determined according to Section 7.2.2. Then, an incident pressure field on the boundary with the evaluated parting wall as well as the spatial average of the quadratic pressure field can be evaluated in the source room. As a **second step**, the external excitation on the system is constructed from the incident pressure field resulting from the first step. A computational model constructed according to Chapters 2, 5 or 6 with respect to the deterministic or random vibroacoustic evaluated system is then solved for the displacement field of the structure on the boundary with the receiving room. As a **third step**, the receiving room is considered as an independent dynamical system. Then, the acoustical excitation of the receiving room is constructed from the displacement field of the structure on the boundary with the receiving room and the spatial average of the resulting quadratic sound pressure field can be evaluated.

External excitation of the evaluated system

Let Γ_S and Γ_R respectively be the interfaces of the structure with the source room and receiving room constituting a partition of $\partial\Omega^{\rm s}_{\rm n}$. Furthermore, $\mathbf{n}^{\rm s}$ is the outward-pointing normal vector with respect to the structure according to the notations of Chapter 2. Let $Q_S(\omega;\mathbf{x})$ be an acoustical source placed into the source room and $p_S(\omega;\mathbf{x})$ the resulting pressure field, solution of the Helmoltz Eq. (2.16). The external excitation field $\mathbf{f}^{\rm s}$ on the system is constructed such that

$$\begin{cases} \mathbf{f}^{\rm s} = -p_S(\omega;\mathbf{x})\,\mathbf{n}^{\rm s}\ , \text{ on } \Gamma_S \\ \mathbf{f}^{\rm s} = \mathbf{0}\ , \text{ on } \partial\Omega^{\rm s}_{\rm n} \setminus \Gamma_S \end{cases} . \tag{7.13}$$

Thus, the vector of the external excitation $\mathbb{F}^{\rm s}$ on the system is obtained from the finite element discretization of the anti linear form defined by Eq. (2.15). Then, the displacement field of the structure $\mathbf{u}^{\rm s}$, resulting from an external excitation field $\mathbf{f}^{\rm s}$ on the system, is obtained as a solution of previously defined deterministic or stochastic computational models.

Evaluation of the sound reduction index

The acoustical source $Q_R(\omega;\mathbf{x})$ with respect to the receiving room is constructed from the restriction $\mathbf{u}^{\rm s}_R$ of $\mathbf{u}^{\rm s}$ on the interface Γ_R with the receiving room such that $Q_R(\omega;\mathbf{x}) = \omega^2\ \mathbf{u}^{\rm s}_R \cdot \mathbf{n}^{\rm s}$. Following, the pressure field $p_R(\omega;\mathbf{x})$ within the receiving room is obtained as a solution of Eq. (2.16) with the source $Q_R(\omega;\mathbf{x})$. Within the case where the sampling volume V_s covers the whole room volume V, the spatial average per filter band of the quadratic pressure field in a given room can be computed, using the eigenfunctions orthogonality and Eq (7.12), as

$$P^2_{room,b} = \frac{\rho^F c_F^2}{V} \int_{-\infty}^{+\infty} \sum_{p,q,r} |H_b\ A_{p,q,r}(\omega)|^2\ {\rm d}\omega\ . \tag{7.14}$$

A numerical evaluation is otherwise performed for smaller sampling volumes, as prescribed in [135] for example, and the estimation of the sound reduction index per band is performed according to Eq. (7.4).

7.2.4 Concluding remarks about the approach

Such airborne sound insulation performance evaluation model depends on four categories of parameters: room dimensions, modal damping factors, positions of the acoustical sources, sampling volumes. In the following paragraphs, a case study is undertaken in order to obtain an overview of such approach and of the behavior of typical systems within the first third octave bands. In particular, the sentitivy of the airborne sound insulation model to input parameters such as source positions and modal damping factors will be enlightened, as well as the difficulty to translate current experimental data such as

reverberation times into trustworthy input parameters for the model. Thus, the comparison with experimental results below or around the Schroeder frequency [136] which gives an estimation for the validity range of the diffuseness hypothesis, has to be put in perspective with the high sensitivity of the model to small variations within its input parameters as well as with the large experimental standard deviations associated with conventional measurements [121]. Eventually, the confidence regions resulting from the propagation of the uncertainties from the modeled uncertain systems onto the sound reduction indices will be compared in regard to the order of those previously enlightened and resulting from the simulated experimental protocol. It should be noted that the whole approach considers deterministic external excitation as well as radiations into the receiving rooms, as the objective is to compare the performance of a set of uncertain systems in fixed laboratory conditions. For such potential uncertainty quantification, a framework for the construction of the probabilistic models of the parameters for reverberant room model, using the maximum entropy principle, was for example introduced in [137].

7.3 Application to double parting wall separative systems

7.3.1 Nominal systems

The aiborne sound insulation performance of two admissible configurations for a double parting wall, whose dimensions are L_y^W=3.800 m and L_z^W=2.250 m, is investigated and compared with experimental measurements. Both configurations (see Fig. 7.2) are symmetrically designed around a 2 cm air gap and do not involve structural transmission paths between the facing single walls. They are constituted of a load carrying primary wooden frame of 22 studs (11 for each side with 400 mm spacing and whose cross-sectional dimensions are 140 mm $\times$ 45 mm) with a poroelastic material in between, 12 mm thick OSB bracing panels, a secondary frame of 22 vertical battens (cross-sectional dimensions 45 mm $\times$ 27 mm) with air in between and on which are fixed two layers of plasterboards 12.5 mm thick on each side. In Fig 7.2, the grey areas denote the positions of the stud and battens whereas the textured areas denote the positions of the poroelastic and air cavities. From the rooms perspective, the facing consists in two layers constituted of multiple plasterboards, whose positions and orientations are unknown but whose mounting is such that the joint do not overlap, resulting in a more or less homogeneous effective board. As such, it is assumed that the effective behavior is identical to the one of a unique plasterboard, whose thickness is doubled but whose physical properties remain identical. It should be noted that in order to obtain the correct critical frequency of such multilayered plaster panel, the Young's modulus associated with the effective panel as to be modified (divided by 4). At low frequencies however, it is assumed that the vibroacoustic effects responsible for such phenomenon do not appear yet. Moreover, in regard to the assembly of the different structural component as well as to boundary conditions, the connections are supposed to be perfectly rigid, the frame elements are supposed to be clamped at their extremities and the boards have fixed displacements but free rotations over the edges. The variation from one configuration to the other is defined by the position of the OSB bracing panels, towards the outside or towards the inside of the primary frame. Hereinafter, the former is denoted "system 1" and the latter "system 2".

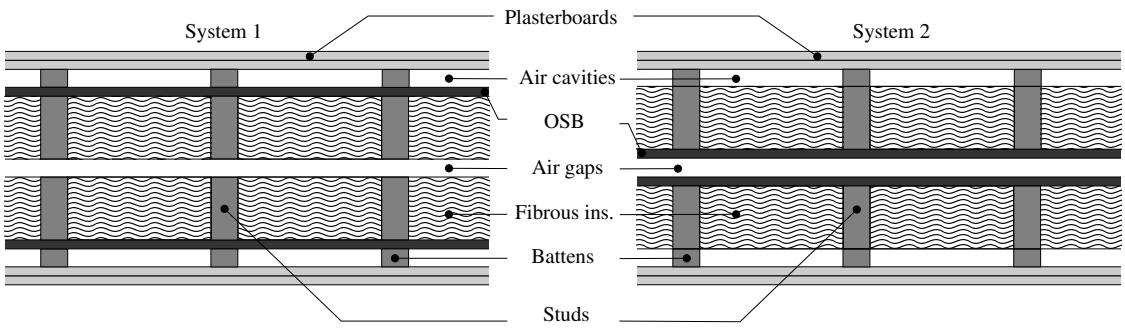

Figure 7.2: Top sectional views of the parting walls.

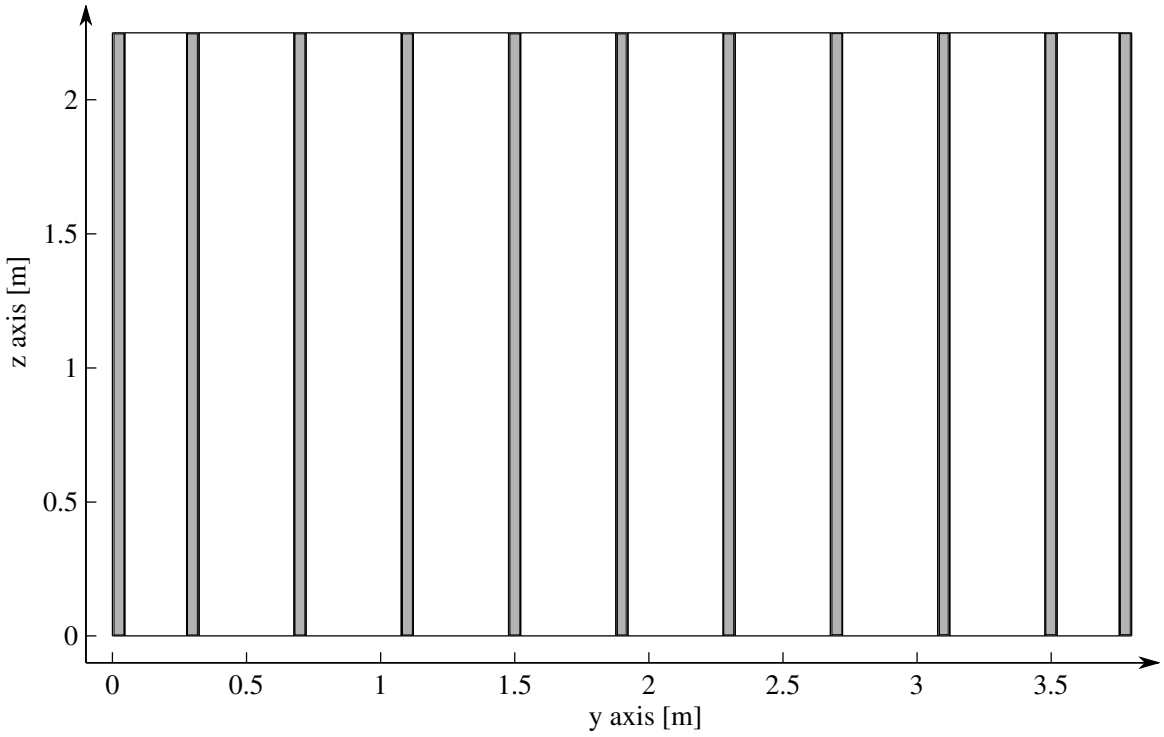

Figure 7.3: Front view of the parting walls with the apparent stud pattern.

Young's modulus [kPa]	400
Poisson's ratio	0
Mass density $(1-\phi)\rho^{p_s}$ [kg/m^3]	70
Porosity ϕ	0.9
Flow resistivity σ [N.s/m^4]	50000
Tortuosity α_∞	1.7
Viscous length Λ [μm]	60
Thermal length Λ' [μm]	150
Structural loss factor	0.05

(a) Poroelastic medium parameters.

Standard pressure P_0	1.015×10^5 Pa
Mass density ρ^F	1.21 kg/m^3
Heat capacity ratio γ	1.4
Sound velocity c_F	340 m/s
Prandtl number Pr	0.72
Dynamic viscosity η_f	1.81×10^{-5} N.s/m^2

(b) Air parameters.

Table 7.1: Poroelastic medium and air parameters.

With respect to the structural components, the nominal physical parameters are the mean values that were identified within Chapter 3 for the pine beams, plasterboards and oriented strand boards. In regard to the fibrous insulation material, the nominal parameters corresponding to the associated poroelastic modeling are given in Table 7.1. In the following paragraphs, computational models constructed using the displacement formulation as well as equivalent fluid formulation with respect to the poroelastic medium will be compared and the effects of hypothesis such as bonding between the poroelastic medium and the structure (in the present case with the oriented strand boards), will be investigated.

7.3.2 Mean computational models

Computational models are constructed according to Sections 2.4 and 2.5, using the physical parameters given within the previous paragraph and suited for the frequency band $\mathbb{B} = [10, 220]$ Hz. First, compatible meshes are generated with respect to the structure, internal acoustic cavities and poroelastic media. It should be noted that the structures display quite contrasted bending stiffness within the orthogonal directions of the plane due to the unidirectional stiffening. By way of consequence, mesh density in

both directions could be adapted in order to not over-mesh the stiffest direction for which the structural wavelengths are naturally longer. However due to the code being reliant on compatible meshes, the density has to be determined with respect to the homogeneous acoustic cavities or poroelastic components. The mesh density is chosen according to the smallest wavelength displayed by any of the aforementioned media at 220 Hz. Thus, due to its higher modal density in the frequency range of interest, the poroelastic medium is responsible for the mesh criterion. Figure 7.4 displays the theoretical wavelenght associated with each solid-borne, fluid-borne and shear Biot waves computed according to the expressions of the wavenumbers given within Appendix A with the properties given in Table 7.1. The shear wave has the smallest wavelength at 220 Hz with 0.24 m. According to the results presented in [75] and due to the fact that the detrimental shear locking effects mentioned in [75] were treated beforehand within the finite element formulation (see Section 2.4.1), the number of six elements is chosen per wavelength, which yields a density of 25 elements per meters.

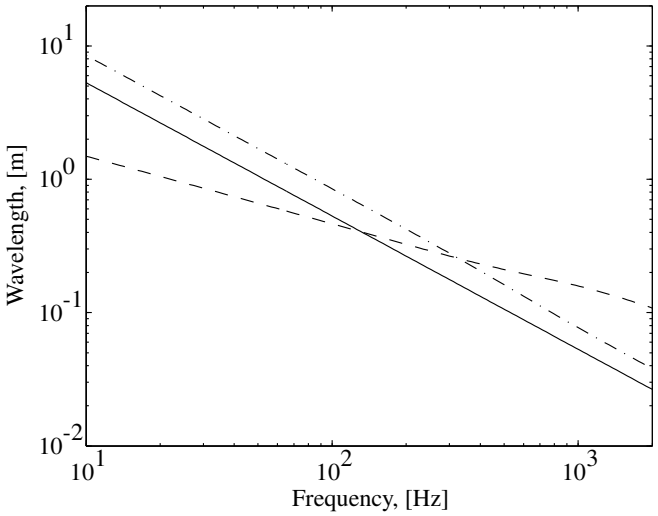

Figure 7.4: Biot waves wavelengths function of the frequency. Solid-borne wave (thin black dash-dot line); fluid-borne wave (thin black dashed line); shear wave (thin black solid line).

From compatible meshes of the different structural, acoustic and poroelastic components, the finite element method yields, in the physical coordinates, $N_s = 226152$ degrees of freedom for the structure, $N_f = 57456$ degrees of freedom for the internal acoustic cavities and respectively $N_p = 284544$ and $N_e = 47424$ degrees of freedom for the poroelastic medium modeled as coupled solid and fluid phases with displacements as primary variables or equivalent fluid with pressure as primary variable. In [48], a case study in regard to a double panel system with bonded or unbonded lightweight poroelastic media, such as fibrous insulation materials, showed little to no difference in the dynamical behavior due to the neglectible solid-borne Biot waves in such limp materials. Moreover, in [49], similar results were observed in regard to poroelastic displacement formulation without bonding and equivalent fluid formulations. In the present case, preliminary investigations converged towards the same conclusions. Thus, in the following, considering that the fibrous insulation materials are filled within the wall cavities such that no OSB to poroelastic frame displacement continuity is enforced, the limp frame equivalent fluid model, less computationally intensive, is retained. In regard to the cases where stiffer insulating materials would be involved, possibly glued or nailed to the structure, the full displacement formulation would have to be considered due to the solid-borne waves into the poroelastic medium.

Furthermore, in the aim of obtaining a reduced order computational model, the equations associated with the two distinct structural subsystems are projected on the truncated basis constituted of their respective 100 first elastic modes and constructed according to Section 5.2 for a total of $n_s = 200$ structural eigenmodes. The equations associated with the 21 internal acoustic cavities are projected on the truncated basis constituted of the first rigid cavity modes constructed according to Section 5.3 using a total

of $n_{\mathrm{f}} = 200$ acoustic eigenmodes. Finally the equations associated with the 20 poroelastic components, with respect to the limp frame equivalent fluid model, are projected on the truncated basis constructed according to Section 5.5 using a total of $n_{\mathrm{e,I}} = 3000$ eigenmodes. Consequently, the dimension of the resulting reduced order computational models is 3400. It should be noted that even if the dimension of the reduced problem appears as quite high, the dynamic substructuring in fact leads to a relatively sparse reduced system of equations, diagonal for the most part, such that the resolution is not too cumbersome (less than a minute for a 500 point frequency resolution using 8 cores on a modern computer).

7.3.3 Definition of the external excitation for the computational model

Laboratory setup

The laboratory setup is such that L_x^S=5.390 m, L_y^S=4.320 m and L_z^S=3.000 m for the source room, L_x^R=5.850 m, L_y^R=3.800 m and L_z^R=2.800 m for the receiving room. Moreover, the opening of the source room is centered with respect to the y direction. A mean reverberation time for the receiving room was associated with the experimental data provided by the laboratory and is given in Table 7.2 for the third octave bands going from 50 to 250 Hz. It is then assumed that the reverberation time within the source room is comparable over frequency. Moreover, it can be noted that such laboratory dimensions does not meet the standards given in [124] in which a minimal dimension of 6.88 m is stated necessary to assess a good reproductibility at low frequencies [123].

Third octave band [Hz]	50	63	80	100	125	160	200	250
T_{60} [s]	2.8	3.3	2.1	1.3	1.4	1.2	1.1	1.3

Table 7.2: Mean reverberation time for both rooms.

Number and positions of the acoustical sources

As it was previoulsy mentioned, the standard evaluation procedure laboratory conditions consists generating an incident pressure field on the considered system. Has every laboratory has its own particularities, only general requirements for the number and positions of the acoustical sources are formulated within the standards. Thus, in the following, the acoustical excitation of the source room is constructed from arbitrarily positionned omnidirectional point sources consistent with the aforementioned requirements.

Thus, in the standard [135] is introduced a methodology for the determination of the number and positions of the acoustical sources in regard to the evaluation of airborne sound reduction indices. First, a set of sound pressure level differences is measured using successively a number m of source positions, in which m depends on the volume of the source room and verifies

$$m \geq 152/V_S^{\frac{2}{3}} \, . \tag{7.15}$$

By way of consequence, according to the dimensions of the source room given within the previous paragraph, the number of $m = 12$ sources is chosen and arbitrarily placed in the source room at a minimal distance of 0.7 m from each others. Positions are chosen according to the additional requirements provided in [135]. In particular, a minimal distance of 0.7 m with respect to the room boundaries, denoted by the grey area in Fig 7.5, is verified. Such positions are displayed on Fig 7.5 by the red dots. The coordinates of the first source on the left of the figure are $\mathbf{x}_{Q_{S,1}} = (0.72, 0.8, 0)$ and the other coordinates can be found with successive translations along the vectors (1.4,0.1,0) or (0.1,1,0). Then, two sources cannot belong to a same plane, parallel to room boundaries, which could potentially be an acoustic mode nodal. Following, for each acoustical source $Q_S(\omega; \mathbf{x}) = \omega^2 \, \delta(\mathbf{x} - \mathbf{x}_{Q_{S,s}})$, the external excitation on the parting walls is constructed from the pressure field in the source room according to Section 7.2. Given the reverberation time in Table 7.2, Eq. (7.11) yields the modal damping factors given in Table 7.3. No

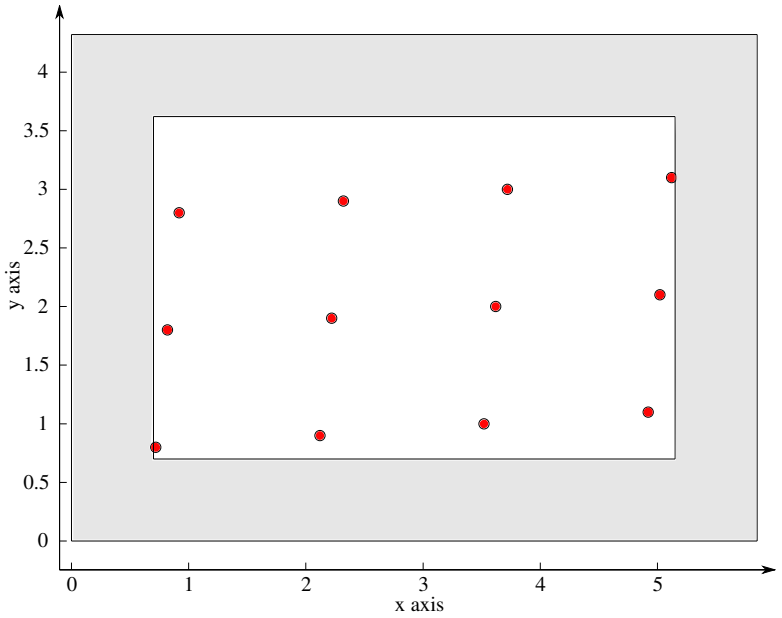

Figure 7.5: Top view of the source room. Acoustical sources (red dots).

experimental data is provided below 50 Hz for the reverberation time such that the modal damping factors are arbitrarily set to 0.010.

Third octave band [Hz]	< 50	50	63	80	100	125	160	200	250
Modal damping factor ξ	0.010	0.008	0.005	0.006	0.008	0.006	0.006	0.005	0.003

Table 7.3: Modal damping factors computed from the reverberation times given by the laboratory.

Then, the sound pressure level difference is evaluated with respect to each source position, using a spatial sampling of the quadratic sound pressure over the volumes excluding areas closer than 0.7 m to the boundaries of the rooms, and the differences between the source room and the receiving room are displayed on Fig. 7.6. First of all, from Fig 7.6 it can be observed that sound pressure level difference are quite similar with respect to both systems in the frequency range from 60 to 80 Hz. A closer look at this particular interval will be taken later on. Moreover, Fig. 7.7 displays the sound pressure level differences associated with each source, in third octave band. Then, due to the low modal density in the rooms, 15 to 20 dB differences can be observed function of the position of the acoustical source in the source room and tend to decrease with frequency, in particular with respect to the system 2. However, it should be noted that real laboratory facilities make use of acoustic diffusing elements. It is then reasonable to assume that such disparities are lowered in amplitude in regard to experimental measurements and limited to a lower frequency range.

In the spirit of [135], this first set of measurements, using a substantial number of sources, is aimed to give an estimate of the standard deviation resulting from different source locations. Then, it is possible to find the number of sources required to reach a given level of precision. Following, the methodology in [135] considers the standard deviation estimator S_b associated with the sound pressure level difference D_b within the third octave band b such that

$$S_b = \left(\frac{1}{m-1} \sum_{j=1}^{m} (D_{b,j} - \mu_b)^2 \right)^{\frac{1}{2}}, \tag{7.16}$$

where μ_b is the mean value of D_b in b. Given the dispersions observed on Fig. 7.7 it is clear that, with respect to the present model, any statistical estimator associated with the mathematical expectation or

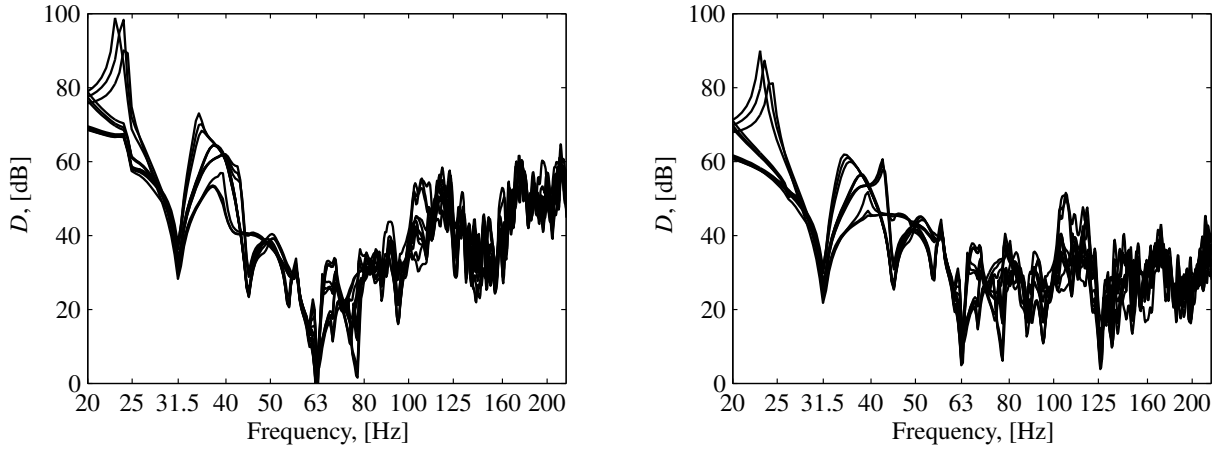

(a) System 1 (b) System 2

Figure 7.6: Sound pressure level differences with respect to the twelve source positions (thin black solid lines).

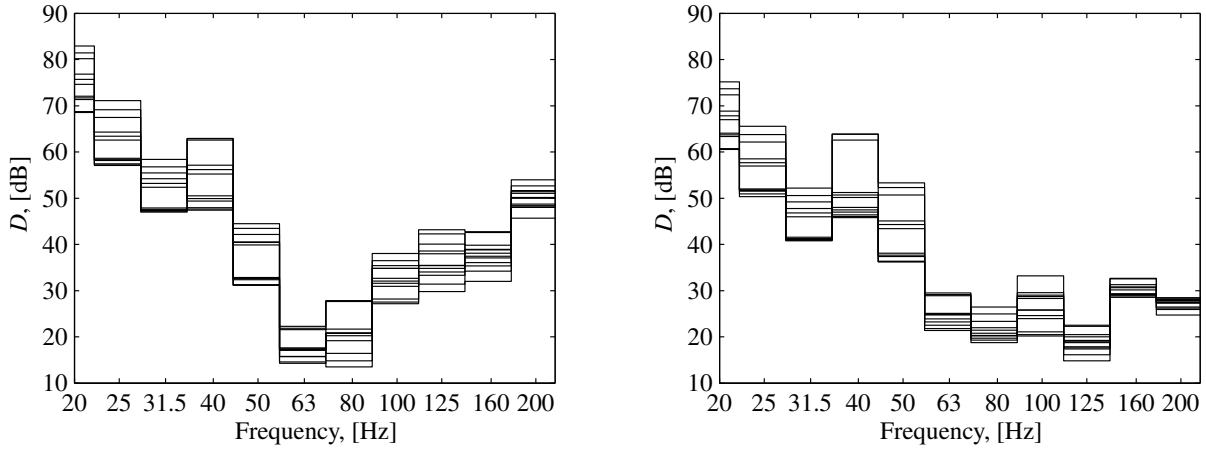

(a) System 1 (b) System 2

Figure 7.7: Sound pressure level differences with respect to the twelve source positions (thin black solid lines).

variance has not converged yet, meanwhile it is impossible to add sources according to the constraints given in [135]. In regard to the considered laboratory and systems, according to this room model, there is consequently an irreductible error associated with the positions of the sources, to be expected below 200 Hz. Thus, the totality of the twelve previously defined sources will be used for the evaluation of the sound reductions indices. A number $N = 12$ of sound reduction indices $R_{b,j}$ will then be computed per third octave band, with respect to each source, and the mean sound reduction index per band is determined according to the standard [124] as

$$R_b = -10 \log_{10} \left(\frac{1}{N} \sum_{j=1}^{N} 10^{-R_{b,j}/10} \right) . \tag{7.17}$$

7.3.4 Evaluation of the sound reduction indices

In regard to the comparison with laboratory data, Fig 7.8 displays experimental as well as predicted sound reduction indices according to the previously introduced approach. In particular the sound reduc-

tion indices are mean values resulting from Eq. (7.17) using the twelve previously defined acoustical sources and a quadratic pressure averaging over the volume comprised between the boundaries of the room minus 0.7 m, according to the aforementioned standards.

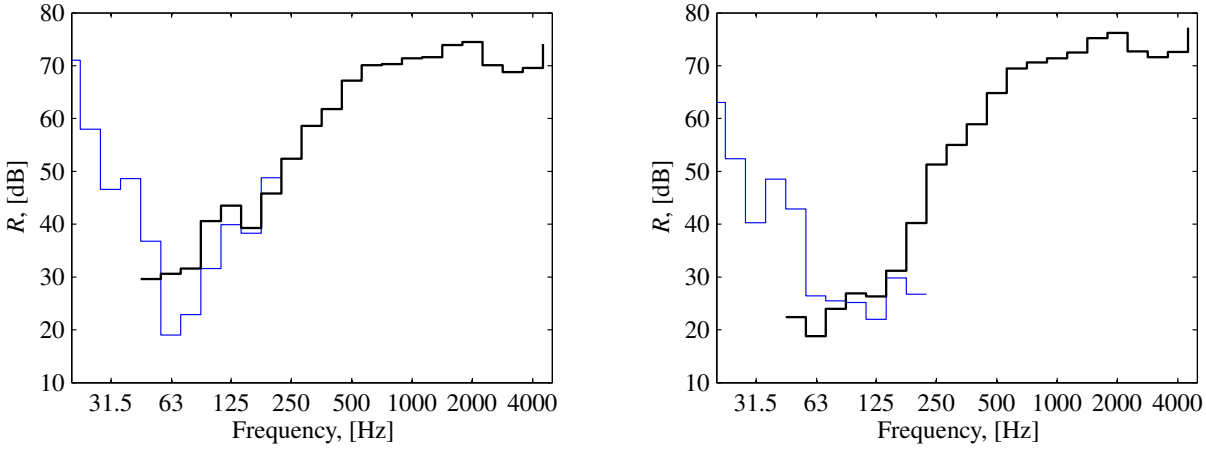

(a) System 1 (b) System 2

Figure 7.8: Mean sound reduction indices R with respect to both systems. Computational model (thin blue solid lines); experimental measurements (thin black solid lines).

First of all, a discrepancy of more than 20 dB at the 50 Hz third octave band with respect to the system 2, for which the measured airborne sound insulation is lower than the predicted one, can be interpreted as a modeling issue where the structures display too much stiffness within the computational model. From numerical modal analysis, the first structural resonances are respectively identified at 65.8 Hz with respect to the the system 1 and 76.7 Hz with respect to the system 2. Indeed, in regard to the system 2, single walls (associated with a single primary frame) display higher bending stiffness because the OSB is set further from the neutral bending axis of the stud plus batten system, leadind to a first resonance at higher frequency. Then, as no transmissions really happen below the first structural resonances, it means that for such low experimental sound reduction indices associated with the 50 Hz third octave band to be osbserved, structural resonances of the real structure must exist at lower frequencies than predicted by the computational model. Thus, the boundary conditions and connections of the different subparts can be questionned, in particular in regard to the findings of Chapter 4. Later on, the generalized probabilistic approach of uncertainties will be used in order to evaluate the sensitivity of the computed sound reduction indices to model uncertainties. However, comparable trends are able to be observed and, notably, the variations in performance due to the variations in the design from system 1 to system 2 are consistent between the experimental measurements and the mean computational models past 80 Hz.

Close look at the 63 and 80 Hz third octave bands

In order to have a better understanding of the dips observed at the 63 and 80 Hz third octave band, a close look is taken at the mean sound pressure level difference in narrow band, computed according to Eq (7.18) within the frequency band $[55, 90]$ Hz, and displayed on Fig 7.9 in parallel with the resonances frequencies respectively associated with the source room (blue vertical lines), single walls (black vertical lines) and receiving room (red vertical lines).

$$D = -10 \log_{10} \left(\frac{1}{N} \sum_{j=1}^{N} 10^{-D_j/10} \right) . \tag{7.18}$$

First of all, in such frequency range, it can be understood that, all other things being equal, the systems behave almost solely has a stiffness component as it can be observed that for the system 2,

stiffer, the mean sound pressure level difference is roughly shifted upward below 80 Hz. It should be noted that, with respect to both systems, mass-air-mass configurations exist, some associated with lower theoretical resonance frequencies due to deeper cavities. Thus, in regard to system 1, such mass-air-mass phenomenon is theoretically expected to first happen with respect to the two OSB panels separated by the 300 mm air plus fibrous gap. At normal incidence, the theoretical mass-air-mass frequency is given by Eq. (7.19), in which H denote the distance between the two plates, and is consequently equal to $f_r = 58.9$ Hz for the system 1.

$$f_r = \frac{1}{2\pi}\sqrt{\frac{\rho^{\mathrm{f}} c_0^2}{H}\left(\frac{1}{\rho^{\mathrm{s}1}} + \frac{1}{\rho^{\mathrm{s}2}}\right)} \tag{7.19}$$

In regard to system 2, the mass-air-mass phenomenon associated with the plasterboard and OSB panel separated by the 160 mm air layer is expected to happen first, at a frequency $f_r = 67.3$ Hz. The resulting dips are not apparent on Fig (7.9) and expected to be pushed towards higher frequencies due to the stiffening of the plates and the multi-incidence pressure field [95]. In [138] it is also mentioned how poroelastic filling and wooden studs can modify the frequency range of apparition for such phenomenon.

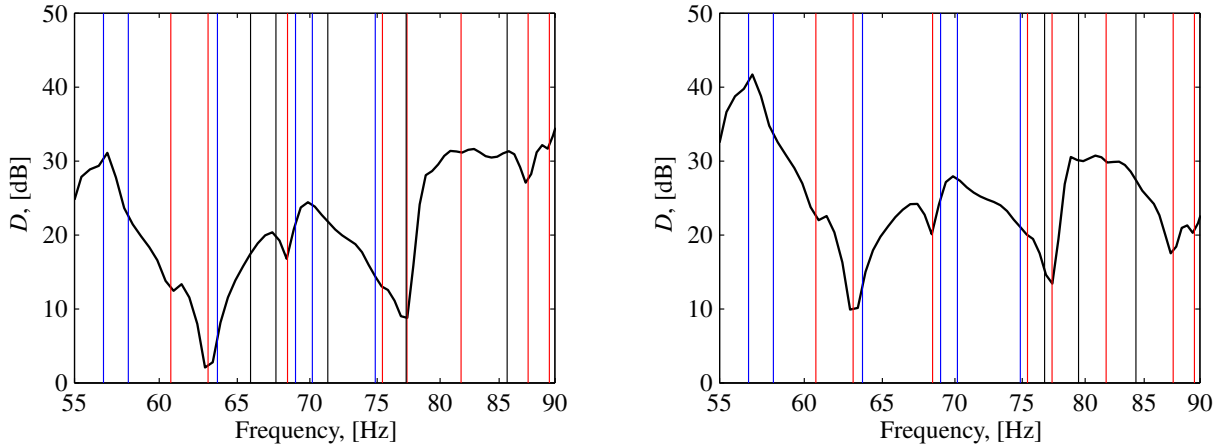

Figure 7.9: Sound pressure level differences (thin black solid lines). Source room resonances (blue vertical lines); structure resonances (black vertical lines); receiving room resonances (red vertical lines).

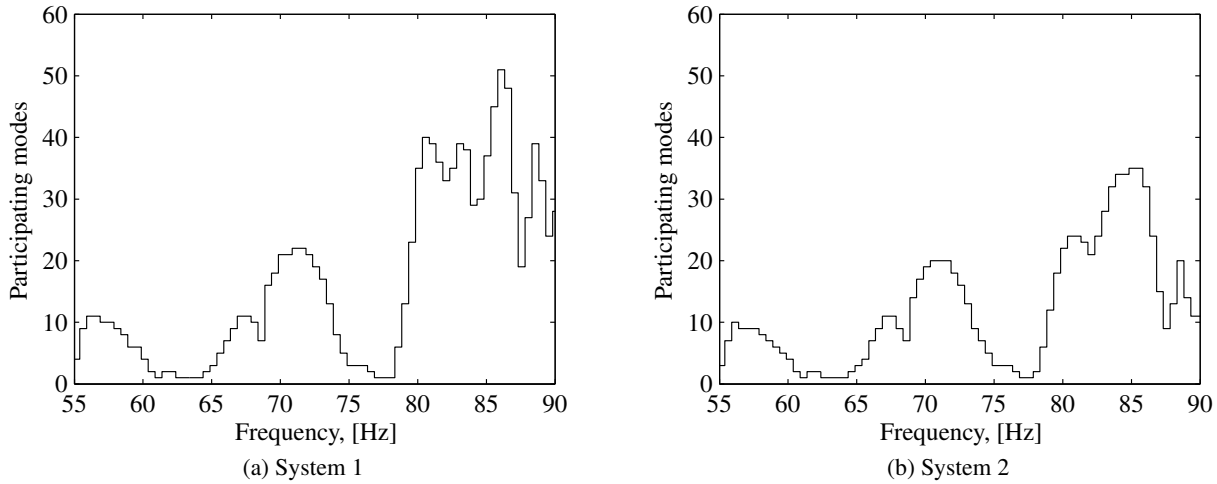

Figure 7.10: Number of modes from the receiving room contributing to 99% of the sound pressure level.

Moreover, Fig 7.10 displays the number of modes participating to 99% of the sound pressure level within the receiving room. Thus, it can be seen how the evaluated performance is influenced by the receiving room resonances between 60 and 65 Hz and between 75 and 80 Hz, where only one mode contributes to the sound pressure level. Disturbances in regard to the two room modes that respectively control the receiving room pressure field at 63 and 77 Hz would entirely change the sound pressure level from the receiving side and consequently the evaluated sound reduction index. In particular, diffusing systems or absorbers can have a huge impact on the acoustic energy per third octave band [120]. In regard to experimental observation of the influence of room modes one can refer to [139]. Furthermore, it can be seen that both systems radiate in a similar way below 80 Hz as they excite the exact same number of acoustical modes within the receiving room.

Influence of the acoustical damping in the room model

In order to illustrate the remarks from the previous paragraph, different modal damping factors are associated with the two room modes single-handedly controlling the sound pressure level in the receiving room at 63 and 77 Hz. Following, such damping factors are computed according to Eq. (7.11) using the arbitray value of $T_{60} = 1s$ which can be found within the standard [135] and sets a maximum admissible level of acoustical damping in the rooms. Thus, the damping factors associated with the aforementioned two modes are respectively set to 0.018 and 0.014, actually tripled from those given Table 7.3. Following, Fig 7.11 displays the mean sound pressure level difference resulting from the change of modal damping factors for the two modes previously mentioned. In terms of third octave band results, this small variation respectively yields 5 and 3 dB discrepancies for the 63 and 80 Hz bands in regard to system 1, 5 and 1 dB in regard to system 2. Thus, it can be imagined how a drastic disturbance of such modes, using diffusers for example, would modify the evaluated quantities.

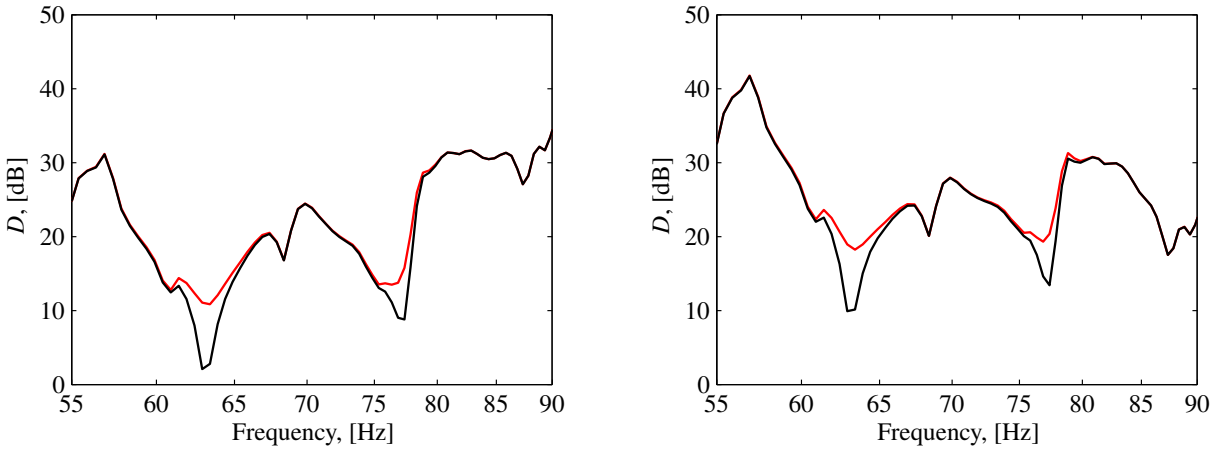

(a) System 1 (b) System 2

Figure 7.11: Sound pressure level differences. Modal damping factors computed from the experimental reverberation time (thin black solid lines). Modified modal damping factors according to $T_{60} = 1s$ for the two receiving room modes at 63 and 77 Hz. (thin red solid lines)

In fact, if the reverberation time at low frequencies can give a first estimate of the damping in the rooms, its measurement principle assume high modal overlap and identical decays among the modes of the considered frequency band, which is not verified at low frequencies [140]. By way of consequence, third octave band measurements do not constitute a sufficient information for a damping quantification at low frequencies and correction terms such as used in Eq. (7.4) are not sufficient to set the final result independent of the room damping with respect to the lowest third octave bands.

Concluding remarks about the airborne sound insulation models

From the previous paragraphs, it is clear that the comparison with experimental measurements below 100 Hz requires additional information to enrich the models. Below this threshold, third octave band quantities such as reverberation time are not sufficient for damping quantification and an accurate modal characterisation of the rooms is needed. According to the current model, variations in the evaluation conditions influence the final airborne sound reduction indices, in particular below 80 Hz were room modes can single-handedly control the sound pressure levels. However, all other things being equal, such model can be used to evaluate the performance of systems with respect to each others.

7.3.5 Uncertainty quantification

Hereinafter, we focus on the propagation of the uncertainties associated with the different structural, acoustic and poroelastic components of the system for given probabilistic models constructed according to Chapter 6. Then, the order of the computed confidence intervals can be compared with the variations observed with respect to the evaluation conditions within the previous section. Such an approach aims at discriminating the effects of the different involved phenomena on the final evaluated performance. To the best knowledge of the author, such question remain currently open as, in general, experimental quantification is quite challenging due to the difficulty to isolate a specific phenomenon out of the global complexity of the systems. However, extensive experimental studies such as [8,90] can be used to support computational trends associated with a focused source of uncertainty, to which experimental variations could correspond.

Probabilistic approach of system parameters uncertainties

In this paragraph, stochastic computational models are constructed using the probabilistic approach of system parameters uncertainties only, according to the prior probabilistic model introduced in Section 6.4. Thus, the respective hyperparameters associated with the elastic properties and mass densities are those previously identified within Chapter 6 and briefly recalled in Table 7.4.

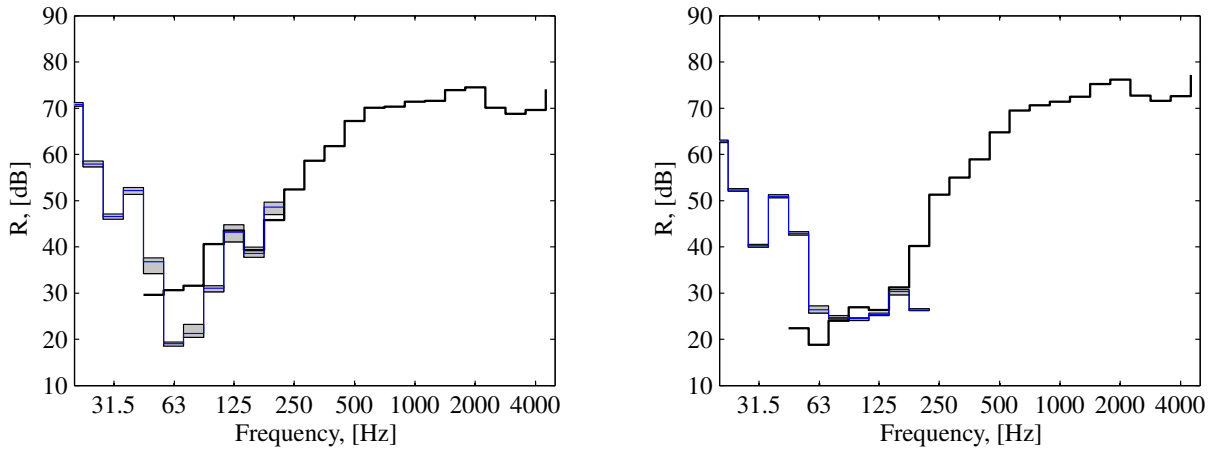

(a) System 1 (b) System 2

Figure 7.12: Sound reduction indices R. Confidence regions associated with a probability $P_c = 0.98$ for the indices R resulting from the parametric probabilistic approach with respect to structural uncertainties (grey areas); mean computational model (thin blue solid line); experimental measurements (thick black solid lines).

Following, confidence regions associated with a probability $P_c = 0.98$ for the sound reduction indices in third octave band resulting from such parametric probabilistic approach are displayed on Fig 7.12

and compared with the experimental values. The statistical fluctuations of the sound reduction indices induced by structural system parameters uncertainties remain limited, which is consistent with the experimental rebuild repeatability that was investigated in [8] for airborne and impact sound insulation. Indeed, good rebuild repeatability with respect to measured airborne sound reduction indices suggests that the sensitivity to fluctuations among the physical parameters is low. Moreover, it should be noted that the propagation of the uncertainties, from the structural system parameters to the sound reduction indices, result in fluctuations whose order similar to inferior in comparison to those resulting from variations in the experimental setup (source positions, acoustical damping etc.).

Pine beams		OSB		Plasterboards 12.5	
δ_{E_l}	δ_ρ	δ_{ela}	δ_ρ	δ_{ela}	δ_ρ
0.08	0.065	0.10	0.020	0.15	0.009

Table 7.4: Dispersion hyperparameters with respect to each structural component.

Generalized probabilistic approach of uncertainties

In this paragraph, the sensitivity of airborne sound insulation to model uncertainties is investigated using the generalized probabilistic approach of uncertainties. Thus, stochastic computational models are constructed in order to successively perform uncertainty quantification in regard to structural, acoustic and poroelastic components. In particular, it was shown in Section 6.5.2 that the generalized probabilistic approach of uncertainties was able to take into account model uncertainties induced by modeling errors associated with the connections of the different subparts of the structure which, together with boundary conditions, are suspected to be responsible for the discrepancies observed at the 50 Hz third octave band in Section 7.3.4. Thus, with respect to structural uncertainties, independent probabilistic model are constructed to take into account system parameters as well as model uncertainties according to Chapter 6. With respect to internal acoustic cavities or poroelastic components, only the nonparametric approach of model uncertainties is used as no information is available for the identification of the system parameters probabilistic models.

Structural uncertainties The generalized probabilistic approach of uncertainties is used for uncertainty quantification with respect to structural uncertainties. Thus, the stochastic computational models depend on the hyperparameters of the probabilistic models associated with the probabilistic approach of system parameters uncertainties, which are the ones used in Section 7.3.5, as well as on the hyperparameters associated with the nonparametric probabilistic approach. Because no identification of the latter with respect to experimental measurements was possible due to the lack of data, values of $\delta_{M^s} = \delta_{D^s} = \delta_{K^s} = 0.3$ are arbitrarily chosen for a sensitivity analysis. However, according to Section 6.5.2 such values and the resulting confidence intervals were consistent with experimental measurements.

Following, confidence regions associated with a probability $P_c = 0.98$ for the sound reduction indices in third octave band resulting from such generalized probabilistic approach, with respect to structural uncertainties, are displayed on Fig 7.13 and compared with experimental values as well as with the outputs of the mean computational models. First of all, it can be seen that below 50 Hz the sound reduction index associated with the nominal model is actually the superior envelope of the sound reduction indices resulting from the stochastic computational model. As there is no structural resonances in the model associated with such frequency bands, and the response of the structure is limited to the static response of its modes without mass effects, it can be interpreted that the nominal model yields the stiffest model at very low frequencies and that the generalized probabilistic approach tends to lower the structural resonance frequencies of the system (as it can also be observed on Fig. 6.11). Such effect can also explain the lowest performance in the 63 Hz hird octave band in regard to system 2 according to the stiffness

controlled behavior mentioned within the previous paragraphs. Moreover, it can be noted that with respect to given third octave bands, such as the 80 Hz one in regard to system 1 or past 125 Hz in regard to both systems, the prediction from the nominal model is out of the confidence regions resulting from the generalized probabilistic approach. Thus, the performance in such frequency bands is particularly sensitive to model uncertainties and such result illustrate the relevance of the probabilistic approach to evaluate the sensitivity of the prediction around the nominal model. It should be noted that the nonparametric approach of uncertainties is contructued around the means mass, damping and stiffness matrices. By way of consequence, there is a non-linear transformation between the constructed random variables and the random observables (inversion of the dynamic stiffness) and as a result no reason for the response of the nominal computational model to be the mean response of the stochastic computational model.

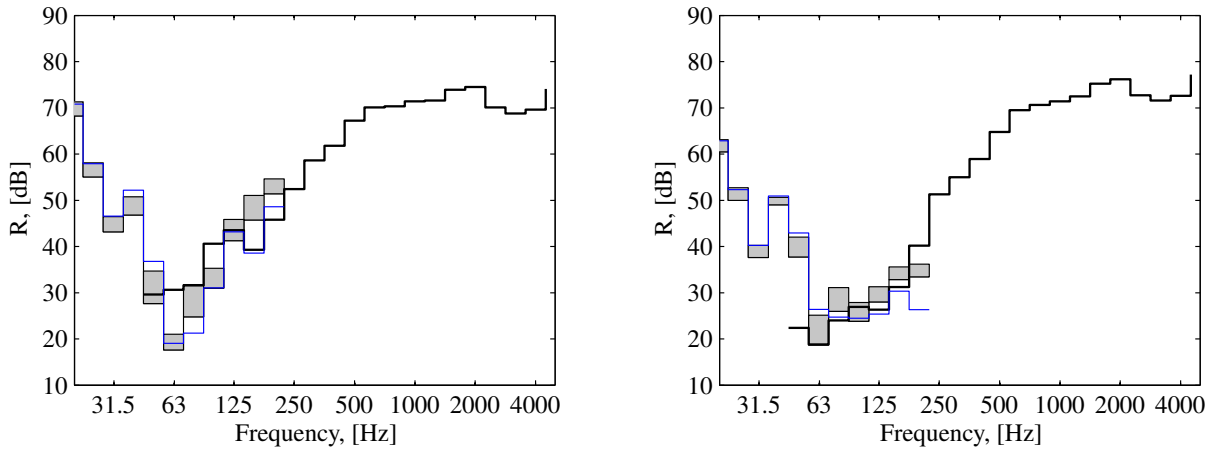

(a) System 1 (b) System 2

Figure 7.13: Sound reduction indices R. Confidence regions associated with a probability $P_c = 0.98$ for the indices R resulting from the generalized probabilistic approach with respect to structural uncertainties (grey areas); mean computational model (thin blue solid line); experimental measurements (thick black solid lines).

Uncertainties associated with the internal acoustic cavities In a second stage, the sensitivity of the sound reduction indices to statistical fluctuations within the generalized matrices associated with the internal acoustic cavities is analysed using the nonparametric approach. Let δ_{M^f}, δ_{D^f} and δ_{K^f} respectively be the hyperparameters controlling the nonparametric statistical fluctuations within random mass matrix $[\mathbf{M}^f]$, damping matrix $[\mathbf{D}^f]$ and stiffness matrix $[\mathbf{K}^f]$ associated with the internal acoustic cavities. Values of $\delta_{M^f} = \delta_{D^f} = \delta_{K^f} = 0.3$ are arbitrarily chosen for the sensitivity analysis.

Figure 7.14 compares the confidence regions associated with a probability $P_c = 0.98$ for the sound reduction indices in third octave band resulting from such nonparametric probabilistic approach associated with the internal acoustic cavities. With respect to both systems, uncertainties start to be influential above the 80 Hz third octave band which results in a widening of the confidence regions. Indeed, it should be noted that the 2 cm central air gap displays a first resonance at 45 Hz (0,1,0) and the second one at 76 Hz (0,0,1), meanwhile the acoustic cavities comprised between the battens display a first resonance at 76 Hz (0,0,1). By way of consequence, substantial effects of fluctuations around the mean values of the resonances frequencies associated with internal acoustic cavities are observable past 80 Hz. A slight influence of the uncertainties in regard to the first resonance associated with the 2 cm central air gap can be observed with respect to system 1 in the 40 Hz third octave band. Resulting confidence intervals are of comparable order than those associated with the structural system parameters.

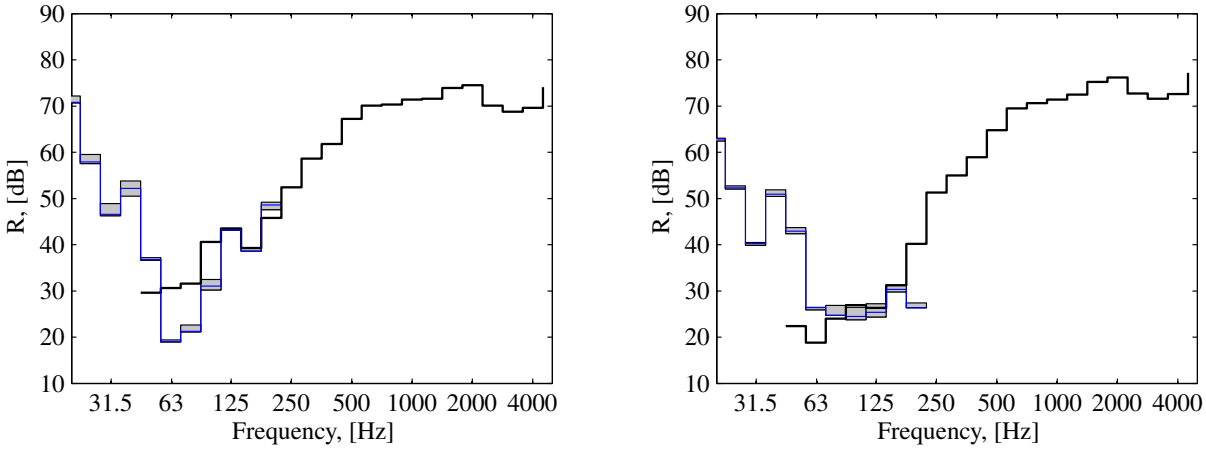

(a) System 2 (b) System 2

Figure 7.14: Sound reduction indices R. Confidence regions associated with a probability $P_c = 0.98$ for the indices R resulting from the nonparametric probabilistic approach associated with the internal acoustic cavities (grey areas); mean computational model (thin blue solid line); experimental measurements (thick black solid lines).

Uncertainties associated with the poroelastic medium Finally, the sensitivity of the sound reduction indices to statistical fluctuations within the generalized matrices associated with the poroelastic medium is analysed in the same way than for the internal acoustic cavities, using the nonparametric approach only. Let $\delta_{M_1^e}$, $\delta_{M_2^e}$, $\delta_{K_1^e}$ and $\delta_{K_2^e}$ respectively be the hyperparameters controlling the nonparametric statistical fluctuations within the random matrices $[\mathbf{M}_1^e]$, $[\mathbf{M}_2^e]$, $[\mathbf{K}_1^e]$ and $[\mathbf{K}_2^e]$ respectively associated with the static and frequency dependent parts of the equivalent fluid mass and stiffness matrices (according to the notations of Section 5.5.2). Values of $\delta_{M_1^e} = \delta_{M_2^e} = \delta_{K_1^e} = \delta_{K_2^e} = 0.3$ are arbitrarily chosen.

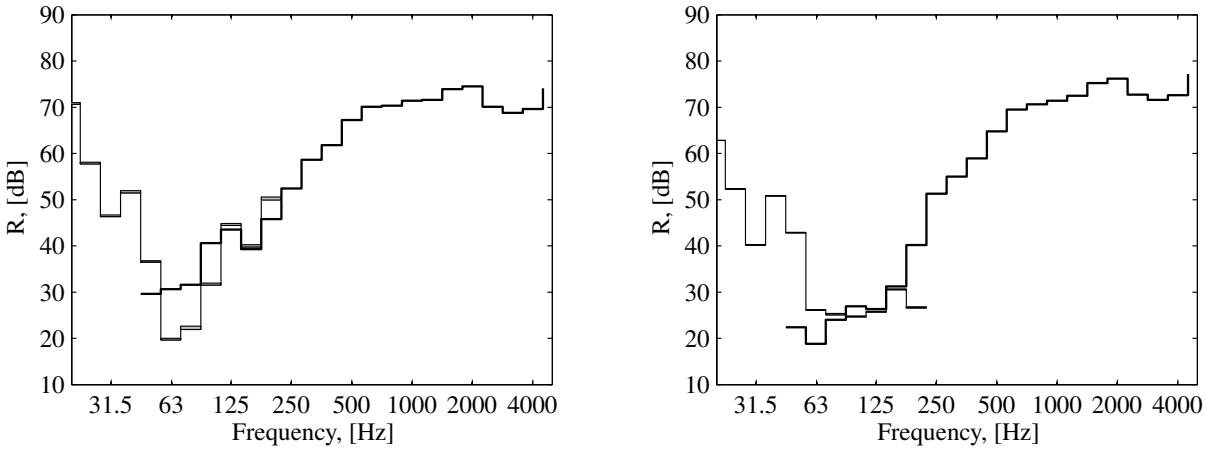

(a) System 1 (b) System 2

Figure 7.15: Sound reduction indices R. Confidence regions associated with a probability $P_c = 0.98$ for the indices R resulting from the nonparametric probabilistic approach associated with the poroelastic medium (grey areas); experimental measurements (thick black solid lines).

Figure 7.15 compares the confidence regions associated with a probability $P_c = 0.98$ for the sound reduction indices in third octave band resulting from such nonparametric probabilistic approach associated with the internal acoustic cavities. With respect to both systems, the statistical fluctuations introduced within the generalized matrices associated with this high modal density and high damping medium al-

most does not propagate to the sound reduction indices at low frequencies. Such result is consistent with experimental invetigations in [90], in which, all other things held constant, different insultating materials (close with respect to their physical properties) gave identical results below 300 Hz.

7.4 Conclusion

In this chapter, a methodology was presented in regard to the airborne sound insulation prediction of lightweight building systems in laboratory conditions. The laboratory rooms were modeled as uncoupled rigid parallelepiped acoustic cavities whose associated pressure disturbance fields were expanded on the classical analytical cosines basis. According to this model, it was emphasized how the performance can be single-handedly controlled by room modes. In order to improve the quality of the predictive model in regard to laboratory measurements, rigorous characterisation of the laboratory facilities is needed. Thus, as it was clear that reproductibility was an incompressible issue with respect to such evaluation procedure, a simple external excitation was constructed. Ensuing, the focus was set on the influence of the uncertainties coming from the system itself, successively considering different probabilistic computational models constructed in order to analyse the sensitivity of the evaluated sound reduction indices to uncertainties respectively associated to the structure, internal acoustic cavities and poroelastic medium. All other things held constant, the predicted airborne sound insulation indices displayed a large band sensitivity to structural model uncertainties, resulting from a generalized probabilistic modeling in which the hyperparameters controlling the statistical fluctuatins were set to values consistent with previous experimental comparisons. In regard to the findings of Chapter 4, further reasearchs would have to be conducted with respect to the connections and more generally boundary conditions of such systems, in order to improve the quality of the prediction at low frequencies.

8

Impact sound insulation

Contents

8.1 Introduction

In this chapter, we introduce a computational model adapted to the evaluation of the impact sound insulation performance of diverse lightweight floor elements. Within laboratory conditions, the tested lightweight floor is placed over a receiving room and a standard tapping machine is used for the generation of a steady excitation in various positions. Then, microphones in the receiving room provide the spatial sampling of the sound pressure field in the receiving room used to evaluate the spatial and time average of the quadratic pressure field. A methodology consistent with the one presented in Chapter 7 will be used for the evaluation of the sound pressure level in the receiving room such that, in the following, the emphasis is put on the structural excitation, sequence of impacts resulting from the standard tapping machine [135, 141]. Motivations are dual, first of all the low insulation performance of the lightweight structures at low frequencies associated with the high levels of excitation spectrum for the standardised evaluation procedure makes the impact noise a delicate question [6, 7, 9, 10]. Moreover, as emphasized in [81, 93, 142], the impact force is structure dependent due to the interaction of the floor with the falling hammer and, consequently, an optimisation procedure with the objective of lowering the impact noise levels might have to consider a structure dependent excitation spectrum. In Chapter 6, probabilistic models were constructed within the framework of the generalized probabilistic approach of uncertainties, in order to obtain stochastic computational models able to propagate uncertainties to the observable of steady-state dynamical problems. A challenging problem is then to quantify the propagation, to the impact forces, of the uncertainties from the probabilistic model of the structure.

The excitation force spectrum, associated with the impact sequences, is constructed through a set of transient responses associated to the free response of the structure to punctual impacts. As the free response is considered and the impact time is short, the first elastic modes might not constitute a sufficient truncated basis for an accurate representation of the dynamic and a new stochastic reduced order computational model, statistically dependent on the one used for the steady-state problem, has to be introduced. Thus, from a set of Ritz-vectors well suited to the representation of the impact dynamic and mass orthogonalized with respect to the first elastic modes, a new reduced order probabilistic stochastic model is constructed for the impact problem. The explicit separation of the contributions from the first elastic modes and from the higher frequency modes allows to set the random operators, associated with the impact problem, dependent on the random variables from the steady-state stochastic computational model. The uncertainties from the different contributions can then be propagated to the force. It should be noted that this methodology is general and can be applied for the class of problems where the truncated basis of the first elastic modes has to be completed in order to obtain a sufficiently good representation of the dynamics (non-linear problems, etc..).

8.2 Model for the evaluation of impact noise level

In laboratory conditions, the floor is placed between two rooms, following the same principle than within the previous chapter with the only difference being the horizontal orientation of the evaluated system. As the name suggests, in regard to impact sound insulation the external excitation of the evaluated system is structural, opposite to the acoustical excitation used for airborne sound insulation. Thus, a tapping machine lays on top of the floor and hammers successively strike the walking surface. Hereinafter, the influence of the source room for the impact problem is neglected, the dynamical system is consequently constituted of the evaluated floor and a receiving room (Fig. 8.1) whose characteristic dimensions are $L_x^R \times L_y^R \times L_z^R$ for the receiving room and $L_x^F \times L_y^F$ for the floor. A decoupled approach consistent with the one presented in Chapter 7 is undertaken. The system is first submitted to an *ad hoc* structural external excitation, modeling the action of the tapping machine, which is constructed within the following paragraphs. Then, the displacement field on the boundary with the receiving room is computed, in the frequency domain, as a solution of a stochastic or deterministic steady-state computational model constructed according to Chapters 2, 5 or 6. Using the analytical eigenmodes of a rigid parallelepiped room and for appropriate damping within the receiving room, the spatial average of the

quadratic pressure field can be evaluated according to Section 7.2.2. The resulting sound pressure level yields the so-called impact sound level L_I, which is then normalized with respect to the acoustical damping in the receiving room, using the measured reverberation time, according to [141]. The normalized impact sound level is then written as

$$L_n = L_I + 10 \log_{10}\left(\frac{A}{A_0}\right) , \tag{8.1}$$

where A denote the acoustic equivalent absorption area as defined in Section 7.1 and $A_0 = 10$ m^2. Eventually, the impact sound insulation performance of the floor system can be rated according to [143].

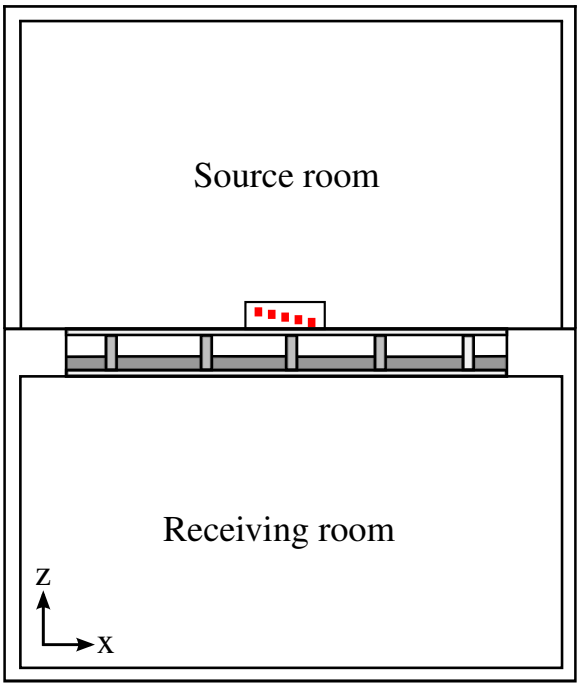

Figure 8.1: Evaluation conditions of a floor. The five hammers of the standard tapping machine placed on top of the floor hit the system periodically.

8.3 Model for the tapping machine excitation force

The following description of the standard tapping machine can be found in [93, 135, 142]. The measurement configuration is such that five equally spaced hammers of mass $M_h = 0.5$ kg hit the structure along a 40 cm line after a free fall from a $h_f = 4$ cm height. Each hammer strikes the floor with the velocity $v_0 = \sqrt{2gh_f} = 0.886$ m/s (standard acceleration du to gravity $g = 9.81$ m.s^{-2}) at a given time period $T = 0.5$ s and with a time shift from the previous one of $\Delta T = 0.1$ s. By way of consequence, the force time signal $f_h(t)$ resulting from a periodic impact from the hammer h can be expanded using a complex Fourier series such that

$$f_h(t) = \sum_{n=-\infty}^{+\infty} f_n^h \, \mathrm{e}^{i2\pi\frac{n}{T}t} , \tag{8.2}$$

in which

$$f_n^h = \frac{1}{T}\int_0^T f_h(t) \, \mathrm{e}^{-i2\pi\frac{n}{T}t} \mathrm{d}t . \tag{8.3}$$

The Fourier transform and inverse Fourier transform are defined with the convention

$$\hat{f}(\omega) = \int_{-\infty}^{+\infty} f(t) \, \mathrm{e}^{-i\omega t} \mathrm{d}t \quad \text{and} \quad f(t) = \int_{-\infty}^{+\infty} \hat{f}(\omega) \, \mathrm{e}^{i\omega t} \mathrm{d}\omega , \tag{8.4}$$

and, consequently, coefficients of the Fourier series are directly resulting from the Fourier transform of a single impact time signal divided by the time period T. According to Eq. (8.2), the spectrum $\hat{f}_h$ of the periodic impact force for the hammer h is written as

$$\hat{f}_h(\omega) = \sum_{n=-\infty}^{+\infty} f_n^h \, \delta(\omega - \omega_n) \, , \tag{8.5}$$

in which $\omega_n = 2\pi\frac{n}{T}$ and $\delta(\cdot)$ denotes the Dirac distribution. Let $\mathbb{E}_h$ be the vector of $\mathbb{R}^{N_S}$ that has null elements but 1 on the line corresponding to the degree of freedom impacted by the hammer h. Given the single impact force spectrum Eq. (8.5), the vector resulting from the finite element discretization of the external excitation field, in the physical coordinates and in the frequency domain, associated with the five hammers, is then written as

$$\mathbb{F}^{\mathrm{s}}(\omega) = \sum_{h=0}^{4} \hat{f}_h(\omega) \mathrm{e}^{-i\omega h \Delta T} \mathbb{E}_h \, . \tag{8.6}$$

In order to determine the Fourier series coefficients, a transient analysis following an impact of the hammer h is performed and the time signal of the impact force is computed for $0 \leq t \leq T$. The dynamical system consists in the structure only with the mass added by the hammer h during the contact period. The latter is written, in the physical coordinates, as

$$[\Delta\mathbb{M}_h^{\mathrm{s}}] = M_h \, \mathbb{E}_h \mathbb{E}_h^{\mathrm{T}} \, . \tag{8.7}$$

For any $t \geq 0$ the mean finite-element model of the elastic structure subjected to a single impact of the mass M_h at the velocity v_0 is then written, in the physical coordinates and in the time domain, as

$$([\mathbb{M}^{\mathrm{s}}(\mathbf{p})] + [\Delta\mathbb{M}_h^{\mathrm{s}}]) \, \ddot{\mathbb{U}}^{\mathrm{s}}(t) + [\mathbb{D}^{\mathrm{s}}(\mathbf{p})] \, \dot{\mathbb{U}}^{\mathrm{s}}(t) + [\mathbb{K}^{\mathrm{s}}(\mathbf{p})] \, \mathbb{U}^{\mathrm{s}}(t) = \mathbf{0} \, , \tag{8.8}$$

The initial displacement and velocity vectors at the time $t = 0$ of the impact are

$$\dot{\mathbb{U}}^{\mathrm{s}}(0) = v_0 \mathbb{E}_h \, , \tag{8.9}$$

$$\mathbb{U}^{\mathrm{s}}(0) = \mathbf{0} \, . \tag{8.10}$$

After the impact the system is freely evoluting from the kinematical initial conditions. An unconditionnaly stable Newmark scheme (see for example [116]) is used for the direct numerical integration of the equations with a time step Δt and the simulation is stopped at the time t_{cut}, corresponding to n_{step}, of the first zero-crossing of the acceleration at the impact point. Indeed, the null acceleration at the impact point means that the hammer is projected away from the system. The impact force time signal is then obtained by isolating the hammer such that

$$\begin{cases} f_{cut}^h(t) = \mathbb{E}_h^{\mathrm{T}} \, [\Delta\mathbb{M}_h^{\mathrm{s}}] \, \ddot{\mathbb{U}}^{\mathrm{s}}(t), \; 0 \leq t \leq t_{cut} \\ f_{cut}^h(t) = 0, \; t > t_{cut} \end{cases} \, . \tag{8.11}$$

Thus, Fig. 8.2 displays two examples of impact force time signals with respect to impacts performed on different points of the floor treated within the application case Section 8.5. Thick solid lines denote the time signal before t_{cut} that will be used to compute de Fourier series coefficients using Eq. (8.3). Without dwelling too much on the discussion of such results, it can be seen that the impact on top of a joist, closer to an elastic impact, displays higher magnitude and shorter impact time than the impact between two joists. Furthermore, with decreasing impact time getting closer and closer to a perfect impulse, a large band frequency excitation can be expected. Such observations are consistent with the results presented in [142] for example. It should be noted that the present model assumes that the system is at rest by the time of the impacts. In [144], the effect of an initial velocity of the floor, due to the standing waves resulting from the steady excitation, is investigated. However, the proposed model remain dependent on an *a priori* knowledge of the input mobilities of the system. An association of the present method to the approach introduced in [144] could constitute a straight follow up but is not considered in this work.

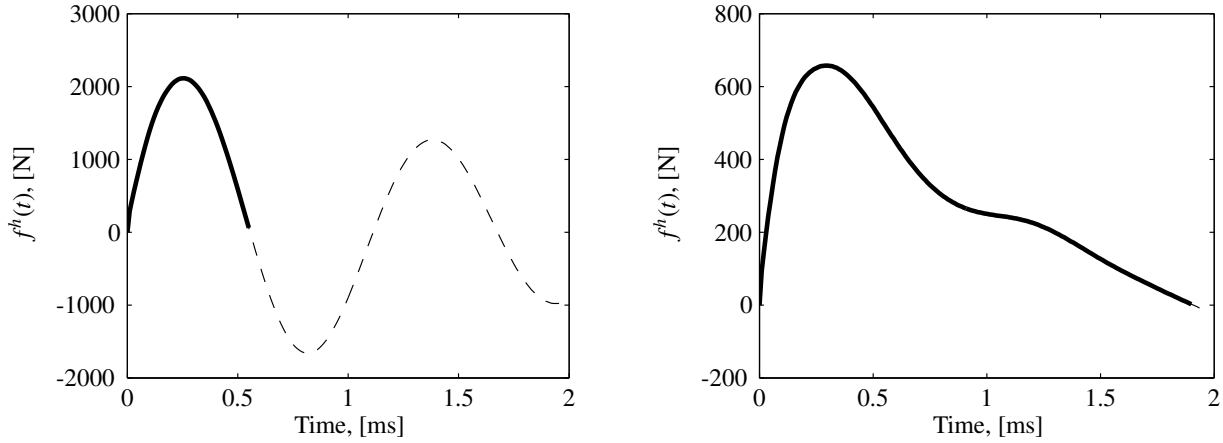

(a) Impact on top of joist

(b) Impact between two joists

Figure 8.2: Time history of the impact force, the thick solid lines denote the kept time signals before t_{cut}.

8.3.1 Probabilistic model for the external excitation resulting from the tapping machine

According to the the approach presented in the previous paragraph, it is clear that the constructed external excitation depends on the structure. In Chapter 6, stochastic computational models were constructed using generalized structural matrices projected on a truncated basis constituted of the first elastic modes. In the present case, as the free response of the system is involved, the first elastic modes might not constitute a sufficient basis to describe the dynamics of the structure during the impact time. Thus, Fig. 8.3 shows the magnitudes of the normal displacement fields resulting from one impact on top of a joist (denoted by the horizontal bars) and one impact in the middle of a particle board between to joists, according to the computational model defined by Eqs. (8.8) to (8.10). It can be seen that during such short impact time, deformations remain localized in the sense that bending waves have yet to travel back to the impact points. It should be noted that such displacement fields are associated with one single impact, during the short time where the hammer is in contact with the structure, and not with a steady excitation.

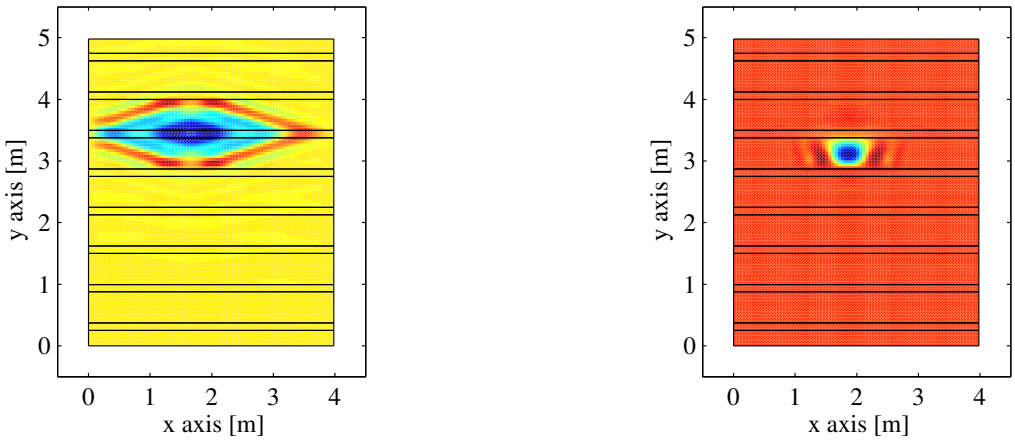

(a) Impact on top of a joist

(b) Impact between two joists

Figure 8.3: Magnitude of the normal displacement fields on top of the floor, at the time $t = t_{cut}$, for different impact locations (colors are chosen for contrast and do not imply any order comparison between both figures).

The problematic is consequently the following: probabilistic models are constructed for the steady-state problem in the frequency domain, using generalized structural matrices projected on the first elastic modes. However, such basis cannot be used for the propagation of the structural uncertainties to the single impact forces resulting from a transient analysis. Then, a methodology to translate the statistical information from the steady-state random generalized matrices to a stochastic reduced order model suited to the transient impact analysis is needed. First of all, such methodology requires the definition of a new reduced order computational model suited to the impact dynamics.

Mean reduced order computational model for the impact problem

Hereinafter we derive a set of *ad hoc* Ritz-vectors, suited for a good representation of the dynamics during the impact time. This projection basis is extracted from the proper orthogonal decomposition (see [145] for a review in regard to non-linear applications) of a set of nodal displacement vectors solutions of the transient problem defined by Eq. (8.8) in the physical coordinates, with the initial conditions defined by Eqs. (8.9) and (8.10). It should be noted that any adequate set of vectors could be chosen, for example solutions from different set of problems. Then, a mass orthogonalization of the Ritz-vectors solutions of Eq. (5.1) with respect to the first elastic modes of the structure allows to discriminate the low and high frequency contributions to the displacement field.

From a preliminary resolution of Eq. (8.8) in the physical coordinates and for a given $\mathbf{p}$ in C_{par} let $[\mathrm{U}(\mathbf{p})]$ be the $(N_\mathrm{s} \times n_{step})$ real matrix whose columns are the n_{step} time realisations of the nodal displacement vector $\mathbb{U}^\mathrm{s}(t)$. We then introduce the following eigenvalue problem: find the eigenvectors $\mathbb{V}^\mathrm{s}_\alpha(\mathbf{p})$ respectively associated with the first N_pod largest eigenvalues $\mu^\mathrm{s}_\alpha(\mathbf{p})$ such that

$$[\mathrm{U}(\mathbf{p})]\,[\mathrm{U}(\mathbf{p})]^\mathrm{T}\,\mathbb{V}^\mathrm{s}_\alpha(\mathbf{p}) = \mu^\mathrm{s}_\alpha(\mathbf{p})\mathbb{V}^\mathrm{s}_\alpha(\mathbf{p})\;. \tag{8.12}$$

Let $[\mathcal{V}^\mathrm{s}(\mathbf{p})]$ be the $(N_\mathrm{s}\times n_{pod})$ matrix whose columns are the POD vectors $\mathbb{V}^\mathrm{s}_\alpha(\mathbf{p})$, orthogonal with respect to the usual Euclidian inner product and normalised such that $\langle \mathbb{V}^\mathrm{s}_\alpha(\mathbf{p}), \mathbb{V}^\mathrm{s}_\beta(\mathbf{p})\rangle = \delta_{\alpha\beta}$. The vectors $\mathbb{V}^\mathrm{s}_\alpha(\mathbf{p})$ constitute an orthonormal family of vectors for $\mathbb{R}^{N_\mathrm{s}}$ and we have the following approximation

$$\mathbb{U}^\mathrm{s}(t) \simeq \sum_{\alpha=1}^{n_{pod}} \mathbb{V}^\mathrm{s}_\alpha(\mathbf{p}) r_\alpha(t)\;. \tag{8.13}$$

We then introduce the vectors $\tilde{\mathbb{V}}^\mathrm{s}_\alpha(\mathbf{p})$, orthogonal to the N_e first elastic structural modes $\mathbb{U}^\mathrm{s}_\beta(\mathbf{p})$, with respect to the inner product defined with respect to the mass matrix $[\mathbb{M}^\mathrm{s}(\mathbf{p})]$, such that

$$\tilde{\mathbb{V}}^\mathrm{s}_\alpha(\mathbf{p}) = \mathbb{V}^\mathrm{s}_\alpha(\mathbf{p}) - \sum_{\beta=1}^{N_e} \mathbb{U}^\mathrm{s}_\beta(\mathbf{p}) \left(\mathbb{U}^\mathrm{s}_\beta(\mathbf{p})^\mathrm{T}[\mathbb{M}^\mathrm{s}(\mathbf{p})]\mathbb{V}^\mathrm{s}_\alpha(\mathbf{p})\right)\;. \tag{8.14}$$

Let $[\tilde{\mathcal{V}}^\mathrm{s}(\mathbf{p})]$ be the $(N_\mathrm{s} \times n_{pod})$ matrix whose columns are the POD vectors $\tilde{\mathbb{V}}^\mathrm{s}_\alpha(\mathbf{p})$ mass orthogonalized with respect to the first elastic modes. The projection defined by Eq. (8.13) is rewritten as

$$\begin{aligned}\mathbb{U}^\mathrm{s}(t) &\simeq \sum_{\alpha=1}^{n_{pod}} \tilde{\mathbb{V}}^\mathrm{s}_\alpha(\mathbf{p}) r_\alpha(t) + \sum_{\alpha=1}^{n_{pod}} \left(\sum_{\beta=1}^{N_e} \mathbb{U}^\mathrm{s}_\beta(\mathbf{p}) \left(\mathbb{U}^\mathrm{s}_\beta(\mathbf{p})^\mathrm{T}[\mathbb{M}^\mathrm{s}(\mathbf{p})]\mathbb{V}^\mathrm{s}_\alpha(\mathbf{p})\right)\right) r_\alpha(t) \\ &= [\tilde{\mathcal{V}}^\mathrm{s}(\mathbf{p})]\mathbf{r}(t) + [\mathcal{U}^\mathrm{s}(\mathbf{p})][\mathrm{T}(\mathbf{p})]\mathbf{r}(t)\;,\end{aligned} \tag{8.15}$$

in which

$$[\mathrm{T}(\mathbf{p})] = [\mathcal{U}^\mathrm{s}(\mathbf{p})]^\mathrm{T}[\mathbb{M}^\mathrm{s}(\mathbf{p})][\mathcal{V}^\mathrm{s}(\mathbf{p})]\;. \tag{8.16}$$

Let $[\mathbb{Z}^\mathrm{s}(\mathbf{p})]$ denote any of the mass, damping or stiffness matrices in the physical coordinates. By projecting $[\mathbb{Z}^\mathrm{s}(\mathbf{p})]$ according to Eq. (8.15) we then have

$$\begin{aligned}[\mathcal{Z}^S(\mathbf{p})] =& [\mathrm{T}(\mathbf{p})]^\mathrm{T}[\mathcal{U}^\mathrm{s}(\mathbf{p})]^\mathrm{T}[\mathbb{Z}^\mathrm{s}(\mathbf{p})][\mathcal{U}^\mathrm{s}(\mathbf{p})][\mathrm{T}(\mathbf{p})] + [\tilde{\mathcal{V}}^\mathrm{s}(\mathbf{p})]^\mathrm{T}[\mathbb{Z}^\mathrm{s}(\mathbf{p})][\tilde{\mathcal{V}}^\mathrm{s}(\mathbf{p})] \\ &+ [\mathrm{T}(\mathbf{p})]^\mathrm{T}[\mathcal{U}^\mathrm{s}(\mathbf{p})]^\mathrm{T}[\mathbb{Z}^\mathrm{s}(\mathbf{p})][\tilde{\mathcal{V}}^\mathrm{s}(\mathbf{p})] + [\tilde{\mathcal{V}}^\mathrm{s}(\mathbf{p})]^\mathrm{T}[\mathbb{Z}^\mathrm{s}(\mathbf{p})][\mathcal{U}^\mathrm{s}(\mathbf{p})][\mathrm{T}(\mathbf{p})]\;.\end{aligned} \tag{8.17}$$

In the case where $[\mathbb{Z}^s(\mathbf{p})]$ denotes $[\mathbb{M}^s(\mathbf{p})]$ the mass matrix of the system without the additional hammer mass, Eq. (8.14) implies that $[\mathbb{Z}^s(\mathbf{p})]$ verifies

$$[\tilde{\mathcal{V}}^s(\mathbf{p})]^T[\mathbb{Z}^s(\mathbf{p})][\mathcal{U}^s(\mathbf{p})][\mathrm{T}(\mathbf{p})] = [0] \,, \tag{8.18}$$

$$[\mathrm{T}(\mathbf{p})]^T[\mathcal{U}^s(\mathbf{p})]^T[\mathbb{Z}^s(\mathbf{p})][\tilde{\mathcal{V}}^s(\mathbf{p})] = [0] \,. \tag{8.19}$$

In the case where $[\mathbb{Z}^s(\mathbf{p})]$ denotes $[\mathbb{K}^s(\mathbf{p})]$ the stiffness matrix of the system, the association of Eq. (5.1) and Eq. (8.14) leads once again to Eqs (8.18) and (8.19). In the case where $[\mathbb{Z}^s(\mathbf{p})]$ denotes $[\mathbb{D}^s(\mathbf{p})]$ the damping matrix of the system and the associated damping model (Kelvin-Voigt for example) is such that $[\mathbb{D}^s(\mathbf{p})]$ is a linear combination of $[\mathbb{M}^s(\mathbf{p})]$ and $[\mathbb{K}^s(\mathbf{p})]$ then the cross coupling terms nullify again. Let denote $[\tilde{Z}^s(\mathbf{p})] = [\tilde{\mathcal{V}}^s(\mathbf{p})]^T[\mathbb{Z}^s(\mathbf{p})][\tilde{\mathcal{V}}^s(\mathbf{p})]$, we then have

$$[\mathcal{Z}^S(\mathbf{p})] = [\mathrm{T}(\mathbf{p})]^T[Z(\mathbf{p})][\mathrm{T}(\mathbf{p})] + [\tilde{Z}^s(\mathbf{p})] \,, \tag{8.20}$$

where $[Z(\mathbf{p})]$ is any of the generalized mass, damping or stiffness structural matrices from the steady-state reduced order computational models defined in Section 5.6.

Stochastic reduced order computational model for the impact problem

The uncertain generalized matrices $[\mathcal{Z}^S(\mathbf{p})]$, $[Z(\mathbf{p})]$ and $[\tilde{Z}^s(\mathbf{p})]$ are respectively modeled by the random matrices $[\boldsymbol{\mathcal{Z}}^s]$, $[\mathbf{Z}^s]$ and $[\tilde{\mathbf{Z}}^s]$. The probabilistic model of random matrix $[\mathbf{Z}^s]$ was previously constructed according to Section 6.3. Let $[\tilde{\mathbf{G}}_m]$ be a random matrix with values in $\mathbb{M}_m^+(\mathbb{R})$ and constructed according to Section 6.3. The nullspace of $[\tilde{\mathcal{V}}^s(\mathbf{p})]$ is by construction reduced to $\mathbf{0}$ and $[\tilde{Z}(\mathbf{p})]$ has the same nullspace than $[\mathbb{Z}^s(\mathbf{p})]$. Therefore it exists a factorization of $[\tilde{Z}^s(\mathbf{p})]$ such that

$$[\tilde{Z}^s(\mathbf{p})] = [\tilde{B}^s(\mathbf{p})]^T[\tilde{B}^s(\mathbf{p})] \,, \tag{8.21}$$

where $[B^s(\mathbf{p})]$ is a $(m \times n_s)$ matrix and m is the rank of $[\tilde{Z}^s(\mathbf{p})]$. The generalized probabilistic model of the random matrix $[\tilde{\mathbf{Z}}^s]$ is then written as

$$[\tilde{\mathbf{Z}}^s] = [\tilde{B}^s(\mathbf{P})]^T[\tilde{\mathbf{G}}_m][\tilde{B}^s(\mathbf{P})] \,. \tag{8.22}$$

Associating Eqs. (6.11) and (8.22) the generalized probabilistic model of the random matrix $[\boldsymbol{\mathcal{Z}}^s]$ is written as

$$[\boldsymbol{\mathcal{Z}}^s] = [\mathrm{T}(\mathbf{P})]^T[\mathbf{Z}^s][\mathrm{T}(\mathbf{P})] + [\tilde{\mathbf{Z}}^s] \,. \tag{8.23}$$

Such probabilistic model consequently depends on the random vector of the system parameters $\mathbf{P}$ as well as on two sets of hyperparameters $(\delta_{M^s}, \delta_{D^s}, \delta_{K^s})$ and $(\delta_{\tilde{M}^s}, \delta_{\tilde{D}^s}, \delta_{\tilde{K}^s})$ respectively associated with nonparametric modeling of uncertainties constructed on the generalized matrices projected on the first elastic modes or first mass-orthogonalized POD vectors.

By projecting Eqs. (8.8), (8.9) and (8.10) according to Eq. (8.15) and using the generalized probabilistic modeling of uncertainties defined by Eq. (8.23) yields the following stochastic reduced order model, suited to the impact dynamics and statistically dependent on the random variables from the steady-state computational model

$$([\boldsymbol{\mathcal{M}}^s] + [\Delta\mathcal{M}^s(\mathbf{P})])\ddot{\mathbf{R}}^s(t) + [\boldsymbol{\mathcal{D}}^s]\dot{\mathbf{R}}^s(t) + [\boldsymbol{\mathcal{K}}^s]\mathbf{R}^s(t) = \mathbf{0} \,, \tag{8.24}$$

$$\dot{\mathbf{R}}^s(0) = [\mathcal{V}^s(\mathbf{P})]^T v_0 \mathbb{E}_h \,, \tag{8.25}$$

$$\mathbf{R}^s(0) = \mathbf{0} \,, \tag{8.26}$$

where $\mathbf{R}^s(t)$ is a complex vector valued random variable. After resolution, the random impact force time signal is written as

$$\begin{cases} F^h_{cut}(t) = \mathbb{E}_h^T[\Delta\mathbb{M}_h^s][\mathcal{V}^s(\mathbf{P})]^T\ddot{\mathbf{R}}^s(t), \ 0 \le t \le t_{cut} \\ F^h_{cut}(t) = 0, \ t > t_{cut} \end{cases} . \tag{8.27}$$

According to Eq. (8.3), we then obtain the random Fourier series coefficients

$$F_n^h = \frac{1}{T}\hat{F}_{cut}^h(\omega_n) \, , \tag{8.28}$$

and the random force spectrum for one impact of the hammer h

$$\hat{F}_h(\omega) = \sum_{n=-\infty}^{+\infty} F_n^h \, \delta(\omega - \omega_n) \, . \tag{8.29}$$

Finally, the random external excitation force vector associated with the whole tapping machine, statistically dependent on the random variables from the stochastic steady-state problems introduced in Section 6.2, is written as

$$\mathbf{F}^{\mathrm{s}}(\omega) = [\mathcal{U}^{\mathrm{s}}(\mathbf{P})]^{\mathrm{T}} \sum_{h=0}^{4} \hat{F}_h(\omega) \mathrm{e}^{-i\omega h \Delta T} \mathbb{E}_h \, . \tag{8.30}$$

8.3.2 Concluding remarks about the approach

In the previous section, an approach was presented for the construction of the steady external excitation resulting from the action of the tapping machine on the evaluated floor. In the case where uncertainties are associated with the structure, the external excitation consequently becomes a random variable statistically dependent on the uncertainties of the structure. The generalized probabilistic approach of uncertainties was chosen in order to model those uncertainties with respect to steady-state problems in the frequency domain. A methodology is then introduced for the construction of a probabilistic model of the external excitation which is statistically dependent on the latter.

For the sake of clarity, the proposed methodology for the prediction of impact sound level is briefly summarized. As a **first step**, successive transient problems respectively associated with each impact position and involving the structure only are solved in the physical coordinates. Thus, deterministic as well as probabilistic models for the external excitation associated with the whole tapping machine can be constructed according to Eqs. (8.3), (8.5) and (8.6) or Eqs. (8.28), (8.29) and (8.30). As a **second step**, the displacement field of the structure on the boundary with the receiving room is obtained as the solution of a steady-state computational model constructed according to Chapters 2, 5 or 6 with respect to the deterministic or random vibroacoustic evaluated system, using the aforementioned external excitation. As a **third step**, the receiving room is considered as an independent dynamical system. Then, the acoustical excitation of the receiving room is constructed from the displacement field of the structure on the boundary with the receiving room and the spatial average of the resulting quadratic sound pressure field can be evaluated in order to define the so-called impact sound level.

8.4 Validation of the computational model for the impact problem and uncertainty quantification

In this section, the computational model constructed for the determination of the spectrum associated with a single impact force, which consist in a transient problem with initial conditions, is validated using experimental measurements performed onto a simple lightweight structural assembly. Then, uncertainty quantification is undertaken, using the probabilistic model of the impact force proposed in Section 8.3.1, in order to evaluate the sensitivity of the impact forces to structural system parameters uncertainties as well as to model uncertainties. In particular, the aim is to determine the sensitivity of impact forces to model uncertainties whose probabilistic models were constructed, within the framework of stochastic steady-state problems in the frequency domain, unsing the nonparametric approach of uncertainties and the mean generalized mass, damping and stiffness matrices projected on the first elastic modes.

8.4.1 Experimental validation of the computational model for a simple lightweight system

The simple assembly of one oriented strand board on top of beams that was treated in Section 4.3.2 is considered and single impacts are performed manually using a hammer of mass $M_h = 0.31$ kg. The time signals of the force on two points of the structure are recorded and compared to those issued from the computational model defined by Eqs. (8.8) to (8.10). The different nominal physical properties are given in Tables 4.5 and 4.4 and the identified mounting parameters are given in Table 4.6. Impact points are displayed on Fig 8.4 and their coordinates are given in Table 4.7. Furthermore, as impacts are performed manually, the initial velocity is a free parameter and was sought to best match the measurements. In regard to the impact on point 1 we then have $v_0 = 0.38$ m/s and for the impact on point 2 we have $v_0 = 0.50$ m/s.

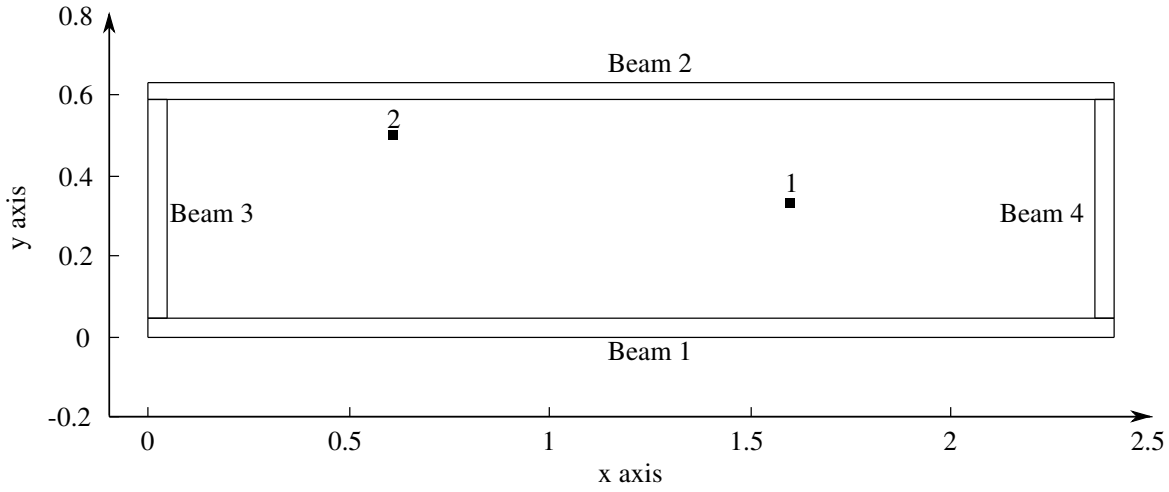

Figure 8.4: Assembly of one oriented strand board on top of wooden beam elements. Impact points (black squares).

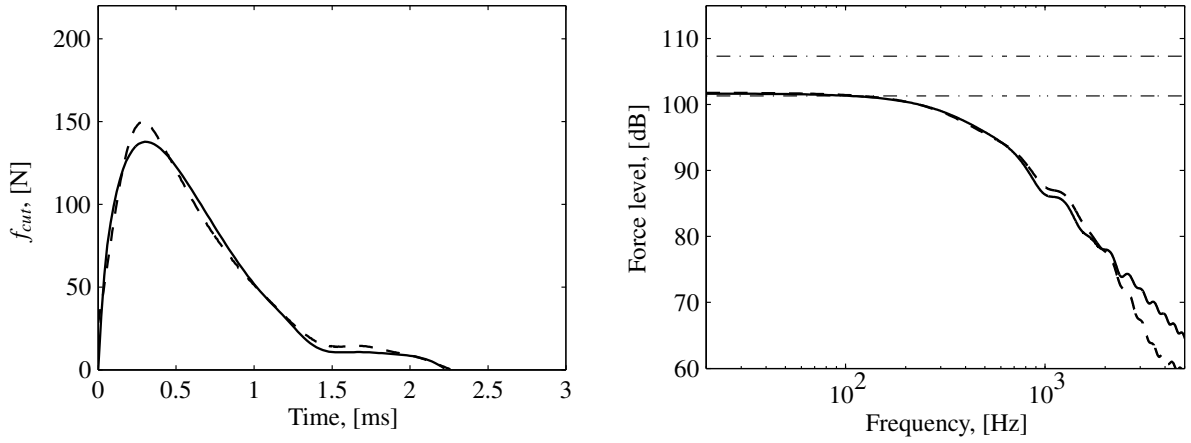

(a) Time domain

(b) Frequency domain

Figure 8.5: Impact point 1: (a) Force time signal. Experimental measurements (thin black dashed line); computational model (thin black solid line). (b) Impact force level in the frequency domain (ref. 10^{-6} N). Experimental measurements (thin black dashed line); model (thin black solid line); low frequencies theoretical bounds (thin dash-dot lines).

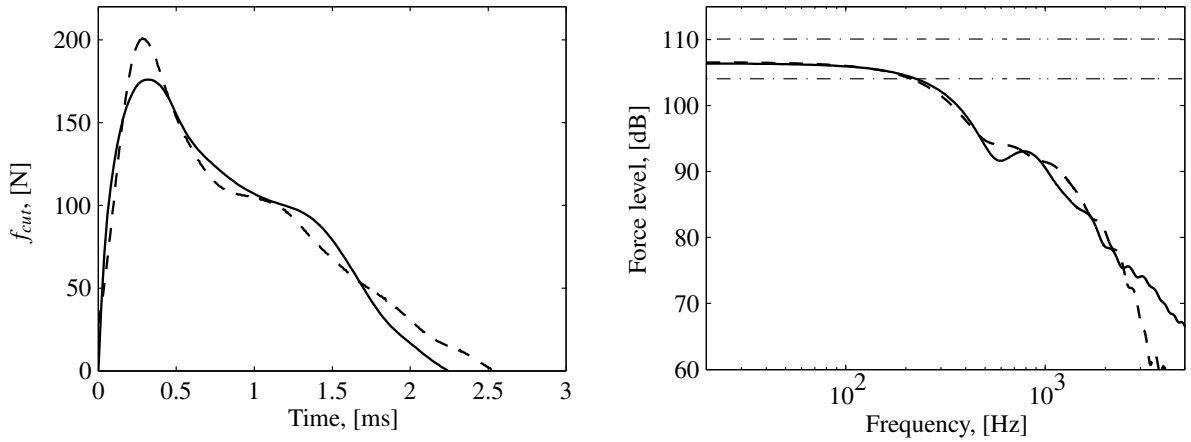

(a) Time domain

(b) Frequency domain

Figure 8.6: Impact point 2: (a) Force time signal. Experimental measurements (thin black dashed line); computational model (thin black solid line). (b) Impact force level in the frequency domain (ref. 10^{-6} N). Experimental measurements (thin black dashed line); model (thin black solid line); low frequencies theoretical bounds (thin dash-dot lines).

Impact force spectrum levels in the frequency domain displayed in Figs. 8.5 (b) and 8.6 (b), resulting from the Fourier transforms of the impact force time signals displayed in Figs. 8.5 (a) and 8.6 (a), clearly show that, with respect to the considered system, structural resonances do not control the response at low frequencies. Hence the expansion of the displacement field on the truncated basis of the first elastic modes defined by Eq. (5.2) is not sufficient for an accurate representation of the impact dynamics. Moreover, it can be seen that the prediction of the force spectrum is good up to 400 Hz, and enable to cover the whole frequency band of interest for the steady-state problems introduced in Chapter 2.

Minimum and maximum momentum variations, respectively $M_h v_0$ for an impact without rebound and $2M_h v_0$ for an elastic impact, are used as the low frequency bounds for the impact force spectrum and displayed on Figs. 8.6 (b)(d). The impact on point 1 in the middle of the oriented strand board almost corresponds to an impact without rebound whereas the impact on point 2 closer to a beam, associated with lower mobility, is subjected to a rebound resulting in a higher impact force.

8.4.2 Uncertainty quantification

In this section, the objective is twofold. First, quantify the propagation, to the impact forces, of the structural uncertainties that were modeled in Chapter 6 with the generalized probabilistic approach of uncertainties, using the stochastic reduced order models introduced in Section 8.3 and suited to the impact problem. Then, the aim is to assess the ability of such stochastic reduced order models to take into account potential new sources of uncertainties, in particular associated with high frequency contributions to the impact forces.

Propagation of the uncertainties associated with the random generalized matrices from the steady-state stochastic computatinal model

In this paragraph, the oriented strand board as well as the beams are supposed uncertain. Moreover, it is assumed that model uncertainties induced by modeling errors propagate to the solutions of the steady-state problem in the frequency domain. Thus, a stochastic computational model is constructed using the generalized probabilistic approach of uncertainties. The nominal physical properties as well as the hyperparemeters associated with the system parameters probabilistic approach of uncertainties are taken from Section 6.5. Moreover, in regard to the nonparametric approach, values of $\delta_{M^s} = \delta_{D^s} =$

$\delta_{K^s} = 0.3$ are chosen, as they were previously shown as consistent with experimental measurements. The methodology introduced in Section 8.3 is used for the construction of the probabilistic model of the generalized matrices associated with the stochastic reduced order computational model suited to the impact problem, using the generalized mass, damping and stiffness matrices projected on the $n_s = 100$ first elastic modes (computed up to approximately 850 Hz) and on the $n_{pod} = 40$ first mass orthogonalized POD vectors.

First of all, nonparametric fluctuations are introduced in the generalized matrices projected on the first elastic modes only, in order to quantify the propagation of such uncertainties to the impact force. Hence a probabilistic model of the generalized operators used for the random transient problem written, according to the previous notations, as

$$[\mathcal{Z}^s] = [\mathrm{T}(\mathbf{P})]^{\mathrm{T}}[\mathbf{Z}^s][\mathrm{T}(\mathbf{P})] + [\tilde{Z}^s(\mathbf{P})] \, . \tag{8.31}$$

Following, Fig. 8.7 displays the confidence regions associated with a probability $P_c = 0.98$, using 800 Monte Carlo simulations, for the impact force levels on point 1 and 2, in the frequency domain. Thus, at low frequencies, the sensibility of the force spectrum to fluctuations within the generalized matrices projected on the first elastic modes is negligible with respect to the sensibility to mobility disparities due to the proximity of stiffeners for example. In this class of impact problems, the impact time is in fact too short and structures too larges for standing waves to appear and contribute to the dynamics.

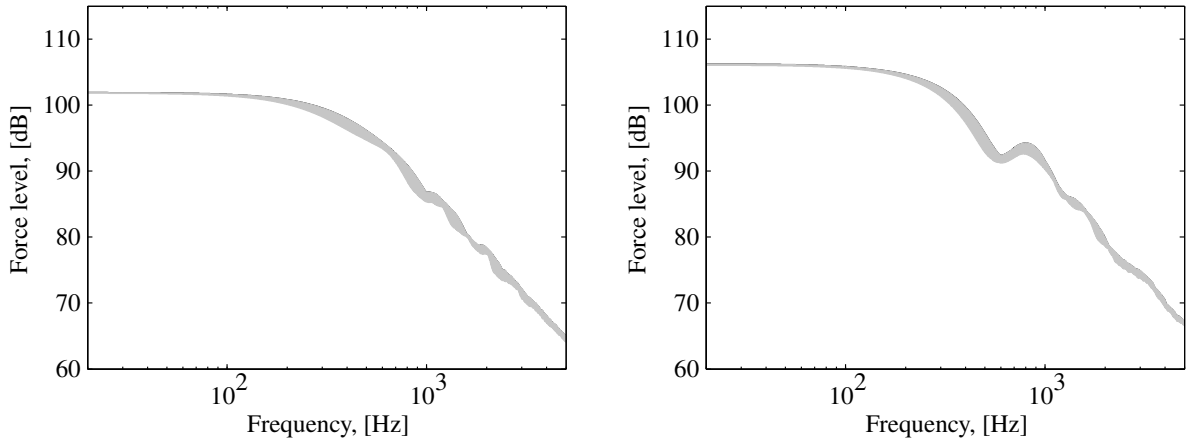

(a) Impact on point 1

(b) Impact on point 2

Figure 8.7: Confidence intervals associated with a probability $P_c = 0.98$ for the single impact force spectrum levels over frequency (ref. 10^{-6} N).

Propagation of the uncertainties associated with the random generalized matrices projected on the first POD vectors

In a second stage, nonparametric flucuations are introduced in the generalized operators projected on the first mass-orthogonalized POD vectors only. Hence a probabilistic model of the generalized operators used for the random transient problem written, according to the previous notations, as

$$[\mathcal{Z}^s] = [\mathrm{T}(\mathbf{P})]^{\mathrm{T}}[Z^s(\mathbf{P})][\mathrm{T}(\mathbf{P})] + [\tilde{\mathbf{Z}}^s] \, . \tag{8.32}$$

Then, Fig. 8.8 displays the confidence regions associated with a probability $P_c = 0.98$, using 800 Monte Carlo simulations, for the impact force level on point 1 and 2, in the frequency domain, resulting from for the probabilistic model constructed using the set of hyperparameters $\delta_{\tilde{M}^s} = \delta_{\tilde{D}^s} = \delta_{\tilde{K}^s} = 0.3$. It can be seen that the uncertainties on the generalized matrices projected on the first mass-orthogonalized POD vectors, whose range is spanned by the contributions of the high frequency modes excluding the

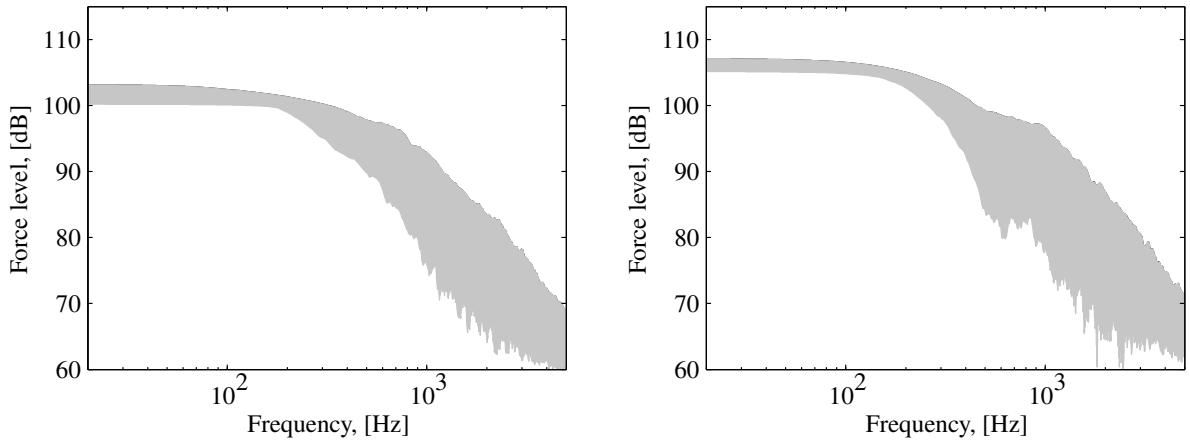

(a) Impact on point 1

(b) Impact on point 2

Figure 8.8: Confidence intervals associated with a probability $P_c = 0.98$ for the single impact force spectrum levels over frequency (ref. 10^{-6} N).

first elastic modes, propagate over the whole frequency range onto the force levels. Such probabilistic model would consequently be able, function of the problem, to quantify different phenomena associated with different frequency ranges. In particular, modeling errors can be expected due to the kinematic reduction inherent to shell elements or to the limits of the finite element model in its ability to include very high frequency contributions due to mesh restrictions. However, below 200 Hz it can be observed that confidence intervals remain centered around the impact spectra resulting from the nominal model. Thus, in the case of low frequency problems, an output-error probabilistic model might be more adequate, meanwhile in regard to medium frequencies, such approach could be of interest.

8.4.3 Concluding remarks about impact forces modeling

In this section, the computational approach proposed for the construction of impact force spectra was validated using experimental measurements. In a second stage, it was shown that system parameters uncertainties do not propagate to impact forces at low frequencies. The same applies to model uncertainties taken into account using a nonparametric approach of uncertainties associated with the generalized matrices projected on the first elastic modes. However, model uncertainties associated with high frequency contributions included in the range of the first POD vectors, and taken into account using a nonparametric approach, propagate to impact forces at low frequencies but remain centered around the mean values. Thus, the proposed model for which uncertainty propagation depends on the state of the computational model would be more adapted to medium frequency range problematics.

By way of consequence, in the following, the external excitation resulting from the tapping machine is considered as statistically independent of any steady-state stochastic computational models associated with the system. Moreover, as things currently stand and without additional information for the identification of hyperparameters $\delta_{\tilde{M}^s}$, $\delta_{\tilde{D}^s}$ and $\delta_{\tilde{K}^s}$, such external excitation is considered deterministic in the frequency band $\mathbb{B} = [10, 220]$ Hz of interest, in regard to any further application. The structural excitation resulting from the tapping machine is then constructed according to Section 8.3 in order to take into account the contrasts in mobilities over the floor for the determination of the force associated with each of the five hammers.

8.5 Application to a full scale lightweight floor system

In this section, nominal and stochastic computational models are constructed in regard to a typical lightweight floor, corresponding to the floor C1 from the standard [135]. Then, deterministic external excitations, associated with the tapping machine, are constructed according to the methodology defined in Section 8.3. Detailed measurements in regard to the response of a lightweight floor C1 to tapping machine excitation were performed by Fraunhofer-IBP in laboratory conditions, within the AcuWood project, and transmitted to the Silent Timber Build project partners. First of all, velocity levels over different points of the walking surface and ceiling were measured, using a unique known tapping machine position. Then, a standard impact sound level measurement was performed. For successive tapping machine positions, whose number and locations are unknown, sound pressure levels were measured in the receiving room and averaged in order to obtain a mean impact sound level.

8.5.1 Nominal system

Dimensions of the considered floor are L_x^F=3.98 m and L_y^F=4.98 m. According to [135], the C1 reference floor is constituted of a 22 mm thick particle board topping on top of 8 equally spaced (625 mm off center) wooden joists whose cross-sectional dimensions are 180 mm × 120 mm. Moreover, a 100 mm thick fibrous insulation material layer lays on 8 equally spaced battens (500 mm off center), perpendicularly oriented with respect to the joists and whose cross-sectional dimensions are 24 mm × 48 mm. Finally, the ceiling is constituted of 12.5 mm thick plasterboards screwed every 300 mm onto the battens. Schematic layout associated with such floor is depicted on Fig. 8.9.

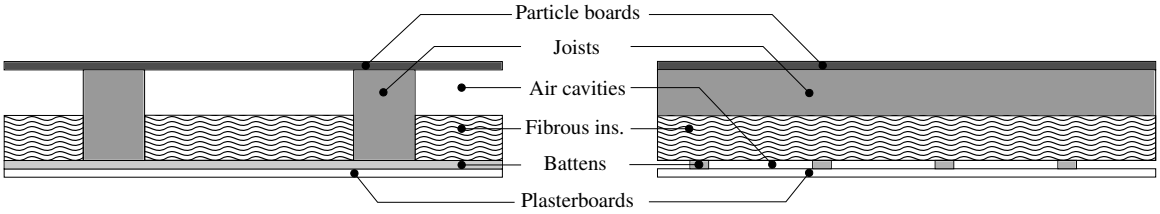

Figure 8.9: Schematic layout (left and right views) of a C1 floor according to [135].

Mean elasticity matrices for the particle boards, pine joists, wooden battens as well as plasterboards are constructed from the values identified in Chapter 3. However, mass density constraints are formulated in appendix C of [135] with respect to particle boards and plasterboards that cannot be fulfilled using the identified mass densities. Thus, the nominal values of 660 kg/m^3 and 800 kg/m^3 are respectively chosen for the latter. In Chapter 3 particle boards displayed a slight orthotropy, in particular the strongest bending direction was not the longitudinal direction of the boards. It is assumed that, in the present case, boards are mounted with the longitudinal direction perpendicular to the joists.

In regard to the fibrous insulation material, nominal parameters are given in Table 8.1, taken from [146] and verify the constraints in [135]. Such poroelastic properties correspond to a limp glass wool insulating material, hence a limp frame equivalent fluid modeling. In regard to boundary conditions, zero displacement is imposed on the edges of the boards while the joists are simply supported on their extremities. Particle boards are considered perfectly connected to the joists on their whole surface of contact. In Chapter 4, the bending wavelength was mentioned as a criterion for the validity of such hypothesis and, due to the high stiffness displayed by such thick boards, the assumption is justified. According to Eq. (4.4) one can estimate the transition frequency around 200 Hz. However, in regard to the plasterboard, and as the information of the nominal distance between the screws is available, point connections are assumed with the battens every 300 mm (transition frequency would be in that case around 100 Hz).

Mass density $(1-\phi)\rho^{p_s}$ [kg/m^3]	25
Porosity ϕ	0.96
Flow resistivity σ [N.s/m^4]	7500
Tortuosity α_∞	1.1
Viscous length Λ [μm]	50
Thermal length Λ' [μm]	150

(a) Poroelastic medium parameters.

Standard pressure P_0	1.015×10^5 Pa
Mass density ρ^F	1.21 kg/m^3
Heat capacity ratio γ	1.4
Sound velocity c_F	340 m/s
Prandtl number Pr	0.72
Dynamic viscosity η_f	1.81×10^{-5} N.s/m^2

(b) Air parameters.

Table 8.1: Poroelastic medium and air parameters.

8.5.2 Mean steady-state computational model

A mean steady-state computational models is constructed according to Section 2.5 for the steady-state problem in the frequency domain, with the poroelastic medium modeled as an equivalent fluid and suited to the frequency band $\mathbb{B} = [10, 220]$ Hz. Due to the limp frame equivalent fluid poroelastic modeling, the mesh criterion is chosen with respect to the Biot fluid borne wavevelength, equal to 54 cm at 220 Hz, in a similar way than within Section 7.3.2. Thus, a density of 12 elements per meter is chosen. In the particular cases of impact transient analysis used for the construction of the impact forces, involving high frequency modes, a refined mesh of the structure is created using 24 elements per meter. From compatible meshes of the different structural, acoustic and poroelastic components, the finite element method yields, in the physical coordinates, $N_s = 102020$ degrees of freedom for the structure, $N_f = 21310$ degrees of freedom for the internal acoustic cavities and $N_e = 11682$ degrees of freedom for the poroelastic medium modeled as an equivalent fluid with pressure as primary variable.

In order to obtain a reduced order computational model, the equations associated with the structure are projected on the truncated basis constituted of the $n_s = 400$ first elastic modes and constructed according to Section 5.2. It should be noted that due to long joist span, floor systems are naturally more flexible than walls and consequently display higher structural modal density and require a larger structural basis for an identical frequency range. Equations associated with the 18 internal acoustic cavities are projected on the truncated basis constituted of the first rigid cavity modes constructed according to Section 5.3 using a total of $n_f = 540$ acoustic eigenmodes. Finally the equations associated with the 9 poroelastic components, with respect to the limp frame equivalent fluid model, are projected on the truncated basis constructed according to Section 5.5 using a total of $n_{e,I} = 1125$ eigenmodes. Consequently, the dimension of the resulting reduced order computational models is 2065.

8.5.3 Stochastic steady-state computational model

A stochastic steady-state computational model is constructed, according to Section 6.2, using the generalized probabilistic approach of uncertainties. The mean values in regard to the structural system parameters are the aformentioned nominal values. Dispersion hyperparameters result from Chapter 6 and are recalled in Table 8.2. In a way which is consistent with the previous chapters, hyperparameters associated with the nonparametric modeling of uncertainties are set to $\delta_{M^s} = \delta_{D^s} = \delta_{K^s} = 0.3$ with respect to random mass, damping and stiffness structural matrices. Considering the prevailing structural transmission path and the results from the previous chapter, uncertainties are not considered in regard to acoustic or poroelastic components.

Pine beams		Particle board		Plasterboards 12.5	
δ_{E_l}	δ_ρ	δ_{ela}	δ_ρ	δ_{ela}	δ_ρ
0.08	0.065	0.08	0.007	0.15	0.009

Table 8.2: Dispersion hyperparameters with respect to each structural component.

8.5.4 Comparison with experimental measurements: velocity levels

For a steady structural excitation of the floor resulting from a single tapping machine position, whose hammers are depicted on depicted on Fig. 8.10, velocity measurements were performed at ten different positions: 6 on the floor walking surface (positions 1 to 6) and 4 on the ceiling (positions 7 to 10). Positions 1 to 4 are located on top of a joist whereas position 5 and 6 are located in between. Positions 7 and 9 correspond to the intersection of a batten and joists on the ceiling (position 9 being actually on a screw). Position 8 is located on a ceiling batten and position 10 below a joist but between battens.

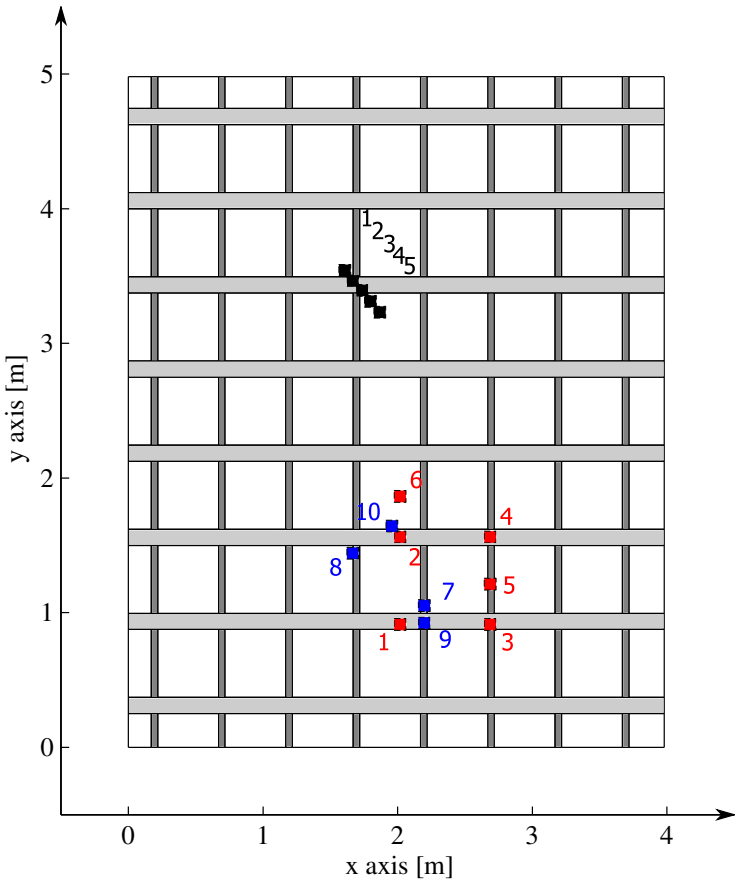

Figure 8.10: Top view of the C1 reference floor according to [135]. Joist and batten positions are resepctively denoted by the light and dark grey areas. Hammers (black squares); accelerometers on top of the floor (red squares); accelerometers on the ceiling (blue squares).

Definition of the external excitation for a single tapping machine position

A single tapping machine position, shown on Fig. 8.10, is used for the generation of a steady velocity field over the structure. Impact forces spectra associated with each hammer location, whose coordinates are given in Table 8.3, are then constructed according to Section 8.3. Thus, successive transient analyses involving the structure only are undertaken. For an initial velocity of the considered impact point, Fourier transform of the resulting impact force time signals yield the force spectra displayed on Fig. 8.11. It can be seen that impact forces are maximal on top of the joist, which is expected due to the associated low mobility, and sweep a 2.5 dB range at low frequencies. Past 300 Hz, it is quite clear that in regard to any extension of the present methodology to medium or high frequency range, the variations among impact forces due to the hammer positions would have to be carefully considered as discrepancies of impact forces among hammer positions quickly increase.

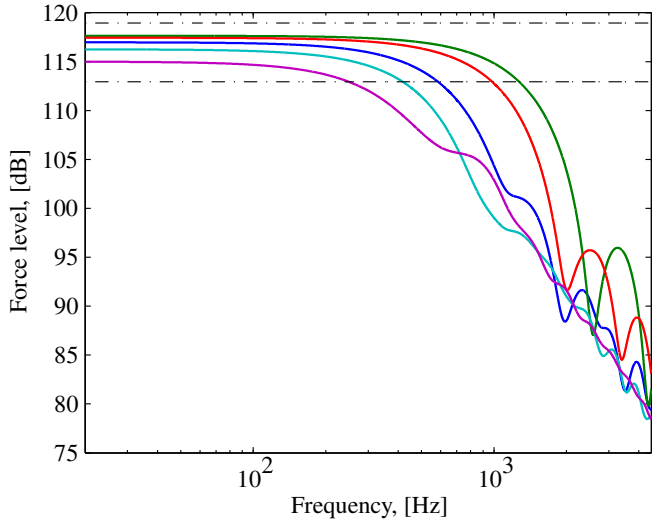

Figure 8.11: Force levels associated with the different impact points. Hammer 1 (thin blue solid line); hammer 2 (thin gree solid line); hammer 3 (thin red solid line); hammer 4 (thin cyan solid line); hammer 5 (thin magenta solid line); min. and max. momentum variations (thin black dash-dot lines).

	H1	H2	H3	H4	H5
x [m]	1.600	1.664	1.728	1.793	1.857
y [m]	3.530	3.453	3.377	3.300	3.224

Table 8.3: Hammers coordinates.

Velocity levels on various points of the system

From the knowledge of the impact force spectra, the vector of the external excitation in the physical coordinates can be constructed using Eqs. (8.3), (8.5) and (8.6) and the velocity field of the structure is obtained as the solution of the mean or stochastic steady-state computational model in the frequency domain. Thus, predicted velocity levels as well as confidence intervals for the velocity levels, respectively resulting from the mean computational model and the stochastic computational model, are compared with experimental values. Figures 8.12 and 8.13 respectively compare predicted and measured velocity levels on the particle boards (walking surface) and the plasterboards (ceiling) according to accelerometers positions given in Table 8.4 and displayed on Fig. 8.10.

	A1	A2	A3	A4	A5	A6	A7	A8	A9	A10
x [m]	2.010	2.010	2.680	2.680	2.680	2.010	2.190	1.660	2.190	1.660
y [m]	0.900	1.550	0.900	1.550	1.200	1.850	1.040	1.430	0.910	1.630

Table 8.4: Accelerometers coordinates.

First of all, it can be observed that deterministic as well as stochastic computational models are once again over stiffened with respect to the real system. Indeed, first structural resonances for the computational models are identified around 28 Hz whereas it can be seen that, in regard to the experimental system, high velocity levels exist down to 20 Hz. Moreover, the stochastic computational model, constructed using hyperparameters whether identified for similar materials with respect to probabilistic models associated with system parameters uncertainties, or shown consistent with experimental measurements with respect to probabilistic models associated with model uncertainties, is not able to take into account such level of modeling error around first structural modes. The present observations sug-

gest that an accurate prediction of the dynamical behavior of lightweight systems within the first third octave bands would necessit a particular attention towards boundary conditions. Other than that, it can be seen that besides the frequency band controlled by the first structural modes, relatively good orders of prediction with respect to velocity levels can be obtained.

As a side note, it should be specified that peaks respectively observed within the 12.5 and 20 Hz third octave bands with respect to the nominal computed velocity levels do not correspond to resonances of any sort, but in fact to the tapping machine 10 Hz overall impact frequency. From Eq. 8.6 it can be undestood that resulting from the impact frequency of 2 Hz associated with each hammer and the phase shift of 0.1 s between hammers, harmonic components of the excitation are in phase every 10 Hz, hence peaks in the otherwise static response of the system below the first structural resonance. Within experimental studies including measurements below 20 Hz and using the standard tapping machine [6, 7] such peaks can be guessed. A potential weak point of the standard evaluation procedure in regard to low frequencies might be enlightened, as unfortunate structural resonances of the evaluated system around 10, 20 or 30 Hz could result in a worse rating than maybe deserved.

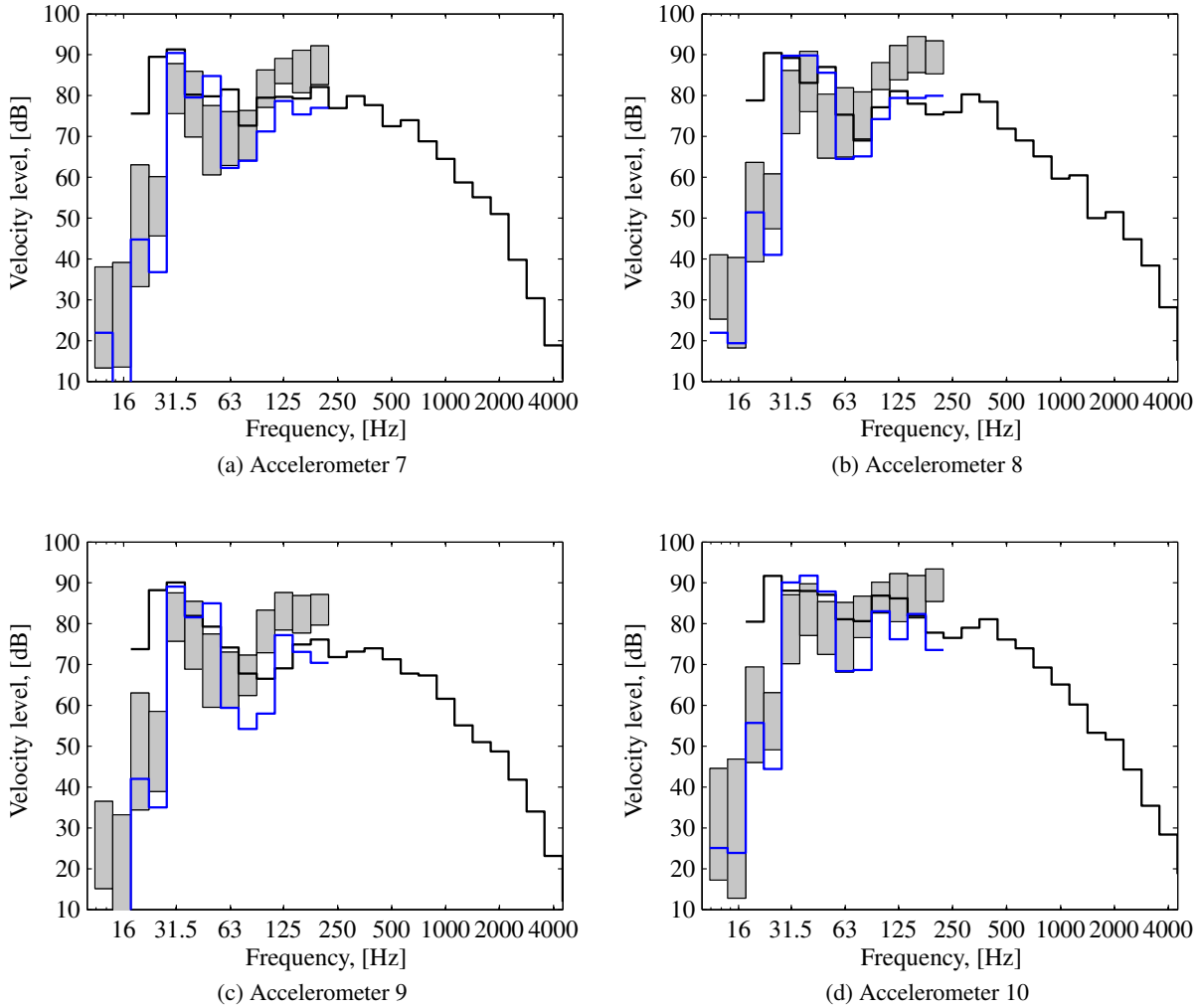

(a) Accelerometer 7

(b) Accelerometer 8

(c) Accelerometer 9

(d) Accelerometer 10

Figure 8.12: Velocity levels on the plaserboard (ref. 8.10^{-8} m/s). Mean computational model (thin blue solid line); confidence regions associated with a probability $P_c = 0.98$ resulting from the stochastic computational model (grey areas); experimental measurement (thin black solid line).

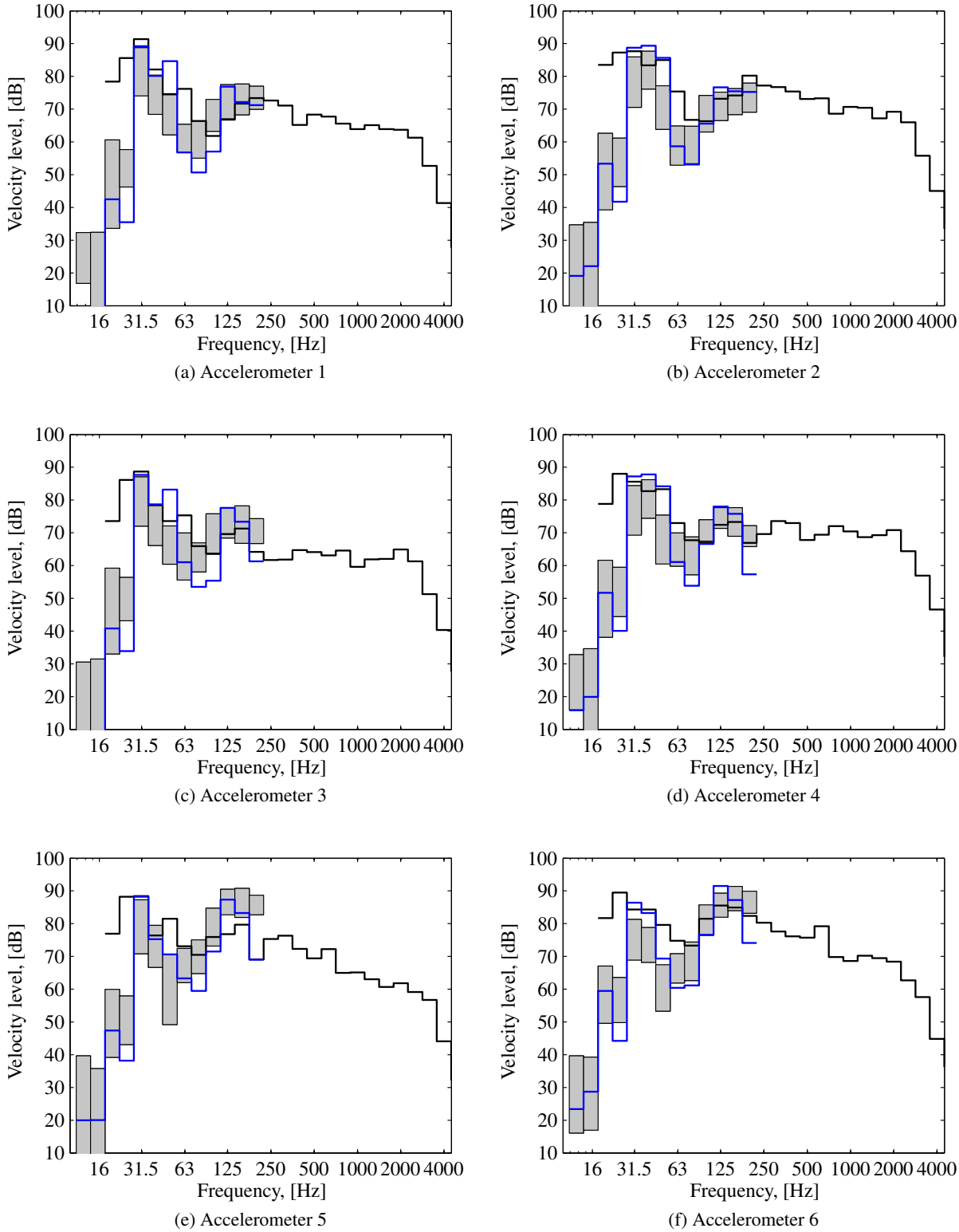

(a) Accelerometer 1 (b) Accelerometer 2

(c) Accelerometer 3 (d) Accelerometer 4

(e) Accelerometer 5 (f) Accelerometer 6

Figure 8.13: Velocity levels on the particle board (ref. 8.10^{-8} m/s). Mean computational model (thin blue solid line); confidence regions associated with a probability $P_c = 0.98$ resulting from the stochastic computational model (grey areas); experimental measurement (thin black solid line).

8.5.5 Comparison with experimental measurements: impact sound level

Methodology for the impact sound evaluation in laboratory conditions

The laboratory setup is such that the dimensions of the receiving room respectively are L_x^R=3.78 m, L_y^R=4.78 m and L_z^R=2.67 m. The floor, larger than the opening of the receiving room, is centered with respect to the latter. A mean reverberation time with respect to the receiving room was associated with the experimental data provided by the laboratory and is given in Table 8.5 for the third octave bands going from 20 to 250 Hz. Thus, it can be seen that the laboratory exhibits a substential amount of acoustical damping, inducing reverberation times inferior to 1 s past 50 Hz. Using Eq. 7.11, modal damping factors can be computed with respect to the room modes belonging to each third octave band. Then, with the knowledge of the structure displacement field on the boundary with the receiving room, the sound pressure level in the latter can be computed according to the decoupled room model introduced in Chapter 7. In particular, the sound pressure level in the receiving room is constructed using a sampling of the quadratic pressure field over the volume of the room excluding areas closer than 0.7 m from its boundaries.

T.o. band [Hz]	20	25	31,5	40	50	63	80	100	125	160	200	250
T_{60} [s]	2.17	1.76	1.41	1.39	0.87	0.46	0.33	0.53	0.47	0.51	0.60	0.52

Table 8.5: Mean reverberation time for the receiving room.

In order to be able to compare the impact sound performance associated with different designs there is a need to minimize the dependence of the result on the evaluation procedure. The position of the tapping machine has two direct consequences on the definition of the external excitation of the system. The first one is the dependence of the force magnitude on the mobility at the impact point. At low frequencies, a theoretical maximum discrepancy of 6 dB in the force magnitude, resulting from the difference between an impact with and without rebound, can be expected. In Section 8.5.4, a 2.5 dB maximum difference was observed at low frequencies. Such influence is consequently more of a prevailing issue when considering medium to high frequency range. The second one result from differences in the projection of the external excitation, function of its position, onto the structural mode shapes. Thus, such influence is mostly a concern in regard to the first structural modes and, by way of consequence, an issue at low frequencies. Indeed, within the framework of an optimisation problem for example, the position of the excitation could be determining for the outcome and, by way of consequence, standard measurements require multiple tapping machine positions and averages. In this work, 21 tapping machine positions are considered, such as depicted in Fig. 8.14. In [94], even if the formulation is quite different, 15 positions were used. It should be noted that the minimal number of positions required by the standard [141] is four. Hereinafter, the definition of the impact noise level L_I is then the mean level, computed according to Eq. (8.33), resulting from 21 different excitations of the evaluated floor.

$$L_I = 10 \log_{10} \left(\frac{1}{21} \sum_{j=1}^{21} 10^{L_{I,j}/10} \right) . \tag{8.33}$$

In order to illustrate the previous remarks about the dependence of the evaluated impact sound level on the position of the source, and in particular the low frequency issues associated with the projection of the external excitation onto modal shapes, Fig. 8.15 displays the $L_{I,j}$ associated with each of the 21 positions as well as the mean impact sound level resulting from the nominal computational model. Then, discrepancy of about 20 dB between extremum values is found within the 31.5 Hz third octave band, which includes the first structural resonances. Minimal values in such band correspond in fact to the tapping machine positions which are close to the center of the floor in the "y" direction. Considering modal shapes displayed in Fig. 8.16, it can be understood that those 6 tapping machine positions result in structural excitations that do not project that well onto the modal shape of the second structural mode,

hence a reduced transmission. Within higher third octave bands, 10 dB maximum differences are observed and a reduced number of excitations could be conceivable. Increasing dispersions due to high frequency issues, associated with varying mobilities over the system, are not observed yet.

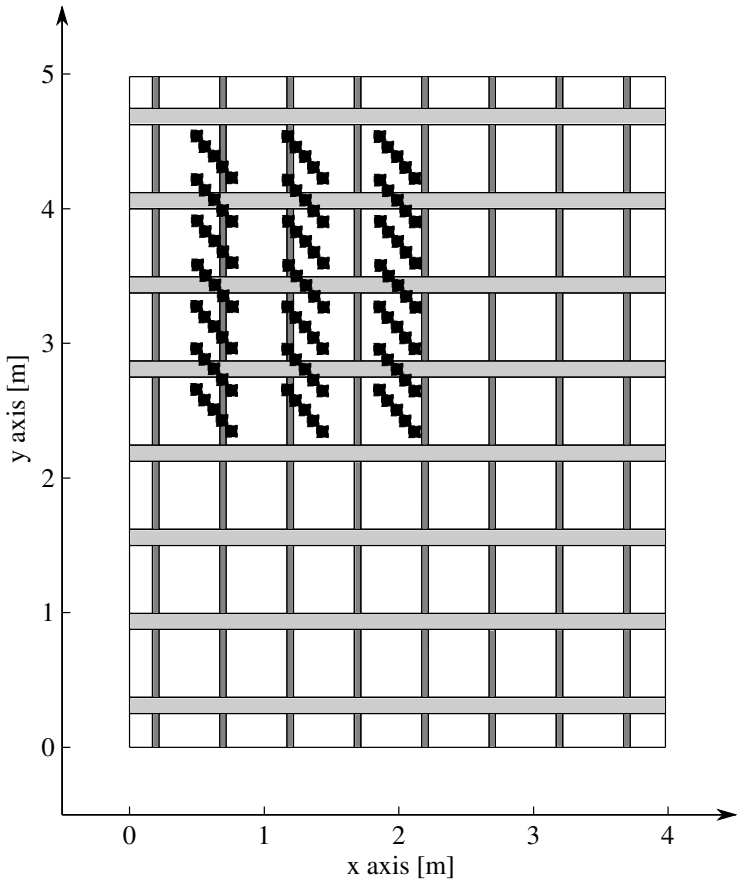

Figure 8.14: Top view of the C1 reference floor according to [135]. Joist and batten positions are respectively denoted by the light and dark grey areas. Hammers (black squares).

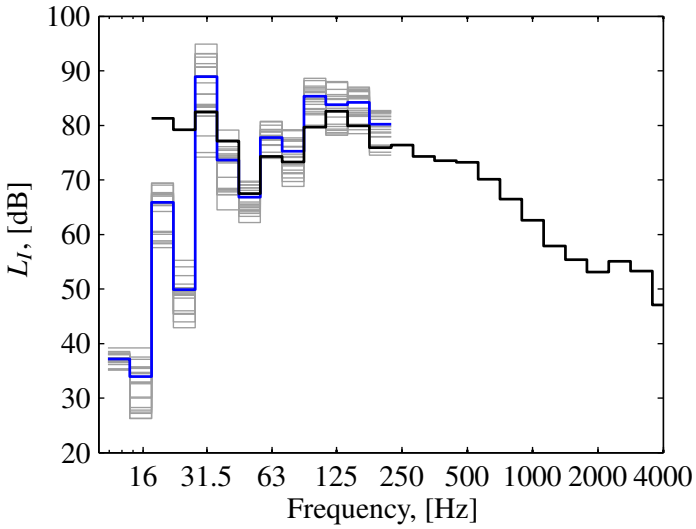

Figure 8.15: Impact sound levels. Solutions of the mean computational model (thin grey solid lines); mean value obtained from the 21 evaluations (thin blue solid line); mean experimental values (thin black solid line).

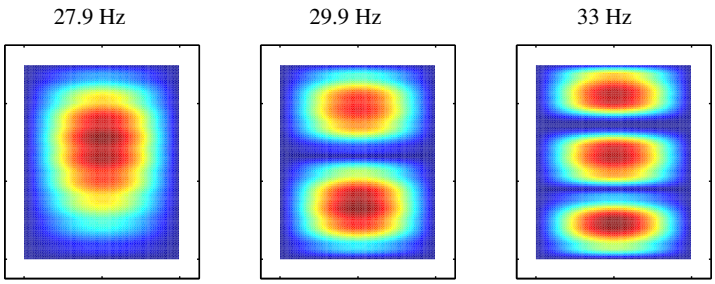

Figure 8.16: Modal shapes for the walking surface associated with the three first structural modes belonging to the 31.5 Hz third octave band.

Confidence regions for the mean impact sound level

From the stochastic computational model constructed using the generalized probabilistic approach of uncertainties, confidence regions associated with a probability $P_c = 0.98$ are obtained for the mean impact sound level computed from 21 different excitations. Fig. 8.17 compares such confidence intervals with experimental measurements. Thus, the propagation of the modeled structural uncertainties result in confidence regions that are comparatively small in regard to the dispersion that could be observed among the single impact sound levels associated with different excitation positions in Fig. 8.15. Moreover, the non-linear transformation of the random generalized coordinates associated with the structure into the spatial average of the quadratic pressure into the receiving room yields smaller confidence regions in comparison with single point velocities displayed in the previous paragraph. Finally, the discrepancies past 125 Hz between the stochastic computational model and the mean computational model can be put in perspective with the discrepancies that were observed in the same frequency range with respect to the velocities of the plasterboard in the previous section. It should be recalled that hyperparameters associated with the nonparametric probabilistic approach of uncertainties, which typically yields such discrepancies, were chosen arbitrarily. Such values were however consistent with experimental measurements associated with a comparable structure.

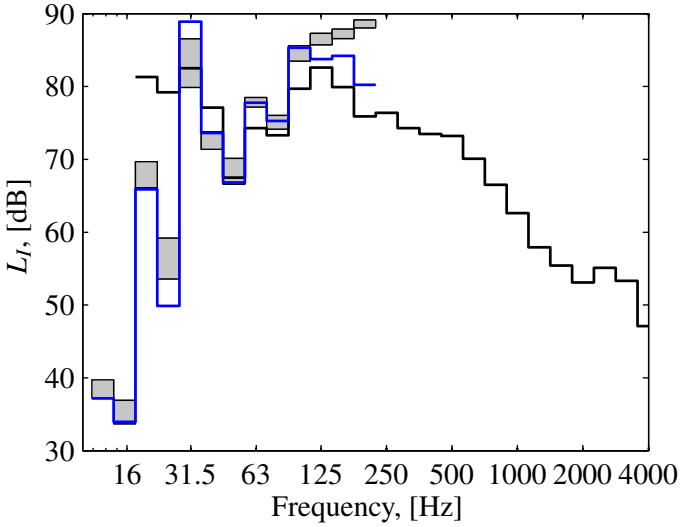

Figure 8.17: Impact sound levels. Mean computational model (thin blue solid line); confidence regions associated with a probability $P_c = 0.98$ resulting from the stochastic computational model (grey areas); experimental measurement (thin black solid line).

8.6 Conclusion

In the case of structures submitted to impacts, the external excitation force is dependent on the structure. Within the framework of stochastic computational models, the probabilistic model associated with the force is consequently dependent on the one of the structure. In this chapter, a probabilistic model was proposed for the impact force spectrum allowing uncertainty quantification to be performed while separating the propagation of parameter uncertainties and the propagation of model uncertainties from different frequency scales. The deterministic computational model was validated with measurements on a simple lightweight structure, showing the influence of the mobility disparities over the structure on the resulting impact forces for a simple lightweight system. Then, the sensitivity of the latter to different sources of uncertainties was investigated. In the case of a single impact, system parameters uncertainties as well as nonparametric fluctuations associated with generalized matrices projected on the first elastic modes are, at low frequencies, of negligible order.

Then, the model for the deterministic external excitation resulting from a standard tapping machine was applied to a full scale lightweight floor for which experimental measurements were available. Matching orders of magnitude for velocity levels over different points of the walking surface and ceiling where shown, out of the frequency range influenced by the first structural resonances. Finally, a methodology was presented for the evaluation of a mean impact sound level in laboratory conditions. At this stage, no floor covering is considered. Given an appropriate modeling, their inclusion in the approach would be straightforward.

9 Optimisation

Contents

9.1 Introduction

It has been shown within the previous chapters as well as with laboratory [8, 147, 148] or numerical parametric studies [21, 35, 98, 101, 129] that the vibrational displacement field over a separative lightweight element as well as its vibroacoustic behavior are sensitive at low frequencies to variations within materials, mounting conditions or, in general, configurations. Moreover, some level of statistical fluctuation exists and was highlighted, modeled and quantified for typical lightweight materials. Finally, due to the complexity of the systems which consist in the assembly of multiple elements, whose connections and boundary conditions are not perfectly known and worksmanship is questioned [8, 14–19], model uncertainties propagate to the output of the current computational models. Consequently, in order to find an optimal design robust to uncertainties, one has to consider a different approach, as mentioned in [41, 63], than the traditional one of considering deterministic models and system parameters. Indeed there is *a priori* no reason for an optimal design resulting from a deterministic problem to remain optimal when uncertainties are introduced.

In the previous chapters, a methodology was presented to construct stochastic computational models able to propagate different sources of uncertainties to the dynamic observables. A problematic, which goes beyond the scope of this work, is then to define objective performance indicators for the acoustic comfort which is by definition subjective with respect to inhabitant perceptions. Historically, objective criteria were defined from the comparison of experimental field measurements and reference curves dow to 100 Hz [118, 143], later extended to low frequencies down to 50 Hz in using weighted summation of the low third octave band energy content. However, in regard to the very low frequencies down to 20 Hz, the agreement of standard single values with subjective perception is target of critical opinions [6, 9–12, 149], in particular with respect to impact noise comfort prediction. The most recent findings about this topic [11, 12] will consequently be used in order to construct taylored fitness functions.

An other problematic related to the optimisation algorithm itself lies in the continuous against discrete representation of the search space [150]. In the framework of lightweight building construction, the separative elements are constituted of engineered industry products whose dimensions and characteristics belong to standard numbers. Moreover and worth example and argument, in regard to wooden frames constituted of a discrete number of stiffeners a variation from one configuration to another can be an increment in the number of stiffeners. By way of consequence, due to the non continuous mapping from the search space of the configurations to the fitness function representative of the objective performance of an element, the derivatives cannot be defined. Then, the class of evolutionnary algorithm, particularly well suited to discrete search spaces, is chosen to treat the robust optimisation problem. Moreover, beside airborne sound insulation performance and impact sound insulation performance, one can imagine additional criteria, such as mass minimisation for example. Then, the class of evolutionnary algorithm is also convenient to handle various multi-objective optimisation problems involving various fitness functions. An extensive litterature survey of such a class of algorithm can be found in [41]. Hereinafter, before introducing the algorithm developed for this specific application, the general structure and principles will be briefly presented.

9.2 Optimisation algorithm

9.2.1 Definition of the fitness functions

The problem of the definition of an objective function for the evaluation of the acoustic performance of lightweight systems, within the framework of an optimisation problem, refers directly to the problem of the definition of single number quantities for the rating, from experimental data, of those systems. In the standards respectively associated with the definition of single number quantities for airborne and impact sound insulation [118, 143], the single numbers R_w and L_w, resulting from the reference curve methods, are corrected with respect to a frequency band $\mathbb{B}$ using the respective adaptation terms $C_{\mathbb{B}}$ and $C_{I,\mathbb{B}}$. Thus, in the frequency band $\mathbb{B}$ the performance is rated by the quantities $R_w + C_{\mathbb{B}}$ and $L_{n,w} + C_{I,\mathbb{B}}$. By construction, the latter directly consist in the weighted summation of the energy content with respect

to the third octave band that belong to $\mathbb{B}$. Then, according to [118, 143], such single number quantities can be written as

$$R_w + C_{\mathbb{B}} = -10 \log_{10} \left(\sum_{b \in \mathbb{B}} 10^{(W_{b,A} - R_b)/10} \right), \tag{9.1}$$

$$L_{n,w} + C_{I,\mathbb{B}} = 10 \log_{10} \left(\sum_{b \in \mathbb{B}} 10^{(L_{n,b} - W_{b,I})/10} \right), \tag{9.2}$$

where $W_{b,A}$ and $W_{b,I}$ respectively are frequency dependent weighting coefficients. In particular, according to [118], $W_{b,A}$ is constituted of A-weighted levels. By way of consequence, the single number $R_w + C_{\mathbb{B}}$ is mostly dependent on the higher third octave bands in $\mathbb{B}$, as can be seen in [11, 12]. Furthermore, according to [143], $W_{b,I} = 15$ dB over the whole frequency band of interest. Recently, researches showed that single values resulting from such weighting coefficients, in particular in regard to impact noise, cannot discrimate the good designs from the worse in a way which is consistent with inhabitant perceived performance [11, 12]. Adapted weighting coefficients were consequently introduced in regard to impact noise, such that the adequation of the resulting single number quantities was improved with respect to inhabitant perception. Thus, in order to focus to low frequency problems associated with airborne sound insulation, it is proposed to introduce a fitness function J_A, computed over the frequency band $\mathbb{B} = [20, 200]$ Hz in the spirit of Eq. (9.1) but without A-weighted coefficients. Let $\mathbf{d}$ be the vector of the n_d design parameters belonging to $\mathbb{R}^{n_d}$. Thus J_A is set as an objective performance indicator of the design indexed by $\mathbf{d}$ and we have

$$J_A(\mathbf{d}) = -10 \log_{10} \left(\sum_{b \in \mathbb{B}} 10^{-R_b/10} \right). \tag{9.3}$$

Moreover, in regard to impact sound insulation performance, the adapted weighting coefficients from [11, 12] and given in Table 9.1, which emphasize the frequencies below 50 Hz, are used to construct a fitness function J_I over the frequency band $\mathbb{B} = [20, 200]$ Hz, indicative of the objective performance, such that

$$J_I(\mathbf{d}) = -10 \log_{10} \left(\sum_{b \in \mathbb{B}} 10^{(L_{n,b} - W_{b,I,Akulite})/10} \right). \tag{9.4}$$

It should be noted that $J_I(\mathbf{d})$ is set negative because the objective is to minimise the impact sound level and consequently to maximise J_I.

Third octave band [Hz]	20	25	31.5	40	50-200
$W_{b,I,Akulite}$	7	9	11	13	15

Table 9.1: Weighting coefficients with respect to impact sound according to [11, 12].

9.2.2 Genetic algorithm

In the following, the aim is not to give an overview of evolutionary algorithms but whether to introduce their general structure and the associated vocabulary that could help the reader situate this work among others. First of all, evolutionary algorithms inspire from early Darwinian concepts such as survival and reproduction of the fittest on one hand and non-directed mutation of individuals on the other hand. From an initial population, only the best individuals will survive, reproduce and mutate from a generation to another. Thus, algorithms inspired by such concepts involve the following general structure [41, 150], with the usual terminology:

- **Intiatilization** of the individuals constituting the first generation

- **Evaluation** of the individuals with respect to a fitness function
- **Selection** of the parents for the future generation
- **Reproduction** of the parents, through cross breeding, elitism or mutation

We have $\mathbf{d}$ the vector of the n_d design parameters belonging to $\mathbb{R}^{n_d}$ (hereinafter denoted as the phenotypic space). As it was mentioned within the introduction, the admissible designs are such that most design parameters can only take discrete values in $C_{\mathbf{d}}$ subset of $\mathbb{R}^{n_d}$ and the optimisation problem is consequently equivalent to a combinatorial problem. Then, such parameters are naturally well suited for a change of variables from the so-called phenotypic space to a binary representation in a genotypic space, because no continuous mapping from one to another needs to be defined. Thus, assuming each design parameter can take a power of two number of admissible values, there exists a bijection between the phenotypic and genotypic spaces and, consequently, a system or individual is completely described by the knowledge of a bit string of fixed length such that for example

Design parameter	d_1				d_2	$\cdots$	d_{n_d}	
Genotype of the individual	0	1	0	1	1	$\cdots$	0	1

A usual initialization procedure for the creation of the first generation, which is adopted in this work, is the random generation with independent uniform distributions with support $[0, 1]$ and a staircase function with threshold at 0.5 associated with each bit. Let Π_0 be the initial population, or first generation, constituted of P individuals and let $\mathbf{d} \mapsto J(\mathbf{d})$ denote any of the fitness functions defined in Section 9.2.1. The evalutation of the individuals from the first generation yields a ranking with respect to J and the selection of the best parents for the next generation is then performed using a tournament of size T_s. For each parent that has to be selected, a tournament is organized between T_s individuals picked at random, with a uniform probability distribution, among the population. This popular selection procedure is an arbitrary choice among others, but which has the advantage of not being too much of an elitist selection as, depending on the size of the tournament (concept of selection pressure), intermediate individuals can survive and maintain some level of diversity among the population. However, in order to ensure that the best individual survive, an elite ratio among the children is introduced such that part of the next generation is constituted of the best individuals from the preceding. Following, the creation of the remaining individuals for the next generation takes place in two steps: crossbreeding and mutation. In regard to crossbreeding, part of the parents (defined by a crossbreeding ratio) mix their genotypes, using once again a random uniform selection of the alleles, or group of bits, respectively associated with each design parameter. Such process can be schematically depicted as

Parent 1	**1**	**1**	**0**	**0**	0	$\cdots$	1	1
Parent 2	0	1	0	1	**1**	$\cdots$	**0**	**1**
Children	**1**	**1**	**0**	**0**	**1**	$\cdots$	**0**	**1**

In regard to mutations, the remaining parents are submitted to so-called bit-flips (from 0 to 1 or 1 to 0) which happen when the realisation of a uniform random variable with support $[0, 1]$, associated with a given bit, surpasses a threshold fixed by a mutation rate. As soon as the creation of the new generation is completed, the evaluation takes place again until a maximum number of generation or any other exit criterion is reached.

The resulting genetic algorithm consequently depends on multiple parameters such as the population size, tournament size, elite ratio, crossbreeding ratio and mutation rate. The tuning of such parameters with respect to the optimisation problem determines the global efficiency of the algorithm in its ability to find an optimal design and avoid local minima within a satisfying computational time.

9.3 Robust optimisation problems

In this section, a set of optimisation problems is constructed with respect to given admissible classes of systems in the presence of uncertainties. In particular, system parameters uncertainties and model uncertainties with respect to the structure are taken into account using the generalized probabilistic approach of uncertainties. Then, given a deterministic external excitation defined acccording to Chapters 7 or 8, the optimisation problem consists in maximising the objective performance, associated with airborne or impact sound insulation, with respect to the stochastic model of the evaluated uncertain design. In the following, relatively simple problems are presented in the sense that admissible designs are not spread out within too large search spaces and that physical interpretations remain possible. Thus, trends in the way designs evolve along generations of the algorithm can be analyzed.

Stochastic computational models associated with uncertain designs

Stochastic computational models are constructed with respect to each evaluated uncertain design. The generalized probabilistic approach of uncertainties is used for the construction of the probabilistic models for random generalized mass, damping and stiffness matrices associated with the structure only. The probabilistic approach of system parameters uncertainties makes use of hyperparameters that were identified in Chapter 6 meanwhile hyperparameters associated with the nonparametric probabilistic approach of model uncertainties are set to $\delta_{M^s} = \delta_{D^s} = \delta_{K^s} = 0.3$. Preliminary convergence studies, carried out with respect to a limited set of admissible designs for each considered problem, yield the dimension of the reduction basis that will be used for the construction of the generalized matrices, as well as the number of Monte Carlo simulations required for a reasonable mean-square convergence of the random generalized coordinates.

Definition of the objective performance associated with uncertain designs

Let $X_b(\mathbf{d})$ denote without distinction a random sound reduction index or random normalised impact sound level evaluated for a given third octave band $b \in \mathbb{B}$ with respect to the stochastic computational model associated with an uncertain design, indexed by the vector of design parameters $\mathbf{d}$. Then, the 1% and 99% quantile $x_{b,min}(\mathbf{d})$ and $x_{b,max}(\mathbf{d})$ are defined according to Section (6.2.3) such that $\mathcal{P}(x_{b,min}(\mathbf{d}) \leq X_b(\mathbf{d}) \leq x_{b,max}(\mathbf{d})) = 0.98$, in which $\mathcal{P}$ denote the probability. Thus, in regard to the airborne sound insulation, the fitness function J_A is evaluated using $x_{b,min}(\mathbf{d})$ in order to maximise the inferior envelope of the confidence region associated with the sound reduction index. Moreover, in regard to the impact sound insulation, the fitness function J_I is evaluated using $x_{b,max}(\mathbf{d})$ in order to minimise the superior envelope of the confidence region associated with the normalised impact sound level.

9.3.1 Lightweight double parting wall systems

In this section, the optimisation algorithm is applied to the class of double parting wall systems such as those presented in Chapter 7. The acoustic performance of such systems is rated in regard to airborne sound insulation only. Single objective optimisations are then considered and the following problem is formulated: given a class of admissible designs, indexed by the vector $\mathbf{d}$ belonging to the admissible set of design parameters $C_{\mathbf{d}} \subset \mathbb{R}^{n_d}$, and given a stochastic computational model associated with each uncertain design, find the optimal configuration indexed by $\mathbf{d}^{opt}$ that maximises the airborne sound insulation such that

$$\forall \mathbf{d} \in C_{\mathbf{d}},\ J_A(\mathbf{d}) \leq J_A(\mathbf{d}^{opt})\ . \tag{9.5}$$

Admissible systems

Two classes of systems are considered which are such that the layouts displayed on Fig. 9.1 remain identicals for any admissible design belonging to the aforementioned classes. It can be noted that such

classes belong to a same larger class of systems which consists in the designs resulting from every possible layer permutation.

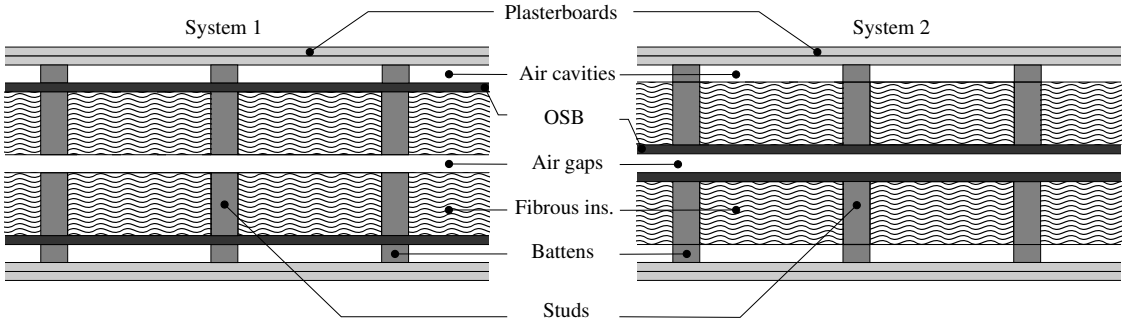

Figure 9.1: Top sectional views of the layer patterns with respect to the considered classes of parting walls.

Then, the vector **d** is constituted of five design parameters respectively associated with plasterboards, cross-sectional dimensions of the studs, stud spacing, thickness of the air gap and orientation of the battens. In particular, admissible configurations result from the combination of the different discrete states associated with each parameter. Thus, in regard to the plasterboards, the design parameter d_1 maps to eight admissible sets of system parameters and hyperparameters according to Table 9.2. Three different materials P1, P2 and P3 correspond to the different types that were measured in Chapter 3. Thus, P1, P2 and P3 respectively refers to standard, fire resistant fiber reinforced and high hardness plasterboards. In a similar way than in Chapter 7, each facing can be doubled, resulting in an assumed homogeneous effective plasterboard. Moreover, in regard to the highly orthotropic fire resistant boards, different orientations with respect to the primary wooden frame are admissible (effect of the orientation was experimentally observed in [90]). Furthermore, parameter d_2 maps to four admissible cross-sections for the studs $\{100\text{ mm} \times 45\text{ mm}, 120\text{ mm} \times 45\text{ mm}, 145\text{ mm} \times 45\text{ mm}, 180\text{ mm} \times 45\text{ mm}\}$. Parameter d_3 maps to two admissible stud spacings $\{400\text{ mm}, 600\text{ mm}\}$. Parameter d_4 maps to two admissible central air gap depth $\{20\text{ mm}, 40\text{ mm}\}$. Finally parameter d_5 maps to the orientation of the secondary frame with respect to the primary frame $\{\parallel, \perp\}$.

	B1	B2	B3	B4	B5	B6	B7	B8
Material	P1	P1	P2	P2	P2	P2	P3	P3
Orientation	$\parallel$	$\parallel$	$\perp$	$\perp$	$\parallel$	$\parallel$	$\parallel$	$\parallel$
δ_{ela}	0.15	0.15	0.1	0.1	0.1	0.1	0.11	0.11
$\underline{\rho}^S$ [kg/m^3]	705	705	1070	1070	1070	1070	911	911
δ_ρ	0.009	0.009	0.014	0.014	0.014	0.014	0.011	0.011
Thickness [mm]	12.5	25	15	30	15	30	18	36

Table 9.2: Each admissible value of parameter d_1 maps to a set of parameters associated with the plasterboard model.

Following, the change of basis from the admissible integer values of parameters d_1 to d_5 into a binary representation in the genotypic space yields a coding of each admissible configuration on a 8 bit long string. Thus, the resulting combinatory problem consists in finding the best design in the sense of the previously defined fitness function J_A among the search space constituted of the $2^8 = 256$ admissible configurations.

Definition of the external excitation and evaluation of J_A

For the sake of simplicity, evaluation conditions are identical to those used in Section 7.3.5: twelve acoustical point sources are placed into the source room and spatial average of the quadratic pressure

field is performed over the room volumes excluding forbidden areas closer than 0.7 m to the boundaries. Room dimensions and properties as well as wall dimensions L_y^W=3.800 m and L_z^W=2.250 m are taken as identical with respect to Chapter 7.

Genetic algorithm setup

In paragraph 9.2.1, classical vocabulary associated with evolutionnary algorithms was introduced. Then, an algorithm belonging to the class of the so-called genetic algorithms was chosen and implemented. In particular, such algorithm is controlled through the definition of five parameters: population size, tournament size, elite ratio, crossbreeding ratio and mutation rate. Thus the population size, directly related to a more or less initial fine mesh of the search space, is set to 30 individuals, namely around one eighth of the search space dimension. Other paremeters are related to the way the information translates from one generation to another. Thus, each of those parameters is associated with one type of children for the next generation. First, the elite ratio is set to one sixth of the population size, meaning that the best five individuals of a generation, in the sense of the aforementioned fitness function, are directly transmitted as children to the next generation. Then, the second category of children results from a breeding of selected parents. The number of 24 individuals are chosen to result from such process and, by way of consequence, 48 parents have to be selected. Ensuing, a tournament size of 4 is chosen, such that each parent ensues from a tournament between four randomly selected parents among the current generation. It can be noted that the size of the tournament, associated with the concept of selection pressure, directly influences the ability of the algorithm to quickly converge towards an optimum. Indeed, in the case where the tournament is opened to the whole population, only the very best individual reproduces. With the present low selection pressure, the aim is to not converge too fast towards a local optimum and to seek as far as possible for a global one. Finally, in regard to the remaining childrens, the mutation rate of one percent is set such that, from a selected parent, each bit as a one percent probability to be fliped.

Results

In regard to each class of parting wall systems, chosen for the optimisation of the airborne sound insulation performance, Figs. 9.2 and 9.3 show the proportion of given design traits associated with each generation of the genetic algorithm. Thus, for both classes, similar trends are observed as the individuals converge towards configurations for which the stud spacing is minimal, the stud cross-sectional dimensions are maximal and the central air gap is maximal. Moreover, within the final generations, battens are exclusively parallel with respect to the primary frame. Only plasterboard diversity persists among generations, which can be interpreted as a second order influence on the evaluated performance such that a selection only happens as soon as other design parameters have been clearly selected. It can be seen that, in regard to both systems, the algorithm eventually yields the stiffest admissible structural systems and at the same time the deepest admissible acoustic cavities. Such results are consistent with the stiffness controlled behavior in the 63 and 80 Hz third octave bands observed in Chapter. 7 as the system with the higher bending stiffness displayed higher airborne sound insulation performance within such frequency bands.

Such results must be put in perspective with existing knowledge in regard to the behavior of such systems in higher frequency range. It should be noted that, in [90], the sensitivity of the sound reduction indices of single walls to stud spacing was emphasized through experimental measurements. In particular, low and high frequencies were shown in competition, as smaller stud spacing implied better low frequency performance but worse high frequency performance. By way of consequence, it can be understood that such single objective optimisations can converge towards solutions displaying maximum admissible structural stiffness, which possibly could be the best solutions at low frequencies, but some sort of information from high frequency predictions, which are out of the scope of this work, might be needed as a counterbalancing. In particular in regard to airborne sound insulation for which high frequency performance is also a perceived acoustical comfort criterion [13].

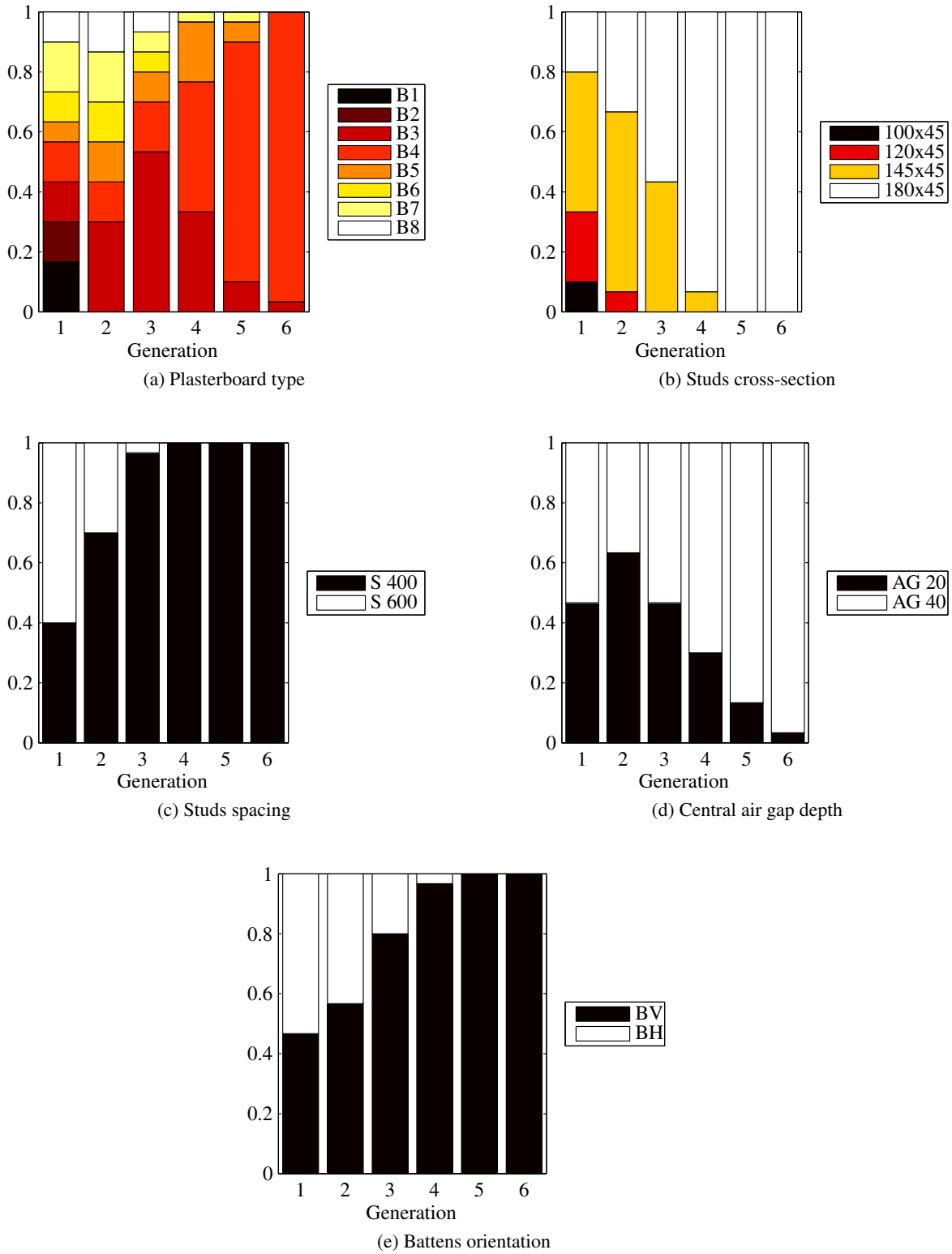

(a) Plasterboard type

(b) Studs cross-section

(c) Studs spacing

(d) Central air gap depth

(e) Battens orientation

Figure 9.2: System 1. Proportion of individuals displaying a given trait among generations.

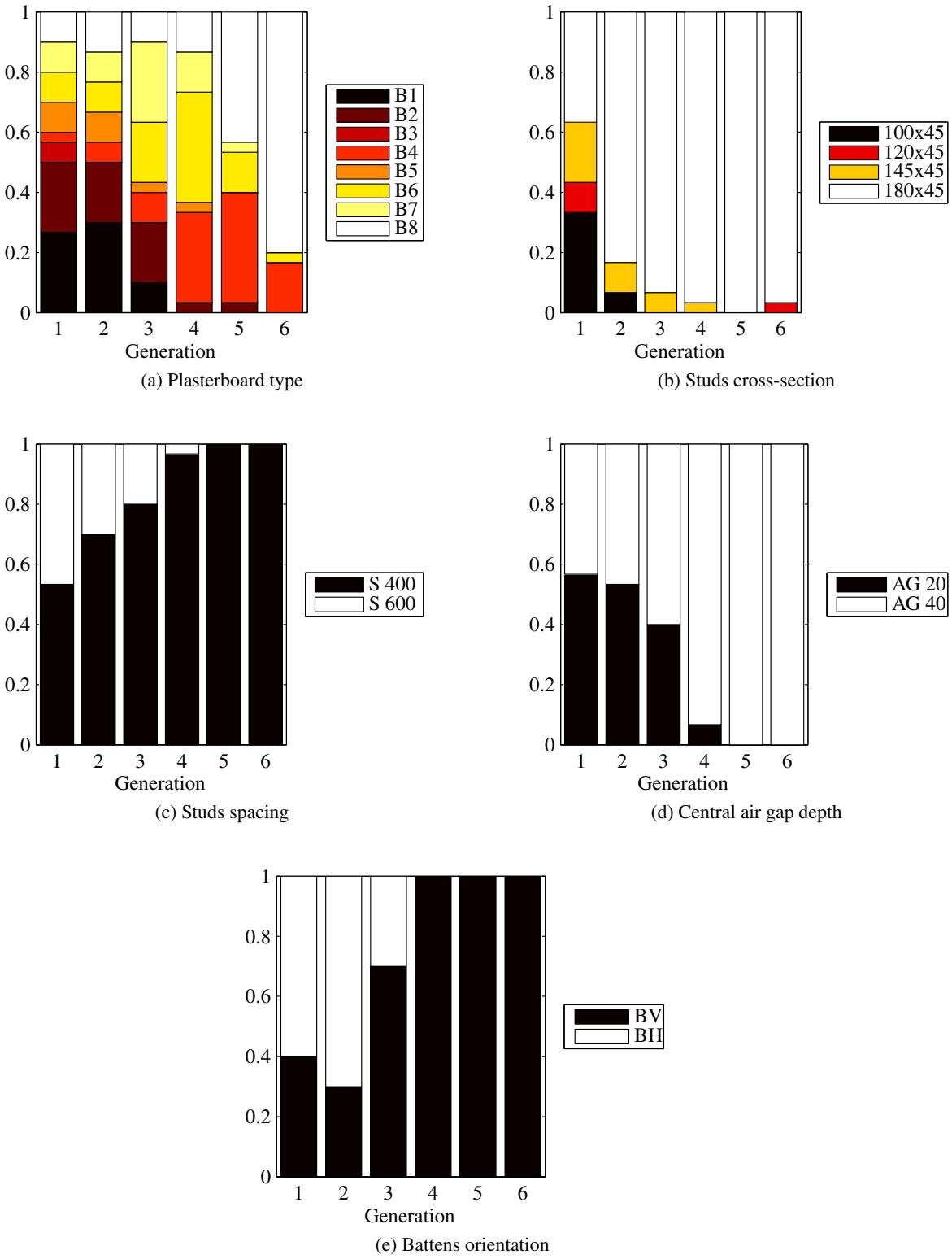

(a) Plasterboard type

(b) Studs cross-section

(c) Studs spacing

(d) Central air gap depth

(e) Battens orientation

Figure 9.3: System 2. Proportion of individuals displaying a given trait among generations.

Eventually, given that systems treated in Chapter 7 belong to the considered search spaces, comparison is possible between the nominal predictions as well as measurements associated with such systems and the confidences regions for the sound reduction indices associated with the obtained optimal designs. Thus, Fig. 9.4 shows that increasing the global stiffness of the systems such that they remain stiffness controlled higher in frequency would allow, according to this model, a gain of 10 to 20 dB in the frequency range $[20, 200]$ Hz. It should be noted that such observation only relate to the individual performance of systems in laboratory conditions, without structural transmission paths between single walls.

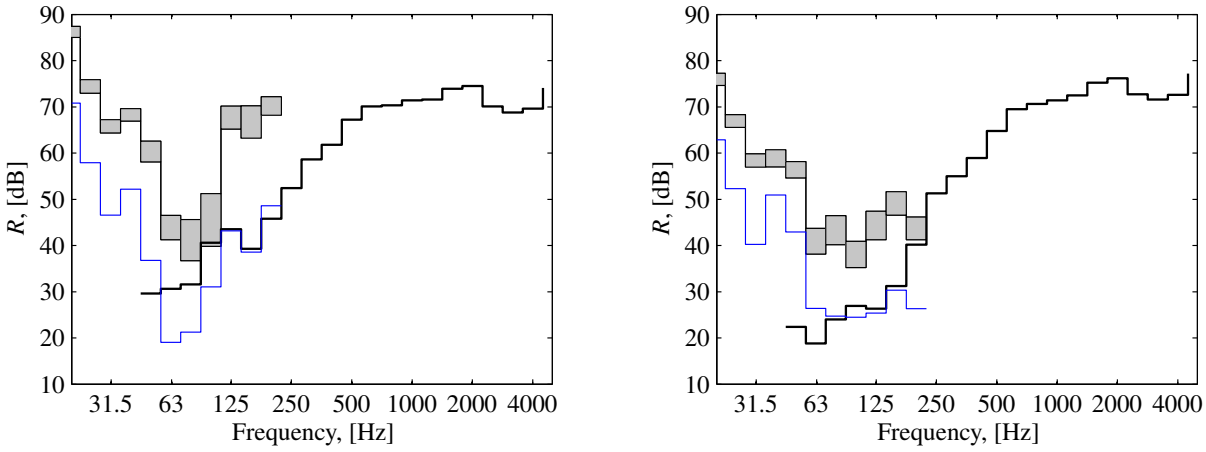

(a) System 1 (b) System 2

Figure 9.4: Sound reduction indices R. Confidence regions associated with a probability $P_c = 0.98$ for the indices R resulting from the obtained optimal designs (grey areas); mean computational model predictions for systems treated in Chapter 7 (thin blue solid line); experimental measurements for systems treated in Chapter 7 (thick black solid lines).

9.3.2 Lightweigth floor system

In this section, the optimisation algorithm is applied to the class of floors whose layout are similar to the C1 floor from [135] treated in Chapter 8. This time, impact sound insulation as well as airborne sound insulation are considered. Hence a two objectives optimisation problem formulated as: given a class of admissible designs and a stochastic computational model associated with each uncertain admissible design, find the optimal configuration indexed by $\mathbf{d}^{opt}$ that maximises airborne sound insulation as well as impact sound insulation in the sense of fitness functions J_I and J_A. In the general case, there is *a priori* no reason for an optimal design with respect to one objective to be optimal with respect to the second objective, although it is generally considered that both objectives are not in competition [10]. By way of consequence, in regard to the genetic algorithm, a methodology has to be defined for the rating of individuals. If need be, an additional constraint would have te be defined to decide of the final best design among nondominated, or Pareto efficient, individuals of the last generation.

Admissible systems

The construction of the set of dmissible configurations is inspired from the experimental parametric study presented in [148] and allows comparison of the results. Parallel and perpendicular stiffening of the primary frame are investigated, as well as different toppings or plasterboards. No resilent channels are considered in this work such that structural transmission paths prevail. Furthermore, the optimisation focuses on bare floors without covering, whose effect is generally limited at low frequencies. Hereinafter, admissible configurations indexed by $\mathbf{d}$ verify the layout defined by Fig. 9.5. Perpendicular stiffening

is not depicted but consists in blocking potential lateral bending of the joists using regularly spaced (600 mm off center) 45 mm thick wooden struts. An 100 mm thick fibrous insulation material layer is used, whose properties can be found in Chapter 8.

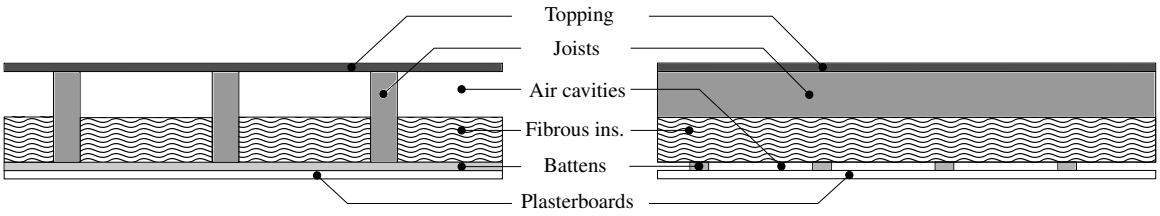

Figure 9.5: Schematic layout (left and right views) for the considered admissible class of floors.

Then, the vector **d** is constituted of five design parameters respectively associated with topping material, cross-sectional dimensions of the joists, joist spacing, perpendicular stiffening of the primary frame and finally with the plasterboards that constitute the ceiling. Thus, in regard to the topping, design parameter d_1 maps to four admissible sets of system parameters and hyperparameters according to Table 9.3. A 22 mm thick particule board is set in competition with different oriented strand boards and, in the case of the markedly orthotropic 18 mm thick OSB, different orientations with respect to the primary frame are admissible.

	T1	T2	T3	T4
Material	OSB	OSB	PB	OSB
Orientation	$\parallel$	$\perp$	$\perp$	$\perp$
δ_{ela}	0.1	0.1	0.08	0.1
$\underline{\rho}^S$ [kg/m^3]	577	577	637	577
δ_ρ	0.020	0.020	0.007	0.020
Thickness [mm]	18	18	22	15

Table 9.3: Each admissible value of parameter d_1 maps to a set of parameters associated with the topping model.

Furthermore, parameter d_2 maps to two admissible cross-sections for the joists {220 mm $\times$ 45 mm, 220 mm $\times$ 90 mm} associated with a parallel stiffening of the floor with respect to the primary frame. Parameter d_3 maps to four admissible joist spacings {400 mm, 450 mm, 500 mm, 550 mm}. Parameter d_4 relates to the presence of perpendicular blocking or not {Blocking, No blocking}. Finally, in regard to the plasterboard ceiling, parameter d_5 maps to four admissible sets of system parameters and hyperparameters according to Table 9.4. In agreement with the previous section, P1, P2 and P3 respectively refers to standard, fire resistant fiber reinforced and high hardness plasterboards.

	B1	B2	B3	B4
Material	P1	P2	P2	P3
Orientation	$\perp$	$\parallel$	$\perp$	$\perp$
δ_{ela}	0.15	0.1	0.1	0.11
$\underline{\rho}^S$ [kg/m^3]	705	1070	1070	911
δ_ρ	0.009	0.014	0.014	0.011
Thickness [mm]	12.5	15	15	18

Table 9.4: Each admissible value of parameter d_5 maps to a set of parameters associated with the plasterboard model.

The change of basis from the admissible integer values of parameters d_1 to d_5 into a binary repre-

sentation in the genotypic space yields a coding of each admissible configuration on a 8 bit long string. By way of consequence the resulting combinatory problem consists in finding the best design in the sense of the fitness functions J_I and J_A among the search space constituted of the $2^8 = 256$ admissible configurations.

Definition of the external excitation and evaluation of J_I and J_A

In regard to impact noise level evaluation and for the sake of simplicity, dimensions of the admissible systems (L_x^F=3.98 m and L_y^F=4.98 m), joist orientations as well as evaluation conditions are identical to those used in Section 8.5.5. Twenty-one tapping machine positions are consequently used for the evaluation of a mean impact sound level. In regard to airbone sound, the dimensions of the source room, which is smaller in comparison with the laboratory considered in Chapter 7, are L_x^S=3.78 m, L_y^S=4.78 m and L_z^S=3.82 m. Then, nine acoustical point sources are successively used for the evaluation of a mean sound reduction index. The respective coordinates associated with the point sources are $\mathbf{x}_{Q_S,1} = (0.7, 0.7, 3.82)$, $\mathbf{x}_{Q_S,2} = (1.7, 0.8, 3.82)$, $\mathbf{x}_{Q_S,3} = (2.7, 0.9, 3.82)$, $\mathbf{x}_{Q_S,4} = (0.8, 2.1, 3.82)$, $\mathbf{x}_{Q_S,5} = (1.8, 2.2, 3.82)$, $\mathbf{x}_{Q_S,6} = (2.8, 2.3, 3.82)$, $\mathbf{x}_{Q_S,7} = (0.9, 3.5, 3.82)$, $\mathbf{x}_{Q_S,8} = (1.9, 3.6, 3.82)$, $\mathbf{x}_{Q_S,9} = (2.9, 3.7, 3.82)$.

Genetic algorithm setup

As the dimension of the combinatory problem does not change from the previously treated optimisation problems to the present one, population size, tournament size, elite ratio, crossbreeding ratio and mutation rate are taken as identical. Due to the multi-objective nature of the optimisation, an adapted strategy has to be selected in order to assign a rank to the individuals belonging to a given generation of the genetic algorithm. Thus, among individuals belonging to a given generation, successive Pareto fronts are identified. Such fronts are constituted of nondominated individuals, in the sense that any other individual of the given generation that would be superior with respect to one fitness function would be inferior with respect to the second fitness function. Individuals belonging to a same Pareto front are then tied for the rank of the front. Figure 9.6 displays the schematic ranking principle. By way of consequence, the genetic algorithm will preferably select non dominated individuals from the first Pareto front as parents, and so on until the required number of parents for the next generation is reached.

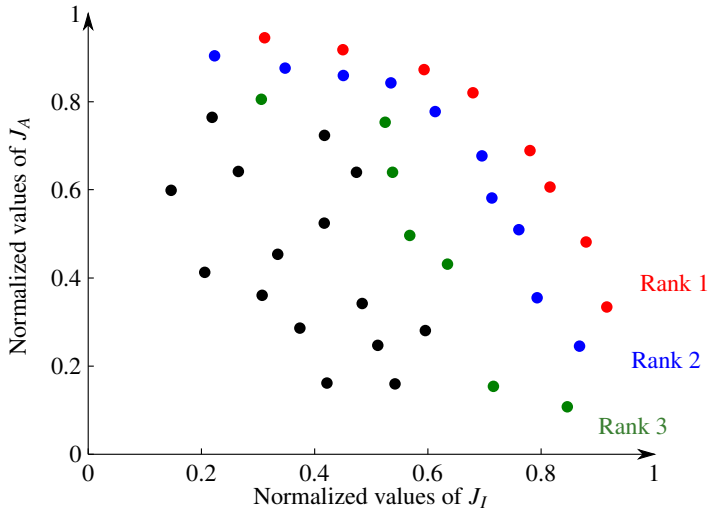

Figure 9.6: Schematic ranking principle for the two objectives optimisation. Dots denote the values taken by both fitness functions with respect to individuals belonging to a given generation of the genetic algorithm.

Results

In order to illustrate the previous remark about potential existing competition between airborne and impact sound insulation performance, Fig. 9.7 displays the evaluation of ($J_I(\mathbf{d})$, $J_A(\mathbf{d})$) for the individuals belonging to the first generation. Thus, no clear competition is observable, as improvements in performance with respect to one finess function tend to result in improvements with respect to the other. Observation which is further confirmed by the convergence of the algorithm towards a rather unique direction, as seen with Fig. 9.8, and not towards a wide range of Pareto efficient designs.

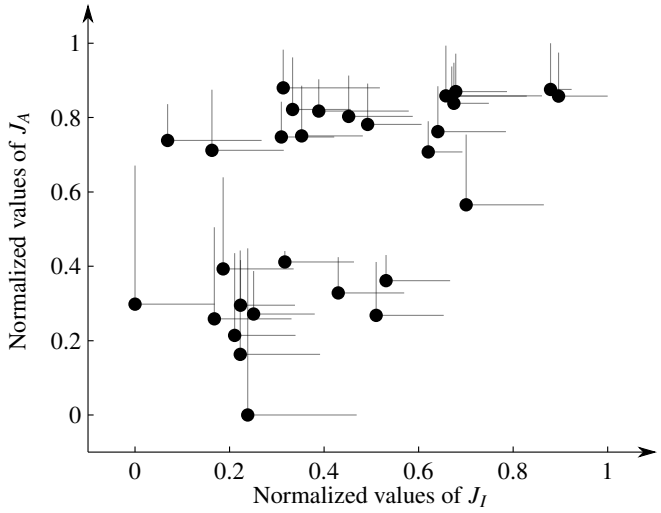

Figure 9.7: Positioning of the individuals of the first generation in the space of the normalized fitness functions. Dots denote the points of coordinates ($J_I(\mathbf{d})$, $J_A(\mathbf{d})$). Grey lines denote the dimensions of the confidence area associated with each individual.

Let briefly recall that, in the present work, fitness functions respectively associated with airborne and impact sound performances are constructed from the envelopes of random sound reduction indices and impact sound levels. Using inferior or superior envelopes, confidences regions can be constructed with respect to each fitness function, whose dimensions are denoted by the grey lines in Fig. 9.7. Following, the constructed dual objectives optimisation problem consist in maximising the coordinates of the inferior left corner associated with such confidence areas. Finally, it can be observed that, with respect to this particular problem, the probabilistic approach do not drastically modify the ranking of individuals as there is no overlap between confidence regions of the least efficient individuals and the best ones.

In Fig. 9.8 it is observed that the genetic algorithm converges towards two nondominated individuals corresponding to two very similar designs. In fact, the only difference is about the topping, whether constituted of particle boards or oriented strand boards perpendicularly oriented with respect to the joists. In regard to both designs, largest admissible joists are involved. Interestingly enough, joist spacing is not maximal nor minimal and takes quite some time to be selected. After two generations, all four admissible parameters associated with joist spacing are still appearing with comparable proportions among the population, meanwhile after one generation only, more thant 80% of the population involves perpendicular blocking for example. Finally, the selected plasterboard displays maximal mass density as well as bending stiffness. Thus, every present observation is consistent with experimental sensitivities observed in [148]. Standard lightweight floor C1 treated in Chapter 8 do not belong to the search space. However, nominal predictions as well as experimental measurements are worth reference for the comparison of the confidence regions for sound reduction indices and normalized impact sound levels associated with obtained optimal designs. An improvement of 10 to 20 dB is observed with respect to airborne insulation over the whole frequency range $[20, 200]$ Hz, however, most of impact sound insulation improvements are localized around or below the first structural resonances that could not be predicted whether by nom-

inal or stochastic computational models. If impact sound insulation performance is to be rated from low frequencies, and if the individual performance of the separative systems is the main factor, accurate modeling of boundary conditions definitely seems an obligatory step forward.

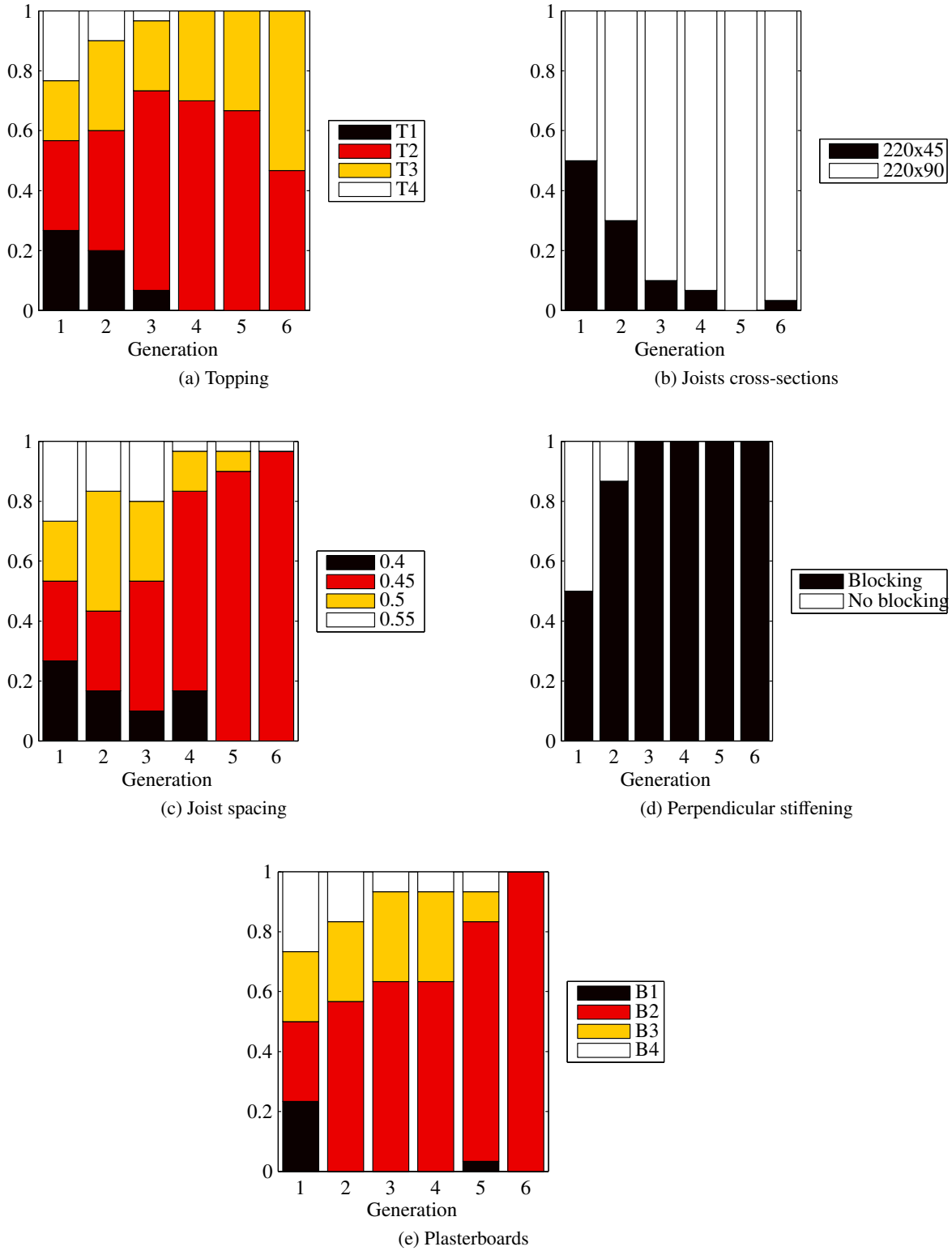

(a) Topping

(b) Joists cross-sections

(c) Joist spacing

(d) Perpendicular stiffening

(e) Plasterboards

Figure 9.8: System 1. Proportion of individuals displaying a given trait among generations.

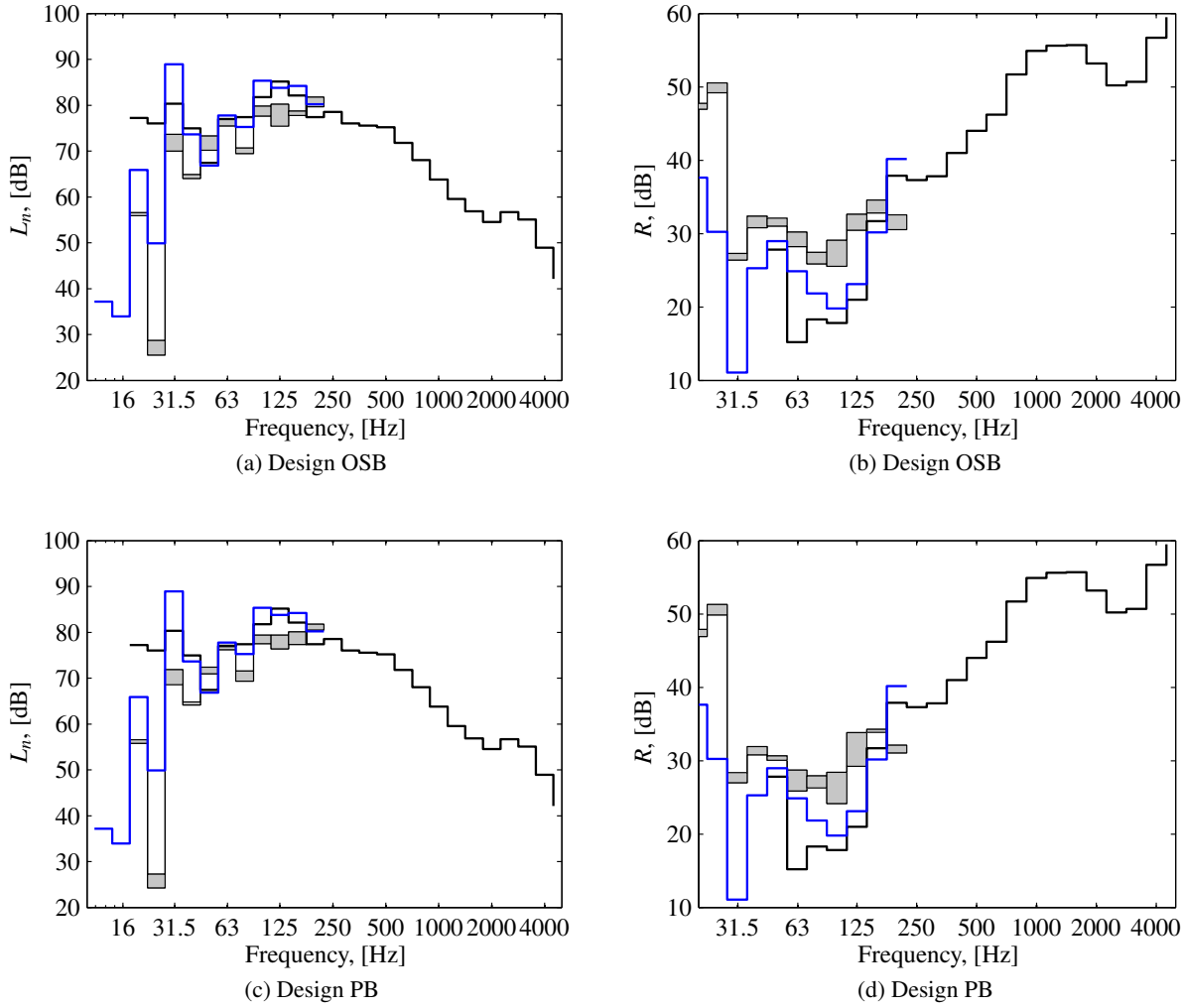

(a) Design OSB (b) Design OSB

(c) Design PB (d) Design PB

Figure 9.9: Sound reduction indices R and normalized impact sound levels L_n. Confidence regions associated with a probability $P_c = 0.98$ resulting from the obtained optimal designs (grey areas); mean computational model predictions for C1 reference floor treated in Chapter 8 (thin blue solid line); experimental measurements for C1 reference floor treated in Chapter 8 (thick black solid lines).

9.4 Conclusion

In this chapter, a methodology was presented, illustrated with different application cases, for the robust multi-criterion optimisation of the acoustic performance of lightweight building systems. The framework of evolutionnary algorithms was selected in response to the combinatorial nature of the optimisation problem, induced by discrete admissible values of the design parameters resulting from the consideration of standard building products for example. Such approach is moreover suited to multi-objective optimisation. Thus, a genetic algorithm was implemented, in Matlab, within the previously mentioned software framework.

Deterministic fitness functions were constructed according to most recent publications about objective performance definition from experimental measurements. Then, using the confidence regions resulting from stochastic computational models associated with the considered evaluated uncertain designs, the performance of the latter could be rated. In the case of a dual optimisation problem, consisting in the maximisation of airborne as well as impact sound insulation performance, a strategy was presented in the general case for the rating of individuals among generations. Finally, in regard to treated systems, the optimisation algorithm tended to converge towards designs displaying the highest bending stiffness.

It is reasonable to assume, in regard to experimental studies, that such solutions might be efficient at low frequencies, but potentially result in a downgrade with respect to high frequency performance. In such case additional information would have to be considered from the high frequency range and formulated as an additional fitness function for an *ad hoc* multi-objective optimisation problem.

Conclusions and perspectives

Summary of present work

Formulated objective for the present work was to propose a methodology for the robust design of lightweight wood-based building systems in the low frequency range. Considering the state of the art, existing models and the overall lack of knowledge about the vibroacoustic behavior associated with such systems in the frequency range of interest, research efforts were directed towards a number of targeted objectives.

First of all, focus was given to the definition of a modeling framework able to take into account the inherent complexity of lightweight systems, constituted of the assembly of multiple structural elastic components, internal acoustic cavities and poroelastic media. Thus, classical linear vibroacoustic theory is deployed. In addition, the Biot-Allard theory is used for poroelastic modeling with, depending on the nature of the frame, both solid phase and fluid phase considered or fluid phase only. Then, a finite element computational environment was implemented from scratch in Matlab allowing flexibility and adaptability.

In a second time, experimental measurement were carried out in dynamics, over a range of full scale structural elements. Associated objective was triple. First, constitutive laws could be identified in regard to materials that are not so well or not at all documented with respect to dynamical modeling. Second, statistical fluctuations within elastic properties or mass densities could be enlightened. Third, assemblies of structural elements could be characterised. Indeed, a particularity of lightweight building systems is the presence of a high number of structural connections. Thus, a necessary step in the understanding of their vibroacoustic behavior consists in being able to predict structural transmission paths. Following, it was shown that flexible connections are prerequisite for an accurate prediction of structural frequency response functions, in particular around first structural resonances, and that perfectly tied models induce substantial modeling errors.

In response to the recurrent problematic of uncertainties within lightweight construction, corroborated by aforementioned experimental observations, a probabilistic approach was undertaken. In particular, prior probabilistic models were constructed within the framework of the generalized probabilistic approach of uncertainties introduced by Soize. Such approach requires a mean reduced order computational model. Within the framework of three-dimensional poroelastic modeling, dedicated researches are still investigating for standard reduction strategies. As a follow-up to recent publications using coupled phases poroelastic eigenmodes, a component mode synthesis strategy was presented for the whole vibroacoustic system with poroelastic medium, whether modeled as coupled solid and fluid phases with displacements as primary variables or as an equivalent fluid with pressure as primary variable. Such strategy was then implemented in the unified software framework in Matlab. Following, the generalized probabilistic approach of uncertainties could be carried on in order to take into account system parameters uncertainties as well as model uncertainties induced by modeling errors. In regard to structural system parameters uncertainties, prior probabilistic models were constructed using the Maximum Entropy Principle. Given a limited number of experimental observables, stochastic inverse problems were introduced using the Maximum Likelihood method to find optimal hyperparameters associated with the prior probabilistic models of the structural system parameters. Finally, prior probabilistic models of random generalized matrices could be constructed using the so-called nonparametric approach of model uncertainties. Thus, the generalized probabilistic approach displayed its ability to take into account some level of modeling errors associated with structural connections.

In order to find a robust optimal design, a strategy was defined with respect to the evaluation of

physical quantities representative of the objective acoustic performance associated with a given evaluated system. The choice was made to define sets of problems in keeping with standard experimental evaluation procedures. Following, laboratory rooms are included in the model using a decoupled approach. In regard to airborne sound insulation, successive acoustical point sources are used for the evaluation of a mean sound reduction index. In regard to impact sound insulation, successive tapping machine positions are used for the evaluation of a mean impact sound level. In particular, a general methodology was presented for the construction of the structure dependent external excitation resulting from the tapping machine. Emphasis was put on the sensitivity of the observables to the definition of the evaluation. Eventually, the evaluation of the performance associated with an uncertain design consists in solving an *ad hoc* stochastic computational model for a set of fixed deterministic external excitations.

Finally, considering the problem of seeking for a robust optimal design among a class of admissible systems, a specific strategy was defined. Indeed, with respect to lightweight designs constituted of the assembly of engineered products and whose characteristics have to be consistent with the regulation, search space is discrete and the problem becomes combinatorial. Moreover, multi-objective optimisation problems ultimately have to be considered, and the class of the evolutionary algorithms is chosen for its ability to handle such problems. Fitness functions were proposed according to most recent findings about single number quantities and comfort perception. Set of treated optimisation problems converged towards identical directions, for which bending stiffness is maximised, thus pushing structural resonances higher in frequency and keeping systems in their stiffness controlled state as far as possible.

Perspectives

Along this work, explicit or underlying perspectives could be perceived with respect to the robust design of lightweight stuctural elements. Those would be separated in two categories. First of all, before any further modeling considerations, there is a crucial need for the definition of a work basis and of what has to be observed. If objective performance criteria are starting to head towards a good adequation with inhabitant perceptions, the translation of this *in situ* information to laboratory evaluation is currently unclear at low frequencies, in particular considering the influence of laboratory characteristics onto evaluated quantities. If objective performance is to be rated from first third octave bands comprised between 20 and 100 Hz, in which first structral resonances take place and pressure fields expand onto few room modes, a close attention has to be directed towards boundary conditions, structural connections as well as room characteristics, *in situ* as well as in laboratory conditions.

Then, from the modeling and understanding of individual systems standpoint, constructed nominal models appeared self-sufficient to be able to take into account the complexity of systems which do not include resilient channels or floor coverings. Such features would necessit further investigations and validations which are straightforward from the existing basis. Furthermore, experimental characterisation of the interaction between structural components and different poroelastic media would be necessary in order to define adequate modeling strategies function of the poroelastic frame properties and mounting.

In general, ambitious experimental campaign with targeted measurements has to be conducted in order to enrich nominal as well as stochastic predictions. In particular, evaluation of statistical dispersions among nominally identical products but from different manufacturers could be of interest. Furthermore, it could be observed that local quantities (such as velocities) or global quantities (such as sound pressure levels) displayed high sensitivity to structural model uncertainties. On the one hand, this is a sign that predictions resulting from nominal computational models are not trustworthy. On the other hand, a strategy has to be chosen accordingly, whether hyperparameters for prior probabilistic models associated with model uncertainties need to be identified, or nominal models need to be improved. In this work, experimental investigations were performed from single structural components to full scale structural shear panel. The next step forward would be the addition of boundary conditions and consideration of systems within evaluation conditions. Localised quantities such as velocities or single point pressures appear as the best source of informations in regard to current modeling capacities.

Finally, in order to ensure that obtained solutions at low frequencies do not result in a downgrade of the performance at high frequencies, as it could have been previously experimentally observed, different

approaches have to meet for the definition of fitness functions over the whole frequency range of interest in building acoustics. Chosen optimisation framework is suited to multi-objective optimisation. Then, considering relatively straightforward subsystem partitioning in regard to lightweight systems, statistical energy analysis methods come to mind for the construction of additional fitness functions.

Appendices

A Validation of the finite element implementation with respect to the Biot displacement formulation

In this appendix, the finite element implementation of the poroelastic elements using the displacement formulation is validated with respect to one dimensional analytical solutions. In [75], reference problems were presented, later used in [35] for similar validation of a finite element implementation.

A.1 Analytical solutions for the sound propagation in a unidimensional poroelastic medium

According to [24, 35, 75], the unidimensional dynamical behavior associated with a poroelastic medium is governed by three waves: one solid-borne compressional wave, one fluid-borne compressional wave and one shear wave. Moreover, wavenumbers k_1, k_2 and k_3 respectively associated with the solid-borne wave, fluid borne wave and shear wave can be written as

$$k_1^2 = \frac{\omega^2}{2(PR - Q^2)} \left(P\rho_{22} + R\rho_{11} - 2Q\rho_{12} - \sqrt{\Delta} \right) , \tag{A.1}$$

$$k_2^2 = \frac{\omega^2}{2(PR - Q^2)} \left(P\rho_{22} + R\rho_{11} - 2Q\rho_{12} + \sqrt{\Delta} \right) , \tag{A.2}$$

$$k_3^2 = \frac{\omega^2}{\mu_{\mathrm{ps}}} \left(\frac{\rho_{11}\rho_{22} - \rho_{12}^2}{\rho_{22}} \right) , \tag{A.3}$$

in which $\Delta = (P\rho_{22} + R\rho_{11} - 2Q\rho_{12})^2 - 4(PR - Q^2)(\rho_{11}\rho_{22} - \rho_{12}^2)$.

For an isotropic poroelastic material and with the underlying hypothesis that the frame material at the micro scale is much more stiff than the homogenised poroelastic material at the macro scale, the parameters P, Q and R from the Biot theory are defined, using a viscous damping model for the frame, by

$$P = (\tilde{\lambda}_{\mathrm{ps}}(\omega) + 2\tilde{\mu}_{\mathrm{ps}}(\omega)) + \frac{(1-\phi)^2}{\phi} \tilde{K}^{\mathrm{f}}(\omega) , \tag{A.4}$$

$$Q = (1-\phi)\, \tilde{K}^{\mathrm{f}}(\omega) , \tag{A.5}$$

$$R = \phi\, \tilde{K}^{\mathrm{f}}(\omega) . \tag{A.6}$$

Parameters $\tilde{\lambda}_{\mathrm{ps}}(\omega)$ and $\tilde{\mu}_{\mathrm{ps}}(\omega)$ are complex and frequency dependent to account for a viscous damping such as in Eq. (2.10). Moreover, parameters ρ_{11}, ρ_{22} and ρ_{12} associated with inertial and viscous effects, are defined by

$$\rho_{11} = (1-\phi)\, \rho_{\mathrm{ps}} + \rho_a + \frac{\tilde{b}(\omega)}{i\omega} , \tag{A.7}$$

$$\rho_{22} = \phi\, \rho_{\mathrm{f}} + \rho_a + \frac{\tilde{b}(\omega)}{i\omega} , \tag{A.8}$$

$$\rho_{12} = -\rho_a - \frac{\tilde{b}(\omega)}{i\omega} . \tag{A.9}$$

The dilatational and rotational waves are decoupled such that, within the unidimensional poroelastic material, the normal displacement field in the solid and fluid phases can be expanded on a functional basis of plane compressional waves as

$$u^{\mathrm{ps}}(\omega; x) = u^{\mathrm{ps}}_{1+}\, \mathrm{e}^{ik_1 x} + u^{\mathrm{ps}}_{1-}\, \mathrm{e}^{-ik_1 x} + u^{\mathrm{ps}}_{2+}\, \mathrm{e}^{ik_2 x} + u^{\mathrm{ps}}_{2-}\, \mathrm{e}^{-ik_2 x}\,, \tag{A.10}$$

$$u^{\mathrm{pF}}(\omega; x) = u^{\mathrm{pF}}_{1+}\, \mathrm{e}^{ik_1 x} + u^{\mathrm{pF}}_{1-}\, \mathrm{e}^{-ik_1 x} + u^{\mathrm{pF}}_{2+}\, \mathrm{e}^{ik_2 x} + u^{\mathrm{pF}}_{2-}\, \mathrm{e}^{-ik_2 x}\,, \tag{A.11}$$

meanwhile the transverse displacement fields can be expanded on a functional basis of plane shear waves as

$$v^{\mathrm{ps}}(\omega; x) = v^{\mathrm{ps}}_{1+}\, \mathrm{e}^{ik_3 x} + v^{\mathrm{ps}}_{1-}\, \mathrm{e}^{-ik_3 x}\,, \tag{A.12}$$

$$v^{\mathrm{pF}}(\omega; x) = v^{\mathrm{pF}}_{1+}\, \mathrm{e}^{ik_3 x} + v^{\mathrm{pF}}_{1-}\, \mathrm{e}^{-ik_3 x}\,. \tag{A.13}$$

A.2 Unidimensional reference problems

A poroelastic material sample, whose thickness $L = 0.1$ m, is considered and discretized using eight hexaedron poroelastic elements. Depending on the problem, transverse or normal displacements are set to zero to emulate unidimensionality. According to [35, 75], the response of the poroelastic medium to three load cases is investigated. The first one consists in a normal incidence acoustic plane wave of unitary amplitude. The poroelastic medium is bonded to an impervious wall on the opposite end and the normal impedance is observed. Such load case was also presented in [52]. The second one consists in a prescribed normal displacement on one end. The resulting solid and fluid phases normal velocities are observed on the other end. Finally, a transverse displacement is prescribed on one end and the resulting transverse displacements are observed on the other end.

Furthermore, the physical parameters corresponding to the poroelastic material 1 and 2 with respect to the cases presented in [35] are given in Table 5. According to [52], material 1 corresponds to a fiber-glass type of poroelastic, whose frame is very limp, whereas material 2 corresponds to glasswool which is more representative of a typical lightweight insulating material associated with building construction.

	Por. 1	Por. 2
Young's modulus [kPa]	42	4400
Poisson's ratio	0	0
Mass density $(1-\phi)\rho^{\mathrm{ps}}$ [kg/m^3]	30	30
Porosity ϕ	0.95	0.94
Flow resistivity σ [N.s/m^4]	25000	40000
Tortuosity α_∞	1.4	1.06
Viscous length Λ [μm]	93.2	56
Thermal length Λ' [μm]	93.2	110
Structural loss factor η_{ps}	0.05	0.1

(a) Poroelastic medium parameters.

Standard pressure P_0	1.015×10^5 Pa
Mass density ρ^F	1.21 kg/m^3
Heat capacity ratio γ	1.4
Sound velocity c_F	340 m/s
Prandtl number Pr	0.72
Dynamic viscosity η_{f}	1.81×10^{-5} N.s/m^2

(b) Air parameters.

Table 5: Poroelastic medium and air parameters.

Normal impedance

A normal incidence plane wave excites the poroelastic sample at $x = -L$ whereas the other end is fixed. Thus, assuming harmonic excitation and according to [35, 75], the following boundary conditions

hold

$$u^{\mathrm{ps}}(0) = 0\,, \tag{A.14}$$

$$u^{\mathrm{pf}}(0) = 0\,, \tag{A.15}$$

$$P\frac{\partial u^{\mathrm{ps}}}{\partial x}\bigg|_{x=-L} + Q\frac{\partial u^{\mathrm{pf}}}{\partial x}\bigg|_{x=-L} = (1-\phi)\,p\,, \tag{A.16}$$

$$Q\frac{\partial u^{\mathrm{ps}}}{\partial x}\bigg|_{x=-L} + R\frac{\partial u^{\mathrm{pf}}}{\partial x}\bigg|_{x=-L} = \phi\,p\,. \tag{A.17}$$

Then, one can refer to [35, 75] for the solutions u^{ps} and u^{pf} of Eqs. (A.10) and (A.11). Following, the normal impedance at $x = -L$ is written as

$$Z = \frac{p}{i\omega\left((1-\phi)\,u^{\mathrm{ps}}(-L) + \phi\,u^{\mathrm{pf}}(-L)\right)}\,. \tag{A.18}$$

Figure 10 compares the real and imaginary parts of the analytical and predicted normal impedance. Good match is observed over the whole frequency band with respect to both materials.

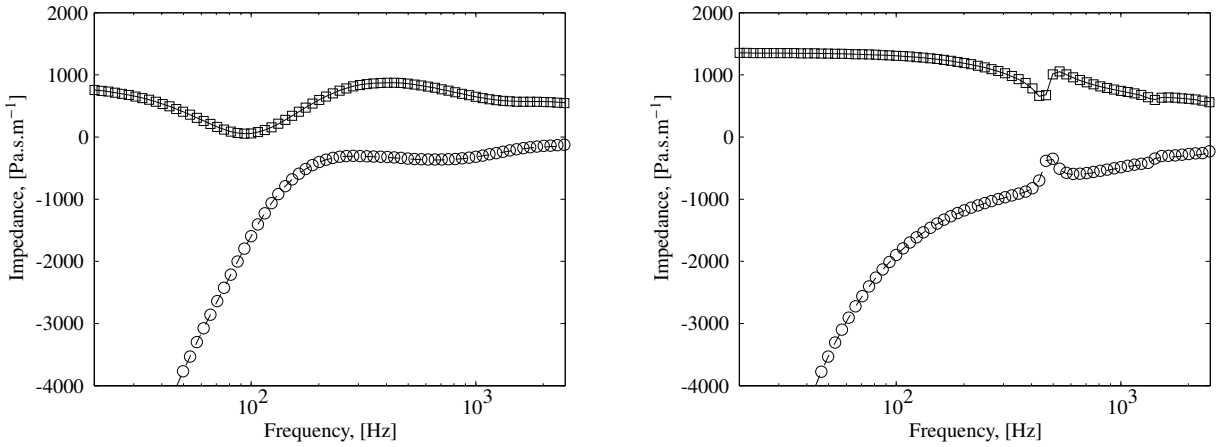

(a) Poroelastic material 1

(b) Poroelastic material 2

Figure 10: Normal impedance of the considered unidimensional poroelastic sample. Real part: analytical solution (thin black solid line), finite element model (black squares); imaginary part (thin black dashed line), finite element model (black circles).

Prescribed normal displacement

The prescribed normal displacement u_{ex} excites the poroelastic sample at $x = -L$ whereas the other end is free. Thus, assuming harmonic excitation and according to [35, 75], the following boundary conditions hold

$$u^{\mathrm{ps}}(-L) = u_{ex}\,, \tag{A.19}$$

$$u^{\mathrm{pf}}(-L) = u_{ex}\,, \tag{A.20}$$

$$\frac{\partial u^{\mathrm{ps}}}{\partial x}\bigg|_{x=0} = 0\,, \tag{A.21}$$

$$\frac{\partial u^{\mathrm{pf}}}{\partial x}\bigg|_{x=0} = 0\,. \tag{A.22}$$

Once again, one can refer to [35, 75] for the solutions u^{ps} and u^{pf} of Eqs. (A.10) and (A.11). Figure 11 compares the analytical and predicted normal velocities with respect to the solid and fluid phases of the

poroelastic medium. Good match is observed over the whole frequency band with respect to material 2. However, it can be seen that the model has yet to converge past 400 Hz in regard to the extremely limp material 1 (which is also observed in [35]). Indeed, due to the low stiffness of the frame the modal density associated with the solid phase of the poroelastic medium rapidly increases and the mesh has to be refined. Therefore, it can be noted that the biggest discrepancies are observed with respect to the solid phase velocity.

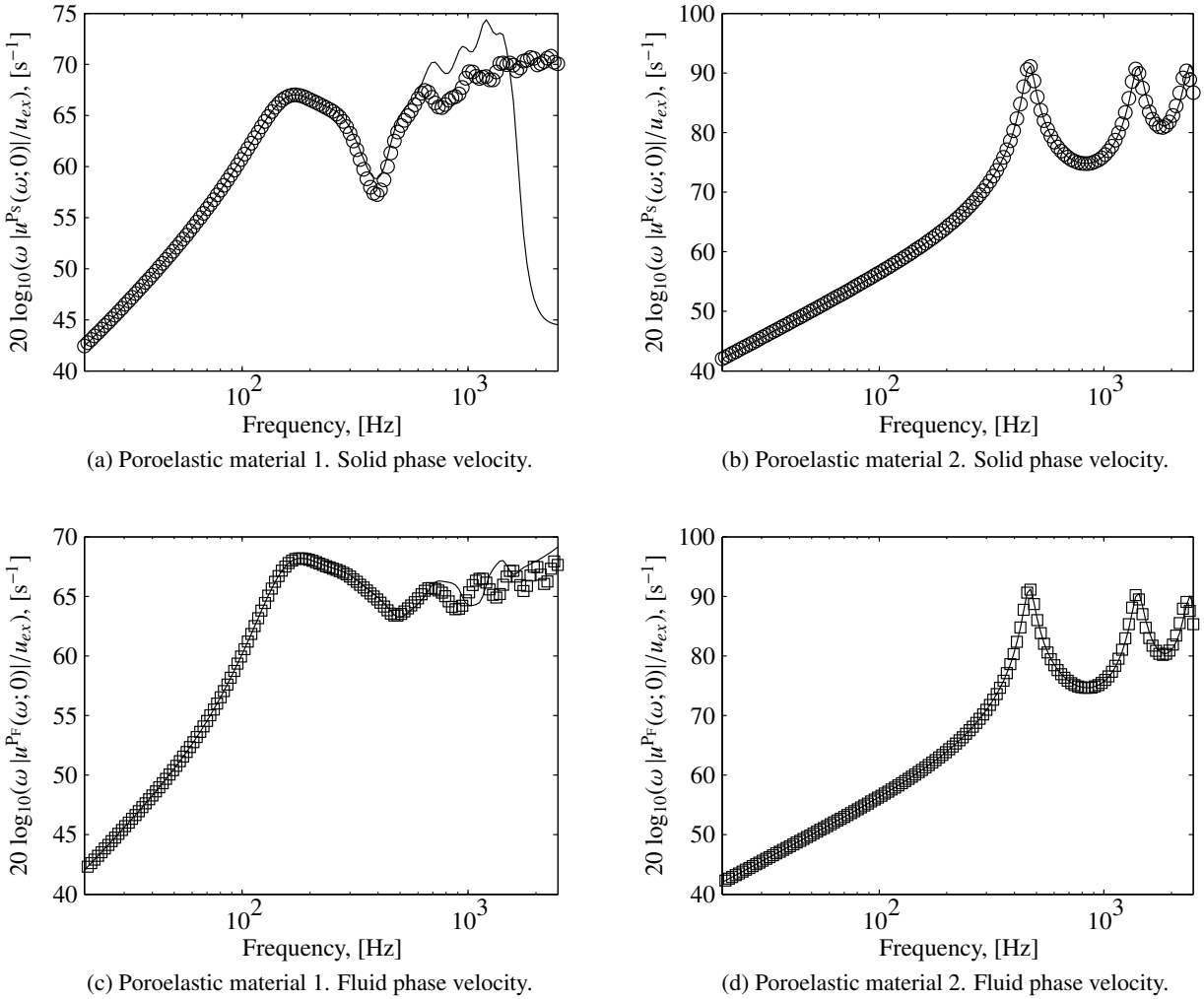

(a) Poroelastic material 1. Solid phase velocity.

(b) Poroelastic material 2. Solid phase velocity.

(c) Poroelastic material 1. Fluid phase velocity.

(d) Poroelastic material 2. Fluid phase velocity.

Figure 11: Normal impedance of the considered unidimensional poroelastic sample. Real part: analytical solution (thin black solid line), finite element model (black squares); imaginary part (thin black dashed line), finite element model (black circles).

Prescribed shear displacement

The prescribed transverse displacement v_{ex} excites the poroelastic frame at $x = -L$ whereas the other end is free. The following boundary conditions hold

$$v^{\mathrm{ps}}(-L) = v_{ex} \,, \tag{A.23}$$

$$\left.\frac{\partial v^{\mathrm{ps}}}{\partial x}\right|_{x=0} = 0 \,. \tag{A.24}$$

Figure 12 compares the analytical and predicted transverse velocities with respect to the solid and fluid phases of the poroelastic medium. Once again, good match is observed over the whole frequency band

with respect to material 2 and the same observations than for the prescribed normal displacement load case can be made for the extremely limp material 1. However, as the shear wave is dominated by the frame, large discrepancy also appears in regard to the fluid phase velocity.

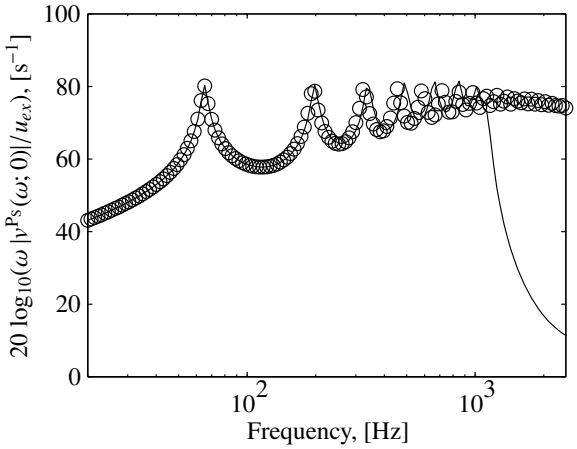

(a) Poroelastic material 1. Solid phase velocity.

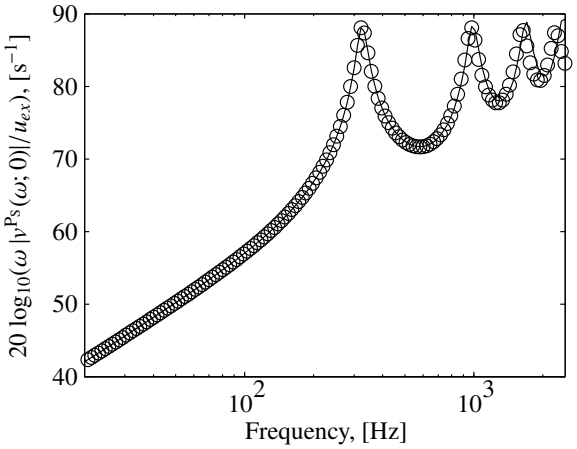

(b) Poroelastic material 2. Solid phase velocity.

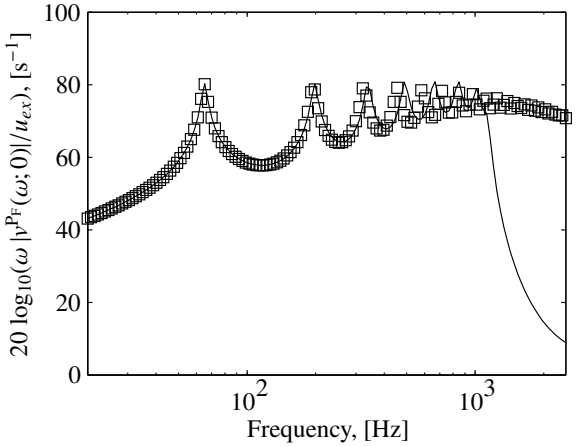

(c) Poroelastic material 1. Fluid phase velocity.

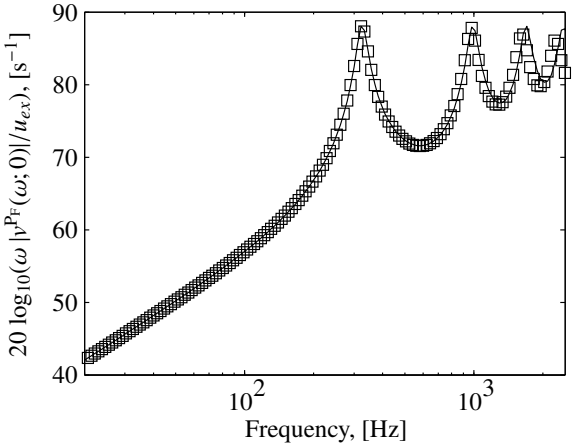

(d) Poroelastic material 2. Fluid phase velocity.

Figure 12: Normal impedance of the considered unidimensional poroelastic sample. Real part: analytical solution (thin black solid line), finite element model (black squares); imaginary part (thin black dashed line), finite element model (black circles).

B Limp frame poroelastic medium equivalent fluid model

In this appendix, we derive the equations associated with the poroelastic medium modeled as an equivalent fluid from a simplification of the full displacement formulation, in a comparable manner than in the classical references [24, 52] for the derivation of the mixed displacement-pressure formulation. Within the case where the poroelastic medium can be modeled as an equivalent acoustic fluid, the poroelastic solid phase, or frame, is considered motionless. Consequently, Eq. (2.29) becomes

$$-\ \omega^2(\phi\,\rho^{\mathrm{f}}+\rho^{a})\,u_j^{\mathrm{p_f}}+i\omega\,\tilde{b}(\omega)\,u_j^{\mathrm{p_f}}-\sigma_{jk,k}^{\mathrm{p_f}}(\mathbf{u}^{\mathrm{p_s}},\mathbf{u}^{\mathrm{p_f}})=0\quad\text{in}\quad\Omega^{\mathrm{p}}\,. \tag{B.1}$$

Let p^{e} be the equivalent fluid pressure disturbance field such that the stress tensor associated with the fluid phase of the poroelastic medium is written as

$$\sigma_{jk}^{\mathrm{p_f}}(\mathbf{u}^{\mathrm{p_s}},\mathbf{u}^{\mathrm{p_f}})=-\,\delta_{jk}\,\phi\,p^{\mathrm{e}}\,. \tag{B.2}$$

Then, using Eqs. (2.25) and (B.2) into Eq. (B.1), we obtain

$$- \omega^2 \phi \, \tilde{\rho}^{\mathrm{f}} \, u_j^{\mathrm{p_f}} + \phi \, p_{,j}^{\mathrm{e}} = 0 \quad \text{in} \quad \Omega^{\mathrm{p}} \, . \tag{B.3}$$

Moreover, the constitutive Eqs. (2.36) and (2.40) yield

$$- p^{\mathrm{e}} = \tilde{K}_{\mathrm{f}}(\omega) \, \mathrm{tr}\{\epsilon^{\mathrm{p_f}}(\mathbf{u}^{\mathrm{p_f}})\} \quad \text{in} \quad \Omega^{\mathrm{p}} \, , \tag{B.4}$$

and finally, using Eq. (B.4) into the divergence of Eq. (B.3) gives the wave equation associated with the poroelastic medium modeled as an equivalent fluid

$$- \omega^2 \frac{\phi}{\tilde{K}_{\mathrm{f}}(\omega)} p^{\mathrm{e}} - \frac{\phi}{\tilde{\rho}^{\mathrm{f}}(\omega)} p_{,jj}^{\mathrm{e}} = 0 \quad \text{in} \quad \Omega^{\mathrm{p}} \, . \tag{B.5}$$

The remaining normal stress continuity boundary condition with the internal acoustic fluid, defined by Eq. (2.34), yields

$$p^{\mathrm{e}} = p \quad \text{on} \quad \Sigma \, . \tag{B.6}$$

In regard to the structure however, the displacement continuity with the poroelastic medium can no longer be prescribed due to the solid phase being assumed motionless. Consequently, it is supposed that a thin air gap separates the structure from the poroelastic medium and the mass flux continuity across the pervious interface, from which derives Eq. (2.18), then gives

$$u_j^{\mathrm{s}} n_j^{\mathrm{s}} = - \phi \, u_j^{\mathrm{p_f}} n_j^{\mathrm{p}} \quad \text{on} \quad \Gamma \, . \tag{B.7}$$

Using Eq. (B.7) into Eq. (B.3), we then have

$$p_{,j}^{\mathrm{e}} \, n_j^{\mathrm{p}} = - \omega^2 \, \frac{\tilde{\rho}^{\mathrm{f}}(\omega)}{\phi} \, u_j^{\mathrm{s}} n_j^{\mathrm{s}} \quad \text{on} \quad \Gamma \, . \tag{B.8}$$

The equivalent fluid modeling is also adapted to limp media such as fibrous materials but in this case the frame cannot be assumed motionless and there is a need to account for its inertial effect, in particular at low frequencies [24, 44, 46, 47]. The corrected effective fluid density $\tilde{\rho}^{\mathrm{f}\prime}(\omega)$, taking into account the limp frame inertial effect, is then constructed according to [24, 46] such that

$$\tilde{\rho}^{\mathrm{f}\prime}(\omega) = \frac{\tilde{\rho}^{\mathrm{f}}(\omega) \, \rho_t^{\mathrm{p}} - \phi \, {\rho^{\mathrm{f}}}^2}{\tilde{\rho}^{\mathrm{f}}(\omega) + \phi \, \rho_t^{\mathrm{p}} - 2 \, \phi \, \rho^{\mathrm{f}}} \, , \tag{B.9}$$

where ρ_t^{p} denotes the total mass density, which is written as

$$\rho_t^{\mathrm{p}} = (1 - \phi) \, \rho^{\mathrm{p_s}} + \phi \, \rho^{\mathrm{f}} \, . \tag{B.10}$$

Let $C_{\Omega^{\mathrm{e}}}$ be the function space constituted of all the sufficiently differentiable complex-valued functions defined on Ω^{p}. For any p^{e} and δp^{e} in $C_{\Omega^{\mathrm{e}}}$ the complex frequency dependent mass and stiffness sesquilinear forms for the limp frame poroelastic medium modeled as an equivalent acoustic fluid are defined by

$$m^{\mathrm{e}}(p^{\mathrm{e}}, \delta p^{\mathrm{e}}; \omega) = \frac{\phi}{\tilde{K}^{\mathrm{f}}(\omega)} \int_{\Omega^{\mathrm{f}}} p^{\mathrm{e}} \, \overline{\delta p^{\mathrm{e}}} \, \mathrm{d}V \, , \tag{B.11}$$

$$k^{\mathrm{e}}(p^{\mathrm{e}}, \delta p^{\mathrm{e}}; \omega) = \frac{\phi}{\tilde{\rho}^{\mathrm{f}\prime}(\omega)} \int_{\Omega^{\mathrm{f}}} p_{,j}^{\mathrm{e}} \, \overline{\delta p_{,j}^{\mathrm{e}}} \, \mathrm{d}V \, . \tag{B.12}$$

Moreover, the sesquilinear coupling form between the equivalent fluid and the structure is defined by

$$c_{\Gamma}(p^{\mathrm{e}}, \delta \mathbf{u}^{\mathrm{s}}) = \int_{\Pi} p^{\mathrm{e}} \, n_j^{\mathrm{p}} \, \overline{\delta u_j^{\mathrm{s}}} \, \mathrm{d}S \, . \tag{B.13}$$

References

[1] "Accord Cadre Bois-Construction-Environnement," 2001.

[2] Alcimed, "Marché actuel des nouveaux produits issus du bois et évolutions à échéance 2020," tech. rep., PIPAME, 2012.

[3] M. Villot, J.-l. Kouyoumji, E. Gerretsen, D. Bard, B. Zhang, B. Rasmussen, B. Ingelaere, C. Hopkins, U. Schanda, F. Schopter, C. Guigou-Carter, A. Homb, N. Labonnote, S. Lentzen, A. Koopman, A. Jorissen, and A. Harte, "WG1 : Prediction Methods for Sound and Vibration Performances, Including Low Frequencies," tech. rep., COST Action FP0702 - Forests, their Products and Services, 2012.

[4] C. Guigou-Carter, M. Villot, and R. Wetta, "Prediction Method Adapted to Wood Frame Lightweight Constructions," *Building Acoustics*, vol. 13, no. 3, pp. 173–188, 2006.

[5] *NF EN 12354 Building acoustics - Estimation of acoustic performance of buildings from the performance of elements*. 2000.

[6] W. Blazier and R. DuPree, "Investigation of low-frequency footfall noise in wood-frame, multifamily building construction," *Journal of the Acoustical Society of America*, vol. 96, no. 3, pp. 1521–1532, 1994.

[7] J. Parmanen, P. Sipari, and S. Uosukainen, "Sound insulation of multi-storey houses. Summary of impact sound insulation.," tech. rep., Technical Research Centre of Finland, Espoo, 1999.

[8] A. Warnock and J. Birta, "Detailed Report for Consortium on Fire Resistance and Sound Insulation of Floors: Sound Transmission and Impact Insulation Data in 1/3 Octave Bands," tech. rep., NRC-CNRC, 2000.

[9] H. Chung, G. Dodd, G. Emms, K. Mcgunnigle, and G. Schmid, "Maximising impact sound resistance of timber framed floor / ceiling systems," Tech. Rep. February, Forest and Wood Products Research and Development Corporation, 2006.

[10] J. Forssenn, W. Kropp, J. Brunskog, S. Ljunggren, D. Bard, G. Sandberg, F. Ljunggren, A. Agren, O. Hallström, H. Dybro, K. Tillberg, K. Larsson, K. Jarnerö, L.-G. Sjökvist, B. Östman, K. Hagberg, Å. Bolmsvik, A. Olsson, C.-G. Ekstrand, and M. Johansson, "Acoustics in wooden buildings State of the art 2008," tech. rep., SP Sveriges Tekniska Forskningsinstitut, 2008.

[11] F. Ljunggren, C. Simmons, and K. Hagberg, "Findings from the AkuLite project : Correlation between measured vibro-acoustic parameters and subjective perception in lightweight buildings," in *Proceedings Internoise*, 2013.

[12] F. Ljunggren, C. Simmons, and K. Hagberg, "Correlation between sound insulation and occupants' perception - Proposal of alternative single number rating of impact sound," *Applied Acoustics*, vol. 85, pp. 57–68, 2014.

[13] C. Guigou-Carter and N. Balanant, "Acoustic comfort evaluation in lightweight wood-based and heavyweight concrete-based buildings," in *Proceedings Internoise*, 2015.

[14] C. Johansson, "Field Measurements of 170 Nominally Identical Timber Floors - A Statistical Analysis," in *Proceedings Internoise*, 2000.

[15] R. Öqvist, *Variations in sound insulation in multi-storey lightweight timber constructions*. Licentiate thesis, Lulea University of Technology, 2010.

[16] R. Öqvist, F. Ljunggren, and A. Agren, "Variations in Sound Insulation in Nominally Identical Prefabricated Lightweight Timber Constructions," *Building Acoustics*, vol. 17, no. 2, pp. 91–103, 2010.

[17] R. Öqvist, F. Ljunggren, and A. Agren, "On the uncertainty of building acoustic measurements - Case study of a cross-laminated timber construction," *Applied Acoustics*, vol. 73, no. 9, pp. 904–912, 2012.

[18] R. J. Craik and J. A. Steel, "The effect of workmanship on sound transmission through buildings: Part 1—Airborne sound," *Applied Acoustics*, vol. 27, no. 1, pp. 57–63, 1989.

[19] R. J. Craik and J. a. Steel, "The effect of workmanship on sound transmission through buildings: Part 2—Structure-borne sound," *Applied Acoustics*, vol. 27, no. 1, pp. 137–145, 1989.

[20] K. A. Dickow, P. H. Kirkegaard, and L. V. Andersen, "An evaluation of test and physical uncertainty of measuring vibration in wooden junctions," *Proceedings of the International Conference on Uncertainty in Structural Dynamics*, 2012.

[21] A. Bolmsvik, A. Linderholt, A. Brandt, and T. Ekevid, "FE modelling of light weight wooden assemblies – Parameter study and comparison between analyses and experiments," *Engineering Structures*, vol. 73, pp. 125–142, 2014.

[22] R. Ohayon and C. Soize, *Advanced Computational Vibroacoustics*. Cambridge University Press, 2014.

[23] G. Sandberg and R. Ohayon, eds., *Computational Aspects of Structural Acoustics*. Springer-Verlag Wien, 2009.

[24] J. F. Allard and N. Atalla, *Propagation of Sound in Porous Media*. Wiley, 2nd ed., 2009.

[25] M. P. Mignolet, C. Soize, and J. Avalos, "Nonparametric Stochastic Modeling of Structures with Uncertain Boundary Conditions/Coupling Between Substructures," *AIAA Journal*, vol. 51, no. 6, pp. 1296–1308, 2013.

[26] C. Soize, "Generalized probabilistic approach of uncertainties in computational dynamics using random matrices and polynomial chaos decompositions," *International Journal for Numerical Methods in Engineering*, vol. 81, no. 8, pp. 939–970, 2010.

[27] C. Soize, "A nonparametric model of random uncertainties for reduced matrix models in structural dynamics," *Probabilistic Engineering Mechanics*, vol. 15, no. 3, pp. 277–294, 2000.

[28] C. Soize, "Random matrix theory for modeling uncertainties in computational mechanics," *Computer Methods in Applied Mechanics and Engineering*, vol. 194, no. 12-16, pp. 1333–1366, 2005.

[29] R. Ohayon and C. Soize, *Structural Acoustics and Vibration*. Academic Press, 1998.

[30] R. Ohayon and C. Soize, "Advanced computational dissipative structural acoustics and fluid-structure interaction in low-and medium-frequency domains. Reduced- order models and uncertainty quantification," *International Journal of Aeronautical and Space Sciences*, vol. 13, no. 2, pp. 127–153, 2012.

[31] F. C. Sgard, N. Atalla, and R. Panneton, "A modal reduction technique for the finite element formulation of Biot's poroelasticity equations in acoustics applied to multilayered structures," *The Journal of the Acoustical Society of America*, vol. 103, no. 5, p. 2882, 1998.

[32] O. Dazel, F. Sgard, C.-H. Lamarque, and N. Atalla, "An Extension of Complex Modes for the Resolution of Finite-Element Poroelastic Problems," *Journal of Sound and Vibration*, vol. 253, no. 2, pp. 421–445, 2002.

[33] O. Dazel, B. Brouard, N. Dauchez, and A. Geslain, "Enhanced Biot's finite element displacement formulation for porous materials and original resolution methods based on normal modes," *Acta Acustica united with Acustica*, vol. 95, no. 3, pp. 527–538, 2009.

[34] O. Dazel, B. Brouard, J.-P. Groby, and P. Göransson, "A normal modes technique to reduce the order of poroelastic models: application to 2D and coupled 3D models," *International Journal for Numerical Methods in Engineering*, vol. 96, no. July, pp. 110–128, 2013.

[35] P. Davidsson, *Structure-acoustic analysis; finite element modelling and reduction methods*. PhD thesis, Lund University, 2004.

[36] P. Davidsson and G. Sandberg, "A reduction method for structure-acoustic and poroelastic-acoustic problems using interface-dependent Lanczos vectors," *Computer Methods in Applied Mechanics and Engineering*, vol. 195, no. 17-18, pp. 1933–1945, 2006.

[37] C. Batifol, M. N. Ichchou, and M. A. Galland, "Hybrid modal reduction for poroelastic materials," *Comptes Rendus - Mecanique*, vol. 336, no. 10, pp. 757–765, 2008.

[38] R. Rumpler, *Efficient Finite Element Approach for Structural-Acoustic Applications Including 3D Modelling of Sound Absorbing Porous Materials*. PhD thesis, CNAM - Royal Institute of Technology, 2012.

[39] R. Rumpler, J.-F. Deü, and P. Göransson, "A modal-based reduction method for sound absorbing porous materials in poro-acoustic finite element models.," *The Journal of the Acoustical Society of America*, vol. 132, no. 5, pp. 3162–79, 2012.

[40] R. Rumpler, P. Göransson, and J.-F. Deü, "A residue-based mode selection and sorting procedure for efficient poroelastic modeling in acoustic finite element applications," *The Journal of the Acoustical Society of America*, vol. 134, no. 6, p. 4730, 2013.

[41] R. Kicinger, T. Arciszewski, and K. De Jong, "Evolutionary computation and structural design: A survey of the state-of-the-art," *Computers and Structures*, vol. 83, no. 23-24, pp. 1943–1978, 2005.

[42] V. Hongisto, *Airborne sound insulation of wall structures - Measurement and prediction methods*. PhD thesis, Helsinki University of Technology, 2000.

[43] A. Craggs, "A finite element model for rigid porous absorbing materials," *Journal of Sound and Vibration*, vol. 61, no. 1, pp. 101–111, 1978.

[44] P. Göransson, "Acoustic Finite Element Formulation of a Flexible Porous Material - A Correction for Inertial Effects," *Journal of Sound and Vibration*, vol. 185, no. 4, pp. 559–580, 1995.

[45] R. Panneton, *Modélisation Numérique Tridimensionnelle Par Eléments Finis Des Milieux Poroélastiques*. PhD thesis, Sherbrooke, 1996.

[46] R. Panneton, "Comments on the limp frame equivalent fluid model for porous media," *The Journal of the Acoustical Society of America*, vol. 122, no. 6, 2007.

[47] H.-Y. Lai, S. Katragadda, J. Bolton, and J. H. Alexander, "Layered Fibrous Treatments for a Sound Absorption and Sound Transmission," in *Proceedings Noise and Vibration Conference*, 1997.

[48] J. Bolton and E. Green, "Normal incidence sound transmission through double-panel systems lined with relatively stiff, partially reticulated polyurethane foam," *Applied Acoustics*, vol. 39, no. 1-2, pp. 23–51, 1993.

[49] R. Panneton, "Numerical prediction of sound transmission through finite multilayer systems with poroelastic materials," *The Journal of the Acoustical Society of America*, vol. 100, no. 1, p. 346, 1996.

[50] Y. J. Kang and J. S. Bolton, "Finite element modeling of isotropic elastic porous materials coupled with acoustical finite elements," *Journal of the Acoustical Society of America*, vol. 98, no. 1, pp. 635–643, 1995.

[51] Peter Göransson, "A 3-D, symmetric, finite element formulation of the Biot equations with application to accoustic wave propagation through an elastic porous medium," *International Journal for Numerical Methods in Engineering*, vol. 41, no. September 1996, pp. 167–192, 1998.

[52] N. Atalla, R. Panneton, and P. Debergue, "A mixed displacement-pressure formulation for poroelastic materials," *Journal of the Acoustical Society of America*, vol. 104, no. 3, pp. 1444–1452, 1998.

[53] N. Atalla, M. A. Hamdi, and R. Panneton, "Enhanced weak integral formulation for the mixed (u,p) poroelastic equations," *The Journal of the Acoustical Society of America*, vol. 109, no. 6, pp. 3065–3068, 2001.

[54] N.-E. Hörlin, M. Nordström, and P. Göransson, "A 3-D Hierarchical FE Formulation of Biot's Equations for Elasto-Acoustic Modelling of Porous Media," *Journal of Sound and Vibration*, vol. 245, no. 4, pp. 633–652, 2001.

[55] O. Dazel, B. Brouard, C. Depollier, and S. Griffiths, "An alternative Biot's displacement formulation for porous materials.," *The Journal of the Acoustical Society of America*, vol. 121, no. 6, pp. 3509–3516, 2007.

[56] N.-E. Hörlin, "A symmetric weak form of Biot's equations based on redundant variables representing the fluid, using a Helmholtz decomposition of the fluid displacement vector field," *International Journal for Numerical Methods in Engineering*, vol. 84, no. June, pp. 1613–1637, 2010.

[57] C. Desceliers, C. Soize, and S. Cambier, "Non-parametric-parametric model for random uncertainties in non-linear structural dynamics: Application to earthquake engineering," *Earthquake Engineering and Structural Dynamics*, vol. 33, no. 3, pp. 315–327, 2004.

[58] R. Cottereau, D. Clouteau, and C. Soize, "Probabilistic impedance of foundation: Impact of the seismic design on uncertain soils," *Earthquake Engineering and Structural Dynamics*, vol. 37, no. 6, pp. 899–918, 2008.

[59] C. Desceliers, C. Soize, S. Naili, and G. Haiat, "Probabilistic model of the human cortical bone with mechanical alterations in ultrasonic range," *Mechanical Systems and Signal Processing*, vol. 32, pp. 170–177, 2012.

[60] J. Guilleminot and C. Soize, "On the statistical dependence for the components of random elasticity tensors exhibiting material symmetry properties," *Journal of Elasticity*, vol. 111, no. 2, pp. 109–130, 2013.

[61] C. Soize and H. Chebli, "Random Uncertainties Model in Dynamic Substructuring Using a Non-parametric Probabilistic Model," *Journal of Engineering Mechanics*, vol. 129, no. 4, pp. 449–457, 2003.

[62] J.-F. Durand, C. Soize, and L. Gagliardini, "Structural-acoustic modeling of automotive vehicles in presence of uncertainties and experimental identification and validation.," *The Journal of the Acoustical Society of America*, vol. 124, no. 3, pp. 1513–1525, 2008.

[63] E. Capiez-Lernout and C. Soize, "Design Optimization With an Uncertain Vibroacoustic Model," *Journal of Vibration and Acoustics*, vol. 130, 2008.

[64] C. Desceliers, R. Ghanem, and C. Soize, "Maximum likelihood estimation of stochastic chaos representations from experimental data," *International Journal for Numerical Methods in Engineering*, vol. 66, no. 6, pp. 978–1001, 2006.

[65] C. Desceliers, C. Soize, and R. Ghanem, "Identification of chaos representations of elastic properties of random media using experimental vibration tests," *Computational Mechanics*, vol. 39, no. 6, pp. 831–838, 2007.

[66] C. Desceliers, C. Soize, Q. Grimal, M. Talmant, and S. Naili, "Stochastic inverse problem for the experimental identification in the ultrasonic range of a mechanical model for cortical bones," *Journal of Physics: Conference Series*, vol. 135, p. 012036, 2008.

[67] C. Soize, E. Capiez-Lernout, J.-F. Durand, C. Fernandez, and L. Gagliardini, "Probabilistic model identification of uncertainties in computational models for dynamical systems and experimental validation," *Computer Methods in Applied Mechanics and Engineering*, vol. 198, no. 1, pp. 150–163, 2008.

[68] B. Faverjon and C. Soize, "Equivalent acoustic impedance model. Part 1: Experiments and semi-physical model," *Journal of Sound and Vibration*, vol. 276, no. 3-5, pp. 571–592, 2004.

[69] B. Faverjon and C. Soize, "Equivalent acoustic impedance model. Part 2: Analytical approximation," *Journal of Sound and Vibration*, vol. 276, no. 3-5, pp. 593–613, 2004.

[70] C. Fernandez, C. Soize, and L. Gagliardini, "Fuzzy structure theory modeling of sound-insulation layers in complex vibroacoustic uncertain systems: theory and experimental validation.," *The Journal of the Acoustical Society of America*, vol. 125, no. 1, pp. 138–153, 2009.

[71] N.-E. Hörlin and P. Göransson, "Weak, anisotropic symmetric formulations of Biot's equations for vibro-acoustic modelling of porous elastic materials," *International Journal for Numerical Methods in Engineering*, vol. 84, pp. 1519–1540, 2010.

[72] W. R. Case and R. E. Vandegrift, "Improved Isoparametric Solid and Membrane Elements," in *Fourteenth NASTRAN Users' Colloquium*, pp. 28–38, 1986.

[73] R. H. MacNeal, "A Simple Quadrilateral Shell Element," *Computers & Structures*, vol. 8, pp. 175–183, 1978.

[74] R. H. MacNeal and R. L. Harder, "A Refined Four-Noded Membrane Element With Rotational Degrees Of Freedom," *Computers & Structures*, vol. 28, no. I, pp. 75–84, 1988.

[75] N. Dauchez, S. Sahraoui, and N. Atalla, "Convergence of poroelastic finite elements based on Biot displacement formulation," *The Journal of the Acoustical Society of America*, vol. 109, no. 1, pp. 33–40, 2001.

[76] R. D. Cook, D. S. Malkus, M. E. Plesha, and R. J. W. Witt, *Concept and Applications of Finite Element Analysis*. Wiley, 4th ed., 2002.

[77] Laboratory Forest Products, *Wood handbook - Wood as an engineering material*. United States Department of Agriculture, Forest Service, 2010.

[78] W. J. Drugan and J. R. Willis, "A micromechanics-based nonlocal constitutive equation and estimates of representative volume element size for elastic composites," *Journal of the Mechanics and Physics of Solids*, vol. 44, no. 4, pp. 497–524, 1996.

[79] N. Labonnote, A. Ronnquist, and K. A. Malo, "Semi-analytical prediction and experimental evaluation of material damping in wood panels," *Holzforschung*, vol. 67, no. 3, pp. 333–343, 2013.

[80] N. Labonnote, A. Ronnquist, and K. A. Malo, "Experimental evaluations of material damping in timber beams of structural dimensions," *Wood Science and Technology*, vol. 47, no. 5, pp. 1033–1050, 2013.

[81] L. Cremer, M. Heckl, and B. A. T. Petersson, *Structure-Borne Sound*. Springer, 3rd ed., 2005.

[82] T. C. T. Ting and T. Chen, "Poisson's ratio for anisotropic elastic materials can have no bounds," *Quarterly Journal of Mechanics and Applied Mathematics*, vol. 58, pp. 73–82, 2005.

[83] H. Berger, L. Barthe, and R. Ohayon, "Parametric updating of a finite element model from experimental modal characteristics," *Mechanical Systems and Signal Processing*, vol. 4, no. 3, pp. 233–242, 1990.

[84] *NF EN 338 : Structural timber - Strength classes*. 2009.

[85] *NF EN 12369-1 : Wood-based panels - Characteristic values for structural design - Part 1 : OSB, particleboards and fiberboards*. 2001.

[86] M. Villot, J.-l. Kouyoumji, E. Gerretsen, D. Bard, B. Zhang, B. Rasmussen, B. Ingelaere, C. Hopkins, U. Schanda, F. Schopter, C. Guigou-Carter, A. Homb, N. Labonnote, S. Lentzen, A. Koopman, A. Jorissen, and A. Harte, "WG4 : Acoustic Design of Lightweight Timber Frame Constructions," tech. rep., COST Action FP0702 - Forests, their Products and Services, 2012.

[87] J. N. Lee and Q. Wu, "Continuum Modeling of Engineering Constants of Oriented Strandboard," *Wood and Fiber Science*, vol. 35, no. 1, 2003.

[88] S. Sakji, C. Soize, and J.-V. Heck, "Probabilistic Uncertainty Modeling for Thermomechanical Analysis of Plasterboard Submitted to Fire Load," *Journal of Structural Engineering*, vol. 134, no. 10, pp. 1611–1618, 2008.

[89] *NF EN 520 : Gypsum plasterboards - Definitions, requirements and tests methods*. 2009.

[90] J. Quirt, A. Warnock, and J. Birta, "Sound Transmission Through Gypsum Board Walls: Sound Transmission Results," tech. rep., NRC-CNRC, 1995.

[91] G.-F. Lin and M. Garrelick, "Sound transmission through periodically framed parallel plates," *Journal of the Acoustical Society of America*, vol. 61, no. 4, pp. 1014–1018, 1977.

[92] C. Guigou-Carter and M. Villot, "Modelling of Sound Transmission Through Lightweight Elements with Stiffeners," *Building Acoustics*, vol. 10, no. 3, pp. 193–209, 2003.

[93] J. Brunskog, *Acoustic Excitation And Transmission Of Lightweight Structures*. PhD thesis, Lund University, 2002.

[94] J. Brunskog and P. Hammer, "Prediction model for the impact sound level of lightweight floors," *Acta Acustica united with Acustica*, vol. 89, no. 2, pp. 309–322, 2003.

[95] J. Wang, T. J. Lu, J. Woodhouse, R. S. Langley, and J. Evans, "Sound transmission through lightweight double-leaf partitions: Theoretical modelling," *Journal of Sound and Vibration*, vol. 286, no. 4-5, pp. 817–847, 2005.

[96] R. J. M. Craik and S. Smith, "Sound transmission through lightweight parallel plates: part 2 - structure borne sound.," *Apllied Acoustics*, vol. 61, pp. 247–269, 2000.

[97] R. J. M. Craik and L. Galbrun, "Vibration transmission through a frame typical of timber-framed buildings," *Journal of Sound and Vibration*, vol. 281, pp. 763–782, 2005.

[98] C. K. Hui and C. F. Ng, "Improvement of lightweight floating ceiling design with optimum stiffener and isolator locations," *Journal of Sound and Vibration*, vol. 327, no. 3-5, pp. 333–353, 2009.

[99] L. Galbrun, "Vibration transmission through plate/beam structures typical of lightweight buildings: Applicability and limitations of fundamental theories," *Applied Acoustics*, vol. 71, pp. 587–596, 2010.

[100] J. Negreira Montero, A. Sjöström, and D. Bard, "Experimental investigation about the influence of the use of glue in joints in lightweight structures," in *Proceedings COMPDYN*, 2011.

[101] K. A. Dickow, P. G. Domadiya, L. Andersen, and P. H. Kirkegaard, "A Parameter Study of Coupling Properties in Finite Element Models of Single-stud Double-plate Panels," *Inter Noise 2011*, pp. 1–7, 2011.

[102] *DTU 31.2 - Building works - Timber frame houses and buildings construction*. 2011.

[103] *DTU 51.3 - Building works - Floors of timber or wood-based panels*. 2004.

[104] M. A. Hamdi and G. Verchery, "A Displacement Method For The Analysis Of Vibrations Of Coupled Fluid-Structure Systems," *International Journal for Numerical Methods in Engineering*, vol. 13, no. April, pp. 139–150, 1978.

[105] V. L. Guadalupe, C. Militello, and M. Recuero, "Acoustoelastic pure-displacement elements based on Biot's poromechanics theory," *Computers and Structures*, vol. 96-97, pp. 54–60, 2012.

[106] H. C. Chen and R. L. Taylor, "Vibration Analysis Of Fluid-Solid Systems Using a Finite Element Displacement Formulation," *International Journal for Numerical Methods in Engineering*, vol. 29, pp. 683–698, 1990.

[107] A. Bermúdez and R. Rodríguez, "Finite element computation of the vibration modes of a fluid—solid system," *Computer Methods in Applied Mechanics and Engineering*, vol. 119, no. 3-4, pp. 355–370, 1994.

[108] K. C. Park, C. A. Felippa, and R. Ohayon, "Partitioned formulation of internal fluid-structure interaction problems by localized Lagrange multipliers," *Computer Methods in Applied Mechanics and Engineering*, vol. 190, no. 24-25, pp. 2989–3007, 2001.

[109] D. M. Tran, "Component mode synthesis methods using partial interface modes: Application to tuned and mistuned structures with cyclic symmetry," *Computers and Structures*, vol. 87, no. 17-18, pp. 1141–1153, 2009.

[110] R. Ohayon, C. Soize, and R. Sampaio, "Variational-Based Reduced-Order Model in Dynamic Substructuring of Coupled Structures Through a Dissipative Physical Interface: Recent Advances," *Archives of Computational Methods in Engineering*, vol. 21, pp. 321–329, 2014.

[111] R. Ohayon and C. Soize, "Clarification about Component Mode Synthesis Methods for Substructures with Physical Flexible Interfaces," *International Journal of Aeronautical and Space Sciences*, vol. 15, no. 2, pp. 113–122, 2014.

[112] C. E. Shannon, "A mathematical theory of communication," *The Bell System Technical Journal*, vol. 27, no. July 1928, pp. 379–423, 1948.

[113] E. T. Jaynes, "Information theory and statistical mechanics," *Physical Review*, vol. 106, no. 4, pp. 620–630, 1957.

[114] K. Burnham and D. Anderson, *Model Selection and Multimodel Inference: A Practical Information-Theoretic Approach*. Springer, 2002.

[115] R. Rubinstein and D. Kroese, *Simulation and the Monte Carlo method*. Wiley, 2nd ed., 2008.

[116] K.-J. Bathe, *Finite Element Procedure*. Prentice-Hall, 1996.

[117] *NF EN ISO 10140-2 : Acoustics – Laboratory measurement of sound insulation of building elements – Part 2: Measurement of airborne sound insulation*. 2013.

[118] *NF EN ISO 717-1 : Acoustics – Rating of sound insulation in buildings and of building elements – Part 1: Airborne sound insulation*. 2013.

[119] T. Kihlman and a.C. Nilsson, "The effects of some laboratory designs and mounting conditions on reduction index measurements," *Journal of Sound and Vibration*, vol. 24, no. 3, pp. 349–364, 1972.

[120] H. Fuchs, X. Zha, and M. Pommerer, "Qualifying freefield and reverberation rooms for frequencies below 100 Hz," *Applied Acoustics*, vol. 59, no. 4, pp. 303–322, 2000.

[121] D. B. Pedersen, J. Roland, G. Raabe, and W. Maysenhölder, "Measurement of the Low-Frequency Sound Insulation of Building Components," *Acta Acustica united with Acustica*, vol. 86, pp. 495–505, 2000.

[122] T. Bravo and S. J. Elliott, "Variability of low frequency sound transmission measurements," *The Journal of the Acoustical Society of America*, vol. 115, pp. 2986–2997, 2004.

[123] C. Hopkins and P. Turner, "Field measurement of airborne sound insulation between rooms with non-diffuse sound fields at low frequencies," *Applied Acoustics*, vol. 66, no. 12, pp. 1339–1382, 2005.

[124] *NF EN ISO 10140-4 : Acoustics – Laboratory measurement of sound insulation of building elements – Part 4: Measurement procedures and requirements*. 2013.

[125] J. Brunskog and P. Davidsson, "Sound Transmission of Structures. A Finite Element Approach with Simplified Room Description," *Acta Acustica united with Acustica*, vol. 90, no. 5, pp. 847–857, 2004.

[126] L. Gagliardini, J. Roland, and J.-L. Guyader, "The use of a functional basis to calculate acoustic transmission between rooms," *Journal of Sound and Vibration*, vol. 145, no. 3, pp. 457–478, 1991.

[127] S. Maluski and B. M. Gibbs, "Application of a finite-element model to low-frequency sound insulation in dwellings," *Journal of the Acoustical Society of America*, vol. 108, no. 4, pp. 1741–1751, 2000.

[128] S. Maluski and B. M. Gibbs, "The effect of construction material, contents and room geometry on the sound field in dwellings at low frequencies," *Applied Acoustics*, vol. 65, no. 1, pp. 31–44, 2004.

[129] P. Davidsson, J. Brunskog, P.-A. Wernberg, G. Sandberg, and P. Hammer, "Analysis of Sound Transmission Loss of Double-Leaf Walls in the Low-Frequency Range Using the Finite Element Method," *Building Acoustics*, vol. 11, no. 4, pp. 239–257, 2004.

[130] P. Jean and J. F. Rondeau, "A Simple Decoupled Modal Calculation of Sound Transmission Between Volumes," *Acta Acustica united with Acustica*, vol. 88, pp. 924–933, 2002.

[131] P. Jean, H. Siwiak, and G. Joubert, "A Decoupled Vibro-Acoustic Development of FEM: Application to Laboratory Modelling," *Building Acoustics*, vol. 13, no. 2, pp. 83–98, 2006.

[132] J.-D. Chazot and J.-L. Guyader, "Prediction of transmission loss of double panels with a patch-mobility method," *The Journal of the Acoustical Society of America*, vol. 121, no. 1, p. 267, 2007.

[133] A. Dijckmans, G. Vermeir, and W. Lauriks, "Sound transmission through finite lightweight multi-layered structures with thin air layers.," *The Journal of the Acoustical Society of America*, vol. 128, no. 6, pp. 3513–3524, 2010.

[134] F. Fahy, *Foundations of Engineering Acoustics*. Academic Press, 2003.

[135] *NF EN ISO 10140-5 : Acoustics – Laboratory measurement of sound insulation of building elements – Part 5: Requirements for test facilities and equipment*. 2013.

[136] M. R. Schroeder and K. Kuttruff, "On Frequency Response Curves in Rooms. Comparison of Experimental, Theoretical, and Monte Carlo Results for the Average Frequency Spacing between Maxima," *The Journal of the Acoustical Society of America*, vol. 34, no. 1, pp. 76–80, 1962.

[137] E. Reynders, "Parametric uncertainty quantification of sound insulation values," *The Journal of the Acoustical Society of America*, vol. 135, no. April 2014, pp. 1907–1918, 2014.

[138] C. Hopkins, *Sound Insulation*. Butterworth-Heinemann, 2007.

[139] A. Osipov, P. Mees, and G. Vermeir, "Low-Frequency Airborne Sound Transmission through Single Partitions in Buildings - Part 2," *Applied Acoustics*, vol. 52, pp. 273–288, 1997.

[140] J. Davy, "The variance of decay rates at low frequencies," *Applied Acoustics*, vol. 23, no. 1, pp. 63–79, 1988.

[141] *NF EN ISO 10140-3 : Acoustics – Laboratory measurement of sound insulation of building elements – Part 3: Measurement of impact sound insulation*. 2013.

[142] J. Brunskog and P. Hammer, "The interaction between the ISO tapping machine and lightweight floors," *Acta Acustica (Stuttgart)*, vol. 89, no. 2, pp. 296–308, 2003.

[143] *NF EN ISO 717-2 : Acoustics – Rating of sound insulation in buildings and of building elements – Part 2: Impact sound insulation*. 2013.

[144] A. Rabold, M. Buchschmid, A. Düster, G. Müller, and E. Rank, "Modelling the excitation force of a standard tapping machine on lightweight floor structures," *Building Acoustics*, vol. 17, no. 3, pp. 175–197, 2011.

[145] R. Sampaio and C. Soize, "Remarks on the efficiency of POD for model reduction in non-linear dynamics of continuous elastic systems," *International Journal For Numerical Methods In Engineering*, vol. 72, no. 1, pp. 22–45, 2007.

[146] J. Negreira and D. Bard, "Conjoint FE-SEA prediction tool – First Steps," *Silent Timber Build Project WG1 working document*, 2015.

[147] B. Zeitler, T. Nightingale, and F. King, "Methods to control low frequency impact noise in wood-frame construction," in *Proceedings Acoustics08*, 2008.

[148] B. Zeitler, S. Schoenwald, and T. Nightingale, "Parametric Study of Sound Transmission Through Lightweight Floors," in *Proceedings Internoise*, 2010.

[149] M. Kylliäinen, "Uncertainty of Impact Sound Insulation Measurements in Field," tech. rep., Tampere University of Technology - Department of Civil Engineering, 2003.

[150] G. Allaire, *Conception optimale de structure*. Springer-Verlag Berlin Heidelberg, 2007.

Résumé

La compréhension et la prédiction du comportement vibro-acoustique des systèmes légers bois du bâtiment constitue un enjeu scientifique d'actualité. En 2015 une étude montrait encore que presque la moitié de ces systèmes constructifs n'offrait pas satisfaction. Un modèle prédictif à l'échelle du bâtiment, en cours de normalisation, permet de prendre en compte la performance individuelle des différents systèmes séparatifs pour remonter à un niveau de performance globale. La difficulté scientifique réside alors dans l'évaluation de la performance individuelle associée à chaque conception admissible, dans un vaste ensemble de systèmes techniquement réalisables.
Dans cette recherche, une méthodologie est proposée pour la construction de modèles numériques capables de prendre en compte, aux basses fréquences, la complexité et la diversité des systèmes bois constitués de multiples plaques, poutres, cavités acoustiques et matériaux poroélastiques. En accord avec les procédures d'évaluation normalisées, des modèles déterministes pour les excitations mécaniques du système sont construits. Une approche probabiliste est alors développée en réponse à la problématique des incertitudes liées à la construction légère. Ainsi, en résolvant un problème stochastique inverse utilisant des données expérimentales pour identifier les hyperparamètres de modèles probabilistes développés, il est possible de quantifier la propagation des incertitudes du système à la performance prédite en conditions de laboratoire.
Par suite, des configurations optimales, robustes aux incertitudes, sont recherchées. Du fait de la nature combinatoire du problème d'optimisation, un algorithme génétique, particulièrement adapté à un espace de recherche discret ainsi qu'à l'optimisation multi-objectif, est mis en oeuvre. Dans les cas traités, les configurations optimales tendent vers une maximisation de la rigidité structurelle.

Mots clefs: Vibro-acoustique linéaire, Incertitudes, Modèles probabilistes, Problème stochastique inverse, Conception robuste, Mesures vibratoires

Abstract

Being able to understand and predict the vibroacoustic behavior of lightweight wood-based building systems contitute a serious scientific concern. In 2015, acoustic comfort investigation claims that unsatisfactions are expressed with respect to around 50% of such constructions. In particular, low frequency discomfort is target of criticism. A methodology was proposed, currently running through standardisation process, which translates the individual performance of the building systems into a global building performance index. The challenge consequently lies in the prediction of the individual performances in regard to the wide spread of wood based designs.
In this research, a methodology is introduced for the construction of computational models able to handle the complexity and diversity of the systems of interest, constituted of multiple boards, stiffeners, cavities and poroelastic media. External excitations are constructed according to standard evaluation procedures. Then, a probabilistic approach is undertaken in order to take into account the uncertainty problematic, inherent to lightweight wood based constructions. In particular, stochastic inverse problems are constructed to identify, from experimental measurements, hyperparameters associated with *ad hoc* probabilistic models. Eventually, uncertainty quantification can be performed in regard to predicted performance in laboratory conditions.
Following, robust optimal designs are sought in the presence of uncertainties. No continuous mapping from the search space of the configurations to the space of the fitness functions representative of the objective performance exists and derivatives cannot be defined. By way of consequence, the class of evolutionnary algorithms, suited to discrete search spaces as well as multi-objective optimisation, is chosen. Considered optimisation problems displayed preferential directions of the genetic algorithm towards stiffest admissible designs.

Keywords: Linear vibroacoustics, Uncertainties, Probabilistic models, Stochastic inverse problem, Robust design, Vibration measurements